

Simulations of CO₂ injection in saline aquifer formations



UNIVERSITY OF BERGEN

Lars Andreas Lågeide

Master degree in process technology

University of Bergen, Norway

August 2009

Acknowledgements

This thesis was performed and completed at the programme for Process Technology, Department of Physics and Technology at the University of Bergen.

I would like to thank my supervisor, Professor Bjørn Kvamme for his suggestions and assistance during the writing of my thesis, even though he is a very busy man. I want to thank Shunping Liu for all her help and shared experience. During the writing and simulating they have both been enthusiastic and supportive about my work. Postdoc Doctor Scient. Tatyana has also been more than helpful in answering my many questions and deserves much gratitude.

I would also like to thank Jordan Bauman for listening to all of my frustrations regarding the use of black boxes, and crashing simulations. And last but not least, I would like to thank my very supporting girlfriend for helping me through these last months of hardship.

Lars Andreas Lågeide

Bergen 14.07.09

Summary

This thesis is devoted to studies of long term storage of carbon dioxide in geological formations such as saline aquifers. The goal of the thesis is to contribute to the development of a totally integrated storage evaluation tool which considers reactive transport as well as geomechanics. Our secondary goal was to investigate the effects of introducing a fracture in the confining cap rock with respect to the mechanical and chemical aspects of gas injections.

In order to safely assume that injected gas will not escape the geological formation, it is imperative to obtain knowledge about reservoirs and the dynamics connected carbon dioxide injections. Laboratory experiments can only provide limited knowledge and large scale projects are economically not feasible and will only produce results after several years. The best approach would be to develop and utilize reservoir simulators capable of predicting the chemical and mechanical behaviour. However such simulators need benchmarking and comparison with respect to injections in real reservoirs.

There is no need to look further than our own continental shelf to find operational fields with pilot projects of CO₂ injections. The SACS-project (Saline Aquifer Carbon dioxide storage) was initiated in 1996 at the Sleipner field and has been continuously monitored is a valuable source of data for simulation comparisons.

The coupled codes called known as Retraso CodeBright (RCB) have been used to simulate the injection of CO₂ in an aquifer. RCB originates from the Technical University of Catalonia, of which the team contributing with the two chemical and mechanical parts of the code consisted of Maarten W. Saaltink, Carlos Ayora and Sebastia Olivella. [RCB manual] The platform was initially intended for standard conditions at 1 atm pressure and 15 celcius. Reservoirs of interest to geological sequestration are generally at larger depths, which mean that the governing equations has to deal with higher pressures, temperature and stresses than originally intended.

Despite of the intended application of the software, RCB was selected as a candidate for project "Observing the effect of long term CO₂ storage in saline aquifers" which is carried out in the Department of Physics and Technology at the University of Bergen, Norway. [art] As part of this project, and as initially intended, the RCB code has received a range of modification in order to apply on deep formation CO₂ storage.

The simulations were run with conditions similar to those found in the Utsira formation supplemented with data from simulations in the FLAC3D model. However, due to limited sources of relevant use and the original application of the code platform, I have spent some time learning how to apply the code on deep formation conditions. Most of my initial simulations diverged and it's only during the last 3 months that I have succeeded in producing presentable data.

Contents

Acknowledgements	1
Summary	2
1. Abbreviations.....	8
3.1. Carbon dioxide storage in geological formations.....	10
3.2. Carbon dioxide injection.....	11
3.3. Utsira	11
4. Porosity, permeability and capillarity	12
4.1. Porosity.....	12
4.2. Permeability.....	14
4.3. Diffusion	16
4.4. Viscosity.....	17
4.5. Henry Darcy	18
4.6. Relative permeability	21
4.7. Surface- and Interfacial tension.....	22
4.8. Surface tension	24
4.9. Miscibility.....	25
4.10. Wetting.....	27
4.11. Capillarity.....	30
4.12. Saturation	32
4.13. Drainage and Imbibition.....	33
5. Mineral chemistry	35
5.1. Solids	35
5.2. Bonding forces	35
5.3. Mineral classes.....	36
5.4. Minerals.....	37
6.1. Concentration and activity	38
6.2. Gibbs free energy.....	38
6.3. Phase rule and chemical potential.....	39
7. Aqueous solutions and minerals.....	43
7.1. Water.....	43
7.2. Mineral solubility	46
7.3. Reaction kinetics	50
8. Poroelasticity and geomechanical model.....	55

8.1.	Stress and strain.....	55
8.2.	Pore pressure.....	57
8.3.	Poroelastic properties	57
9.	Flow equations.....	59
9.1.	Reactive transport.....	59
9.2.	Geomechanics.....	61
10.	Simulation software	63
10.1.	RetrasoCodeBright	63
10.2.	Governing equations and algorithms in CodeBright module	64
11.	Reactive transport in Retraso part	71
12.	User interfaces and simulation software.....	75
12.1.	Visual retraco.....	75
12.2.	GiD.....	76
13.1.	Prior work and related projects	77
13.2.	Basic simulation setup.....	79
13.3.	The simulation data plan.....	85
13.4.	More detailed simulation setup.....	87
13.5.	RCB sampling and GiD	91
14.1.	Simulations and convergence problems	92
14.2.	Break-through of injected carbon dioxide.....	93
14.3.	Point evolution.....	94
14.4.	Tables	99
14.5.	Graphical representations	103
15.	Discussion	122
15.1.	The software	122
15.2.	The results	122
15.3.	Further work	124
16.	Conclusions.....	126
17.	References	127
	Appendix A – Input files for the simulation.....	128
	Appendix B – Guide to creating input files in Visual Retraso	128
	Appendix I	129
17.1.	Case A.....	130
17.1.	Case B.....	131

17.2.	Case C	132
17.3.	Case D.....	133
17.4.	Case A2.....	134
17.5.	Case B2	135
17.6.	Case C2	136
17.7.	Case D2.....	137
Appendix II.....		138
17.8.	Case A.....	139
17.9.	Case B	140
17.10.	Case C.....	141
17.11.	Case D.....	142
17.12.	Case A2.....	143
17.13.	Case B2	144
17.14.	Case C2.....	145
17.15.	Case D2.....	146
17.16.	pH values	147
Appendix III.....		148
17.17.	Case A.....	149
17.18.	Case B.....	149
17.19.	Case C.....	150
17.20.	Case D.....	150
17.21.	Case A2.....	153
17.22.	Case B2	156
17.23.	Case C2.....	158
17.24.	Case D2.....	161
Appendix IV		166
17.25.	Case A.....	167
17.26.	Case B.....	168
17.27.	Case C.....	169
17.28.	Case D.....	170
17.29.	Case A2.....	171
17.30.	Case B2.....	172
17.31.	Case C2.....	173
17.32.	Case D2.....	174

Appendix V	175
17.33. Case A.....	176
17.34. Run B	177
17.35. Case C.....	178
17.36. Case D.....	179
17.37. Case A2.....	180
17.38. Case B2.....	181
17.39. Case C2.....	182
17.40. Case D2.....	183
Appendix VI	184
17.41. Case A.....	185
17.42. Case B.....	186
17.43. Case C.....	187
17.44. Case D.....	188
17.45. Case A2.....	189
17.46. Case B2.....	190
17.47. Case C2.....	191
17.48. Case D2.....	192
Appendix VII	193
17.49. Case A.....	194
17.50. Case B.....	196
17.51. Case C.....	198
17.52. Case D.....	200
17.53. Case A2.....	202
17.54. Case B2.....	204
17.55. Case C2.....	206
17.56. Case D2.....	208
17.1. Tables	210
Appendix VIII	211
17.2. Case A.....	212
17.3. Case B.....	213
17.4. Case C.....	214
17.5. Case D.....	215
17.6. Case A2.....	216

17.7.	Case B2	217
17.8.	Case C2	218
17.9.	Case D2	219
Appendix IIX.....		220
17.10.	Case A	221
17.11.	Case B	221
17.12.	Case C	222
17.13.	Case D	222
17.14.	Run A2	223
17.15.	Run B2	223
17.16.	Run C2	224
17.17.	Run D2	224

1. Abbreviations

T	Temperature (K)
P	Pressure (bar)
ϕ	Fugacity coefficient (I/P)
a	Activity
f	Fugacity
Z	Compressibility factor
ΔG	Gibbs free energy of a reaction
ΔH	Enthalpy
ΔS	Entropy
n	Moles
M	Molar mass
m	Mass (g)
μ	Chemical potential
γ	Activity coefficient for ionic species.
E_a	Apparent activation energy used for mineral kinetics
K	Equilibrium constants for reactions
K	Kinetic constant (n/m^2s)
r	Rate (n/s)
R	Gas constant ($8.3145kJ/nK$)
ρ	Density CO_2 or aqueous phase

2. Introduction

This thesis is related to the studies of long term storage of carbon dioxide in geological formations such as aquifers. It is imperative to obtain knowledge about

The goal of the thesis is to contribute to the development of a totally integrated storage evaluation tool which considers reactive transport as well as geomechanics. As an extension of this goal, the secondary aim is to investigate the effects of introducing a fracture in the confining cap rock with respect to the mechanical and chemical aspects of gas injections.

Information about the changes in earth's climate has been systematically gathered and compared since the middle of the 19th century. The gathered data show trends and changes in the global climate. Among these trends the most obvious is the change in global average temperature and the concentration of carbon dioxide in the atmosphere. However, these observations can be said to vary naturally without the contribution of human activity. [1] As this thesis does not consider the discussions regarding cause and effect of the global warming; the contribution to this debate will only be limited to the discussion regarding geological sequestration of CO₂ as a viable solution to reduce the magnitude of atmospheric emissions.

In the early 21st century the focus on carbon dioxide as a greenhouse gas increased. It is now commonly known that carbon dioxide contributes to the greenhouse effect and there is a larger acceptance within scientific communities that emission of CO₂ gas into the atmosphere is actually causing global warming and thus altering the climate. This acceptance has resulted in the development and investigation of several methods to store greenhouse gases in order to reduce the emissions. To achieve a reduction in the emission of greenhouse gasses there are two obvious and equally important solutions: Reduction of atmospheric emissions through new technology and through storage.

Injecting the carbon dioxide into geological formations may prove to be a secure storage location for long periods of time. However, the injected CO₂ will dissolve and dissociate causing the acidity of the formation to increase. A higher acidity might affect the mineralogy of the solid matrix.

In this thesis, a combination of codes known as Retraso CodeBright (RCB) has been used to simulate the injection of CO₂ in an aquifer. RCB originates from the Technical University of Catalonia, of which the team contributing with the two chemical and mechanical parts of the code consisted of Maarten W. Saaltink, Carlos Ayora and Sebastia Olivella.

The platform was initially intended for standard conditions at 1 atm pressure and 15 celcius. Despite the intended application of the software, RCB was selected as a candidate for project "Observing the effect of long term CO₂ storage in saline aquifers" which is carried out in the Department of Physics and Technology at the University of Bergen, Norway. As part of this project, and as initially intended, the RCB code has received a range of modification in order to apply the code on deep formation CO₂ storage. The larger depths also mean that the code has to deal with higher pressures, temperature and stresses than originally intended.

The simulations were run with conditions similar to those found in utsira/Flac3D article. However, due to limited sources of relevant use and the original application of the code platform, I have spent some time learning how to apply the code on deep formation conditions. Most of my initial simulations diverged and it's only during the last 3 months that I have succeeded in...

With some basic experience and operator knowledge, the simulation platform Retraso CodeBright can be described as a rather user friendly software that requires a relatively small amount of time and effort to initiate and run. In terms of processing time, each case requires a total simulation time ranging from 3 to 7 days, depending on the processing hardware and complexity of the input data. The initial 2-layer cases required an average of 3 days to complete a 100 year simulation containing 60 000 time steps, while the more complex fracture cases presented in this thesis required more than 7 days.

3. Geological sequestration

This chapter starts with an introduction to the general reservoir layout and the properties of the solid matrix and it's containing fluids. The following chapters contain a more elaborate explanation of the most important reservoir properties.

Much of the material found in this chapter is gathered from personal lecture notes and curriculum reading from reservoir subjects.

3.1. Carbon dioxide storage in geological formations

With the increased focus on carbon dioxide as a greenhouse gas, there is a need for solutions that give means for secure long term storage. Injecting CO₂ into geological formations may prove to be a secure storage solution for thousands of years and more. Reservoirs at depths below 1000m, such as the Utsira formation, have high pressures due to the overburden stress. In the pressure ranges at these depths, CO₂ has a density not far from that of a liquid. This enables efficient use of the available storage space in the formation. This thesis is mainly focused on the saline aquifer type of reservoirs, which can be described as porous formations containing brine or water saturated with indigenous species. Operational and depleted oil reservoirs may also be utilized in geological storage.

Geological storage of CO₂ is possible due to a range of mechanisms, such as entrapment below a low permeable or impermeable layer that confines the gaseous species, preventing them from reaching the surface. Dissolution and dissociation of CO₂ in water contained in the formation also plays an important role in the storage of CO₂. Existing gas and oil reservoirs prove that long-term geological storage is possible over millions of years at ideal conditions. That is without earthquakes and similar tectonic forces that might induce fractures in the cap rock

The actual process of carbon dioxide storage will utilize much of the already existing technology and equipment used oil companies today. Procedures for drilling, injection, simulations and monitoring can easily be adapted to CO₂ injection. Since these solutions have already been used for many years under varying conditions, the geological storage can be classified as low risk operations. But even though the risks of leakage are low, the impact of an eventual has to be assessed with respect to the ecological environment and humans.[2]

At the right conditions CO₂ gas can escape from the aquifer. With a billion tonnes of injected CO₂ and additional CO₂ concentrations from calcium carbonates, a small fracture can release large quantities of the stored gases. External reservoir influences such as production wells or can potentially

3.2. Carbon dioxide injection

Carbon dioxide has to be injected with a pressure higher than that of the local static reservoir pressure in order to obtain a desired injection rate. The injected CO₂ will displace the surrounding formation water and gradually increase the pore pressure of the fluids. [2] At deep reservoir conditions CO₂ gas has a lower density than that of the formation water. The injected CO₂ will thus naturally rise in a plume towards the top of the formation due to the buoyancy effect. In a heterogeneous reservoir the gas will be distributed unevenly according to the change in local permeability. The shape of the gas plume will be greatly influenced by these layers. At some point the rising gas will reach the confining layer of low permeable rock and continue the displacement laterally, filling any structural traps and fractures in the cap rock. [1] Local fracturing in the vertical direction outside (not close to casing) the injection well will change the local pressure distribution around the well and may be a tool for reducing the necessary injection pressure. [B.Kvamme](#)

Once CO₂ is injected it will start to dissolve into the formation water and the excess mobile CO₂ gas will migrate buoyantly towards the cap rock and accumulate. The effective storage capacity is influenced by the permeability of the fracture. The migration of mobile CO₂ gas is important for the short time safety of the injection site, as the excess CO₂ might reach fractures or abandoned wells that could potentially release the injected gas. The dissolved CO₂ will further react with the water and form carbonic acid which will lower the pH. A lower pH increases the reactivity of the water with respect to the minerals present in the formation, minerals such as calcite.

3.3. Utsira

The SACS (Saline Aquifer CO₂ Storage) project which is considering the re-injection of CO₂ from the Sleipner field into the Utsira formation is an interesting pioneer project with valuable information for future projects. Since 1996 Statoil has captured CO₂ from Sleipner west and injected it into the saline formation of Utsira. So far more than 10 million metric tons have been injected in an area covering three square kilometres the total 26 000 square kilometres available. That's more than 1 megaton per year.

The obtained seismic data from the carbon dioxide injection at Utsira makes the formation a rather interesting model for benchmarking reservoir simulators. The CO₂ injection has been periodically monitored by means of seismic surveys, providing a four-dimensional overview of the displacement due to the immiscible CO₂ front. However, a four-dimensional surveillance does not provide information about the reactions between the CO₂, water and minerals in the formation. In the southern region where the CO₂ is being injected, the top of the sand is located at depths between 600 to 1150m, reaching a maximum thickness of 300m.[3]

4. Porosity, permeability and capillarity

A porous medium consists of a solid matrix filled with small pockets called pores. In a permeable porous medium the pores are interconnected in a pore network enabling displacement of a fluid.

4.1. Porosity

Approximately every type of rock and sediment contains pores or voids in multiple shapes and sizes. The dimensions vary from the size of a single molecule to the rare extremes such as caverns. Porosity is a dimensionless size and can be found for a given sample by dividing the volume occupied by pores with the total volume of the sample (Equation 4.1.1). This fraction is the total porosity.

$$\Phi_{Tot} = \frac{V_{Pore}}{V_{Total}} = \frac{V_{Total} - V_{Matrix}}{V_{Total}} \quad \text{Equation 4.1.1}$$

A porous medium consists of a solid matrix with an interconnected network of pores. Both the matrix and the pore network are assumed to be continuous, but a fraction of the pores are separated from the network and trapped in the solid matrix along with the containing fluid. Hence the total porosity is divided into two segments; the efficient porosity and the residual porosity. Equation 4.1.2 shows the components of the total porosity. [4]

$$\Phi_{Tot} = \Phi_{Eff} + \Phi_{Res} \quad \text{Equation 4.1.2}$$

The efficient porosity is the part of the total porosity that is interconnected, allowing any containing fluids to be displaced within the network. Pores that are trapped and separated from the network make up the residual porosity. Depending on the constituent minerals the total porosity of a rock formation may vary from close to zero to over 50%, while the effective porosity is less due to the trapped pores.

An average sedimentary rock consists of mineral grains in multiple shapes and sizes that are crushed together at high pressures over time, forming a compact solid with cavities. Porosity changes with the properties of the grain size, shape and dispersion. Figure 4.1.1 is an artificial visualization of a porous media consisting of spheres or grains in different sizes and packing structure.

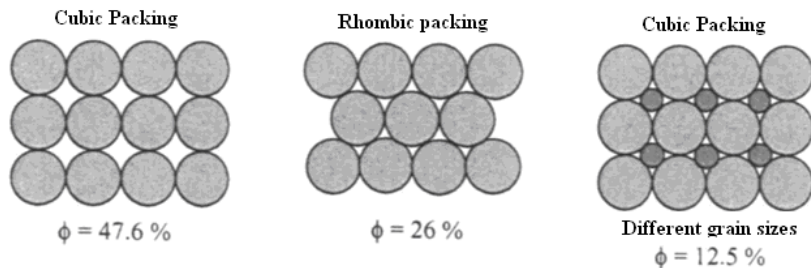


Figure 4.1.1 – Artificial porosity. The connection between porosity and packing of minerals^[4]

Most simulation software calculates the porosities using spheres, but in reality the building blocks are not perfectly spherical, but rather built up by multiple polygons as shown on the left hand side of Figure 4.1.2.

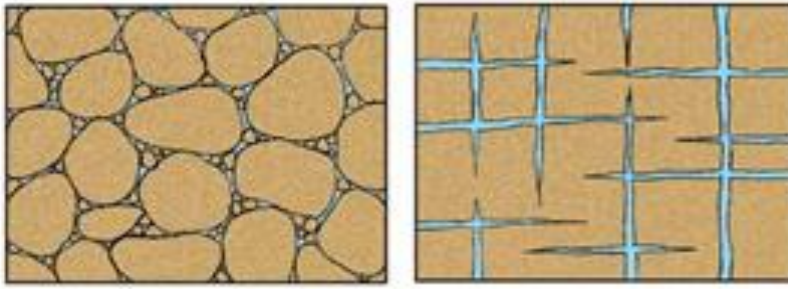


Figure 4.1.2 – A thought porous medium with fractures [5]

The storage capacity of a fluid in a reservoir is determined by the porosity. For a given fluid in a multiphase system, the respective amount is also dependant on the pore saturation properties which will be explained in Chapter 4.12. In a sedimentary aquifer the water is mainly stored in the pores between the granular sandstone. Displacement of water may occur in these pores, but the main transmission system is often the fractures as shown on the right hand side of figure xxx. “These fractured formations are known as dual porosity aquifers, and their permeability reflects the frequency, openness and interconnectivity of the fractures”. [5]

Pores formed at the same time as the rock are called primary openings. Pores or fractures that have appeared after the rock was formed are called secondary openings. Figure 4.2.1 and Figure 4.2.2 shows the difference between primary and secondary porosity. On the right hand side of Figure 4.2.1 there are two cases representing a porous media with well-sorted and poorly sorted sand. [6]

Fractures are caused by formational stress, which in turn usually derives from tectonic forces in folds and faults. These are termed natural fractures, as opposed to induced fractures. Induced fractures are created by stress from drilling operations or by purposely fracturing a reservoir through hydraulic pressure. Most natural fractures are more or less vertical. Horizontal fracture may exist for a short distance, propped open by bridging of the irregular surfaces. Most horizontal fractures, however, are sealed by overburden pressure. Induced fractures may connect the wellbore to natural fractures that would otherwise not contribute to flow capacity. [7]

Sandstone, like the type found in the Utsira formation, has a porosity ranging from 10 to 40 % depending on the cementation and consolidation in the formation. Chalkstone and dolomite has a large variation in porosity from 5 to 25 %. Chalkstone has smaller pores compared to the dolomite, which means less porosity. On the other hand, chalkstone is easily fractured, causing a small increment in porosity and a larger increment in the permeability. Clay and shale has a porosity ranging from 20 to 40 % depending on the reservoir depth. [4]

4.2. Permeability

As explained in the previous chapter, a porous medium may contain a network of pores capable of displacing a fluid. The extent of the network's ability to circulate a one-phase fluid like gasses or liquids is defined as the medium's absolute permeability "K".

The well-sorted sand in Figure 4.2.1 would have a lower permeability than that of poorly sorted sand. By introducing a secondary porosity to a respective porous media, the permeability would increase. However, the total porosity is not influenced in the same magnitude as the permeability. The volume of the fractures is often small compared to the total pore volume of the reservoir.

A fracture is often defined as a high permeability path in a porous rock with a lower permeability. Hence the fractures connect multiple pores and act like a highway for the displacement of fluids. Fractures may also be filled with a cementing material, such as precipitating calcite, leaving the fracture with no permeability. [7]

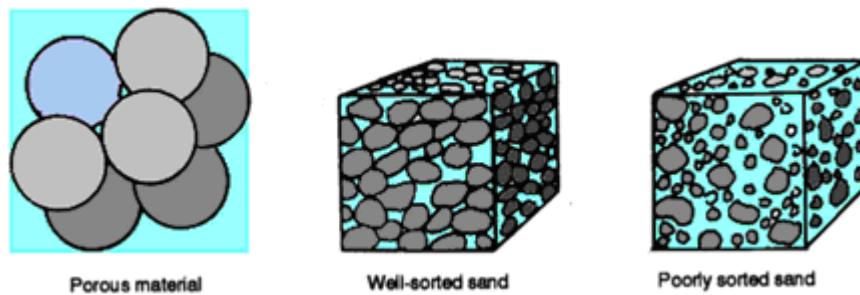


Figure 4.2.1 – Primary openings in a porous media^[6]

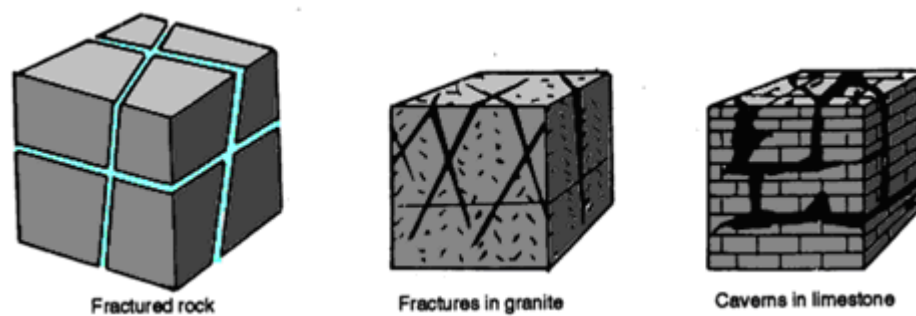


Figure 4.2.2 – Secondary openings in a porous media^[6]

It is obvious that a pressure difference has to be present in order to displace a fluid through the porous formations of a reservoir. The total amount displaced depends on the properties of both the fluid and solid matrix. A correlation between the effective porosity and the permeability is natural, but the permeability is also dependant on a whole range of other physical factors. Factors like the relationship between pore-necks and pore-volumes, the pore size distribution and last, but not least, the tortuosity or curving of the flow pathway.

4.2.1. Pore neck and pore size ratio

In many ways the permeability is a measure of the pore neck size. If the neck of a pore is too small the permeability might be reduced or nonexistent, depending on the wetting properties and viscosity of the fluid. Figure 4.2.3 is a visualisation of a single pore in a porous media.

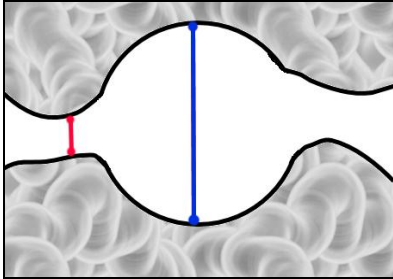


Figure 4.2.3 – Cross-section of a single pore in a porous media

The red line indicates the dimension of the pore neck, while the blue line represents the pore dimension. In diffusion the tortuosity has to be corrected for due to the reduced area of diffusion.

4.2.2. Tortuosity

Describing a medium or shape as tortuous means that it, or in this case that the flow path in the pore network, is twisted or curved. Potential flow paths in a porous medium can be significantly longer than the straight line from A to B. In Figure 4.2.4 below, a straight line is marked by the red arrow, and a potential flow path is indicated by the blue line.

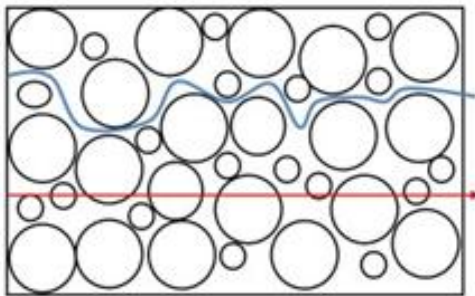


Figure 4.2.4 – The tortuosity of flow paths in a porous media ^[8]

Tortuosity is a curving property contributing to the permeability. One way to describe the path of flow is to estimate the real length by connecting multiple finite lines segments along the curved path. As shown in Equation 4.2.1, a simple mathematic method can then be used to estimate the tortuosity, where L_{Real} is the diagonal line of the flow path, and L_{A-B} is the real path of the flow.

$$\tau = \frac{L_{Real}}{L_{A-B}}$$

Equation 4.2.1

The dimensionless range of tortuosity usually lies between 1.25 and 1.78. [8] The higher the tortuosity of a media, the lower the permeability.

4.3. Diffusion

By definition diffusion is the movement of an individual component through a mixture caused by a physical stimulus like concentration, pressure, temperature or chemical potential. The most common cause of diffusion is a concentration gradient of the diffusing component. In order to equalize the concentration, the component is moved in a direction so that the gradient is nullified. In cases where the gradient is constantly maintained by constantly adding the diffusing component, a steady flow will be established in the respective direction.[9]

Molecular diffusion is typically described mathematically using Fick's laws. Fick's first law describes the relation between diffusive flux and the concentration. The law says that the flux of a component moves from an area of high concentration to an area of low concentration, with a rate proportional to the gradient of the concentration. In one dimension the equation for the flux would be:

$$J = -D \frac{\partial C}{\partial x} \quad \text{Equation 4.3.1}$$

Where J is the diffusion flux; D is the diffusion coefficient; C is the concentration and χ the length. C and χ constitutes the concentration gradient. For a component A diffusing into component B, Equation 4.3.1 can be written as:

$$J = -D_{AB} \frac{dC_A}{\delta\chi} \quad \text{Equation 4.3.2}$$

Where D_{AB} is the respective diffusivity of component A into B. Fick's second law predicts the change in concentration over time due to the diffusion.

$$\frac{dC}{\delta t} = D \left(\frac{dC^2}{\delta^2 \chi} \right) \quad \text{Equation 4.3.3}$$

There are many areas of diffusion with respective modifications and assumptions. Components can diffuse from any phase to another, gas to gas, liquid to liquid - even from solids to gas as some rocks or organic material tend to be porous.

4.4. Viscosity

Viscosity is a property of liquids and solids alike. A fluid with a high viscosity would flow at a lower rate than that of a low viscosity fluid. This is because there is a friction force acting between the molecules in the bulk. Gases experience less or none of the friction due to the distance between the gas molecules, but at high pressures the viscosity is an important factor that should be included in a simulation.

By definition a liquid flows when shear stress is exerted on it. [9] As shown in Figure 4.4.1, the velocity of water flowing in a tube is not constant over the whole cross section. There is a gradient velocity increasing from 0 where the fluid meets the wall, to the maximum velocity (v) at the centre with an average gradient of v/r .

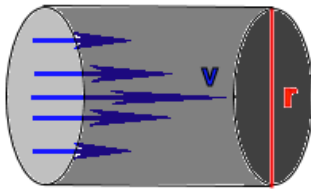


Figure 4.4.1 – Laminar flow in a two-dimensional cross -section

For most liquids the velocity gradient is proportional with the shear stress acting on the fluid so that

$$\nabla v = \frac{\sigma}{\eta}$$

Equation 4.4.1

Where the constant σ is the shear stress and η is the viscosity of the liquid [10] In many situations, we are concerned with the ratio of the viscous force to the inertial force, the latter characterised by the fluid density ρ . Kinematic viscosity can be obtained by dividing the absolute viscosity of a fluid with its mass density. The ratio is characterised by the kinematic viscosity (Greek letter nu, ν), defined as follows:

$$\nu = \frac{\mu}{\rho},$$

where μ is the dynamic viscosity (Pa*s), ρ is the density (kg/m³), and ν is the kinematic viscosity (m²/s).

4.5. Henry Darcy

There is no simple connection between the porosity of a medium and its permeability. The permeability is not even a clearly defined physical size by more fundamental constituents. Although, permeability can be defined the inverse of the mediums resistance to flow, giving rise to its definition through Darcy's law. Darcy's law can be used to estimate the permeability of a sample, which is measured in units of "darcy"

Darcy's law, formulated by Henry Darcy, is an equation that describes the flow of a fluid through a porous medium. The law is based on the results of his experiments with flowing water through filters of sand. He found that the volume flow was proportional with pressure difference through the filter, so that:

$$\frac{Q}{A} = a\Delta p \quad \text{Equation 4.5.1}$$

where A is the cross-section of the flow path, Q is the volume flow, ΔP is the pressure difference and the constant "a" is a proportionality constant that depends on the properties of the pore system and fluid.[11]

4.5.1. Darcy's law - The equation

Using a two-dimensional example as shown in Figure 4.5.1, Darcy's law is the proportional relationship between the discharge rate through a porous medium, the viscosity of the fluid and the pressure drop over a given distance.

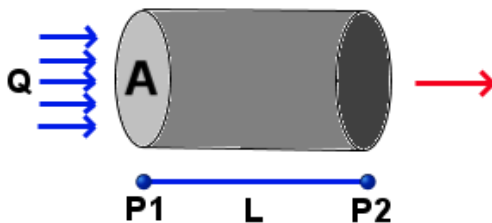


Figure 4.5.1 – Two dimensional cross -section of flow

The pressure drop from P1 to P2 over the distance L, enables a volume flow Q to be displaced through the cross section A of a sample. Equation 4.5.2 shows the connection between the parameters.

$$Q = \frac{-\kappa A \Delta P}{\mu L} = \frac{[\text{m}^3/\text{s}] \cdot [\text{m}^2] [\text{Pa}]}{[\text{kg}/\text{m} \cdot \text{s}] [\text{m}]} \quad \text{Equation 4.5.2}$$

In short; the total discharge equals the product of the Permeability in the medium, the cross-section of flow, and the pressure drop over a length - divided by the product of the viscosity and distance of the pressure drop. K is the absolute permeability of the medium, and μ is the viscosity of the fluid.

The negative sign in the equation is due to the drop from high to low pressure. In differential form Equation 4.5.2 can be written as:

$$Q = \frac{-\kappa A}{\mu} \frac{\delta p}{\delta x}$$

Equation 4.5.3

Where dP/dx is the gradient pressure in the direction of the cross-sectional flow.

With some rearranging, the division of Equation 4.5.3 with the cross-sectional area respectively results in Equation 4.5.4.

$$q = \frac{-\kappa}{\mu} \nabla P$$

Equation 4.5.4

By further dividing Equation 4.5.4 with the porosity of the media we get Equation 4.5.5.

$$v = \frac{q}{\Phi} = \frac{-\kappa}{\mu \cdot \Phi} \nabla P$$

Equation 4.5.5

ΔP is the gradient pressure and ϕ the porosity. The darcy flux (q) in Equation 4.5.4, is the cross-sectional discharge in length over time, while the pore velocity (v) in Equation 4.5.5 is the real velocity experienced by a molecule passing through the porous medium. Dividing Equation 4.5.4 with the porosity (ϕ) takes into account that not all of the porous volume is available for flow. However, Darcy's law is only valid for fluids displaced at rates with a low Reynolds number.[12]

A porous medium has a permeability of one darcy when the flow is at $1 \text{ cm}^3 / \text{cm}^2\text{s}$ under the influence of a pressure gradient estimated to 1 atm/cm and a viscosity of 1cP (20°C). A common unit for permeability is the darcy (D) or more commonly the millidarcy (mD). Other applied units are cm^2 and the SI unit m^2 . One Darcy is approximately $1 \cdot 10^{-12} \text{ m}^2$.

4.5.1.1. Reynolds number

A fluid flowing through piping behaves in two different ways depending on the relationship between the fluid velocity and pressure drop. In experiments conducted by Osborne Reynolds, observations proved that at low flow rates the fluid velocity gradient would be parallel with the direction of flow, but at higher flow rates waves would form. Hence the flow patterns are divided into laminar and turbulent flow.

Reynolds studied the transition between laminar flow and turbulent flow, and found that the critical velocity for the transition depends on the diameter of the flow path, the viscosity, density and the average velocity. The dimensionless variable termed the Reynolds number is defined in Equation 4.5.6.

$$\text{Re} = \frac{\rho v D}{\mu}$$

Equation 4.5.6

Where ρ is the density of the fluid, v is the average velocity, D the diameter of the flow path and μ the viscosity. The magnitude of the Reynolds number is independent of the units used as long as they are coherent. Observations have shown that the transition from laminar to turbulent flow occurs over a wide range of Reynold numbers. [9]

4.5.2. Darcy's law, gases and the Klinkenberg effect

Darcy's law is known to be valid for liquids at low Reynolds's numbers; however the law can't be applied to gases without accounting for the compressibility and other deviations from liquids. Due to the compressibility of gases the flow (Q) will be dependant on the gas pressure. By assuming that the flow rate (Q) is equal to the mean flow rate (Q_m) with a mean pressure $P_m=(P_A+P_B)/2$ we get Equation 4.5.7 which is valid for an isothermal gas flow.

$$Q_m = \frac{-\kappa A}{\mu} \frac{P_A - P_B}{L} \quad \text{Equation 4.5.7}$$

Q_m can be found through Boyles law. For an ideal isotherm gas process we have that $P_m Q_m = P_A Q_A$. By solving this equation with respect to Q_m and substituting it into Equation 4.5.7 we obtain Equation 4.5.8.

$$\frac{P_A Q_A}{\left(\frac{P_A + P_B}{2}\right)} = \frac{-\kappa A}{\mu} \frac{P_A - P_B}{L} \quad \text{Equation 4.5.8}$$

By further solving Equation 4.5.8 with respect to the permeability (K) we obtain Equation 4.5.9

$$\kappa = \kappa_G = \frac{2L}{A} \frac{\mu P_A}{P_B^2 - P_A^2} Q_A \quad \text{Equation 4.5.9}$$

Where K_G is the permeability of gases.

Darcy's law assumes that gases stick to the pore walls in a flow situation; however this is not the case. Viscosity doesn't have a significant influence due to the distances between the gas molecules.

A phenomenon called slippage increases the rate of flow more than what is expected according to Darcy's law. The error increases with decreasing gas pressure. Klinkenberg proposed a correction as shown in Equation 4.5.10

$$K_G = \left(1 + \frac{b}{p_m}\right) K_L \quad \text{Equation 4.5.10}$$

where K_G is the gas permeability and K_L is the permeability for incompressible fluids. The constant b is the Klinkenberg factor which depends on the free distance between gas molecules and the size of the pores in the porous media. The Klinkenberg factor is also correlated to the permeability through the dimension of the pore necks. Slippage will increase with a decreasing pore neck. [12]

4.6. Relative permeability

The defined absolute permeability in the previous section assumed that there was only one fluid present in the porous medium, and that it didn't react chemically or physically with the solid medium. The permeability of a single phase does not depend on the fluid, seeing that the fluid properties are taken care of by the viscosity in Darcy's law.

In reservoirs where there are two or more immiscible liquids present, a permeability for each phase can be made. These defined permeabilities are independent of the flow rate, pressure gradient and the liquid properties; however they are strongly dependent on the properties of the solid porous medium. In a reservoir sample the permeabilities show correlations to the saturation of the respective phases in the porous medium. These are the effective permeabilities and can be described using Darcy's law. Due to practical reasons the relationship between the effective permeability of the phase and the absolute permeability to the medium has been defined as the relative permeability.

The relative permeability for a respective phase can be written as:

$$k_{rw} = \frac{K_w}{K} = \text{relative permeability for water.} \quad \text{Equation 4.6.1}$$

$$k_{ro} = \frac{K_o}{K} = \text{relative permeability for oil.} \quad \text{Equation 4.6.2}$$

$$k_{rg} = \frac{K_g}{K} = \text{relative permeability for gas.} \quad \text{Equation 4.6.3}$$

The relative permeability does not only depend on the porous medium, but also the relative amount of each phase contained is in the medium. This saturation and the interaction between the phases are variables that will affect the permeability. [12]

4.7. Surface- and Interfacial tension

At an atomic level of a fluid there are several forces acting between atoms and molecules. These forces are divided into two categories; the electrostatic interactions (coulomb forces) and the van der Waal type of dispersion forces.

4.7.1. Electrostatic interactions

The electro-negativity of the respective atoms in a molecule can result in an uneven distribution of electrons in the system. Due to the uneven distribution of electron the endpoints of a molecule can obtain a positive or negative charge. The potential energy between two singular charges would then be given by Coulombs equation (Equation 4.7.1):

$$E_c = \frac{q_i q_j}{4\pi\epsilon_0 |r_i - r_j|} \quad \text{Equation 4.7.1}$$

Where q_i is the index charge of the points, ϵ_0 is the dielectric permittivity of vacuum and $|r_i - r_j|$ is the distance between the charged points in space. [13]

4.7.2. Van der Waal

Using the deviation from ideality observed in gas phases as an example, these deviations are normally due to the van der Waal type of interactions. At short distances there is a repulsive force acting between the molecules and at long distances an attractive force. In Figure 4.7.1 the potential of these forces are respectively indicated with a blue and red line. The black line is the Lennard – Jones potential which is explained in the next section.

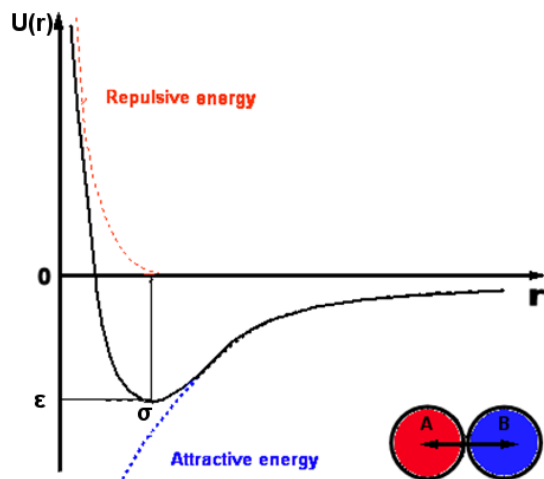


Figure 4.7.1 – Repulsive and attractive forces as a function of distance.

The attractive force is classified as London dispersion forces. These forces arise due to the fluctuating nature of the electron distribution which in turn creates dipoles capable of interacting over relatively large distances. The attractive dispersion forces are weak compared to the repulsion forces at closer distances. When two atoms or molecules continue to approach each other their surrounding

electron densities begin to interpenetrate. Normally such interpenetration would cause bonds to form, but in the absence of such possibilities a property named Pauli repulsion causes the energy of the system to raise exponentially with the decreasing distance between the two objects. It's the sum of these effects that is modelled with the black line in Figure 4.7.1. [13]

The Lennard-Jones Model

The simplest equation used to represent the combination of dispersion and repulsion energies is the Lennard-Jones potential (Equation 4.7.2)

$$U(r_{AB}) = \frac{a_{AB}}{r_{AB}^{12}} - \frac{b_{AB}}{r_{AB}^6} \quad \text{Equation 4.7.2}$$

The constants "a" and "b" are specific to each respective atom. Equation 4.7.3 is a more typical form of Equation 4.7.2, where the "a" and "b" factors have been replaced with σ and ϵ .

$$U(r_{AB}) = 4\epsilon \left[\left(\frac{\sigma_{AB}}{r_{AB}} \right)^{12} - \left(\frac{\sigma_{AB}}{r_{AB}} \right)^6 \right] \quad \text{Equation 4.7.3}$$

The constant σ , found in Equation 4.7.3 and Figure 4.7.1, is the distance between two atoms at minimum energy $U(r)$. ϵ is the well depth at the same radius.

The potential energy, described by Equation 4.7.3 as a function of the distance between the molecules, is plotted as a black line in Figure 4.7.1.

4.8. Surface tension

The surface is the region that divides a gas phase from a liquid or solid phase. The region where a solid or liquid phase contacts another solid or liquid is called an interface. Figure 4.8.1 below visualises the application of the terms with respect to the fluids in contact.

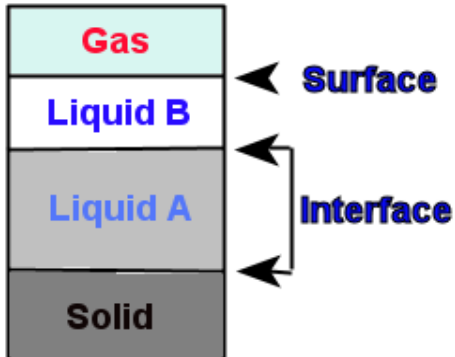


Figure 4.8.1 - Definition of surface and interfacial tension

In the transition between two phases, i.e. from a liquid to a gas phase as shown in Figure 4.8.2, the fluids properties change at the surface. Not only the densities, but the intermolecular forces acting between the constituents in the transition zone, are totally different from the forces acting in the bulk of the phase.

Molecules in the gas phase are separated by great distances relative to the shorter distances in a liquid. Due to the distances and distribution of the molecules in a gas, the liquid will experience close to none of the forces acting from the gas phase. Hence the molecules at the surface of the liquid are only able to interact with the molecules in the bulk, giving rise to the phenomenon called the surface tension.

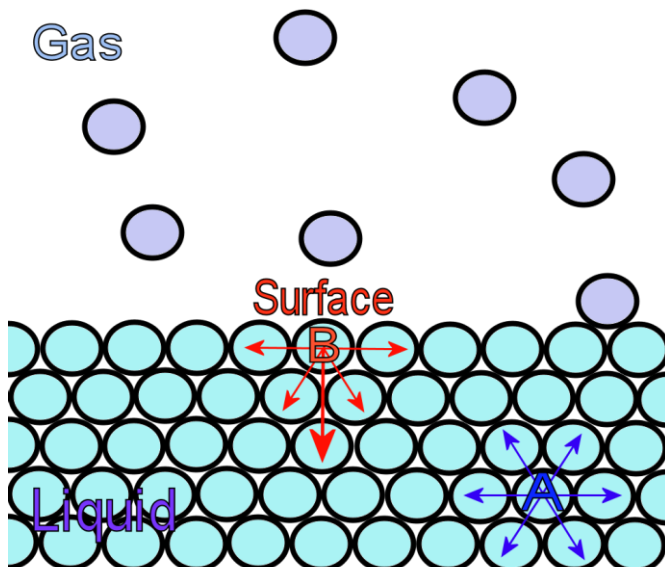


Figure 4.8.2 – Molecules in bulk and at the surface of the phase

In Figure 4.8.2 there are two highlighted molecules in the liquid phase. Molecule A is located in the bulk of the liquid, and molecule B is located at the surface of the liquid. The two molecules have exactly the same properties, but due to the location they will experience a difference in the forces

acting between the neighboring molecules. Molecule A has no acting net force, while molecule B at the surface is experiencing net force acting into the liquid. Hence a molecule at the surface has higher potential energy than a molecule in the bulk, due to the difference in neighboring forces acting on the molecules.

A liquid volume is stable when the potential energy of the molecules is as low as possible. The lowest energy possible is acquired when the least amount of molecules is exposed at the surface. That is when the area is minimized with respect to the volume of the liquid bulk, or when the fluid is perfectly spherical. This physical property is the reason for the spherical shape of for example water drops. [14]

4.9. Miscibility

In the world of fluids some mix and others do not. We have all seen that vegetable oil and water split in two phases when combined, while other fluids like ethanol and water mix easily. This is because of the intermolecular forces that exist between the molecules in both phases, the same type of forces that caused the surface tension explained in the previous chapter.

In a case where two fluids contact, an Interfacial tension will arise. Depending on the magnitude of the forces acting between the molecules of the two phases, the two fluids will either mix or separate. The fluids in Figure 4.8.2 consisted of a liquid with an interface towards a gas phase. If the gas phase were to be substituted by a liquid phase with properties different from the one already present, we would get a situation similar to that in Figure 4.9.1.

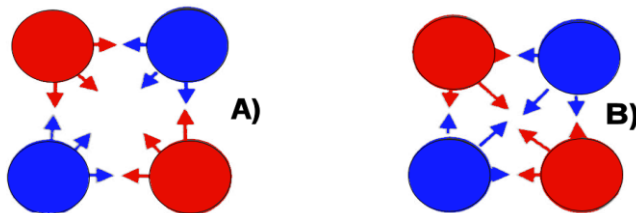


Figure 4.9.1 – Miscibility and intermolecular forces^[12]

In Figure 4.9.1 there are two fluids colour-coded red and blue which are represented in two different miscibility scenarios. Between the molecules there is a set of arrows representing the intermolecular forces. The miscibility, or the ability to mix two fluids, is dependent on which of these binding forces are strongest. In case A the forces between the fluids are equal and in case B the forces are stronger between molecules of the same kind. If the forces between molecules of the same kind are the strongest, the fluids would be characterized as immiscible. On the other hand, if the forces between two molecules of a different kind are the strongest or if all forces are equal, the fluids would be characterized as miscible. Reservoir fluids like water, oil and gas are immiscible. At higher pressures they do mix to an extent. This is due to the pressure and temperature dependency of interfacial tension. [4]

Dependencies

By increasing the pressure at a constant temperature, the distance between the molecules in a fluid will decrease. With increasing pressure the distance between the molecules in a gas phase will also decrease, but at a higher rate than that of liquid. As the gas approaches a higher density, the molecules at the surface of the liquid bulk will eventually experience a decrease in the net force acting into the fluid and thus reduce the interfacial tension.

The temperature dependence of the interfacial tension is related to the internal energy. As the temperature rises, the average kinetic energy of the fluids will also increase. With increasing kinetic energy the distances between the atoms increase and the attractive forces within the bulk decreases. As a result the interfacial tension will be reduced.

It's difficult to measure the exact correlation between the changes in interfacial tension, pressure and temperature because the composition in the phases will also change at the same time.[2]

Surface active agents – Surfactants

Surface tension and interfacial tension is dependent on the thermodynamic state of the system and can be changed accordingly. But both the surface and interfacial tension can also be reduced or entirely removed by adding components known as surfactants.

Surfactants are generally a long hydrocarbon chain connected to a polar functional group of desired properties. The hydrocarbon chain is hydrophobic, which means that it will avoid polar components and obtain the configuration or placement with the least amount of energy. In water surfactants will spread in the surface region with the hydrophobic tails emerged from the surface. At a critical concentration the entire surface area will be occupied and the leftover surfactants will form tiny aggregates called micelles.

Oil and water usually form a thermodynamic unstable emulsion that will separate after time. By adding a respective amount of surfactants, the two phases will become miscible and form a thermodynamically stable micro-emulsion. However these emulsions require large amounts of energy to separate again.[14]

4.10. Wetting

The physical properties of surface tension have been transferred to another phenomenon called wetting. In Figure 4.10.1 there are two scenarios where a liquid volume is placed on a solid surface. In case A the liquid is completely spread across the solid, while in case B the liquid forms a spherical volume resting on the surface.

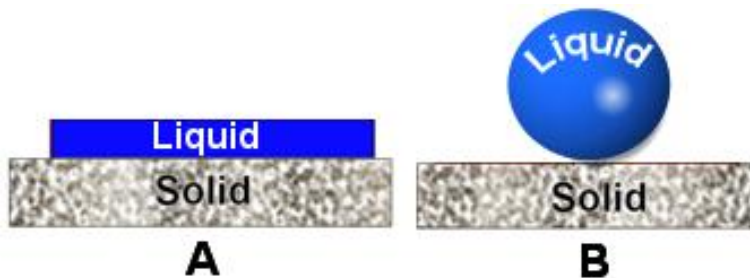


Figure 4.10.1 – Wetting preferences with respect to a solid

If the droplet spreads on the surface like in case A, the interfacial contact area between the solid and liquid increases. In translated significance this means that the surface area of the liquid increases, while the surface of the solid is reduced.

In the case of scenario A, the liquid is said to be wetting or spreading across the surface the solid. The liquid will spread on the solid surface spontaneously if the total free energy of the system is reduced. That is on the cost of the surface area of the solid.

In mathematical terms the spontaneous wetting can be described as

$$\gamma_{\text{Liquid}} + \gamma_{\text{Liquid-Solid}} < \gamma_{\text{Solid}} \quad \text{Equation 4.10.1}$$

where γ_{liquid} and γ_{solid} are the respective surface tensions and $\gamma_{\text{liquid-solid}}$ the interfacial tension between the liquid and solid.[12, 14]

4.10.1. Youngs equation

The two cases shown in Figure 4.10.1 are extremalities. A volume of liquid normally reaches equilibrium where the droplet is neither fully spread nor spherical. Figure 4.10.2 illustrates an example where a droplet has reached equilibrium between the described forces from surface and interfacial tensions.

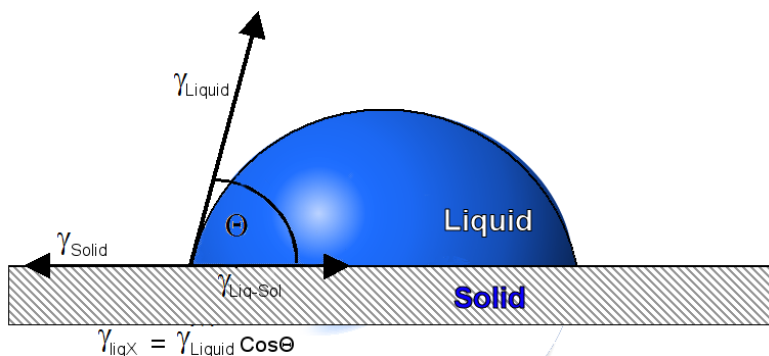


Figure 4.10.2 – A liquid droplet at equilibrium on a solid surface

At equilibrium the forces that seeks to reduce the surface of the solid (γ_{solid}) is at equilibrium with the two forces that seek to reduce the surface area of the liquid and the interface between the solid and liquid, respectively the x component of γ_{liquid} ($\gamma_{\text{liquid}}\cos\Theta$) and γ_{AB} . This relationship is mathematically described in Young's equation (Equation 4.10.2):

$$\gamma_{\text{Solid}} = \gamma_{\text{Liquid-Solid}} + \gamma_{\text{Liquid}} \cdot \cos \Theta \quad \text{Equation 4.10.2}$$

Young's equation gives the connection between the interfacial tension and the contact angle as shown in Figure 4.10.2 and Figure 4.10.3.

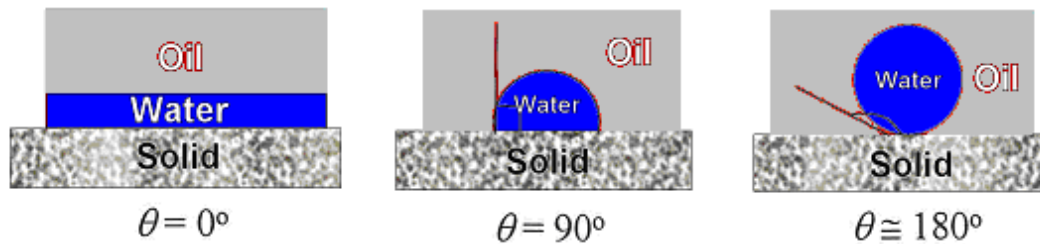


Figure 4.10.3 – Connection between angles and wetting

where the contact angle is correlated to the degree of wetting:

$\Theta = 0^\circ \Rightarrow \text{Complete wetting}$

$\Theta \langle 0^\circ, 90^\circ \rangle \Rightarrow \text{Partially wetting}$

$\Theta \langle 90^\circ, 180^\circ \rangle \Rightarrow \text{Non - wetting}$

$\Theta = 180^\circ \Rightarrow \text{Completely non - wetting}$

Wetability is dependent on the surface energy of both components. Observations show that liquids with low surface tensions wet solids with high surface energy. [11, 14]

4.10.2. Young-Laplace

The Laplace equation is valid for symmetrical interfaces such as those made by droplets. Thomas Young introduced a generalized form of the Laplace equation that was valid for curved interfaces as well.

As mentioned, a spherical volume is the geometrical shape that has the least surface area and interfacial energy, G . The size and shape will always be a competition between the interfacial tension at the surface and the pressure within the volume.

For a respective sphere the interfacial energy is given by:

$$G = 4\pi r^2 \gamma \quad \text{Equation 4.10.3}$$

Where r is the radi of the sphere and γ is the surface tension between two fluids. With a finite increment in the surface area, the interfacial energy will change proportionally according to Equation 4.10.4:

$$dG = 8\pi\gamma \, dr \quad \text{Equation 4.10.4}$$

If the volume of the sphere is reduced, an equivalent amount of energy will be released. Reduction of volume will be resisted by the internal pressure.

When the surface of a sphere experiences an increment the volume will undergo a proportional change. Equation 4.10.5 describes the relationship between the volume, internal pressure and energy.

$$G = \frac{4}{3} \pi r^3 \Delta P \quad \text{Equation 4.10.5}$$

ΔP is the pressure change over the concave interface between two fluids. A finite increment in the surface area will lead to a finite increment in the volume. The coherent change in energy is given by Equation 4.10.6:

$$dG = 4\pi \Delta P r^2 dr \quad \text{Equation 4.10.6}$$

At equilibrium $dG/dr = 0$ with respect to the interfacial tension and pressure. By combining Equation 4.10.4 and Equation 4.10.7 we obtain Equation 4.10.7:

$$4\pi \Delta P r^2 dr = 8\pi\gamma \, dr \quad \text{Equation 4.10.7}$$

By rewriting Equation 4.10.7 with respect to ΔP we obtain the Laplace equation:

$$\Delta P = \frac{2\gamma}{r} \quad \text{Equation 4.10.8}$$

Where ΔP is the pressure difference over the interface between liquid and gas, γ is the surface tension between liquid and air and r is the radius of the concave surface.

Equation 4.10.8 was later generalized by Young so that it would be valid for curved surfaces. Equation 4.10.9 is the modified version known as the Young-Laplace equation.

$$\Delta P = \frac{2\gamma}{r} = \gamma \left(\frac{1}{R_1} + \frac{1}{R_2} \right) \tag{Equation 4.10.9}$$

For a perfect sphere, R1 would be equal to R2 resulting in the original Laplace equation. For a curved surface, R1 would represent one of two axial radii for the respective geometric shape and R2 the radius orthogonal to the one represented by R1.[14]

4.11. Capillarity

The definition of capillarity is basically a spontaneous movement of liquid in a capillary tube due to interfacial tensions and wetting properties. These surface tensions, as previously explained, derive from deviations in molecular attractions at the surface of a liquid resulting in a force pointing into the fluid itself. The same properties create a force that spontaneously moves the liquid along the surface of the solid. Figure 4.11.1 is a cross section of two pores where water is displacing oil in the pore neck.

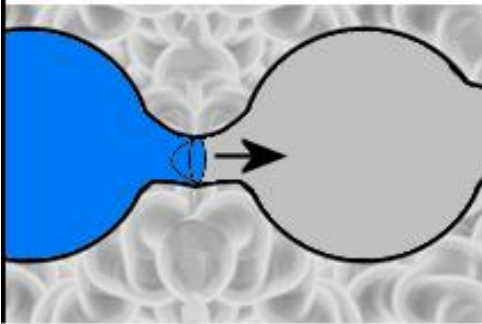


Figure 4.11.1 – Capillary displacement in a cross -section of a pore

In a respective water-wetting reservoir, the capillarity effect would cause water to displace oil or gas in the permeable pore network. The capillary height or driving pressure depends on the wetting preferences of the formation and the radius of the pore and pore necks. The capillary effect is an important factor with respect to displacement of a reservoir fluid.

The capillary pressure will increase when the size of the pores in a media are reduced. Hence the capillary pressure has a larger role in the displacement and accumulation of hydrocarbons. A well sorted sand stone with small amounts of water would experience a large capillary pressure making it an ideal reservoir.

4.11.1. The capillary rise method

The capillary rise method is one of the oldest techniques used to determine the interfacial tension. With respect to the age of the method it is still one of the most accurate, operating with errors within a few hundredths of a percent. The reason for the accuracy is probably due to the accurate and close control of the experimental variables values in addition to the precision work behind the theory.

In a vertical narrow capillary tube mad of glass, as shown in Figure 4.11.2, the fluid will either move in or against the direction of gravity depending on the properties of the solid and liquid. If the fluid is wetting the solid, the liquid will rise.

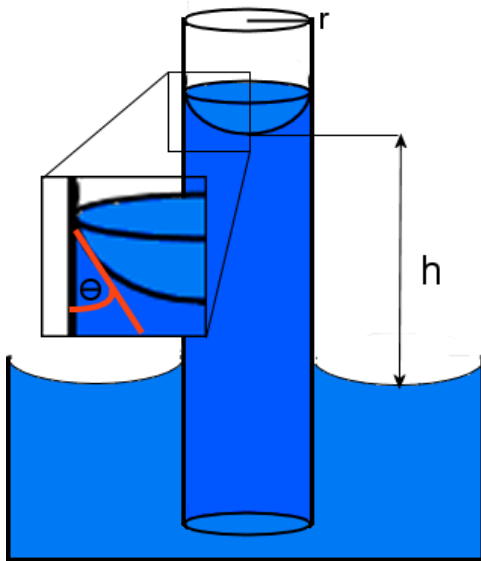


Figure 4.11.2 – The capillary rise of a liquid in a wetting tube

The meniscus that is formed on the top of the liquid pillar can be described by means of Young - Laplace (Equation 4.10.9). The coefficient ΔP in Equation 4.10.8 and Equation 4.11.1 was defined as the pressure difference over the interface between two fluids. In more general terms ΔP is the pressure difference between the wetting and non-wetting phase. This means that the capillary effect requires that the capillary tube has a wetting preference. By substituting ΔP with the equation for overburden liquid pressure we get Equation 4.11.1:

$$\frac{2\gamma\cos\Theta}{r} = \Delta\rho gh = \Delta P \quad \text{Equation 4.11.1}$$

Equation 4.11.1 can be rewritten with respect to the liquid column height, so that:

$$h = \frac{2\gamma\cos\Theta}{rg\Delta\rho} \quad \text{Equation 4.11.2}$$

Where θ is the contact angle between the liquid and solid, $\Delta\rho$ is the density difference between the two fluids, g is the constant of gravity and r is the radius of the capillary tube. Equation 4.11.2 can be used to calculate the height of the estimated capillary rise or the interfacial tension.

4.12. Saturation

A porous media can normally contain more than one fluid and phase at the same time. Using a hydrocarbon reservoir as an example, the saturation is the fraction of the total pore volume V_p that contains the respective fluid. A hydrocarbon reservoir normally contains fluids like water, oil and gas. Equation 4.12.1 to Equation 4.12.3 represent the pore saturations respective to the subscript fluid.

$$\text{Water saturation: } S_w = \frac{V_w}{V_p} \quad \text{Equation 4.12.1}$$

$$\text{Oil saturation: } S_o = \frac{V_o}{V_p} \quad \text{Equation 4.12.2}$$

$$\text{Gas saturation: } S_g = \frac{V_g}{V_p} \quad \text{Equation 4.12.3}$$

Normally the entire pore volume is filled with fluids so that the saturation fraction equals 1.0. For a hydrocarbon reservoir the saturation equation would be:

$$S_w + S_o + S_g = 1.0 \quad \text{Equation 4.12.4}$$

In pores where there are more than one fluid, the respective flows will be determined by saturation on the fluids. Figure 4.12.1 is a representation of two equal pores at a different saturation of oil. The pores are water wetting causing a volume of oil to be trapped in the middle of the pore. Due to the wetting preference of the formation, a limited amount of oil might be trapped as residual saturation.

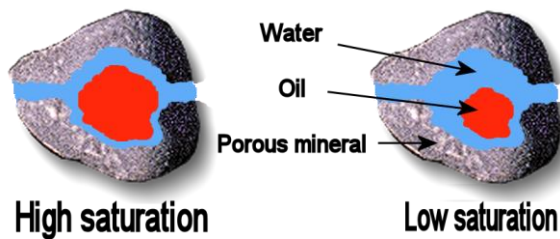


Figure 4.12.1 – Two different saturations of a pore.

The pore on the left hand side of the figure has a high saturation of oil, while in the pore to the right has a lower saturation. Oil will be more easily displaced in a network of highly saturated pores. At low pore saturations the water will easily flow past and the oil will be retained in the pore. [12]

4.13. Drainage and Imbibition

A process where the wetting phase of a porous medium is displaced by a non-wetting phase is called drainage. In contrast, a process where the saturation of the wetting phase is increasing is termed imbibition.

4.13.1. Imbibition

Figure 4.13.1 represents a typical permeability curve for water/oil in a water-wetting porous medium. The curves are related to a process where water is sucked into the pores due to the capillary effect plotted as a function of the intruding fluid, that is, the saturation S_w .

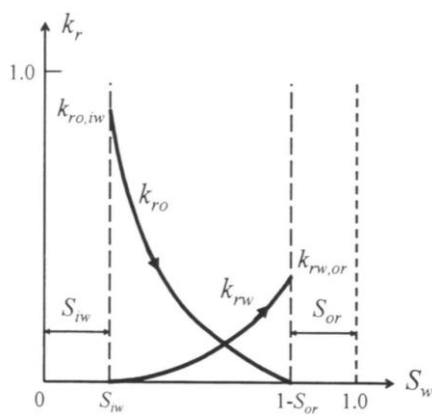


Figure 4.13.1 – Water/oil permeability curves

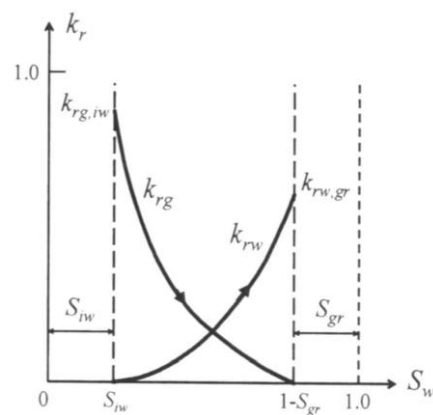


Figure 4.13.2 – Gas /water permeability curves

Because the medium is water-wetting, there will be a non-reducible degree of water saturation, S_{iw} . Due to the mentioned capillary forces the water saturation cannot surpass this value, and the water will not be able to flow i.e. $K_{rw}(S_{iw})=0$. At the same time the oil or intruding fluid has filled most of the pore volume and obtained the maximum permeability at the respective saturation. When S_w increases K_{ro} will subside and eventually approach 0 at residual oil saturation. At this point the oil will no longer flow.

If the oil were to be substituted with gas, the water would similarly displace the gas. The water phase is still the wetting fluid. Figure 4.1.1 illustrates a typical permeability curves for this scenario. In this system the minimum gas saturation is abbreviated S_{gr} . At this point the gas becomes so discontinuous that it no longer will flow and $k_{rg}=0$.

4.13.2. Drainage

Figure 4.13.3 illustrates a scenario where the wetting phase oil, is displaced by a non-wetting gas phase. As mentioned, oil is the wetting phase relative to the gas phase; however it is assumed that some water remains in the formation, but at irreducible immobilities.

The most important characteristics with drainage process, is that K_{rg} is zero until the gas saturation reaches a critical value S_{gc} before the gas permeability starts to increase. This is because the gas phase is not continuous until $S_g = S_{gc}$ and the gas can only flow through the pores above this value. K_{ro} subsides evenly in the area $0 < S_g < S_{gc}$ due to the increasing pore volume of immobile gas. When S_g increases further, the K_{ro} value will drop until it reaches zero.

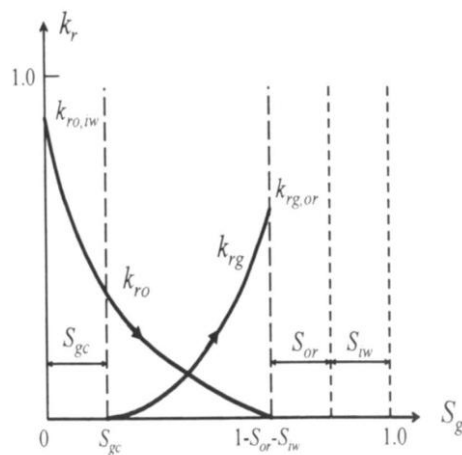


Figure 4.13.3 – Gas/oil permeability curves

Immiscible fluids flowing in a porous medium will create and maintain tortuous pathways through the medium. In a laminar flow, these channels will be sustained and stable, but at the point where the saturation of the non-wetting fluid subsides, the pathway will collapse and the fluid will become immobile. The process is similar for a reduction in the saturation of the wetting fluid. The slippage phenomenon is also present in this scenario.

5. Mineral chemistry

Mineral chemistry, or crystal chemistry, has a focus on the relationships between the structure of solids and their chemical composition. This chapter contains a description of the numerous minerals found in an aquifer and their coherent properties.

5.1. Solids

Solids inhabit properties that separate them from liquids and gases. Hardness is a general definition of such a property, but solids are defined in a more specific manner: "Solids are materials that exhibit a long-range regularity of atomic or molecular arrangements."

Compared to solids, liquids exhibit a similar order but at a much shorter range. Gases show no order at all. By this definition solids such as glass can't be considered as solids, but as very viscous liquids. If the thickness of the glass in a window is measured after 50 years, the bottom would be much thicker than the top, although it was originally equally thick. This is due to the thermodynamically unstable and viscous nature of the crystalline glass.

5.2. Bonding forces

Chapter 4 contains a brief explanation of non-bonded interactions in gases and liquids. Solids, however, are bonded with electron interactions. The type of bonds, along with the number and respective size of the bonded atoms, influence the crystal structuring of a solid mineral. The common types of bonds found in a solid are listed below:

Ionic bonds are formed when an atom donates one or more electrons to another atom. The donated electrons are removed from the electron donor and reside with the electron acceptor. A classic example is table-salt (NaCl/ Sodium chloride). The donor (Na) becomes a cation and the acceptor (Cl) an anion, hence Na^+ and Cl^- .



Figure 5.2.1 – Lewis structure of a ionic bond (NaCl)

Covalent bonds, in contrast to ionic bonds, are formed when two atoms share a pair of electrons with equivalent energy and opposite spin states. Helium, hydrogen, nitrogen etc are examples of gases with covalent bonds. In covalent bonds the electrons are shared equally between the respective atoms if they are similar in both size and electro negativity. Figure 5.2.2 is a Lewis description of the covalent bond in carbon dioxide. The Lewis structure is a description of the outer shell with respect to an atom's electrons.



Figure 5.2.2 –Lewis structure of a covalent bond (CO_2)

If one of the involved atoms is larger and/or more electronegative than the other bonding atom, the electron pairs will not be shared equally. Instead the electrons are pulled towards the larger and more electronegative element. This is known as a *polar covalent bond*. By definition the bonding electrons in a polar covalent spend more time near one atom than the other.

The *metallic bond* is formed due to valence electrons moving freely around a series of cations, effectively binding them together to form a structure. Figure xxx below is a visual representation of such metal cations in a pool of shared electrons.

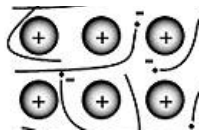


Figure 5.2.3 – Metallic bond, Illustration

Van der Waals bonds form in multiple ways. The bonds form due to dipole-dipole interactions which is a result of the time average electron concentration in the molecules. This time average concentration distorts the charge distribution creating a dipole in the molecule or section of the molecule. These dipole moments can also induce dipole moments in other molecules. A larger fraction of minerals are often hydrated by water molecules due to non-bonded forces.

5.3. Mineral classes

Minerals are natural occurring homogenous inorganic solids with definite chemical compositions and specific repeating arrangements of atoms. The abundance of a particular mineral depends on the availability of its constituent elements and whether the bonding is stable for the physical conditions present and its ability to withstand alteration.[15]

5.3.1. Oxides

The oxide class of minerals can be divided into simple and multiple oxides. The simple oxides consist of a single type of atom bonded with oxygen. Others include corundum (Al_2O_3), hematite (Fe_2O_3), rutile (TiO_2) and magnetite (Fe_3O_4). The minerals spinel (MgAl_2O_4) and chromite (FeCr_2O_4) are common multiple oxide minerals. [15]

5.3.2. Hydroxides

Hydroxide minerals have OH^- groups bond to cations in their structure. The presence of OH^- causes the bond to stretch to cations to be weaker than in oxides, so they tend to have a lower mineral hardness. Brucite ($\text{Mg}(\text{OH})_2$), goethite ($\text{FeO}\cdot\text{OH}$) and gibbsite ($\text{Al}(\text{OH})_3$) are common hydroxides.[15]

5.3.3. Silicates

Silicates are the most common type of minerals encountered on the earth's surface and crust. The silicate class of minerals is built on the silicon-oxygen tetrahedron.[15]

5.3.4. Carbonates

Carbonates are abundant on the earth's surface. They are formed by chemical and biological precipitation from seawater, such as calcite (CaCO_3). Dolomite ($\text{CaMg}(\text{CO}_3)_2$) is often formed when seawater reacts with calcite. [15]

5.4. Minerals

Most geological formations are constituted by numerous minerals, some in larger fractions than others. A sedimentary reservoir is typically made of sandstone and carbonates from shells of organic life forms. Sandstone mainly consists of silicates or quartz with varying amounts of calcite made from the carbonates. Though there are many other constituent minerals, but only calcite and quartz are considered in this thesis.

5.4.1. Calcite

The mineral calcite is a calcium carbonate by the chemical formula CaCO_3 and it is a widely distributed mineral on the earth's surface. It is a common constituent of sedimentary rocks, especially limestone. Calcite is a widely used mineral. It is utilized as a construction material known as cement or concrete. Farmers used it as a soil treatment in order to neutralize acids and even as a component in food for cattle. Calcite is also used within pharmacy to create antacid tablets. In the geological world calcite is the most stable polymorph of calcium carbonate (CaCO_3). Calcite can form rocks of considerable mass and constitutes a significant part of all three major rock classification types.[16]



Figure 5.4.1 – Specimen of limestone, travertine and crystalline marble^[16]

Calcite dissolves in contact with acidic liquids, meaning that calcite can dissolve or precipitate in contact with groundwater, in a magnitude and rate depending on the water temperature, pH, and initial dissolved ion concentrations. When calcite dissolves it will release carbon dioxide gas. Another important property of calcite is the retrograde solubility, meaning that calcite will be less soluble in water as the temperature increases. Depending on the reservoir conditions, calcite can return to its mineral form and act like cement within the formation. This includes filling entire fractures. On the other hand, removal of calcite can dramatically increase the porosity and permeability of the rock.[15]

5.4.2. Quartz

Quartz is the most abundant mineral in the Earth's crust. It is found in most geological environment and is a component in several types of rocks. The density is estimated to 2.6 Kg/m³. Quartz is a silicate mineral of which the structure consists of a silica (SiO_2) tetrahedral. Quartz belongs to the rhombohedral crystal system and in pure crystal form the structure is typically a hexagon prism ending with a six-sided pyramid. The unique structure consists of a cork-screwing helix constituted by chains of silicon tetrahedrons. Pure quartz is colorless or white, and impurities exist in multiple coloured varieties.[15]

6. Geochemistry

The geochemistry of a reservoir deals with the chemical aspects of elements present in the formation, such as the chemistry of charged species from precipitating minerals and material transport throughout the respective formation.

The simulations that are presented in this thesis include two minerals (calcite and quartz), CO₂ gas and water - along with the combinations of their constituent species. Hence the following chapters will consider the chemistry of these aquifer constituents.

In order to fully understand the aspects of the geochemistry in the simulation the first part of this chapter will explain a few basic thermodynamic concepts.

6.1. Concentration and activity

In basic chemistry the equations of equilibrium, pH and buffers considered ideal solutions without any disturbing intermolecular forces. In real solutions these effects have to be accounted for.

A solution, like water, consists of a polar solvent and dissolved charged species. These charged species tend to interact with ion-ion electrostatic forces causing a deviation between estimated properties from concentrations and the real properties of a solution. This error is accounted for by introducing the physical term activity.

Activity, a_i , is defined through the chemical potential of the individual species in a solution. The chemical potential is related to the change in Gibb's free energy, with respect to the change in a component, at constant temperature and pressure, as shown below.

6.2. Gibbs free energy

The conservation of energy is important in all aspects of physics and it is the foundation of the 1st law of thermodynamics. In combination with the 2nd law of thermodynamics, which says that any isolated system will strive towards maximum entropy, we can obtain a function for Gibbs free energy. Equation 6.2.1 is the combined 1st and 2nd law representing the internal energy U for phase s:

$$dU^{(s)} \leq T^{(o)} dS^{(s)} - P^{(s)} dV^{(s)} + \sum_{i=1}^n \mu_i^{(s)} dN_i^{(s)} \quad \text{Equation 6.2.1}$$

The summation in the equation is performed over all the present phases "s" where s=1,2,3,...,n. Where S is the entropy, μ is the chemical potential and N is the number of particles respective to a constituent compound. The relation to Gibbs free energy is obtained by subtracting $d(T^{(o)}S^{(s)})$ and adding $d(P^{(s)}V^{(s)})$ on both sides in a Legendre transformation.

$$dA^{(s)} = dU^{(s)} - d(T^{(o)}S^{(s)}) \leq T^{(o)} dS^{(s)} - d(T^{(o)}S^{(s)}) - P^{(s)} dV^{(s)} + \sum_{i=1}^n \mu_i^{(s)} dN_i^{(s)} \quad \text{Equation 6.2.2}$$

$$dG = dA^{(s)} + d(P^{(s)}V^{(s)}) \leq -S^{(s)}dT^{(o)} - P^{(s)}dV^{(s)} + d(P^{(s)}V^{(s)}) + \sum_{i=1}^n \mu_i^{(s)} dN_i^{(s)} \quad \text{Equation 6.2.3}$$

The resulting function is the Gibbs free energy:

$$dG \leq -S^{(s)}dT^{(o)} + V^{(s)}dP^{(s)} + \sum_{i=1}^n \mu_i^{(s)} dN_i^{(s)} \quad \text{Equation 6.2.4}$$

In a simplified approach, Gibbs free energy can be considered as the available energy level constrained by losses in entropy generation. The second term in Equation 6.2.4 is termed the technical work, or shaft work since the internal work is subtracted. The third term is the chemical work, representing the extraction and insertion of particles in the phase. Removing a molecule from a system or a phase is a process consisting of losing the energy of molecule interaction with the surroundings and reorganising the system (entropic contribution). The change in Gibbs free energy (Equation 6.2.4) at constant pressure and temperature can be obtained through Equation 6.2.5

$$dG \leq \sum \mu_i^{(s)} dN_i^{(s)} \quad dP = dT = 0 \quad \text{Equation 6.2.5}$$

where the contribution to change in free energy is limited to the chemical work. Gibbs free energy is a state variable. Thus the chemical potential is the partial molar Gibbs free energy:

$$\mu_i = \left(\frac{\partial G}{\partial n_i} \right)_{T,P,n_j} \quad \text{Equation 6.2.6}$$

If the same system is isolated under an isobaric or isothermal constraint, an irreversible process will take place over time, minimizing the Gibbs free energy until the lowest energy is reached. With that in mind, the Gibbs free energy can be considered as driving force created by the systems constant quest for minimum free energy. [17]

6.3. Phase rule and chemical potential

When we consider the number of degrees of freedom in a heterogeneous system we need to take into account the results of the proceeding two sections. If the heterogeneous system is not in a state of internal equilibrium, but each phase is, the number of independent variables is $\pi(m+1)$, because for each phase there are $(m+1)$ degrees of freedom, of which a Gibbs-Duhem^[17] equation applies to each phase.

If the entire system is in a state of internal equilibrium, then among the $\pi(m+1)$ variables there are $(\pi-1)(m+2)$ equilibrium relations. Thus the number of degrees of freedom, F , is the number of intensive variables used to characterize the system, minus the number of relations or restrictions.

At equilibrium, the three following conditions expressing thermal, mechanical and chemical equilibrium must be satisfied:

$$T^{(1)} = T^{(2)} = \dots = T^{(\pi)}$$

Equation 6.3.1

$$p^{(1)} = p^{(2)} = \dots = p^{(\pi)}$$

$$\mu^{(1)} = \mu^{(2)} = \dots = \mu^{(\pi)}$$

Thus the number of degrees of freedom is equal to the number of components minus the number of phases plus two:

$$F = \pi(m+1) - (\pi-1)(m+2) = m+2-\pi$$

Equation 6.3.2

For two components (H₂O and CO₂) in gas and liquid phase in equilibrium, we need two independent thermodynamic variables to uniquely define the system. A uniquely defined system means that it could theoretically reach equilibrium over time.[17]

6.3.1. Fugacity

While extremely important in deciding the equilibrium, the chemical potential lacks an obvious physical meaning. The chemical potential does not have any immediate equivalent in the physical world and is therefore desirable to express the chemical potential in terms of some auxiliary function, fugacity. [17]

In gases, the fugacity (f_i) is the measure of the tendency to escape or expand. It is also defined as the respective pressure needed at a prescribed temperature in order to satisfy the ideal gas law for a real gas. The fugacity of a gas component "i" is defined by Equation 6.3.3:

$$f_i = P_{Tot} y_i \phi(T, P, \vec{x})$$

Equation 6.3.3

Where y_i is the mole fraction of gas component "i", $\phi(T,P,x)$ is the fugacity coefficient as a function of pressure, temperature and composition. As a function of pressure the fugacity is also in pressure units. [2]

6.3.2. Residual thermodynamics

In a gas phase such as injected CO₂ gas, the chemical potential of CO₂ can be obtained by considering its deviation from ideal gas behaviour; said deviation will be given by fugacity in Equation 6.3.3. When ideal gas is used as the reference state, the approach is called residual thermodynamics.

$$\mu^{real} = \mu^{Idg} + RT \ln f_i$$

Equation 6.3.4

$$\mu^{real} = \mu_i^{id.gas} + RT \ln(y_i \phi_i)$$

Equation 6.3.5

Where ϕ_i is called the fugacity coefficient.

6.3.3. Excess thermodynamics

A different reference or standard state is often convenient when it comes to solutions: an ideal solution. An ideal liquid solution is one where, at constant temperature and pressure, the fugacity of every component is proportional to some suitable measure of its concentration, usually the mole fraction. This approach gives rise to excess thermodynamics. Activity of component i at some temperature, pressure and composition is defined as the ratio of the fugacity of i in the standard state (same T , different P and composition). When the pure component has been selected as the standard state, chemical potential of ideal solution will be given by the chemical potential of the standard state, μ_i° , corrected by the molar fraction as illustrated in Equation 6.3.6. [18]

$$\mu_i = \mu_i^\circ + RT \ln x_i \quad \text{Equation 6.3.6}$$

By introducing the activity coefficient γ_i in Equation 6.3.6, the deviations from non-ideality in molar fractions can be corrected and absorbed the in the activity.

$$\mu_i^{real} = \mu_i^\circ + RT \ln a_i = \mu_i^\circ + RT \ln(\gamma_i \cdot x_i) \quad \text{Equation 6.3.7}$$

Conditions of equilibrium require the equality of chemical potential in all of the phases. In case of liquid-vapour equilibrium, this means that absolute chemical potential of a liquid component is equal to its value in a gas mixture at saturated pressure. When applied to fugacities, it results in correctly defined fugacities also being equal at equilibrium. If one needs to relate fugacity of vapour and liquid at some other pressure point, a correction must be made by integrating over pressure to find the corresponding change in chemical potential (so-called Pointing correction). Thus in the general case, one obtains the following relationship between vapour and liquid compositions, fugacity and activity coefficients:

$$f_i = P_{Tot} y_i \phi(T, P, \vec{x}) = x_i \gamma_i P^{sat}(T) \phi_i^{liquidpre}(T, P_{(T)}^{sat}) \exp \int_{P_{sat}}^P \frac{\bar{V}_i}{RT} dP \quad \text{Equation 6.3.8}$$

In case of a component at infinite dilution, an approximation entirely applicable to supercritical CO₂ injection into aquifers, the chemical potential of CO₂ can be obtained through the general form derived from excess thermodynamics:

$$\mu = \mu_i^\infty + RT \ln(x_i \gamma_i^\infty) + v_i (P - P_0) \quad \text{Equation 6.3.9}$$

where μ_i^∞ is the chemical potential of component "i" in water at infinite dilution, γ_i^∞ is the activity coefficient of component "i" in the aqueous solution (The activity coefficient will approach 1 as the value of component x vanishes). The third term represents a simplified form of Pointing correction. The chemical potentials at infinite dissolution, as a function of temperature, can be found by assuming equilibrium between fluid and aqueous phase:

$$\mu_i^L = \mu_i^{aq} \quad \text{Equation 6.3.10}$$

This approach is valid at low pressures where the solubility is relatively low. Chemical potential expansion of water in solution can be expanded around zero concentration as follows:

$$\mu_w = \mu_w^0 + RT \ln((1-x)\gamma_w) + v_w(P - P_0) \quad \text{Equation 6.3.11}$$

Where μ_w^0 is the chemical potential of pure water. This equation can be combined with the Gibbs-Duhem equation for experimental values of solubility for a system of two components:

$$x d \ln(\gamma_c) + (1-x) d \ln(\gamma_w) = 0 \quad \text{Equation 6.3.12}$$

Where γ_c is the activity coefficient of CO₂ in the water-CO₂ system and x is the mole fraction of dissolved CO₂.

7. Aqueous solutions and minerals

Water is one of the most abundant liquids on the planet; hence the chemistry which involves water is very important. Aquifers are porous formations containing vast amounts of water. This sub chapter will consider the most important aspects of water chemistry.

7.1. Water

Water is the most abundant liquid on the planet. In addition to the vast amounts in the form of seawater, lakes and rivers - water can also be found in the atmosphere, the soil and in fractures and porous media at large depths.

Water exhibits dipolar characteristics due to O-H bonding explained in, which is the reason for its high boiling point and ampholytic properties. The dipolar nature is important for stabilizing charged species solved in the liquid phase. Using table salt as an example, Na⁺ and Cl⁻ would experience an electrostatic coulomb attraction from the respective dipoles of the water molecule

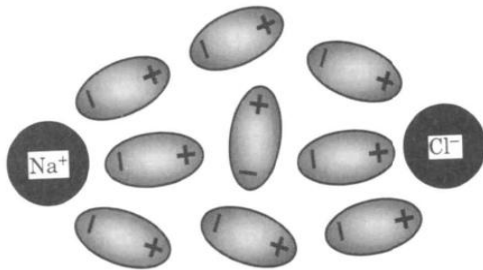


Figure 7.1.1 – Charged species separated by water molecules^[15]

As the salt is solved in liquid water, the dipoles are orientated so that the ionic charge matches the opposing dipole charge. Figure 7.1.1 also shows that the ions are separated by the dipole alignment of water which effectively lowers the attraction between the ions.[15]

7.1.1. Acids and bases in water

Acids are molecules with functional groups that dissociates in water by transferring protons (H⁺) to the solution. This free proton has a tendency to form complexes or clusters with the H₂O molecules and is thereby often abbreviated as H₃O⁺ (Hydronium). The concentration of H⁺ or H₃O⁺ is often used to determine the pH value of the respective solution.

The pH scale is a logarithmic expression of the acidity or alkalinity of a solution of which pH is defined as the negative logarithm of the H⁺ ion concentration in moles per cubic centimeter.

$$\text{pH} = -\log C_{\text{H}^+} = -\log[\text{H}_3\text{O}^+]$$

Equation 7.1.1

Water or solutions with pH-values lower than 7.0 are said to be acidic, while solutions with pH levels above 7.0 are termed alkaline.

Alterations in pH concentrations are generally due to additions of acids or alkaline bases. Water is an ampholytic liquid capable of acting both as an acid and base depending on the pH of the liquid. H₂O can self-dissociate in order to produce H⁺ and OH⁻ according to the reaction described in Equation 7.1.2.



As mentioned pH is defined as the negative logarithm of the H⁺ concentration, but this is not exactly the case. The pH value is actually connected to the activity of H⁺ in a solution. The equilibrium constant for the reaction, with respect to the activity of the species, would then be:

$$K_{\text{H}_2\text{O}} = \frac{a\text{H}^+ \cdot a\text{OH}^-}{a\text{H}_2\text{O}} \quad \text{Equation 7.1.3}$$

The activity of species is not possible to measure experimentally. Instead a relationship to Gibbs free energy is utilized in Equation 7.1.4 in order to calculate the pH values.

$$\log K_{\text{H}_2\text{O}} = \frac{\Delta G_{\text{R}}^0}{-2.3026 \cdot \text{RT}} \quad \text{Equation 7.1.4}$$

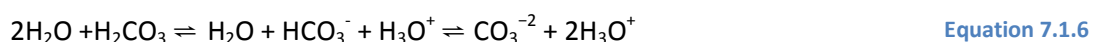
Equation 7.1.4 is known as the law of mass action, which is defined by the chemical potential and its connection to Gibbs free energy through stoichiometric coefficients. K or the equilibrium constant is dependant on standard states which is an important fact in consideration of equilibrium constants. The negative number is a conversion from ln(K) to log¹⁰(K) and R is the universal gas constant. [15]

7.1.2. pH changes in water due to CO₂ dissolution

With a given concentration of CO₂ gas in the atmosphere, small amounts of the gas will dissolve at the surface region of water. Eventually the dissolved CO₂ will obtain equilibrium with carbonic acid, or aqueous CO₂, according to Equation 7.1.5.



The equilibrium between dissolved carbon dioxide and carbonic acid will shift to the right or left depending on increments in thermodynamic conditions like pressure and temperature. At right conditions carbonic acid will further dissociate in water according to Equation 7.1.6.



Equation 7.1.6 shows the transition from carbonic acid (H_2CO_3) to bicarbonate (HCO_3^-) and carbonate (CO_3^{2-}). Depending on the pH of the solution an equilibrium favoring one of the three mentioned species will form. Carbonic acid will dominate at pH values below 6.34. Bicarbonate will dominate at pH values from 6.34 to 10.33, while the equilibrium favors carbonate above pH values of 10.33.

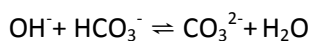
Acids like HCl and H_2SO_4 are strong acids since they dissociate almost completely in H_2O . Weak acids like carbonic acid H_2CO_3 , have remnants in the form of naturally charged species in the solution. I.e. HCO_3^- . [15]

7.1.3. pH buffers

When an acid or an alkali is added to a solution the, pH value will normally either increase or decrease. However, for a fluid containing a significant concentration of a weak acid and its coherent salt, this would not be the case. The weak acid and its salt would regulate pH by dissociating between the salt and acid form and thus keep the pH at the same value. A solution with these properties is called a pH buffer.

A buffer solution must contain a relatively large concentration of acid and base in order to react with any $-\text{OH}$ or H^+ ions that may be added to the solution. The acid or base component must be inert and not consume each other in a neutralization reaction.

The dissolution of carbon dioxide in water was briefly discussed in the previous chapter.

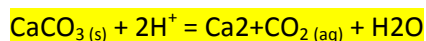


Equation 7.1.7

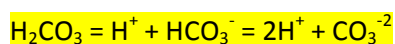
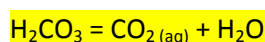
If an amount of acid is added to a buffered solution, the reaction in Equation 7.1.7 would proceed to the left. The carbonate salt (CO_3^{2-}) would consume the added H^+ and form bicarbonate (HCO_3^-). By adding an alkali instead of an acid, the reaction would proceed in the opposite direction, neutralizing the alkaline base. In other words, bicarbonate would donate H^+ by dissociating to carbonate. [15]

A buffered solution can only neutralize a limited amount of added acids and bases. This is due to the limited amount of buffering species solved in the solution. The buffer capacity is thus dependant on the magnitude of the solved acid and conjugate base. The larger the amount, the greater the buffer capacity.

Because calcite is the salt of a weak acid, the solid will dissolve in contact with any stronger acid.



The reaction product CO_2 may participate in several other reactions



7.1.4. Alkalinity

Alkalinity is similar but not to be mistaken with basicity. By definition alkalinity is a solutions ability to neutralize added acids, measured by the number of charged species affected by the change in pH. The difference between alkalinity and basicity can be illustrated with CO₂ and calcite.

If the pH of a buffered solution is altered by dissolving an amount of CO₂ gas, only the basicity of the solution will be affected and the alkalinity will remain unchanged. This is because the net reaction of dissolution produces the same number of positively contributing species (H⁺) as negative contributing species (HCO₃⁻ and/or CO₃²⁻).

However, addition of CO₂ to a solution in contact with a solid mineral can affect the total alkalinity – Especially in solutions that contain carbonate minerals. The precipitation of carbonate rock has a strong influence on the alkalinity. This is because carbonate rock is composed of CaCO₃ and its dissociation will add Ca²⁺ and CO₃²⁻ to the solution. Ca²⁺ will not influence alkalinity, but CO₃²⁻ will increase alkalinity.

In natural waters carbonate alkalinity tends to make up most of the total alkalinity. This is because of the common occurrence of carbonates in addition to the presence of carbon dioxide in the atmosphere. [15]

7.2. Mineral solubility

Sometimes a solid or charged specie will be more soluble as the condition of a fluid changes. Temperature, pressure, pH and even introduction of common ions will shift the solubility in a positive or negative direction.

If a given mineral is solved in pure water and a solution containing common mineral ions, the mineral would experience a difference in solubility. The solution containing the initial concentration of ions would allow less of the mineral to be dissolved compared to that of the pure water. This is known as the common ion effect. This means that the solubility of minerals decreases when ions from the reaction of the mineral dissolution already exist in the solution.

7.2.1. Molar solubility product - K_{sp}

For calcite, the reaction of dissolution in water is given by Equation 7.2.1:



of which the equilibrium constant is given by Equation 7.2.2:

$$K = \frac{[\text{Ca}^{2+}_{(aq)}][\text{CO}_3^{2-}_{(aq)}]}{[\text{CaCO}_3(s)]} \quad \text{Equation 7.2.2}$$

Where K is the equilibrium constant for the reaction and [CaCO₃] is the concentration of the respective specie.

The total solubility product of a mineral (K_{sp}) is equal to the equilibrium constant (K) when the activity of the solid (s) and activity-coefficient of the aqueous species (aq) is unity. Hence the Solubility of the mineral is given by Equation 7.2.3 below.

$$K_{sp} = \frac{[A^+]^2[B^-]}{[AB]} = \frac{[A^+]^2[B^-]}{[1.0]} = [A^+]^2[B^-] \quad \text{Equation 7.2.3}$$

The concentration of a solid in a solution is always 1.0 which means that the K_{sp} is equal to the product of the concentration respective to each charged species in the reaction.

Water exposed to the atmosphere has typically obtained equilibrium between dissolved CO_2 and carbonic acid according to Equation 7.1.5. The pH value of pure water exposed to CO_2 gas would eventually reach equilibrium due to the buffering effect of dissolved CO_2 . For a pure solution the equilibrium pH should stabilize around 5.5.

If a given amount of calcite is placed in a similar acidic solution at standard conditions, the pH value would reach 8.26. Further investigations respective to the concentrations of the species should show that there is more solved CO_2 than calcite in the solution. This is due to the initial CO_2 (aq) concentration.[15]

7.2.2. Solubility of carbonates

Calcite has previously been considered as a key component in buffering and alkalinity. Calcite will react accordingly when in contact with water:



As mentioned, if a solution of water is exposed to carbon dioxide, carbonic acid will form. Normally calcite has a low solubility in cold water, but if calcite is exposed to a buffered acidic solution, the calcite mineral will react with carbonic acid and form bi- carbonate (HCO_3^-). Bicarbonate is much more soluble in water than calcite, thus the solubility of calcite can be said to depend on the acidity of the water. Temperature does also have an impact on the solubility. Calcite has a retrograde solubility, meaning that the amount of soluble calcite decreases as the temperature increases. The mentioned properties allow calcite to dissolve in one location and precipitate in another location where the water has a lower temperature or higher pH value. [15, 19]

Figure 7.2.1 – Solubility of calcite in water at various partial pressures of CO_2 as a function of temperature represent the solubility of calcite in water as a function the temperature and salt

content. The graph shows that the solubility of calcite increases with decreasing temperature and increasing salt content

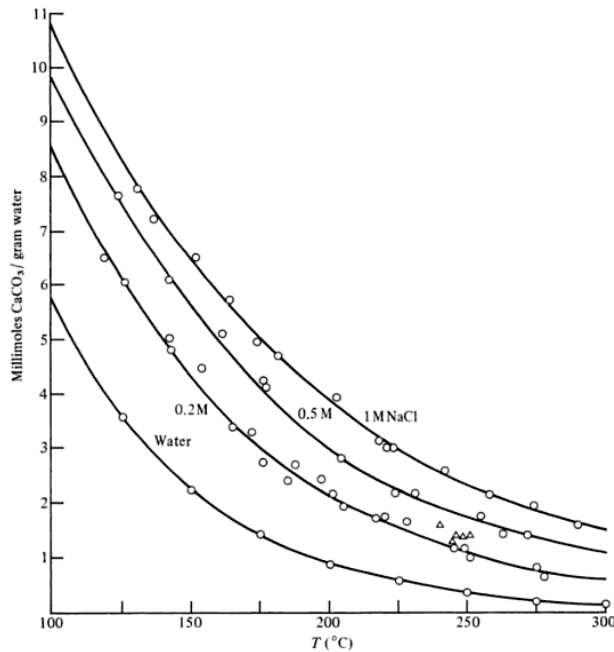


Figure 7.2.1 – Solubility of calcite in water at various partial pressures of CO₂ as a function of temperature

7.2.3. Solubility of silicates

The solubility of quartz is relatively low in water compared to the solubility of CO₂ and calcite. Quartz is the least soluble Si-mineral and hence the most thermodynamically stable SiO₂ polymorph. Equation 7.2.6 shows the reaction of dissolution for quartz.



Equation 7.2.6 defines the dissolved quartz as SiO₂ (aq) which is often termed silicic acid (H₄SiO₄⁰). Silicic acid is formed according to Equation 7.2.7.



H₄SiO₄⁰ (aq) is a weak acid that dissociates in alkaline solutions by protolysing according to Equation 7.2.8. The concentration of H₃SiO₄⁻ increases with the pH-value of the solution.[15]



Figure 7.2.2 shows that the solubility silica is low in acidic concentrations below pH 9. Silicic acid (H_4SiO_4^0) is the favoured species in this pH range. At pH values above 9 the dissociated forms of silicic acid (H_3SiO_4^- and $\text{H}_2\text{SiO}_4^{2-}$) are more dominant.

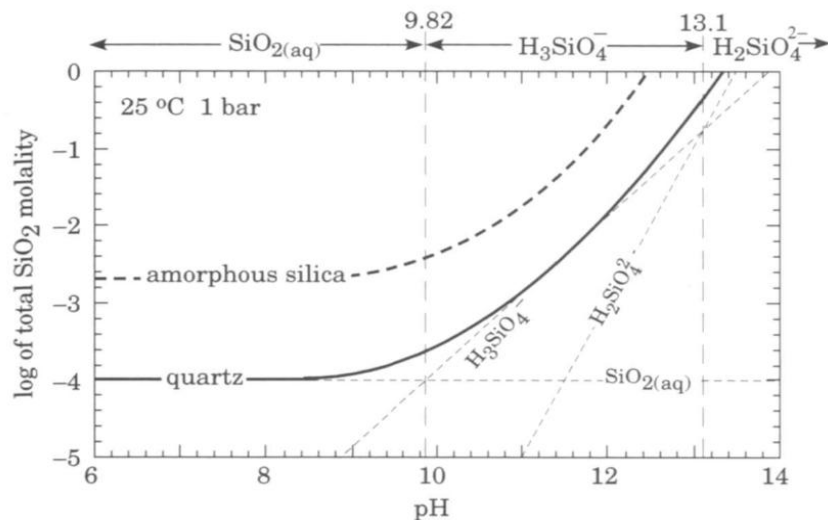


Figure 7.2.2 – Change in solubility for Silicates with increasing with pH^[15]

The figure also shows that the quartz solubility is independent of the pH at values below 9, while its only when the silicid acid start to protolyse to form H_3SiO_4^- and $\text{H}_2\text{SiO}_4^{2-}$, that the solubility increases. This could be translated to a proportionality between the solubility of quartz and silicid acid, however it is a wrong assumption. The pH value of the solution does not affect the solubility of Si minerals, but rather the reaction rate of the dissolution.[15] This will be explained in more detail in the following chapters.

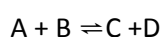
7.3. Reaction kinetics

Thermodynamics can predict the direction of a reaction, but not the speed or rate of the respective process. Nor can it predict the path of a reaction. Reaction kinetics is exactly what the name implies; calculations of reaction rates respective to the chemical processes.

Reaction kinetics considers the energy required to pass the barrier between reactants and products. For all reactions there is a medium, ie a solution, where one or more reactants are distributed with uneven energy levels in terms of kinetic energy. In order to initiate a reaction this kinetic energy has to surpass the energy barrier between the product and reactant. The minimum energy required is termed the activation energy, E_a .

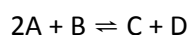
If the activation energy is large relevant to a given thermodynamically state, a fewer number of species would obtain the necessary energy to cross the threshold between product and reactant. Hence there would be close to no noticeable presence until a needed period of time has passed. In short, the higher the activation energy of a reaction, the slower the rates of the process will be.

For a reaction between two species A and B that forms the products C and D, reaction and reaction rate can be written as:



$$\frac{d[A]}{dt} = -k_r^+ [A][B] \quad \text{Equation 7.3.1}$$

Or;



$$\frac{d[A]}{dt} = -k_r^+ [A]^2 [B] \quad \text{Equation 7.3.2}$$

Where $d[A]/dt$ is the change in concentration of specie A over the infinite time dt . The constant $-k_r^+$ is the rate constant for the reaction. Equation 7.3.1 is overall a second order reaction while Equation 7.3.2 is overall a third order reaction.

These are very simplified equations that assume 1st order kinetics. A more modern equation is presented in equation xxx

The order of a reaction is given by the sum of powers to concentration of the components. Compared to a second order reaction, the third order reaction in Equation 7.3.2 would experience a double increase in rate of change in specie A if the concentration of specie B were to be doubled. This is due to the second order in [A] and overall third order of the reaction.[15]

7.3.1. First order reactions

A more relevant reaction to reservoir chemistry is the first order type as shown in Equation 7.3.3. An example of a first order reaction is that of a minerals precipitation and dissolution in water.

For the dissolution of specie A



the first order reaction rate can be written as

$$\frac{d[A]}{dt} = -k_r^+ [A] \quad \text{Equation 7.3.4}$$

A trivial integration of Equation 7.3.4 results in a decay rate type of equation with respect to the concentration of A. The decay rate of specie A would then be:

$$d[A] = [A^0] \exp(-k_r^+) \quad \text{Equation 7.3.5}$$

Where A^0 and k_r^+ is the initial concentration and rate constant of specie A. [15]

7.3.2. Intermediate steps

Sometimes there are intermediate steps between a reactant and the final product. For a reaction A to C there is an intermediate step called B. This intermediate might include a reconfiguration of the molecule structure from A to B so that the reaction can continue to step C.



In Equation 7.3.6 the reaction would have two rate constants, k_A^+ and k_B^+ .

If rate constant for formation of C (k_B^+) is larger than that of the formation of B (k_A^+), the rate for the overall reaction would be governed by first step. The step with the slowest rate would then be the limiting factor of the reaction. [15]

7.3.3. Reaction rates for calcite

As explained earlier calcite has a retrograde precipitation with respect to the temperature. The rate of this precipitation is also dependant on the pH of and the CO₂ pressure of the solution. Figure 7.3.1 is a graph representing the rate of dissolution as a function of pH and CO₂ pressure.

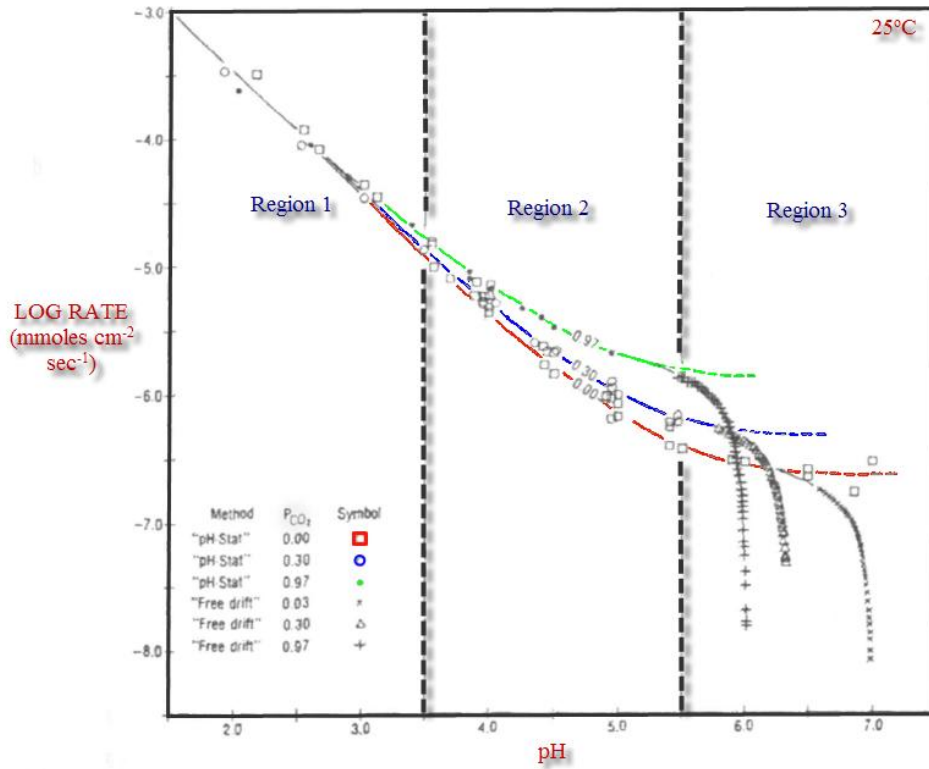


Figure 7.3.1 – The reaction rate of calcite plotted against the pH of the solution[2]

The trends Figure 7.3.1 show that the dissolution rate of calcite increases with decreasing CO₂ pressure and pH. At high pH values the rate decreases due to the backwards precipitation.[2]

7.3.4. Reaction rates for Quartz

It is confirmed that the rate constants are dependent on the temperature and to an extent the pressure. Another property of the solvent that affects the reaction rates is the pH.

Previously we considered the solubility and dissolution of quartz and observed a correlation between the pH and solubility product of quartz. This correlation is also present when comparing the reaction rate with the pH value.

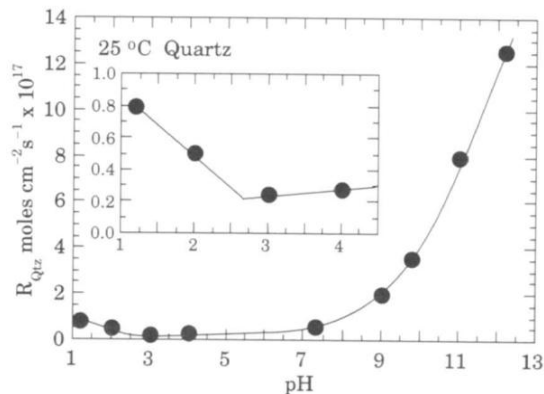


Figure 7.3.2 – Precipitation rate of quartz plotted against the pH[15]

The dissolution of quartz does not depend on the respective amount reacting, but rather the surface exposed to the solution. Figure 7.3.2 shows a slight increase in the reaction rate of dissolution below pH 3. At pH values above 3 the reaction rate increases with the pH.

If the reaction of quartz precipitation contained more than one step, the trend in Figure 7.3.2 could be explained by a rate controlling complex that is dependant on the pH. Silicic acid could be that complex, but the positive trend below pH 3 says otherwise. At pH values in the range of the first increment, the silicic acid should remain unchanged.

The surface of the quartz mineral develops a charge dependant on the pH of the contacting solution. At high pH values the charge is at its most negative and decreases as the pH value approaches 2.5. Quartz has a crystalline structure consisting of silica bound to oxygen in a tetrahedral shape. At the surface of the mineral the silica is bound to a hydroxide (Si-OH). When the pH increases, the fraction of charged surface grid also increases in the form of Si-O⁻.

It is imperative to notice that the equilibrium constant and solubility is independent of the pH, and that the reaction rate increases with the pH. Compared to calcite the precipitation rate of quartz is relatively low and often causes a super saturation in natural waters.[15]

7.3.5. Solubility, Acidity and porosity

The solubility and complexation of minerals in an aquifer is important with respect to change in porosity. Depending on the rates of the precipitation reactions, the size of the pores on pore necks will change and influence the chemical and mechanical properties of the entire reservoir.

Take the precipitation of calcite as an example: As the amount of calcite precipitated into the water contained in the aquifer increases, the pH value will increase proportionally. At a certain point this

increment in pH will cause the precipitation of quartz to increase with respect to the reaction rates. At some point this will reduce the stability of the pore walls.

8. Poroelasticity and geomechanical model

As described in chapter 4, a porous medium consists of a solid matrix with an interconnected network of pores. In a reservoir these pores are often filled with fluids like water, oil or methane gas. A porous media with an elastic solid matrix and a viscous fluid is characterized as poroelastic. The poroelastic medium is defined by its porosity, permeability and the properties of the solid matrix and fluid.

A poroelastic consideration deals with four basic variables. These include stress (σ_{ij}), strain (ϵ_{ij}), pore pressure (p) and the change in fluid content. To give an understanding of poroelasticity the following chapters will define a few relevant terms.

8.1. Stress and strain

The minerals that make constitutes the crust of the earth are constantly exposed to forces. Such forces may cause deformation or changes the shape of the mineral. Gravity is one of the most commonly known forces. Gravitation is directly exerted on all objects with a mass, and indirectly through contact between the said objects. The mineral crust of the earth is connected through a solid matrix framework where the force of gravity is transferred through contact between neighboring solid particles.

This translation of overburden pressure is the foundation for the theories of surface traction and deformation. Surface traction or stress, is defined as the force per unit area exerted on the surface of a particle. [20]

$$T = \frac{\Delta F}{\Delta A} \quad \text{Equation 8.1.1}$$

Stress and strain are synonymously used in context with traction and deformation. However, stress and strain are mathematical terms, while traction and deformation are related to the physical processes.

The traction can be divided into external and internal tractions. External tractions (T) represent the net force per unit area (ΔF) acting on a finite segment of the body's surface (Δs) as shown in Equation 8.1.2:

$$T = \lim_{\Delta s \rightarrow 0} \frac{\Delta F}{\Delta s} = \frac{dF}{ds} \quad \text{Equation 8.1.2}$$

The internal traction as shown in the right hand side of Figure 8.1.1, is defined according to the external traction since it is a propagation of the applied external pressure.

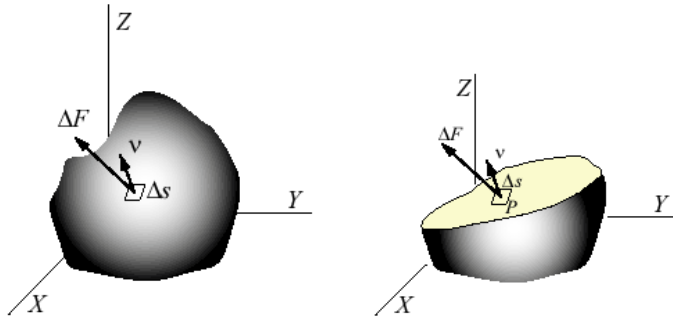


Figure 8.1.1 - External and internal surface traction^[21]

In point a given point P within a solid particle as shown in figure xxx, the traction for a point P can be defined similar to the external tractions (T). [21]

$$P = \lim_{\Delta s \rightarrow 0} \frac{\Delta F}{\Delta s} = \frac{dF}{ds}$$

Equation 8.1.3

The traction vectors are typically not orthogonal, but angled at the surface. The axial constituents of this angled vector are termed the normal and shear traction.

Stress, or traction, can be divided into three orthogonal components in the xyz directions, as shown in Figure 8.1.2. Amongst these axial components, the direct stress is the component normal to the respective surface, while the other two are called shear stresses and are tangential to the same surface. The direct stress influences the volume of the material and is resisted by the body's bulk modulus. The shear stress deforms the material without influencing the volume and is resisted by the body's shear modulus.

Figure 8.1.2 is a visualisation of an infinitesimal cube representing a point P in the matrix of a porous media. With three stress components on each of the six sides we can find the stress state. One component represents direct stress and the two other, the shear components. The stress components are total stress in the respective direction. By assuming that the cube is in static equilibrium the number of required components can be lowered to from a total of 18 to 9 in three planes.

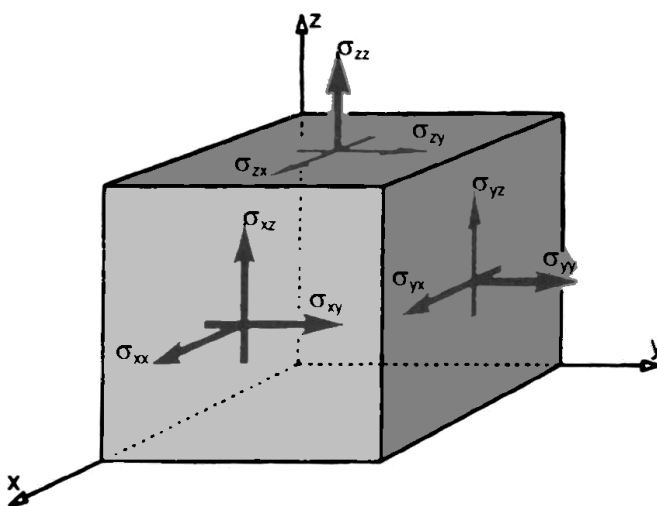


Figure YY.

Figure 8.1.2 - Stress state for a cube in a point P.[20]

For a component σ_{ij} , “i” is the stress on a plane along the direction of “j”. The normal stresses ($\sigma_{i=j}$) are parallel to the normal of the respective surfaces, and the shear stresses ($\sigma_{i \neq j}$) are parallel to the surface. By assuming static equilibrium, we assume that stresses diagonal to each other are identical so that σ_{ij} equals σ_{ji} . These nine components or tensors can be placed in a matrix according to Equation 8.1.4 which is also known as the tensor matrix.

$$\begin{bmatrix} \sigma_{xx} & \sigma_{xy} & \sigma_{xz} \\ \sigma_{yx} & \sigma_{yy} & \sigma_{yz} \\ \sigma_{zx} & \sigma_{zy} & \sigma_{zz} \end{bmatrix} \qquad \text{Equation 8.1.4}$$

Shear stresses have different suffixes and are often denoted by τ . [21, 22]

8.2. Pore pressure

Pore pressure (p) is simply the pressure of the fluid occupying the respective pore space. The pore pressure is measured in a fluid reservoir which is in static equilibrium with the pore.

Together with the mechanical quantities stress and strain, the fluid quantities of pore pressure and fluid content constitute four variables that can be combined into two pairs of dependant and independent variables. The four possible permutations of these variables, together with the tensor stress and strain, is the foundation for several poroelastic moduli. [20]

8.3. Poroelastic properties

The theory of linear poroelasticity describes the interaction between mechanical effects and adding or removing fluid from rock.

The intensive properties of the confined fluids in a pore are dependent on extensive properties of the solid matrix. If an intensive variable like the pressure or density of a fluid is altered, then the extensive pore volume of the matrix might experience a proportional change (I.e. pressure depletion). This relationship is termed as a fluid – solid coupling.

Solid - fluid coupling, on the other hand, occurs when a net change in stress induces a change in fluid properties. Changes in fluid properties like mass or pressure may also induce a change in volume of the porous media. This is termed fluid – solid coupling.

With respect to the solid – fluid coupling, the magnitude depends on a range of factors including the compressibility of the solid matrix, pores and solid grains. The compressibility of the fluid trapped in the pores also important. [20]

The pore compression and subsidence of the sea floor at the Sleipner reservoir occurred due to a decline in the fluid pressure. As the hydrocarbons were removed from the reservoir the by means of fluid expansion and pore compressibility, the solid matrix started to collapse causing the sea floor supporting platform to subside. Even though measures put in action to maintain the pressure the effect was and prolonged by chemical reactions and further weakening of the calcite rich formation.

8.3.1. Hydraulic fracturing

The poroelastic expression for the circumferential stress can be used to estimate the breakdown pressure in hydraulic fracturing. (Haimson and Fairhurst, 1969) The assumption is made that breakdown occurs when the Terzaghi effective stress equals the tensile strength T in Equation 8.3.1:

$$\sigma_{\theta\theta} + p = T$$

Equation 8.3.1

9. Flow equations

This chapter contains the description of the flow equations used in the respective modules of the coupled RCB code.

9.1. Reactive transport

In the reactive module Retraso, the mechanical and reactive flow is governed by three laws:

- Diffusion with respect to Fick's law
- Advection with respect to Darcy's law
- Dispersion with respect to the local heterogeneities of the solid rock matrix and flow pattern

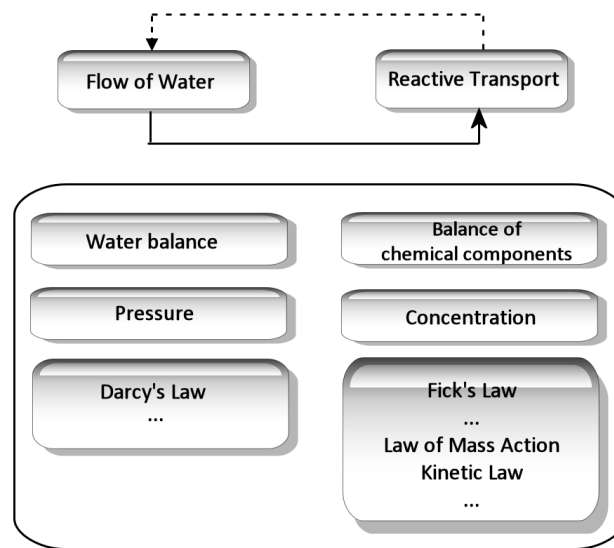


Figure 9.1.1 – Schematic illustration of the iteration in Retraso

Figure 9.1.1 illustrates the iterative process in the reactive module, along with the considered balance variable and governing laws.

9.1.1. Diffusion

The diffusion is governed by Fick's laws. According to the description in chapter 4.3, the flux is obtained by means of Fick's first law:

$$J = -D_0 \frac{\partial c}{\partial x} = -[cm^2 / s] \frac{[mole / cm^3]}{[cm]} = \frac{mole}{cm^2 s}$$

Equation 9.1.1

The diffusion factor D_0 is dependent on the tortosity and reduced area of diffusion (bottlenecks) in the porous medium. For a respective formation segment the diffusion factor is corrected according to equation xxx:

$$D_{Corrected} = \phi \left(\frac{\chi}{\tau^2} \right) D_0$$

Equation 9.1.2

Where ϕ is the porosity, χ is the change in diffusion area and τ is the correction for the tortuosity in the permeable path of flow.

9.1.2. Advection

Advection is transport of dissolved solid particles, governed by Darcy's law with respect to the concentration of the solid particles. As such the flux of solid particles is obtained by means of equation xxx:

$J_{adv} = q_{Darcy} \cdot C = \left[\frac{m^3}{m^2 s} \right] \left[\frac{mole}{m^3} \right] = \left[\frac{mole}{m^2 s} \right]$	
--	--

Equation 9.1.3

Where q is the Darcy flux and C is the concentration. The Darcy flux is described in equation xxx, chapter xxx.

$q = \frac{k\rho g}{\mu} \nabla \left(z + \frac{\rho}{\rho g} \right) \approx -K \nabla h \quad ; \quad \nabla h \in \left[\frac{\partial}{\partial x}, \frac{\partial}{\partial y}, \frac{\partial}{\partial z} \right]$	
---	--

Equation 9.1.4

9.1.3. Dispersion

The velocity of the dispersion front is dependent on the heterogeneity of the reservoir. At initial conditions the liquid would be displaced in a piston while changes in permeability will blablabla

$J_{disp.} = -\phi D_{dis} \nabla C$	
--------------------------------------	--

Equation 9.1.5

Where ϕ is the porosity, D_{dis} is the dispersion tensor and ∇C is the concentration gradient. In the two-dimensional model, there are two considered axial tensors in x and y direction. The dispersion in each direction is obtained by equation xxx and xxx:

$D_L = \alpha_L v_x$	
$D_T = \alpha_T v_x$	

Equation 9.1.6

Where alpha represents the longitudinal and transversal dispersivity [m] in the x and y directions. v_x is the linear velocity [m/s] of the dispersion front.

9.2. Geomechanics

9.2.1. Mass forces

Forces acting on each particle in the body due to relative movements of particles: deformation

$\sigma_{ij} = \sum_{K=1}^3 H_{ijkl} \cdot e_{kl}$	
--	--

Equation 9.2.1

Where σ_{ij} is the stress tensor, H_{ijkl} the material property or elasticity tensor and e_{kl} is the strain tensor as described in equation xxx:

$e_{ij} = \frac{1}{2} \left[\frac{\partial u_i}{\partial \chi_j} + \frac{\partial u_j}{\partial \chi_i} + \sum_{k=1}^3 \frac{\partial u_k}{\partial \chi_i} \frac{\partial u_k}{\partial \chi_j} \right]$	
--	--

Where u_i is the displacement in direction “i” of a fixed coordinate system. χ_i is the displacement coordinate of which “i” equals x, y and z.

9.2.2. Linear elasticity

When the last sum in equation xxx can be said to approach zero, we have linear elasticity. The linear part of the strain tensor is given by equation xxx

$\epsilon_{ij} = \frac{1}{2} \left(\frac{\partial u_i}{\partial \chi_j} + \frac{\partial u_j}{\partial \chi_i} \right)$	
--	--

$\sigma_{ij+j} + F_i = 0$	
---------------------------	--

$\sigma_{ij} = \lambda_{\epsilon_{kk}} \delta_{ij} + 2G_{\epsilon_{ij}} - \beta \Theta \delta_{ij}$	
---	--

9.2.3. Navier stokes

$$G u_{i,ij} + (\lambda + G) u_{i,ij} - \beta \Theta_j + F_i = 0$$

The lame consant lambda is obtained through equation xxx:

$$\lambda = \frac{E\nu}{(1+\nu)(1-2\nu)}$$

Where E is the Young modulus and v is the Poisson's ratio. Likewise the shear modulus and thermal modulus can be obtained by equation xxx and xxx. The factor Θ is simply the temperature relationship given by: $\Theta = T - T_0$

$$G = \frac{E}{2(1+\nu)}$$

$$\beta = \alpha(3\lambda + 2G)$$

10. Simulation software

In the introduction of this thesis the simulation software RetrasoCodeBright was briefly introduced. This chapter contains a more elaborate description of the two coupled modules that constitute the program abbreviated as RCB. The contained material is largely gathered from the previous work of PhD Shunping Liu and Professor Bjørn kvamme [ref]

The version of the code applied in this thesis as received a range of modifications. It has been rewritten and extended to account for CO₂ storage simulations in saline aquifers located at large depths. More specifically code has been rewritten to account for non-ideal gas through corrections of gas density and gas solubility in all transport terms, in addition to improvements in the Newton-Raphson method used to solve the flow and mechanics in RCB in order to ease the convergence even under high gas injection pressures.

10.1. RetrasoCodeBright

RCB is the result of coupling the two different codes consisting of a reactive transport module and geomechanical transport module that also considers flow and heat transport. CodeBright, an abbreviation of “COupled DEformation of BRIne Gas and Heat Transport”, was designed for the thermo-hydraulic-mechanical analysis of three-dimensional multiphase saline formations. The other module Retraso, short for “REactive TRAnsport of Solutes”, solves the two-dimensional reactive transport problems. [Ref ccp2 SPL BK]

The original form of Retraso CodeBright (RCB) was developed at the Technical University of Catalonia, Barcelona. The team contributing with the two parts consisted of Maarten W. Saaltink, Carlos Ayora and Sebastia Olivella. At the time the platform was initially intended for standard conditions at 1 atm pressure and 15 Celsius, but due to the design of implicit coupling between the two modules Retraso and CodeBright the code was perfect for CO₂ injection calculations. [Refccp2]

Due to these promising properties, project “Observing the effect of long term CO₂ storage in saline aquifers” adopted the code with aim modify the equations in order to simulate reservoirs at large depths. The project is carried out at the Department of Physics and Technology at the University Of Bergen. The main focus of the project is to develop a modeling method that can be used in more common situations. [Ref]

As mentioned the RCB coupled code is improved by doing three main corrections in its implementation.

- The first two are the corrections for fugacity coefficients and Poynting corrections in the gas (CO₂)/liquid equilibrium respectively in CodeBright part and Retraso part. These corrections are essentially straightforward to implement.
- The third correction is the density correction in the gas flow equations. These corrections also essentially straightforward give that the compressibility factors are known.
- The other optimization is done by modifying the conventional Newton-Raphson method which introduces a relaxation factor to make the iterative process converge faster. (Spl bk)

10.2. Governing equations and algorithms in CodeBright module

RCB formulates the flow problem in a porous media with a multiphase approach that includes the solid matrix and its contained fluids.

During a single time step the geomechanical module of the coupled code (CodeBright) first calculates the mass flow, heat flow and geomechanical deformation. These variables, along with the physical properties and state conditions such as fluid pressure, flux, temperature and hydraulic saturation, are then sent to the chemical module (Retraso).

As shown in figure xxx both the CodeBright module and Retraso module utilize the Newton-Raphson iteration method to solve the linear algebraic systems of governing equations.

The data received from CodeBright is processed in several sub-groups which consider the integration the individual fluxes of molecules and ions, while at the same time taking into account possible reactions between the reservoir fluids and the solid matrix. These reactions can either be considered in an equilibrium approximation or a kinetic formulation.[23] Eventual changes in porosity as a result of advection, mineral dissolution/erosion and precipitation are updated according to commonly used correlations[23]. All of the updated values from Retraso are then transferred back to the CodeBright module so that the next time step can be initiated.

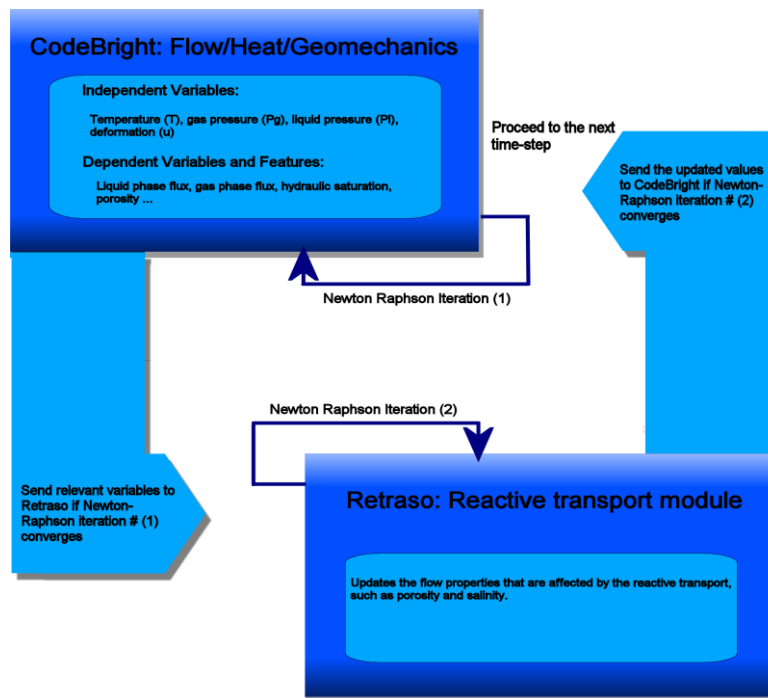


Figure 10.2.1 – graphical representation of the communication and iteration processes in the two modules; Retraso and CodeBright. Schematic coupling of the two modules

With respect to the modifications of the original code the following section will describe the basic changes in detail. The coupling between the two modules is also schematically illustrated in Figure 10.2.1

The governing equations for non-isothermal multiphase flow of water and gas through porous deformable saline media have been presented by Olivella et al. [4]. In the user manual

These equations can be categorized into four main groups, which are balance equations, constitutive equations, equilibrium relationships and definition constraints.

10.2.1.1. Mass balance of water and gas phase

In CodeBright the equations of mass balance were obtained in a compositional approach where water, air and species of salts were considered rather than liquid, gas and solid. The mass balance of water and air is obtained according to Equation xxx and xxx:

$\frac{\partial}{\partial t} (\theta_{liquid}^{water} S_{liquid} \Phi + \theta_{gas}^{water} S_{gas} \Phi) + \dots$ $\dots + \nabla (j_{liquid}^{water} + j_{gas}^{water}) = f^{water}$	
---	--

$\phi \frac{D_s (\theta_{liquid}^{air} S_{liquid} + \theta_{gas}^{air} S_{gas})}{D t} + (\theta_{liquid}^{air} S_{liquid} + \theta_{gas}^{air} S_{gas}) \frac{D_s \phi}{D t} + \dots$ $\dots + (\theta_{liquid}^{air} S_{liquid} \Phi + \theta_{gas}^{air} S_{gas} \Phi) \nabla \frac{du}{dt} + \nabla (j_{liquid}^{air} + j_{gas}^{air}) = f^{air}$	
--	--

Where the variables in both equations are defined as:

- Θ_m^n - is the fraction of component “n” in phase “m”
- S_m - is the hydraulic saturation of phase “m” i.e. the fraction of pore volume occupied phase “m”
- Φ - is the porosity
- J_m^n - is the total flux of component “n” in phase “m”
- f^n - is an external source or drain of component “n”

The two first terms in the mass balance of water represents the change in the mass of water within the gas and liquid phase, while the third term represent the flux of water in gas and liquid phase. Together the three terms constitutes the amount of water added or removed from the respective area, f^w . The amount of component “n” in phase “m” represented by Θ_m^n in equation xxx and xxx can also be defined as:

$\omega_m^n \times \rho_m$		
----------------------------	--	--

Where ω_m^n is the mass fraction of component “n” in phase “m” and ρ_m is the density of phase “m”

10.2.1.2.

Mass balance of solid

The mass balance for the solid phase considers the molality change of the mineral matrix. An infinite change can be described according to equation xxx:

$\frac{\partial}{\partial t}(\theta_s(1-\phi)) + \nabla(j_s) = 0$		
---	--	--

where θ_s is the mass of solid per unit volume of solid, j_s is the flux of solid and ϕ is the porosity. By solving equation xxx with respect to the porosity we obtain equation xxx which represents the change in porosity.

$\frac{D_s\phi}{Dt} = \frac{1}{\theta_s} \left[(1-\phi) \frac{D_s\theta_s}{Dt} \right] + (1-\phi) \nabla \frac{du}{dt}$		
--	--	--

The introduced variable u is the solid displacements.

10.2.1.3.

Momentum balance of the medium

The momentum balance reduces to the equilibrium of stresses if the inertial terms are neglected:

$\nabla\sigma + b = 0$		
------------------------	--	--

where σ is stress tensor and b is the vector of body force.

10.2.1.4.

Internal energy balance of the medium

By taking into account the internal energy, E , for the three phases - the internal energy balance for the porous medium can be expressed according to equation xxx:

$\frac{\partial}{\partial t} (E_{solid}\rho_{solid}(1-\Phi) + E_{liquid}\rho_{liquid}S_{liquid}\Phi + E_{gas}\rho_{gas}S_{gas}\Phi) + \dots$ $\dots + \nabla(i_c + j_{E-solid} + j_{E-liquid} + j_{E-gas}) = f^Q$	
---	--

where the factor f^Q is an internal or external energy supply.

The first three terms in the equation represent the change in energy within the three phases. In the fourth term, i_c represents the energy flux by conduction in the porous medium, while three remaining terms constitutes the advective flux of energy due to the motion of masses.

10.2.2.

Constitutive equations and equilibrium restrictions

In association with this formulation there is a set of necessary constitutive and equilibrium laws. Table xxx contains a list of the laws that should be incorporated in the general formulation. The dependent variables that are computed using each of the laws are also presented in the same table.

Here we need to explain some of the most important constitutive and equilibrium laws.

The Generalized Darcy's law is used to compute the advective flux, q , of the α phase ($\alpha = l$ for liquid, $\alpha = g$ for gas). It is expressed as:

$q_a = -\frac{\kappa k_{\gamma a}}{\mu_a} (\nabla P_a + \rho_a g)$		
--	--	--

where κ is the tensor of intrinsic permeability (m^2), k_{ra} is the relative permeability of the phase, μ_a is the phase's dynamic viscosity (Pa s) and g is the gravity vector (ms^{-2}). Here we need to point out that the dynamic viscosity μ_a highly depends on temperature (T) and the relative permeability (k_{ra}).

The Van Genuchten's [12] retention curves expressing saturation as a function of liquid or gas pressure is used. It is:

$S_l = \left(1 + \left(\frac{P_g - P_l}{P_0} \right)^{\frac{1}{1-n}} \right)^{-n} \quad \text{of which} \quad S_g = 1 - S_l$	
--	--

where P_0 and n are scale pressure and shape parameters. The relative permeability k_{ra} depends on saturation (S_l) which in its turn depends on P_l and P_g .

The relative permeability (k_{ra}) in eq. (7) is a function of the saturation. In various expressions, the Van Genuchten is the most widely used, which is:

$k_{\gamma l} = \sqrt{S_l} (1 - (1 - S_l^{\frac{1}{n}})^n)^2$		
---	--	--

Where n is still the shape parameter, but it does not necessarily have the same value.

Constitutive equations	Variable name	Variable(s)
Darcy's law	Liquid and gas advective flux	q_l, q_g
Fick's law	Vapor and gas non-advective flux	i_g^w, i_l^a
Fourier's law	Conductive heat flux	i_c
Retention curve	Liquid phase degree of saturation	S_l, S_g

Mechanical constitutive model	Stress tensor	σ
Phase density	Liquid density	ρ_l
Gas law	Gas density	ρ_g
Equilibrium restrictions		
	Variable name	Variable
Henry's law	Mass fraction gas dissolved	ω_l^h
Psychometric law	Vapor mass fraction	ω_g^w

10.2.3. Time subdivision in CodeBright

In the coupled code RCB, both CodeBright and Retraso perform the numerical iterations in a Newton-Raphson approach in order to solve the highly non-linear equations. However, the time subdivisions in the two modules are different.

In CodeBright the time interval approach is governed by several criteria. Between an iterated time t and the following time-step $t+1$, there is a time interval dt . The next time step would then be calculated according to equation xxx

$dt_{next} = dt_{updated} \cdot F_{next}$	
---	--

Where dt_{next} and $dt_{updated}$ represents the next time interval and the adjusted time interval, according to the residuals at time $t+1$. The time factor F_{next} is the predicted factor for the next time step, which is always larger than zero and ranges between the empirical values of 0.1 to 1.4. The factor itself is calculated based on the relative error of the variables in the previous time-step. If the relative error is larger than the prescribed value, the time increment dt will be reduced according to the magnitude of deviation in order to ease the convergence.

For each independent variable, there are four parameters of error tolerance that constitutes the criteria of convergence. These four include the maximum absolute error, the maximum relative error, the maximum mass balance error and the maximum correction per iteration. Together they adjust the updated time interval to the most ideal magnitude for the iterative process. If the residual at time $t+1$ is large enough then $dt_{updated}$ will be reduced accordingly. If the same residual at time $t+1$ is small enough then $dt_{updated}$ will be increased.

Boundary conditions

The pressure in a CO2 injection scenario is relatively high. If the simulations were to directly apply the prescribed injection pressure as an initial boundary condition, it would cause large pressure gradients around the injection point which in turn would cause convergence problems in the surrounding nodes and elements. Based on this understanding, a lower pressure slightly above the natural pressure gradient in the area must be applied as the initial boundary condition. In order to obtain the originally prescribed injection pressure, the code will utilize a pressure ramp loading in one or more time intervals. The simulations that will be presented later, demonstrates the applied function of pressure ramp loading. However, this section will further focus on the equations of boundary conditions.

In the thermo-hydraulic calculations performed by CodeBright, the state variables P_l , P_g and T are always used as boundary conditions in combination with a few user-prescribed parameters when specific requirements need defining in the thermo-hydraulic system. CodeBright expresses nodal flow rates for every component (water, air and heat) and every phase (liquid, gas) as function of the state variables and available prescribed values, specified by the user.

The mass balance of water, air and energy were defined in equation xxx to xxx. Based on these equations, the boundary conditions and expressions for the source/sink terms (f^w , f^a and f^Q) have to be rewritten for water, air and heat.

The mass flow rate of water as a component of the gas phase and liquid phase can be written as:

$j_g^w = (\omega_g^w)^0 (j_g^0 + \Delta j_g^0 \frac{dt}{\Delta t})$ $+ (\omega_g^w)^0 \gamma_g ((P_g^0 + \Delta P_g^0 \frac{dt}{\Delta t}) - P_g) + \beta_g ((\rho_g \omega_g^w)^0 - (\rho_g \omega_g^w))$	
--	--

$j_l^w = (\omega_l^w)^0 (j_l^0 + \Delta j_l^0 \frac{dt}{\Delta t})$ $+ (\omega_l^w)^0 \gamma_l ((P_l^0 + \Delta P_l^0 \frac{dt}{\Delta t}) - P_l) + \beta_l ((\rho_l \omega_l^w)^0 - (\rho_l \omega_l^w))$	
--	--

Where the superscript 0 stands for the prescribed values, and the terms $\Delta(-)dt/\Delta t$ allow for imposing a linear variation of the respective variable during the time step.

This general form of boundary condition includes three terms of which the first term represents the mass inflow or outflow governed by flow rate of gas (j_g^0) or liquid (j_l^0). The second term represents mass inflow or outflow that takes place with respect to the defined nodal gas phase pressure (P_g^0) or liquid phase pressure (P_l^0). The coefficients γ_g or γ_l are leakage coefficients. The third term is the mass inflow or outflow that takes place when the mass fraction of vapor or water in liquid phase is prescribed at the boundary.

The phase respective fluxes of a component are the sum of equation xxx and xxx. Hence the total boundary condition of water can be obtained by equation xxx:

$j^w = j_g^w + j_l^w$	
-----------------------	--

Similarly, the mass flow rate of air as a component of the gas phase and liquid phase are:

$j_g^a = (\omega_g^a)^0 (j_g^0 + \Delta j_g^0 \frac{dt}{\Delta t})$ $+ (\omega_g^a)^0 \gamma_g ((P_g^0 + \Delta P_g^0 \frac{dt}{\Delta t}) - P_g) + \beta_g ((\rho_g \omega_g^a)^0 - (\rho_g \omega_g^a))$	
--	--

$j_g^a = (\omega_g^a)^0 (j_g^0 + \Delta j_g^0 \frac{dt}{\Delta t})$ $+ (\omega_g^a)^0 \gamma_g ((P_g^0 + \Delta P_g^0 \frac{dt}{\Delta t}) - P_g) + \beta_g ((\rho_g \omega_g^a)^0 - (\rho_g \omega_g^a))$	
--	--

And the total boundary condition of air is:

$j^a = j_g^a + j_l^a$	
-----------------------	--

For the energy balance equation, the boundary condition also has a similar form

$j_e = (j_e^0 + \Delta j_e^0 \frac{dt}{\Delta t}) + \gamma_e (T^0 + \Delta T^0 \frac{dt}{\Delta t} - T)$ $+ E_g^w (j_g^w) + E_l^w (j_l^w) + E_g^a (j_g^a) + E_l^a (j_l^a)$	
--	--

11. Reactive transport in Retraso part

The reactive module in the coupled RCB code is written with a “state of the art” geochemical solver which has capabilities of treating aqueous complexation (including redox reactions), adsorptions and precipitation/dissolution of minerals along with gas dissolution. The precipitation, dissolution and aqueous complexation can be modeled in either an equilibrium or kinetic approach.

In the current version, the code has been extended from ideal gas to realistic fluid description using an equation of state. Calculations of densities and fugacity coefficients can either be handled through an interface which utilizes an equation of state, or through an interpolation approach using tabulated values for pure CO₂. The simulations presented in this thesis utilizes the Soave Relich Kwong (SRK) equation of state [9] which is applied on the density calculations and fugacity calculations considering the CO₂ phase and dissolution of CO₂ into the groundwater

The dissolution and precipitation of the formation minerals in CO₂ injection scenarios are slow natural processes, where the kinetic law [10] is applied in RCB. The mathematical equations for the system are highly non-linear and are solved numerically [7, 8].

11.1.1. Kinetic rate laws

In RetrasoCodeBright the rates of mineral dissolution and precipitation is calculated according to the general expression formulated by Lasaga et al. [10] (see also Saaltink et al. [7]):

$$r_m = \sigma_m \zeta_m \exp\left(\frac{E_{a,m}}{RT}\right) \sum_{k=1}^{N_k} k_{mk} \prod_{i=1}^{N_s} acc_i^{P_{mki}} \left(\Omega_m^{\theta_{mk}} - 1\right)^{\eta_{mk}}$$

Where r_m is the mineral dissolution rate in moles of mineral per volume of rock and unit time, k_m is the experimental reaction constant in the same units as the dissolution rate. The exponential term containing the activation energy E_a , is a function of the temperature including temperature dependencies defined in equation xxx to xxx. Ω_m is the saturation ratio, or the ratio between the ion activity product and the solubility product as defined in Equation xxx below:

$\Omega_m = \frac{1}{K_m} \prod_{i=1}^{N_c} a_{i,actual}^{v_{mi}}$		
$K_m = \prod_{i=1}^{N_c} a_i^{v_{mi}} = \prod_{i=1}^{N_c} c_i^{v_{mi}} \gamma_i^{v_{mi}}$		

The logarithm of Ω_m is known as the saturation index SI_m

The system reaches the minimum free energy at equilibrium when $\Omega_m = 1$ or $SI_m = 0$. The parameters θ and η must be determined from experiments.

The term inside the parenthesis in Equation 29, called the far-from-equilibrium function, decreases the reaction rate in a non-linear way, as the solution approaches to equilibrium.

The extra subscript "actual" on the activity a in equation (30) distinguishes the actual non-equilibrium activity for the equilibrium activity in equation (31). c in equation (31) is either concentration or mole-fractions depending on the actual units used for the K-values.

and a similar consistent formulation will occur in equation (30) for the real concentrations and corresponding activity coefficients γ for actual non-equilibrium conditions.

The term $acc_i^{p_i}$ accounts for the catalytic effect of some species (particularly of H+) and the value of p_i is determined by fitting experimental data.

For reactions which are slow at ambient conditions the experiments are carried out at temperatures which are sufficiently high to result in dissolution within reasonable reaction times.

Scaling of the rate constants are normally done through the Arrhenius equation:

$k_m = k_0 \exp\left(-\frac{E_{a,m}}{RT}\right)$	
--	--

where k_0 is a constant and $E_{a,m}$ is the apparent activation energy of the overall reaction process, which for most minerals range from 30 to 80 kJ/mol [10]. Parameters k_0 and $E_{a,m}$ are determined from experiments performed at different temperatures.

11.1.2. Time subdivision in Retraso

Both code CodeBright and code Retraso adapt Newton-Raphson iteration method to solve the highly non-linear equations. Nevertheless the method to subdivide the time in one time step in code CodeBright and code Retraso is different.

After one Newton iteration at time $t + 1$ code Retraso will judge whether this iteration is successful by compare the residual of solutions of time $t + 1$ and time t , noted as r_{t+1} , is within the prescribed error accepted area. If not, next time interval will be reduced to dt / fd , where dt is the last time interval, fd is the time decrease factor which is bigger than 1.0. Then calculation goes back to repeat the iteration of time $t + 1$.

If convergence has been achieved, Retraso will judge whether the number of iteration $niter$ is within the prescribed area, that is $(thr\ min, thr\ max)$. If $niter$ is bigger than $thr\ max$, $dt = dt / fd$. If $niter$ is smaller than $thr\ min$, meaning that it has taken a very few iteration steps to converge, dt will be increased to $dt * fi$, where fi means the time increasing factor, which is bigger than 1.0. Otherwise,

niter is between the accepted areas. No matter which routine is taken, calculation will go to the next time step.

11.1.3. Boundary conditions

Since we have taken the pressure ramp loading method in CodeBright part and code Retraso, in its turn, does not allow varying boundary injection pressure, we have to instead use the CO₂ molar fraction as the boundary condition. No matter how different the injecting pressure is changed, the CO₂ molar fraction will be kept to be a constant.

For every chemical component a boundary condition equation in Retraso is to be written for the mass balance. Retraso permits two types of boundary conditions. In the first type, a component mass flux is calculated by multiplying the boundary flux of a phase (j_l , liquid, j_g , gas) by a total concentration of a component, which is that of the node of the boundary (u_a , concentration of total aqueous species, or u_g , concentration of gas) or an externally specified one ($(u_a)^0$ or $(u_g)^0$), depending on whether the phase enters or leaves the medium:

$m_l = j_l(u_a)^0$	$j_l > 0$	
$m_l = j_l u_a$	$j_l < 0$	

$m_g = j_g(u_g)^0$	$j_g > 0$	
$m_g = j_g u_g$	$j_g < 0$	

The second one is a mixed condition according to the following expressions:

$m_l = \gamma_l((u_a)^0 - u_a)$	
---------------------------------	--

$m_g = \gamma_g((u_g)^0 - u_g)$	
---------------------------------	--

where γ_l and γ_g are leakage coefficients. A fixed concentration can be simulated by giving these leakage coefficient very high values. The first type is more preferred for advection dominated cases, whereas a fixed concentration is more preferred for diffusion dominated cases.

The values of the external total concentrations ($(u_a)^0$ or $(u_g)^0$) should be given for every component. For the aqueous phase, Retraso first calculates the concentrations of the primary species by choosing one of the equations in Table 3. Then the total aqueous concentrations will be calculated by equation (28).

Table 3 Options for calculating the chemical composition of the boundary

Option	Equation
Total aqueous component	$(u_a)^0 = \text{fixed}$
Charge balance	$\sum_i z_i (c_{ai})^0 = 0$
Activity	$(a)^0 = \text{fixed}$
Equilibrium with mineral	$(\Omega_m)^0 = 1$
Equilibrium with gas	$(p_f)^0 = \text{fixed}$

12. User interfaces and simulation software

This chapter contains an overview and description of the respective software used in the simulations.

12.1. Visual retraco

Visual Retraso is a software - tool used to create the input files needed for the simulations in RCB which is explained in the following section. The input files contain the grid layout, the description of the zones and the initial conditions within each of the respective areas of the reservoir.

Initially the software goes through a step-by-step progression where chemical elements, species, zones and constants are described. More detailed descriptions of each reservoir zone, containing specifications such as elasticity, retention curves and CO₂ viscosity, can be added after the initial setup of the grid. Figure 10.2.1 is screenshot of the VGUM interface.

In connection to the tweaking of Retraso CodeBright, Visual retraso is also altered at a code level. Hence the input files require some treatment afterwards in order to be compatible with Retraso CodeBright.

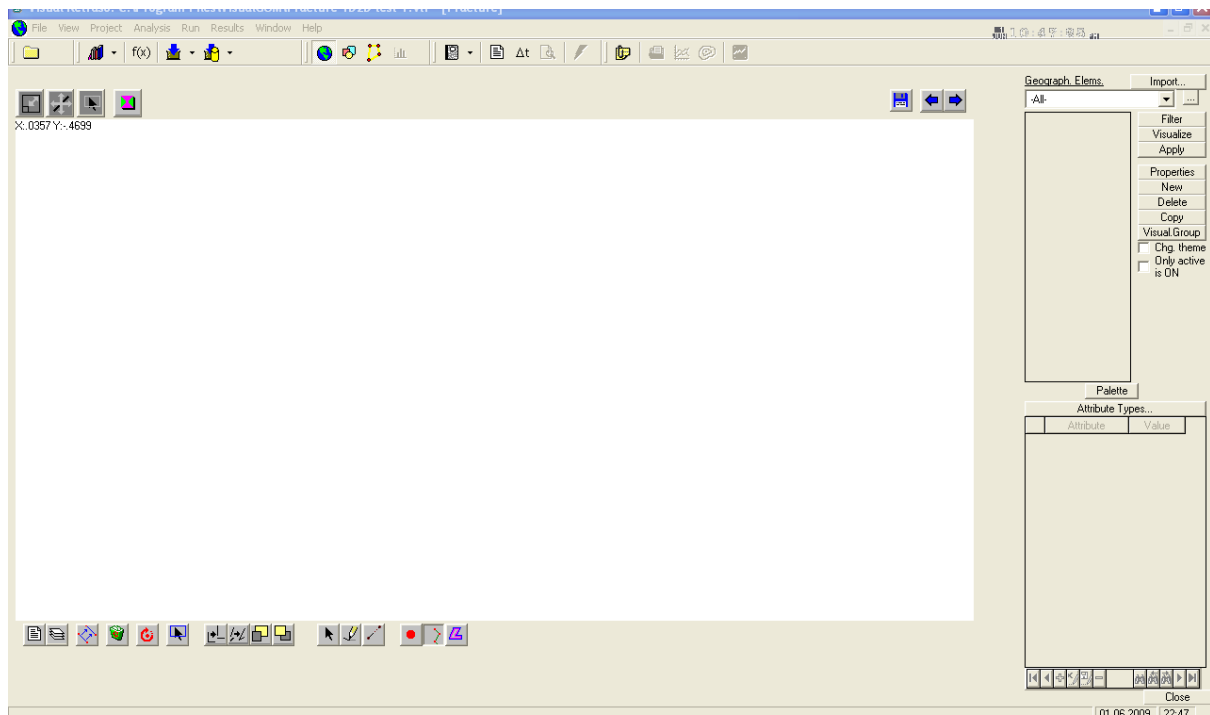


Figure 10.2.1 – VGUM interface

Most functions in the program are accessible through the main toolbar. The initial setup of the simulations has a step by step process guided by the program itself. Appendix XX contains a detailed explanation for the process of creating the input files. Appendix xxx further explains corrections that must be done to ensure compatibility with respect to RCB

12.2. GiD

“GiD is an interactive graphical user interface used for the definition, preparation and visualization of all the data related to a numerical simulation. This data includes the definition of the geometry, materials, conditions, solution information and other parameters. The program can generate a mesh for finite element, finite volume or finite difference analysis and write the information for a numerical simulation program in its desired format. It is also possible to run these numerical simulations from within GiD and then visualize the results of the analysis.

GiD can be customized and configured by users so that the data required for their own solver modules may be generated. These solver modules may then be included within the GiD software system.

The program works, when defining the geometry, in a similar way to a CAD (Computer Aided Design) system but with some differences. The most important of these is that the geometry is constructed in a hierarchical mode. This means that an entity of higher level (dimension) is constructed over entities of lower level; two adjacent entities will then share the same lower level entity.

All materials, conditions and solution parameters can be defined on the geometry itself, separately from the mesh as the meshing is only done once the problem has been fully defined. The advantages of this are that, using associative data structures, modifications to the geometry can be made and all other information will automatically be updated and ready for the analysis run.

Full graphic visualization of the geometry, mesh and conditions is available for comprehensive checking of the model before the analysis run is started. More comprehensive graphic visualization features are provided to evaluate the solution results after the analysis run. This post-processing user interface can also be customized depending on the analysis type and the results provided. “[24]

In relevance to this thesis GiD is utilized as a postprocessor for the output-files created in the RCB code. All the needed data are programmed to be written in a single compiled resource script, or file, named 1_flavia depending on the user settings. This file contains everything from the deformation to the pH and stress simulated in the reservoir through 100 years.

Post-processed data from the flavia file is rendered as a two-dimensional contour plot where the available primary colours display the respective changes over time in an animation. With the settings used during the initial stages of creating the input files, each flavia file contains 60 000 time steps over 100 years. Each of the time steps are marked with a timestamp, allowing the user to select any relevant time steps for comparison.

13. Simulations

The main goal of this thesis is to utilize the Retraso CodeBright software on carbon dioxide injection and further investigate the possibilities of simulating fractures in the containing layer of cap rock.

The entire simulation, from the creation of the input-files to the post-processing, has been run on a stationary computer. This particular computer is a bit more than average as it is equipped with 16 gigabytes of memory, two quad-core “Intel Xeon 2.66 GHz” processors backed up by a high capacity air-cooling system. Depending on the complexity of the respective simulations, the total simulation time might vary from three days to over a week.

A set of eight cases were obtained by applying a cubic data-plan containing eight indexed points as shown in Figure 13.3.1. In lack of real field data from relevant reservoir systems, the eight simulations presented in his thesis are simplified models based on approximations to values in published articles. The papers from H. Hellevang and the TOUGH2 FLAC3D article are the two main sources for the relevant data, however there are some deviations from the provided data. These respective variables are altered according to advice based on the previous experiences of Shunping Liu.

The reactive module is the most common source of convergence problems among several of the existing simulation codes. As such, several of the applied variables are adjusted according to earlier experience in use of the simulation software.

This chapter contains detailed information for the simulation build of the eight presented cases. In addition there are some descriptions of preliminary work and utilized applications.

13.1. Prior work and related projects

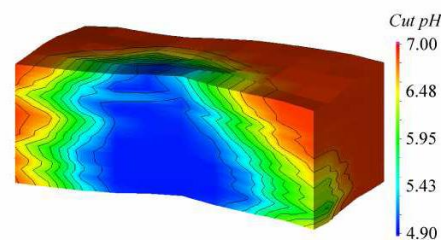
As mentioned there are two main sources for the used variables in this thesis. The papers written by PhD Hellevang have contributed to the chemical composition of the reservoir, whereas the article based on the TOUGH2 FLAC3D project has contributed to the geomechanical values. A short description of the two papers sources:

13.1.1. ATHENA and the SACS project at Utsira

As a part of the NFR project No. 151400/210 “Model studies of safe long term storage of CO₂ in aquifers”, PhD Helge Hellevang presented his thesis in 2006. His paper focused the interactions between CO₂, saline water and minerals during geological storage of CO₂.

The main aim of the project was to investigate the potential of long term CO₂ disposal in deep saline aquifers and reservoirs by means of computational techniques. Further, the specifications of the considered reservoir are an approach to the values from the ongoing CO₂ injection at the Utsira formation from the Sleipner West facility.

The central task for the project was to develop a Secondary Oil Migration (SOM) simulator to a full reactive transport simulator for CO₂ storage problems. CO₂ injections represent complex and difficult processes, which



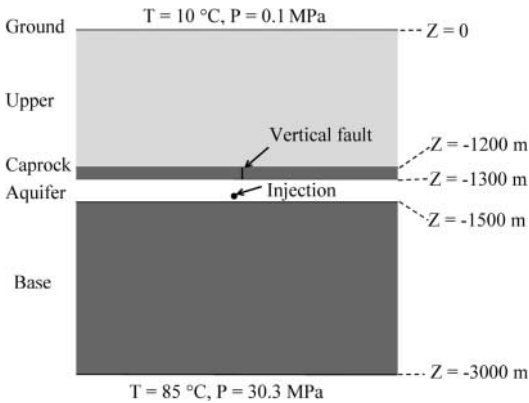
13.1.1 – Graphical representation of the pH development generated by ATHENA.

push computational resources to its limits. The presented version of the SOM simulator was renamed to ATHENA. [3] In addition to the ATHENA simulator there are more papers covering the ACCRETE code.

13.1.2. TOUGH2 FLAC3D

In 2001 Jonny Rutqvist and Chin-Fu Tsang submitted an article that described a study of cap rock hydromechanical changes associated with CO2-injection into a brine formation. The numerical study considered hydromechanical changes during the deep underground injections of supercritical CO2 in a hypothetical brine aquifer/caprock system.

Similar to RCB, the utilized software comprised two coupled computer codes: TOUGH2 and FLAC-3D. According to the article, the TOUGH2 code was designed for geohydrological analysis of a multi-phase, multi-component fluid flow and heat transport, while the FLAC-3D code, for rock and soil mechanics with thermomechanical and hydromechanical interactions. The two codes were coupled together in order to analyse coupled multi-phase flow, heat transport, and rock deformations.



13.1.2 – Graphical representation of the reservoir build at 1500 meters depth

The article considered a 3000m long and 200m thick reservoir model at 1500m depth, confined by a 100m thick cap rock. Slightly off-centre to the right of the injection point there was introduced a virtual fracture with the width of 10m. Above and below the central formation there were two large formations designed to create boundaries for the investigated aquifer. During the simulation the injection pressure of CO2 was prescribed to approach the local lithostatic pressure of the reservoir. When the pressure approached the respective values, there is an increased chance of hydraulic fracturing. However, due to the equivalent increments in the pressure increments, the contained

formation water was allowed to relax and thus reduce the probability of artificial fracturing. [25]

13.2. Basic simulation setup

The cases presented in this thesis are two-dimensional geometries limited to a 1000 m long and 250 m high model, of which the vertical and horizontal axis are respectively divided into 50 and 25 elements. Each element is 20 m long and 10 m high. In order to define the width of the fracture, there was added an additional 4m-wide element as clearly illustrated in the middle of Figure 13.2.1.

Visual Retraso and RCB require that the model is divided into defined zones with respect to the local chemical and mechanical properties. The geometry is thus segmented into the 5 following zones: The injection aquifer, the upper aquifer and two cap rock zones divided by a fracture zone. The fracture zone is situated in the middle of the geometry, enabling the gas to flow from the injection aquifer through the cap rock and into the top aquifer.

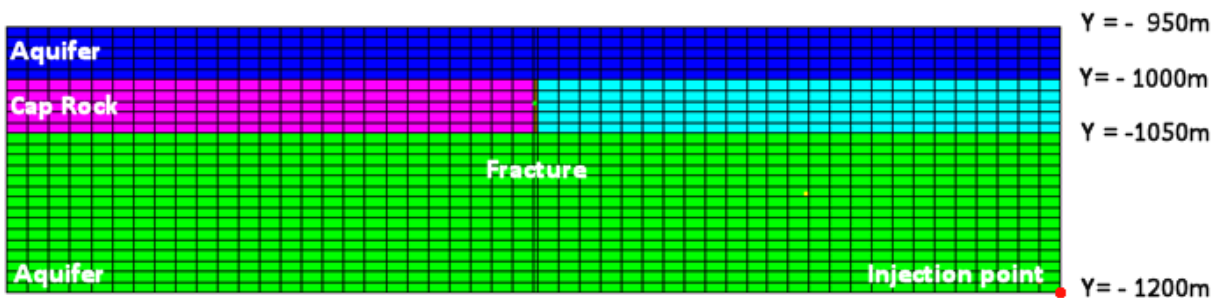


Figure 13.2.1 – Graphical representation of the reservoir zones

The lower boundary of the injection aquifer is located at -1200m below the sea floor. Similar depths are found in a range of aquifers including the Utsira formation off the coast of Norway.

[Hellevang^{ref}] From the lower boundary, the aquifer extends 150m to the cap rock located at -1050m. Contributing with another 50m to the total thickness, the cap rock divides the injection aquifer from the upper aquifer. The 50m thick upper aquifer is placed upon the cap rock in order to observe the gas plume that will form as the gas seeps through the fracture. The injection point of carbon dioxide is located on lower the right hand side of the bottom aquifer.

13.2.1. Introduced fracture

Situated in the middle of the reservoir, there is fracture is dimensioned to a width of 4m. The fracture effectively separates the cap rock layer and creates a highly permeable bridge between the two reservoirs. As shown in Figure 13.2.1 the fracture zone is described by one grid element, which explains the irregular width. By dimensioning the width of the said element, the magnitude of the fracture is adjusted accordingly.

By definition the highly permeable zone can be described as a virtual fracture defined by its permeability and porosity. Ideally a fracture should be described hydrodynamically, however related software information on how to define a fracture as hydrodynamically is hard to obtain. Correspondence with one of the programmers, Maarten Saaltink [^{ref}], indicated that it should be possible to define a fracture hydrodynamically by means of a one-dimensional fracture placed in a two-dimensional grid. His comments were however not applicable to the virtual retraso software itself and thus temporarily a dead end.

Manually describing the same procedure is also not feasible, seeing that a simple grid file contains between 1000 to 1500 nodes in 5 blocks, arranged in a partly symmetric pattern. [ref appendix] The number of nodes constituting the grid obviously depends on the size of the simulated reservoir. Due to the lack of a functional procedure, the hydrodynamically approach was discarded and replaced by the geomechanical virtual fracture approach. Xxx at xxx have utilized the same method while simulation CO₂ injections in the TOUGH2 FLAC3D model. [ref]

The final dimensioning of the virtual fracture is based on a set of preliminary simulations where the width was altered in a range between 10 m and 1 cm. Observations showed that setups similar to the model presented in this thesis, converged with fracture dimensions ranging from 10m to 4m without significant problems. At lower widths the iteration process would reduce the time- steps and end the simulation within a few minutes. Due to these conversion problems the virtual fracture was set to 4m in the final simulations.

13.2.2. Initial pressure, temperature and stress

Visual retraso and RCB has the option to solve or iterate on changes in liquid pressure, gas pressure, temperature and displacements. At default settings only the liquid pressure will be considered and the other properties will remain uniformly constant if nothing else is specified. At normal reservoir conditions properties like pressure, temperature and stress are neither uniform nor constant. As such it is imperative to define these properties in gradients respective to depth and densities.

In the process of defining the zone properties in Visual Retraso, the initial temperature, pressure and stress can either be specified as constant or in a field approach under the section for “Initial value of flow (THM) unknowns”. However, the field approach is complicated and lacks detailed descriptions on how to set it up. With the help of a small program developed in Fortran by PhD student Shunping Liu, it is possible to alter the grid file manually with respect to the initial pressure and stress. By means of a few simple tweaks on my behalf, the same code was enabled to perform a similar operation with respect to the temperature as well. Following is a short description of the functionality of the program.

Gradient software

In order to calculate the gradient values, the application reads a file containing the second block of a grid file. This block contains information about the formation build and axial position of the respective nodes. The combination of these values is used to create two separate files with gradient values of pressure, temperature and overbearing stress. All the gradient values must be manually moved to the original input-file by pasting it into the coherent blocks below the source data. The equations responsible for the calculations will be briefly presented in the following section.

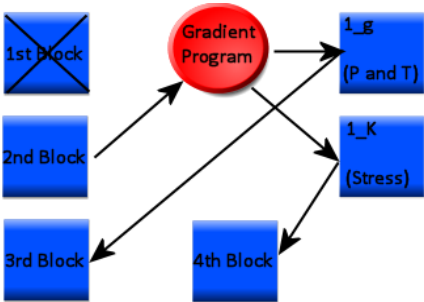


Figure 13.2.2 – Schematic overview of the modification process with respect to initial pressure, temperature and stress. The second block of the generated 1_GRI.inp file is extracted and processed in the Fortran code. Two new files containing the gradient values are then substituted in the original file. Respectively the 3rd and 4th block.

Pressure

The pressure is defined with a simplified formula involving the reservoir depth and a gradient factor. Equation xxx can be used in combination with the created grid file to obtain the pressure at a respective depth.

$$P_y = P_{\max} - y \cdot 0.01 \frac{MPa}{m} \quad \text{Equation 13.2.1}$$

where P_y is the pressure at “y” meters depth, P_{\max} is the maximum pressure at the lower aquifer boundary and y is the representation of the depth according to the grid file. At 1190m depth the pressure is obtained according to equation xxx:

$$P_{1190m} = 12MPa - 10m \cdot 0.01 \frac{MPa}{m} \quad \text{Equation 13.2.2}$$

In this case “y” is equal to 10 because the grid file regards the lower left hand side corner in figure xxx as origo and positive direction for the y-axis is upwards. In other terms “y” can be defined as:

$$Y = Y_{\max} - Y_{\text{current}} \quad \text{Equation 13.2.3}$$

where y_{\max} is the maximum depth and y_{current} the investigated depth.

Temperature

As mentioned the fluid pressure, temperature and matrix displacement can be solved by RCB. While both stress and the fluid pressures are solved in the presented simulations, the temperature remains constant throughout the reservoir due to convergence problems when applying the solver.

The initial approach was to define the reservoir uniformly at 25°C, however with a simple expansion of the gradient software applied to the generated input files; the reservoir temperatures have also been appended with vertical gradients. This extension will allow a more realistic description of the dissolution and precipitation occurring in the aquifer.

Similar to the setup for the pressure gradient, the temperature is also calculated by an equation considering the reservoir depth and a temperature gradient factor:

$$T_y = T_{\max} - y \cdot 0.036 \frac{^{\circ}C}{m} \quad \text{Equation 13.2.4}$$

where T_y the temperature at “y” meters depth, T_{max} is the highest temperature with respect to the current gradient factor and “y” is the considered depth.

With a lower aquifer boundary at 1200 meters, the current gradient of 0.036°C per meter warrants a higher temperature of 43.2°C. At 1190 meters depth the temperature is obtained according to equation xxx:

$$T_{1190m} = 43.2^{\circ}C - 10m \cdot 0.036 \frac{^{\circ}C}{m} = 42.84^{\circ}C \quad \text{Equation 13.2.5}$$

This approach is just a temporary setup, as work is done to further improve and allow temperature solving. Although a constant gradient temperature can be satisfactory, it is imperative to adjust local increments with respect to changes in pressure, density and chemical reactions. For example: As the temperature rises, less carbon dioxide gas and calcite will be able to dissolve in the solution and thus the pH-ranges will be significantly altered.

Stress

In contrast to the pressure and temperature, the stress is calculated at centre of each element. The average solid density is estimated to 2.26 Kg/m³ for the formation. [ref flac density] Thus the total stress can be obtained according to equation xxx

$$\sigma = \overline{\Delta y} \cdot \frac{\rho_{solid} \cdot g}{1.0 \cdot 10^6} \quad \text{Equation 13.2.6}$$

where ρ_{solid} is the density of the solid matrix and g the gravitational acceleration. The variable Δy is a simplified positioning of the stress in an element with respect to the vertical coordinates. The stress at the lower aquifer boundary is obtained according to equation xxx:

$$\sigma_{1195m} = \frac{(1200 + 1190)m}{2} \cdot \frac{2.26Kg / m^3 \cdot 1000 \cdot 9.81m / s^2}{1.0 \cdot 10^6} = 26.49 [MPa] \quad \text{Equation 13.2.7}$$

All simulations presented in this thesis are run with realistic gravity combined with an initial geometry defined in linear gradients of overbearing pressure and stress. These gradients are calculated with respect to gravity, fluid column and the density of the porous medium.

Table xxx below contains an overview of the gradient values with respect to the formation zones. The values are given in ranges as they change according to the depth.

Parameter	Lower aquifer	Cap rock and fracture	Upper Aquifer
Depth [m]	1200 - 1050	1050 - 1000	1000 - 950
Pressure range, P [MPa]	12.0 - 10.5	10.5 - 10.0	10.0 - 9.5
Mean Stress range, σ [MPa]	21.17 - 24.28	24.49 - 25.39	25.61 - 26.49
Temperature range, [°C]	43.2 - 38.16	37.8 - 36.36	36.00 - 34.2
CO ₂ initial injection pressure, P _g [MPa]	12.3	-	-
CO ₂ final injection pressure, P _g [MPa]	27.0	-	-
Gas and liquid outgoing pressure, P [MPa]	12.0	-	9.5

Table 13.2.1 Initial and boundary conditions. Initial values are given as a range because they vary with depth in each formation. CO₂ injection pressure is raised from initially 12.3 MPa to 27.0 MPa in 315 days, after that it is kept constant at 27.0 MPa.

Some simulation programs place low permeable formations above and below the model in order to create a pressure boundary for the fluids in the aquifer. [flac3d] Visual Retraso and RCB, however, perform the same operation by introducing boundary pressure zones at the top and bottom of the model. The aquifer is thus confined vertically and kept open on the sides. In table xxx the lower row identifies these boundary conditions as the outgoing pressure of gas and liquid in units of MPa. With respect to the density and depth of the reservoir, these boundary pressures are set to 12 MPa at the bottom boundary condition and 9.5 MPa at the upper boundary condition.

13.2.1. Carbon dioxide injection and ramp pressure

Preliminary attempts at simulating CO₂ injection at initially high pressures failed due to convergence problems. In order to avoid these problems, which are apparently caused by large pressure gradients in the surrounding nodes and elements, the injection pressure is gradually increased in several small increments. This procedure is feasible by manually introducing a ramp loading approach defined with time intervals and pressure set-points in the input files.

A lower pressure change over a specified time interval smoothens out the steep gradient changes in the system and eases the convergence of the Newton iteration process. However, each increment with respect to the applied time interval is limited to a maximum increment of 25%. This is an observation based on trial and error in process of setting up the increments. As the pressure increases, the solver will allow a larger pressure increment in the same time interval. The eight cases found in this thesis are thus appended with five pressure increments as described in figure xxx and table xxx.

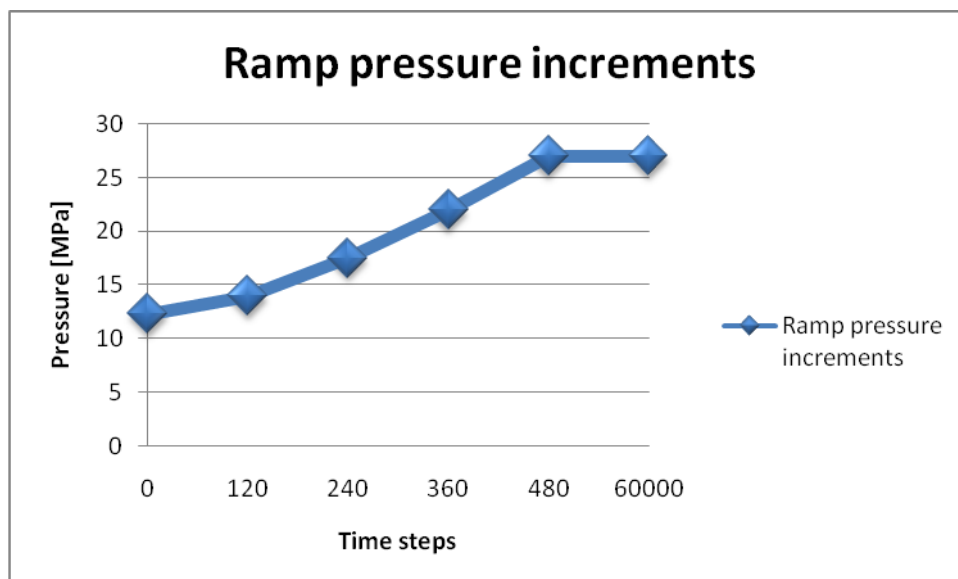


Figure 13.2.3 – Graphical representation of the pressure increments

The first four increments are set to reach the higher pressure set point within 480 time-steps or 315 days, while the fifth increment is stable at the set pressure in the remaining hundred years of the simulation.

Table xxx contains a more detailed overview of the pressure development.

Increment number	Time interval	Number of time steps	Initial pressure [MPa]	Pressure incr. [MPa]	Final pressure [MPa]
1	78.7 days	120	12.3	1.7	14.0
2	78.7 days	120	-	3.5	17.5
3	78.7 days	120	-	4.5	22.0
4	78.7 days	120	-	5.0	27.0
5	~99 years	59520	-	-	27.0

Table 13.2.2 – Detailed description of the injection pressure development

Each of the first four steps is set to run for 78.7 days or 120 time-steps. The final injection pressure after this time is constant 27.0 MPa over the duration of 100 years.

The injection point of the carbon dioxide gas is located at the bottom boundary of the lower aquifer as illustrated in the lower right hand side of figure xxx. At 1200 meters the surrounding pressure is 12 MPa, warranting a higher injection pressure in order to obtain a desired rate of flow. As such the initial injection pressure is set to 12.3 MPa.

13.3. The simulation data plan

Any reasonable investigation related to observing the effects of altering several variables requires a data plan. Figure xxx and table xxx below shows the cubical setup of the eight cases presented in this thesis. The lower layer in figure xxx marked by red corners, represent cases with low calcite volume fractions while the blue corners represent the high calcite volume fractions. By moving from point A to B along the axis of variable 1, the porosity of the fracture will increase. In a similar fashion, moving from point A to D will increase the permeability. As a combination of the variation from point A to D and B, the variables are at their highest bounds point C.

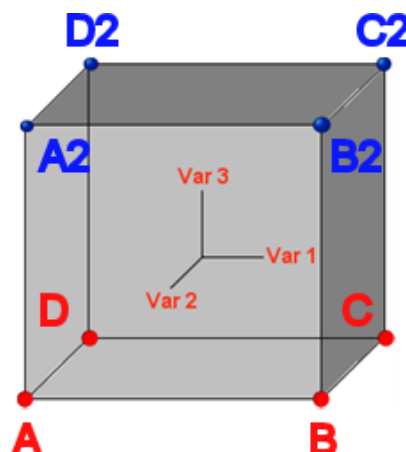


Figure 13.3.1 – Cubical representation of the data plan

The lower bound values used in Case A, as described in table xxx2, are equal to the values of the fault presented in the TOUGH2 FLAC3D article [ref]. With respect to the mineral composition, the lower

bound value of the same case is similar to that found in Utsira [ref] - That is, a simplified model approached with only two constituent minerals as opposed to the more detailed description obtained in the PhD thesis H. Hellevang.[ref] Table xxx1 contains the indexed values of the variables that are applied in the dataplan.

Variable/Index	Lower bound (-1)	Higher bound (+1)
Variable 1 – Fracture porosity	0,05	0,2
Variable 2 – Fracture Permeability [m²]	1e-12 (1D)	1e-10 (100D)
Variable 3 – Reservoir composition	4 % calcite	16% calcite

Table 13.3.1 – Indexed values of the variables used in the data plan

The first two variables are included to investigate the effects on reservoir properties such as displacements and chemical reactions. A variation in the mineral composition with respect to calcite is also included to investigate correlations between the changes in volume fractions of calcite, dissolved CO₂ and changes in porosity due to dissolution and precipitation. The setup in table xxx is the foundation for the simulation plan presented in table xxx.

A number of three variables require eight simulations to obtain all the possible combinations of the variables. These combinations are listed in the table xxx below with respect to each case and its index.

Case	Index	Variable 1 – Fracture porosity	Variable 2 – Fracture Permeability	Variable 3 – Mineral composition
A	(-1)(-1)(-1)	0.05	1.0e-12	4% calcite
B	(+1)(-1)(-1)	0.2	1.0e-12	4% calcite
C	(+1)(+1)(-1)	0.2	1.0e-10	4% calcite
D	(-1)(+1)(-1)	0.05	1.0e-10	4% calcite
A2	(-1) (-1)(+1)	0.05	1.0e-12	16% calcite
B2	(+1)(-1)(+1)	0.2	1.0e-12	16% calcite
C2	(+1)(+1)(+1)	0.2	1.0e-10	16% calcite
D2	(-1)(+1)(+1)	0.05	1.0e-10	16% calcite

Table 13.3.2 – Table containing the settings for the eight cases. The variables are systematically altered in order to obtain easily analysable results.

Case A is simulated with the lowest values, while Case C2 has the highest values. The second column in table xxx represents the index of the cubical positioning. As a reference the lower left corner A in figure xxx is indexed with (-1)(-1)(-1)

13.4. More detailed simulation setup

In Visual Retraso all the constituent elements, minerals and coherent solved species have to be specified in order to determine the number of independent components contained in the system. The chosen primary constituents (C, Ca, H₂O, H⁺ and Si) are the foundation for the available primary and secondary species. Further it is advised to limit the selection to the most abundant species for each component in order to avoid convergence problems BK. Depending on the physical conditions, the software may choose the primary species and the coherent range of secondary species. This can also be done manually, however it is advised to let the software perform the selection. The choice of the aqueous primary species is not unique and the programmed method of selecting the primary and secondary species is based on the approach developed by Peter Lichtner. The same approach is utilized in other codes such as MPATH and used by Carl Steefel for the code 1DREACT [20, 21] BK.

There will only be one injected gas present in the reservoir in the form of pure CO₂ with nitrogen as the reference gas. Table xxx shows the chemical build of all the simulations, and table xxx contains the volume fraction and reactive surface of calcite and quartz with respect to each simulation.

Species	Injection- and upper aquifer	Cap rock	Fracture; 5% porosity	Fracture; 20% porosity
Primary elements	C	C	C	C
	Ca	Ca	Ca	Ca
	H ₂ O	H ₂ O	H ₂ O	H ₂ O
	H ⁺	H ⁺	H ⁺	H ⁺
	Si	Si	Si	Si
Aqueous species	Ca ⁺²	Ca ⁺²	Ca ⁺²	Ca ⁺²
	H ₂ O	H ₂ O	H ₂ O	H ₂ O
	HCO ₃ ⁻	HCO ₃ ⁻	HCO ₃ ⁻	HCO ₃ ⁻
	H ⁺	H ⁺	H ⁺	H ⁺
(Primary and Secondary Aqueous species)	SiO ₂ (aq)	SiO ₂ (aq)	SiO ₂ (aq)	SiO ₂ (aq)
	CaCO ₃ (aq)	CaCO ₃ (aq)	CaCO ₃ (aq)	CaCO ₃ (aq)
	CaH ₂ SiO ₄ (aq)	CaH ₂ SiO ₄ (aq)	CaH ₂ SiO ₄ (aq)	CaH ₂ SiO ₄ (aq)
	CaHCO ₃ ⁺	CaHCO ₃ ⁺	CaHCO ₃ ⁺	CaHCO ₃ ⁺
	CaOH ⁺	CaOH ⁺	CaOH ⁺	CaOH ⁺
	CO ₂ (aq)	CO ₂ (aq)	CO ₂ (aq)	CO ₂ (aq)
	CO ₃ ⁻²	CO ₃ ⁻²	CO ₃ ⁻²	CO ₃ ⁻²
	OH ⁻	OH ⁻	OH ⁻	OH ⁻
	H ₂ SiO ₄ ⁻²	H ₂ SiO ₄ ⁻²	H ₂ SiO ₄ ⁻²	H ₂ SiO ₄ ⁻²
	HSiO ₃ ⁻	HSiO ₃ ⁻	HSiO ₃ ⁻	HSiO ₃ ⁻

Table 13.4.1 – Initial selection of chemical components, with respect to the primary and secondary aqueous species.

Based on the constituent elements selected for the simulations presented in this thesis, the primary aqueous species are limited to Ca⁺², H₂O, HCO₃⁻, H⁺ and SiO₂(aq). The secondary aqueous species of table xxx are generated by the program based on the initial water concentrations found in table xxx at 25°C.

Species	Injection- and upper aquifer	Cap rock	Fracture; 5% porosity	Fracture; 20% porosity
Mineral volume fraction with 4% calcite [m ³ /m ³]	Calcite(0.036), Quartz(0.864)	Calcite(0.0396), Quartz(0.9504)	Calcite (0.038), Quartz (0.912)	Calcite (0.032), Quartz (0.768)
Mineral reactive surface with 4% calcite, [m ² /m ³]	Calcite (36), Quartz (864)	Calcite(39.6), Quartz(950)	Calcite(38), Quartz(912)	Calcite(38), Quartz(912)
Mineral volume fraction with 16% calcite, [m ³ /m ³]	Calcite (0.144), Quartz (0.756)	Calcite(0.1584), Quartz(0.8316)	Calcite (0.152), Quartz (0.798)	Calcite (0.128), Quartz (0.672)
Mineral reactive surface with 16% calcite, [m ² /m ³]	Calcite(144), Quartz(756)	Calcite(158), Quartz(831)	Calcite(152), Quartz(798)	Calcite(128), Quartz(672)
Gas	CO ₂	CO ₂	CO ₂	CO ₂

Table 13.4.2 – Initial composition of minerals and gases.

As defined in table xxx, calcite and quartz needs a defined reactive surface with respect to the volume fraction of the minerals. The exact or closest approach to real reactive surface values is not an exact approach. As such the calculation of volume fraction and surface reactive area of calcite and quartz in the formation is adapted according to the paper by S.P.White (2002) [ref]

Initial water concentrations

With a specified set of elements, primary and secondary aqueous species, the solvers requires defined initial concentrations and constraints with respect to the dissolved species. There are several types of constraints, but only three are necessary in for these simulations. Normally the concentration of dissolved species is described with a total concentration approach, but when there is a need to limit the maximum concentration, a mineral equilibrium approach would be wiser. With respect to bicarbonate, the charged specie originating from dissolved calcite and carbon dioxide, the initial amount in the solution is constrained by the solubility product of calcite.

Element	Specie	Constraint type	Constraint mineral/gas	Constraint value	First guess concentration	Concentration units
C	HCO ₃ ⁻	Mineral equilibrium	Calcite	-	1e-5	mol/Kg
Ca	Ca ²⁺	Total concentration	-	1e-4	1e-4	mol/Kg
H+	OH ⁻	Activity	-	8.0	8.0	pH
H2O	H ₂ O	Total concentration	-	1.0	1.0	mol/Kg
Si	SiO ₂	Total	-	1e-8	1e-8	mol/Kg

(aq) concentration

Table 13.4.3 – Initial water concentrations and constraints

The values presented in the table are oral recommendations passed on from Maarten Saaltink by Shunpiung Liu. Although in the same range as the values presented by Hellevang [ref] they are significantly different. The initial pH value for the entire reservoir solution is adjusted to pH 8 and constrained by the activity of OH⁻. Any change in initial pH will be according to the dissolution of calcite and carbon dioxide. Dissolution of CO₂ will lower the pH of the solution, while dissolved calcite buffers the solution to a higher pH value.

Reactive flow

As explained in chapter xxx, the reactive module (Retraso) considers reactive flow by means of diffusion, advection and dispersion. These approaches are governed by the permeability, dispersivity and diffusion properties of the respective zones in the reservoir. The different zones of the geometry are defined with different initial permeabilities. The initial dispersivity and molecular diffusion is constant in all of the zones. The data for permeability, dispersion and diffusion in the different zones can be found in Table xxx.

	Injection aquifer	Cap Rock	Fracture	Upper aquifer
Permeability [m ²]	1e-13	1e-17	Table 13.3.2	1e-13
Longitudinal Dispersivity [m]	11	11	11	11
Transversal Dispersivity [m]	21	21	21	21
Molecular Diffusion [m ² /s]	1e-10	1e-10	1e-10	1e-10

Table 13.4.4 - g fadh fahad hagh

The permeability's in the table are similar to those found in the TOUGH2 Flac3D article [ref].

The Dispersivity and molecular diffusion

Må være store enn I/H

Tutorial!""

Geomechanical properties

In the simulations we have used a poroelastic model with Young Modulus equal to 3000 MPa for the Aquifer and Cap Rock, while the Fracture is set to 1500 MPa. All the zones in the geometry are operating with a Poisson's ratio equal to 0.2. Kinetic geochemical reactions are assumed for all fluid-mineral reactions.

Property	Injection Aquifer	Cap rock	Fracture	Upper Aquifer
Young's modulus, E [GPa]	0.3	0.3	0.15	0.3
Poisson's ratio, ν	0.2	0.2	0.2	0.2
Permeability [mD]				
Porosity	0.1	0.01	Table 13.3.2	0.1
Saturated rock density, ρ_s [kg/m ³]	2.26	2.26	2.26	2.26
Zero stress porosity, Φ_0	0.1	0.01	Table 13.3.2	0.1
Zero stress permeability, k_0 [m ²]	1.0e-13	1.0e-17	Table 13.3.2	1.0e-13
Irreducible gas and liquid saturation, S_{rg}	0	0	0	0
Van Genuchten's gas-entry pressure, P_0 [MPa], (at zero stress)	0.0196	0.196	0.196	0.0196
Van Genuchten's Surface tension at same Temperature [xx]	0.072	0.072	0.072	0.072
Van Genuchten's exponent, [m]	0.457	0.457	0.457	0.457

Table 13.4.5 – Material properties

Irreducible water saturation in petroleum reservoirs is an entirely nature-driven process influenced only by competition between capillarity and gravity forces. Irreducible water saturation between 20 to 40 percent is common, however values ranging from as low as 5% to 60% have also been reported for some north sea reservoirs. [26] The original

The original programme used 0 at surface conditions.

Currently the fracture is defined and simulated in a hydromechanical approach, but the ultimate future goal would be to simulate the fracture hydrodynamically without the defined parameters in table xxx and xxx.

13.5. RCB sampling and GiD

In Visual Retraso the temporal discretization for the simulations is set to 3000 time steps over 5 years (1.58e8s), which results in a time interval of 52666.67 seconds or 14.6 hours per time step. This ration is transferred to the extended simulation of 100 years according to the setup described in table xxx.

The change in simulated properties at the end of each time-step will be written to a database-file called 1_flavia. As mentioned the time subdivision allows increments in the time intervals in order to ease the convergence process. These interval changes are further reflected in the presented time-steps in GiD read from the flavia file.

14. Results and discussion

Chapter 14 contains the results from eight cases designed according to the data plan. Due to the vast amount of produced data and information, it is not feasible to include every figure in this section. Only the most important highlights will thus be represented in the form of figures and tables. As such, this chapter does not include all the required figures to obtain a necessary overview of the respective simulations. Larger quantities of the produced graphical representations of relevant properties are placed in Appendix I to VII. It is thus advised that the reader confers to the respective appendix for additional information while reviewing the results and discussions.

14.1. Simulations and convergence problems

Out of eight presented simulations, only four managed to cover a hundred years of simulation time. The most probable reason for the reduced runtime lay in convergence problems in either the geomechanical or the reactive module. Table 13.2.1 below lists the simulation and the total duration of simulation for each case.

Case	Total simulation time (years)	Significant dissolution or precipitation	Other
A	100	-	
B	100	-	High gas storage efficiency
C	100	-	
D	30	Yes	
A2	50	Yes	
B2	100	Yes	High gas storage efficiency
C2	50	Yes	
D2	30	Yes	

Table 14.1.1 – Overview of the total simulation time with respect to each simulation.

Observations show the simulations representing the low volume fractions of calcite had a higher rate of convergence compared to the cases with larger amounts of calcite. Additional information, included in the table xxx, indicates that there is a correlation between the convergence problems and iterations in the reactive module of RCB. The details will be discussed in chapter xxx.

14.2. Break-through of injected carbon dioxide

As part of the original simulation build, the injection pressure for all the eight cases were designed to reach 27 MPa after 315 days. However, the reservoir pressure did not reach the set point due to an early gas break-through.

As the CO₂ saturation increases in the injection aquifer, the CO₂ flows more easily, effectively increasing the injection rate over time. However, when the front of the gas saturated fluid reaches the fracture, the saturated zone acts as a highway from the injection point and the pressure will consequently drop to that of the resistance in the reservoir. Table xxx contains the respective time of breakthrough for each case. A set of chosen state variables at the same time-step is also presented in table xxx.

The values presented in table xxx are gathered from the last recorded closest to the actual breakthrough. The time-step length differed from simulation to simulation due to a reduction in time intervals where convergence problems occur. As such the contained values at breakthrough can only be considered as a mere guide when comparing the cases.

Case	Time step	Time [s]	Time [d]
Case A	80	2.20939e7	255.71
Case B	98	2.21236e7	256.06
Case C	83	2.21282e7	256.11
Case D	100	2.21453e7	256.31
Case A2	81	2.20798e7	255.55
Case B2	107	2.21263e7	256.09
Case C2	95	2.21712e7	256.61
Case D2	87	2.21224e7	256.05

Table 14.2.1 – The estimated breakthrough time and maximum values for gas pressure, gas density and |Gas phase flux|

The time of gas break-through is not exact, but limited to the output data closest to the actual break-through. Even so, the presented times of breakthrough for all eight cases are relatively equal with an error of $[256.06 \pm 0.53]$ days. There seems to be a trend between case A and A2, which have an earlier breakthrough than the other cases.

14.3. Point evolution

The grid consists of 1275 elements and 1352 nodes. To present the point evolution of gas pressure, gas density and |gas phase flux|, a set of four nodes have been selected for evaluation purposes. Figure xxx below illustrates the relative positioning of the sampled nodes, forming a line between the fracture and injection point. Values extracted from the respective points are presented in the following figures and tables.

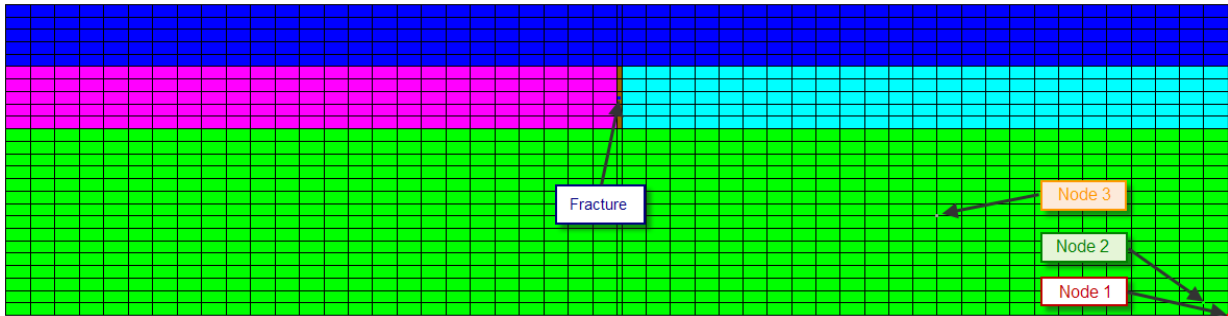


Figure 14.3.1 – Graphical representation of the geological formation appended with illustrated points of measurement. These points are represented in time evolution graphs throughout the section of results and appendix xxx.

Figure xxx to xxx represents point evolutions of the change in the respective properties over time. As illustrated in figure xxx there are four considered positions. Each position is systematically represented with one colour in all eight simulations. With reference to figure xxx; the red, green, gray and blue lines respectively represent the pressure in and between the injection point and fracture. Listing the descriptions from the top as found in figure xxx:

- Red – Measured values at the injection point
- Green – Measured values in the neighboring diagonal node, 22.4 meters from the injection point
- Gray – Measured values at the centre of a diagonal line between the injection point and fracture
- Blue – Measured values at the centre of the fracture

All the presented graphs in this section and appendix xxx, are obtained by means of existing functions in the pre-processor GiD. The measured points and the relevant properties are selected manually through graphical interfaces and then plotted in the time evolution diagram.

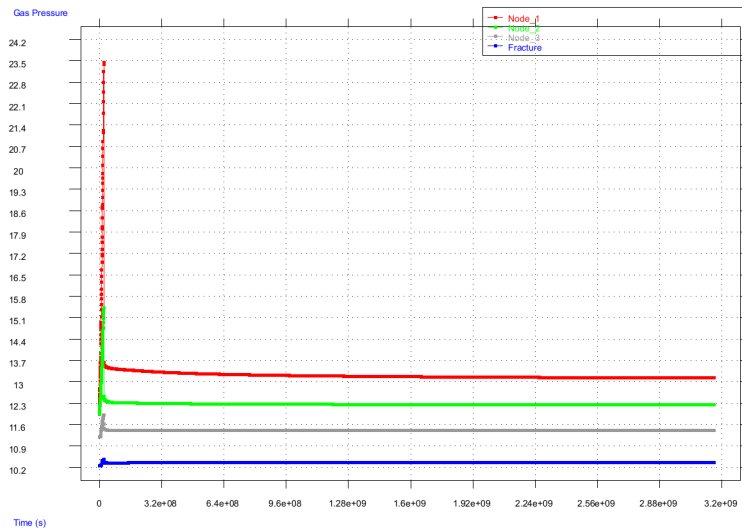


Figure 14.3.2 – Point evolution of the gas pressure in case A

As clearly illustrated in figure xxx, the pressure is highest at the injection point and dissipates with an increasing distance from the gas injection. The mentioned gas break-through is represented by the significant pressure drop at the very beginning of the time scale. A small spike in the gas pressure within fracture, represented by the blue line, indicates that the pressure front barely reached the fracture prior to the gas break-through.

With respect to further evaluations of the simulations, the measured results will be based on two points in time; the point of gas breakthrough and at 30 years of CO₂ injection. The latter is chosen so that all cases have available data.

By applying a rough estimate of 10 years between each marker on the x-axis in figure xxx, the visual observations indicate that the injection pressure after 30 years of gas injection is close to stabilized slightly above 13 MPa. By reducing the timescale in figure xxx from 100 years to 2 years, the gas breakthrough becomes more detailed with respect to the ramp pressure loading.

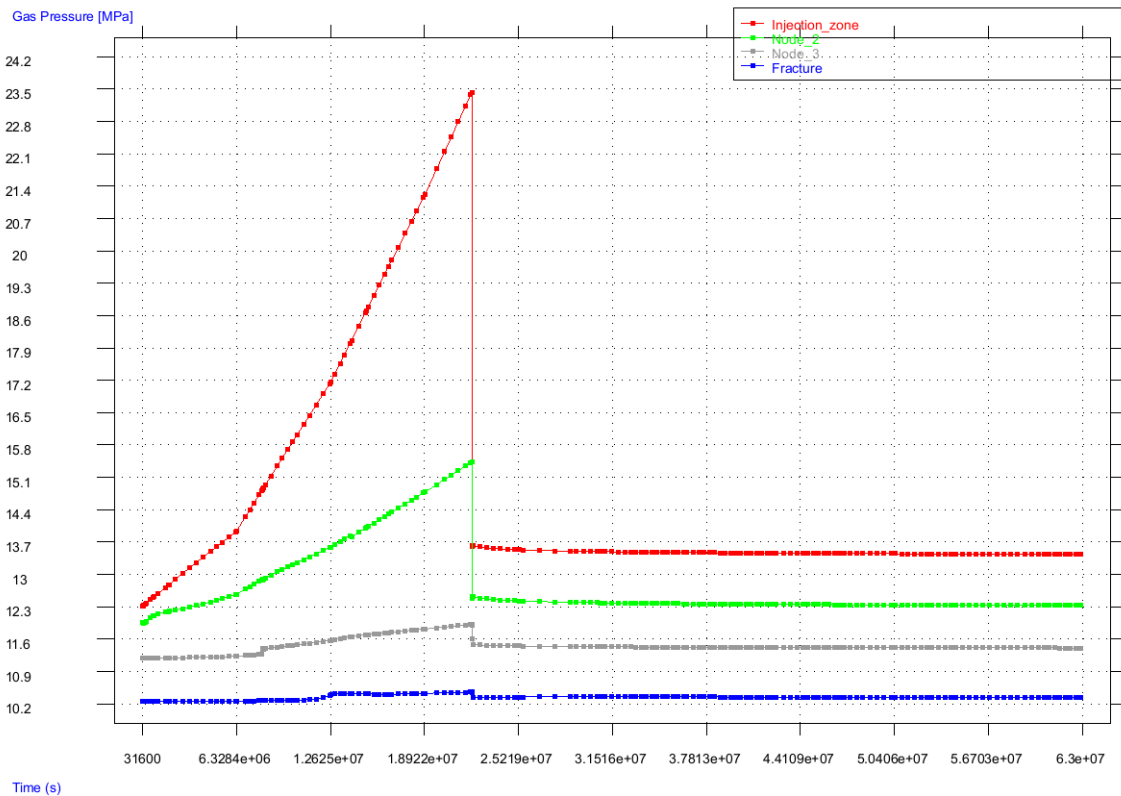


Figure 14.3.3 – Point evolution of the pressure development in case A. The time scale is limited to two years.

The more narrow time interval applied in figure xxx is presented in a smaller time-scale with a higher resolution in figure xxx. The overview of the pressure increments in the CO₂ injection show a significant pressure drop over a very short time-span. The four measured points also displays a latency in the pressure evolution between the nodes. The red line, which represents the injection pressure, clearly illustrates the ramp loading by finite changes in the pressure incline of the time evolution. The magnitude and the evolution of the pressure front is illustrated by the sequential increase at at each measured node

Similar to the pressure development, the pressure correlated gas density presented in figure xxx, follows the same described trends

The measured density is highest at the injection point, followed by the neighboring nodes and the fracture. However, after 60 years there is a slightly observable increase in the gas density within the fracture.

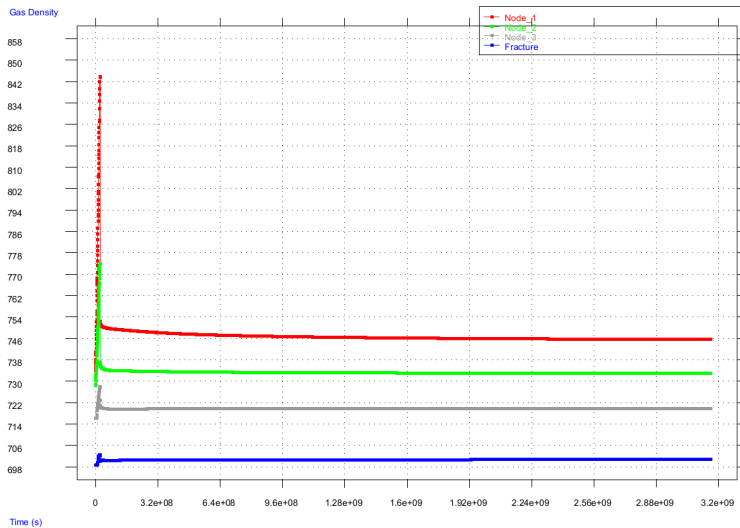


Figure 14.3.4 – Point evolution of the gas density in case A

More interestingly, the increase in gas density is supported by an increasing total gas flux within the same point of the fracture. As shown in figure xxx, the flux in the fracture (blue) overlaps and crosses the flux evolution in the aquifer (purple).

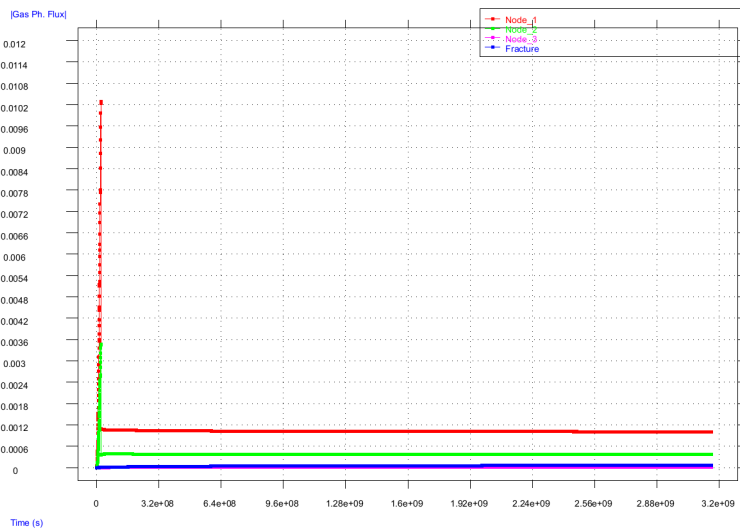


Figure 14.3.5 – Point evolution of the total gas phase flux in case A

The scale of the vertical axis makes it hard define where one line starts and the other ends. As such, a more detailed close-up of the two gas flux evolutions in and near the fracture is illustrated in figure xxx.

The difference in flux is clearly evident and most likely due to the much narrower path through the fracture. Figure xxx provides.

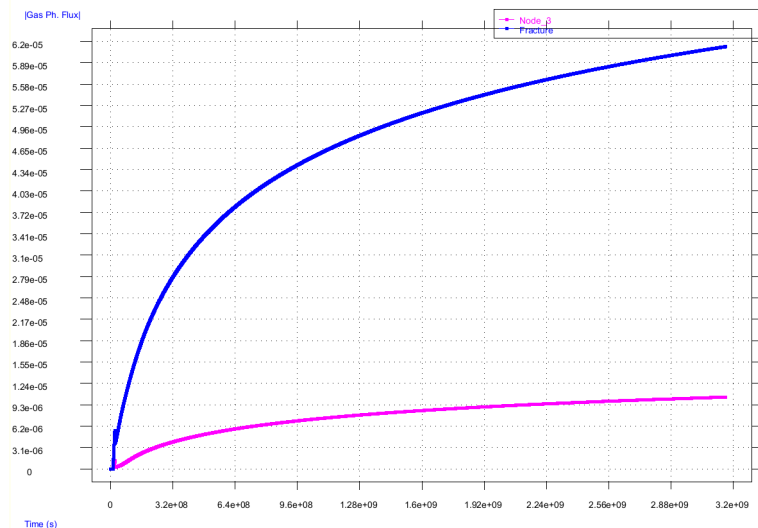


Figure 14.3.6 – Point evolution of the total gas phase flux [m/s] in case A

A closer investigation shows that there is an increasing difference between the entering and exiting flux through the fracture. The deviation is only natural, as the gradient pressure reduces the density of the flowing fluids, and thereby increases the permeability through the porous fracture

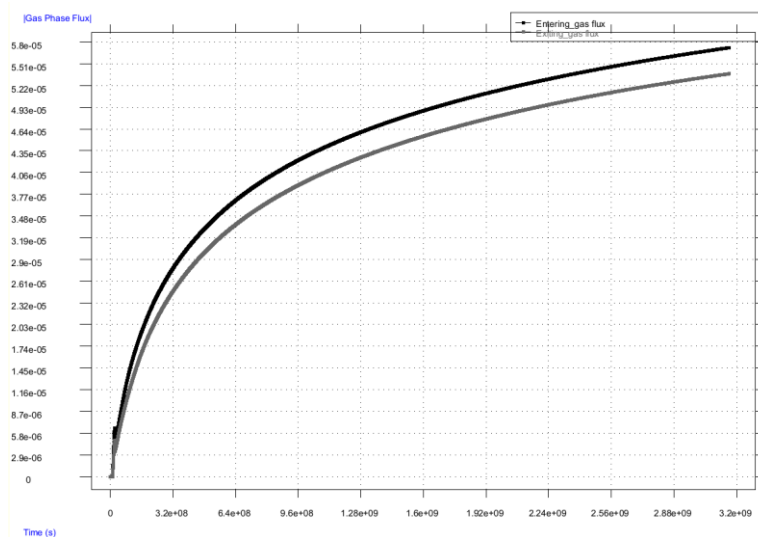


Figure 14.3.7 - Point evolution of the total gas phase flux [m/s] in case A

Observations in the presented figures of case A are similar in all of the other cases. Although the case specific variations that are presented in the next section, are also present in the graphs. The graphs allow a visual interpretation of the reservoir developments with respect to time. The tables in the next section enable further detailed discussion of the eight cases.

Additional and more detailed versions of the graphs are available in Appendix xxx. (High resolution images are also available on the compact disk.)

14.4. Tables

GiD is equipped with an auto-limit function for the colour scales, which represent change in aquifer properties versus time. The auto-limit function is adjusted to the higher and lower bounds of the obtained values throughout the simulated 100 years. Hence the values from the auto-limited scales are used to estimate the maximum values of the respective properties at gas breakthrough.

At gas breakthrough

The previous figures contained a graphical representation of the point evolution in the reservoir. Due to the large difference in the variables and simulation time, it is hard to compare the variations between the eight simulations. As such the same evaluated points have been manually sampled at breakthrough and after 30 years of CO₂ injection. Table xxx and xxx below, represents the measured injection values and the measured values in the reservoir at the time of breakthrough

Case	Maximum gas pressure [MPa]	Maximum gas density [kg/m ³]	Maximum Injection Gas phase flux [m/s]
A	23.479	844.28	0.010307
B	23.503	844.45	0.010304
C	23.506	844.47	0.010302
D	23.520	844.57	0.010287
A2	23.468	844.21	0.010304
B2	23.502	844.44	0.010295
C2	23.504	844.46	0.010270
D2	23.337	843.29	0.010119

Table 14.4.1 – Overview of the maximum values in the injection zone prior to gas break-through.

There is no major difference between the values in the injection zone. With a rapidly increasing injection pressure and coherent gas flux, the observed variations can easily be a result of the variation in time between the measured steps of each case.

Case	Gas pressure [MPa]	Gas density [kg/m ³]	Gas phase flux [m/s]
A	11.918	727.88	1.13649e-6
B	11.935	728.15	1.22047e-6
C	11.953	728.42	1.25963e-6
D	11.911	727.77	1.06363e-6
A2	11.914	727.81	1.53580e-6
B2	11.913	727.79	1.07479e-6
C2	11.896	727.54	1.51358e-6
D2	11.887	727.39	1.07651e-6

Table 14.4.2 – Overview of values in the centre of the injection aquifer prior to the gas break-through.

The measured point in the centre of the aquifer

After 30 years of carbon dioxide sequestration

As observed in Figure 14.3.2 to Figure 14.3.7, the variables in the injection point have dropped to a fraction of the breakthrough conditions after 30 years of gas injection. Table 14.4.3 shows that there are still no major differences between the injection conditions of each case. It is only further away from the injection point that the main differences between the simulations are revealed. These differences are presented in Table 14.4.4.

Case	Maximum gas pressure [MPa]	Maximum gas density [g/dm ³]	Maximum Injection Gas phase flux [m/s]
A	13.212	746.77	0.0010210
B	13.214	746.80	0.0010223
C	13.213	746.79	0.0010209
D	13.217	746.84	0.0010211
A2	13.213	746.78	0.0010208
B2	13.215	745.65	0.0010222
C2	13.213	746.78	0.0010209
D2	13.213	746.79	0.0010208

Table 14.4.3 – Overview of the maximum values in the injection zone after 30 years of CO₂ injection. Stationary after 30 years

The injection conditions in Case A and C are close to equivalent, whereas Case B and D deviate in opposite directions. Case D and D2 have a higher gas flux than the other cases, but there is no

significant deviation in the two remaining variables of pressure and density. Case B and B2, on the other hand, have a higher gas density, gas pressure along with a significantly lower gas flux.

Case	Gas pressure [MPa]	Gas density [g/dm ³]	Gas phase flux [m/s]
A	11.412	719.68	6.92378e-6
B	11.455	720.39	4.19042e-6
C	11.412	719.68	6.93292e-6
D	11.411	719.65	7.22319e-6
A2	11.412	719.68	6.92267e-6
B2	11.455	720.39	4.19060e-6
C2	11.412	719.68	6.93603e-6
D2	11.410	719.65	7.03577e-6

Table 14.4.4 – Overview of measured values in the centre of the injection aquifer after 30 years of CO₂ injection. Stationary after 30 years Stationary after 30 years

The higher pressure and density combined with the significantly lower flux, indicates that there is a lower permeability in the fracture for case B and B2. Likewise, the higher flux in case D and D2 indicates a higher flux through the fracture.

In order to validate the assumptions based on the measured values in the injection point and aquifer at 30 years of CO₂ injection, a set of equivalent measurements were carried out for the fracture. The obtained values are presented in Table 14.4.5 and 2.3.6.

Fracture

The deviating values in Table 14.4.4 indicated that there might be a variation in the gas flux through the fracture for the eight cases. Further investigation of the fluid properties at the entrance and exit of the fracture verified these assumptions. Table 14.4.5 below presents the measured fluid properties in the fracture prior to the gas breakthrough, while Table 14.4.6 evaluates the same variables after 30 years of CO₂ injection.

Case	Flux [m/s]		Pressure [MPa]		Density [kg/m ³]	
	In	Out	In	Out	In	Out
A	6.49418E-06	4.85330E-06	10.699	10.163	707.12	696.79
B	4.61086E-06	3.30092E-06	10.860	10.142	710.07	696.35
C	5.39608E-06	4.29888E-06	10.701	10.169	707.18	696.90
D	6.25724E-06	4.70109E-06	10.663	10.170	706.46	696.93
A2	6.11543E-06	4.56386E-06	10.682	10.148	706.81	696.48
B2	4.48420E-06	3.13746E-06	10.852	10.139	709.94	696.31
C2	6.68983E-06	5.07324E-06	10.687	10.155	706.90	696.62
D2	7.30248E-06	5.47114E-06	10.651	10.160	706.24	696.72

Table 14.4.5 - Overview of the measured values at the entrance and exit of the fracture, prior to the gas breakthrough

Table 14.4.5 and 2.3.6 clearly show that the assumptions based on the fluid properties in Table 14.4.3 and 2.3.4 are correct. The measured deviations in the injection point and center of the aquifer are in fact due to the changes in the permeability through the fracture.

Case	Flux [m/s]		Pressure [MPa]		Density [kg/m ³]	
	In	Out	In	Out	In	Out
A	4,21102E-05	3,87227E-05	10,601	10,102	705,30	695,55
B	2,17089E-05	2,27710E-05	10,828	10,075	709,49	695,00
C	4,23604E-05	3,87636E-05	10,598	10,102	705,25	695,55
D	4,71445E-05	3,91665E-05	10,549	10,111	704,33	695,73
A2	4,21102E-05	3,87227E-05	10,601	10,102	705,30	695,55
B2	2,17102E-05	2,27711E-05	10,828	10,075	709,49	695,00
C2	4,23908E-05	3,87840E-05	10,598	10,102	705,25	695,55
D2	4,71666E-05	3,91757E-05	10,549	10,111	704,33	695,73

Table 14.4.6 - Overview of the measured values at the entrance and exit of the fracture, after 30 years of CO₂ injection.

The overall measurements prior to the gas breakthrough are significantly larger than the measurements after 30 years. Similar to the trend of the fluxes at the center of the aquifer, the flux of Case B/B2 and D/D2 show significant differences in opposite directions. The result of these deviations is graphically illustrated by saturation profiles in Figure 14.5.5 and Figure 14.5.8, in addition to the pH profile of Figure 14.5.9.

14.5. Graphical representations

Additional and more detailed versions of the figures presented in this section are available in the appendix. As the figures from the eight cases are relatively similar, only the most significant details will be presented. Otherwise the presentations will be limited to the development in case A.

Gas Pressure profile

In all of the cases, the pressure front moves ahead of the CO₂ front with the highest reservoir pressures close to the injection point. As pointed out in the pressure diagram (Figure 14.3.2), the reservoir experiences a gas breakthrough shortly after 255 days. That is less than 15 days before the graphical representation at 9 months as illustrated in Figure 14.5.1 (Image a3).

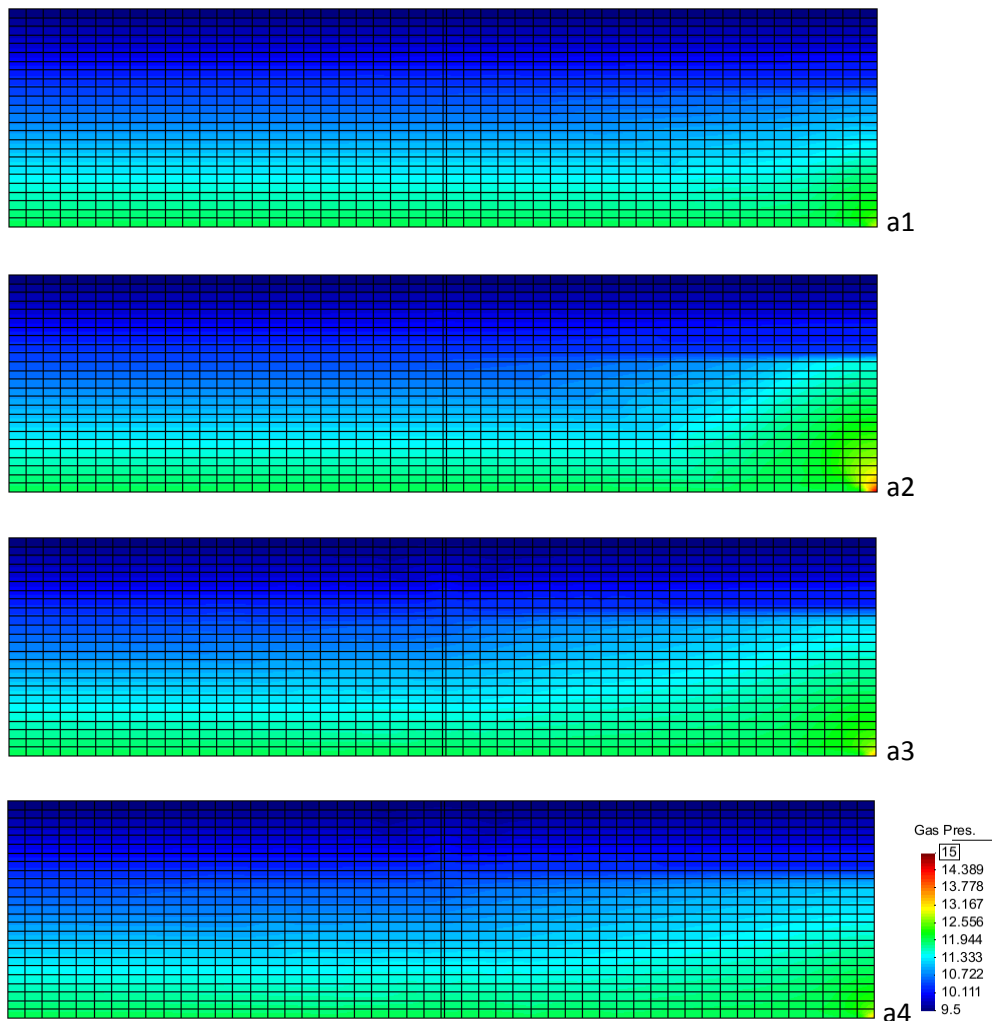


Figure 14.5.1 – Pressure development in case A. a1 (1 month), a2 (3 months), a3 (9 months) and a4 (2 years)

The initial pressure gradient ranging from 9.5 to 15 MPa is still intact on the left hand side of the graphical illustrations. On the right hand side, the pressure front builds up under the cap rock and proceeds in the direction of the fracture. By applying the same pressure scale as in Figure 14.5.1, the graphical representation of the last image before the gas breakthrough is presented in Figure 14.5.2.

The pressure profile is clearly dominated by the buoyant behaviour of the injected gas, as the pressure builds up under the cap rock and proceeds towards the fracture.

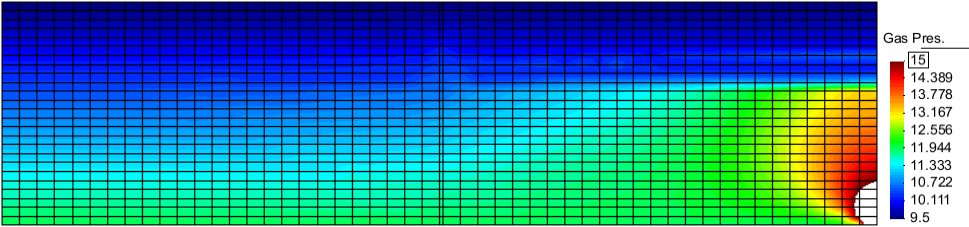


Figure 14.5.2 – Graphical representation of the pressure profile at the time of gas breakthrough. The colourless field in the injection zone is simply values outside the set pressure scale.

After the gas breakthrough the magnitude of the overall pressure is reduced; although the front itself does not subside and continues to move forwards. This is because the pressure in the injection zone stabilizes at a magnitude larger than that of the pressure in the front and continues to provide the necessary driving force.

Gas density profile

The distribution and development in gas density is directly correlated to the overbearing fluid column pressure and injection pressure. Figure 14.5.3 below is the highest measured density for Case A, where the density peaks at 844 [Kg/m³] prior to the gas breakthrough.

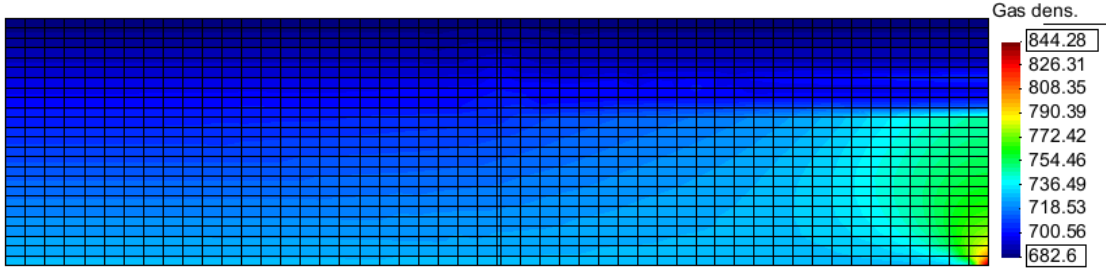


Figure 14.5.3 – Graphical representation of the gas density at the time of gas breakthrough [Kg/m3]

Figure 14.5.4 contains estimated values for the density of CO₂ as a function of pressure and temperature. The graph itself is obtained from a powerpoint presentation created by GasTEK and Project invest at www.tel-tek.no[27]

At the injection point of case A the temperature can be estimated to 40°C, and the pressure of 23.479 MPa is obtained in Table 14.4.1. By comparing the estimated value of density for case A, with graphs in Figure 14.5.4, one can obtain indications on whether the CO₂ calculations of the model are representative.

At the respective conditions, the extrapolated density at 40°C and 23.479 MPa, indicates that the calculated density in the simulation is a bit lower. Similar to the deviations in the injection zone prior to gas breakthrough, the density in the centre of the reservoir after 30 years of CO₂ injection present a lower density than the values presented in the graph.

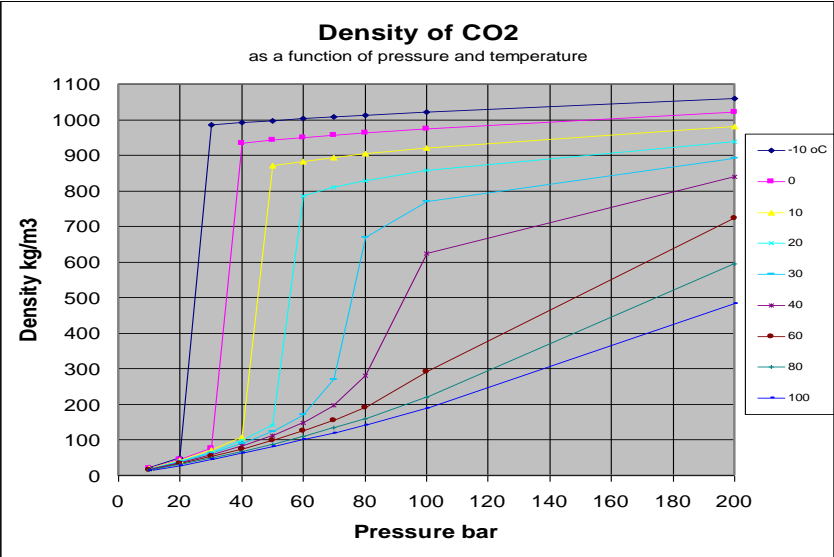


Figure 14.5.4 – The density of CO₂ as a function of pressure and temperature.[27]

The deviation in density is important with respect to the permeability of the mobile CO₂ gas phase. A lower gas density means that the phase has a higher permeability.

Appendix IIX and contains a general overview of the graphical representation of pressure, density, flux and liquid saturation at breakthrough.

14.5.1. Liquid saturation profile

As shown in the time evolution contained in appendix I, the injected carbon dioxide rises buoyantly towards the cap rock and forms a plume stretching towards the fracture located at the centre of the reservoir cap rock. As expected the development of the liquid saturation profile is greatly dominated by the positioning and properties of the introduced fracture. Large amounts of carbon dioxide gas is diverged through the highly permeable zone and transported to the upper aquifer creating a new plume of gas.

The most significant observation related to the liquid saturation profile for the eight cases, is the difference between case B/B2 and the other simulations. As shown in Figure 14.5.5, the two cases have a larger area of liquid saturation influenced by the gas injection and hence a greater storage efficiency. In addition to the observations in case B and B2, there are also noticeable differences in the thickness of the “saturation tail” between the remaining simulations. Observations from the development in liquid saturation after 30 years show that the saturation tail of case A and C are close to equal, while case D has a much thinner tail. The same trend is present in the other cases with high calcite volume fractions (A2- D2).

By comparing the values presented in the Table 14.4.6 for the B and D simulation series, there is a clear correlation between the storage efficiency and the flux through the fracture. As mentioned, the B series has a significantly lower gas phase flux, while the D series has a noticeable higher flux. Basically the lower the flux of the escaping gas, the more gas will pass the fracture and saturate the remaining zones.

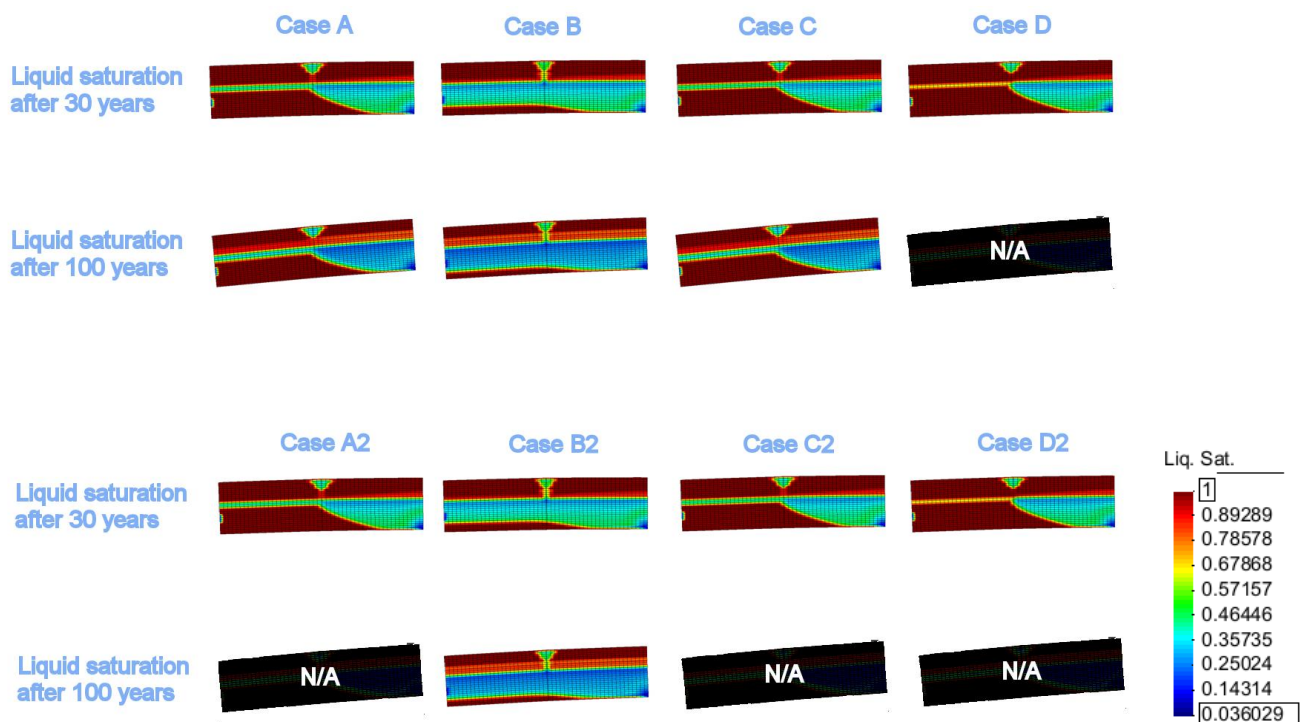


Figure 14.5.5 – A Graphical representation of the development in liquid saturation for the eight represented cases. There are two represented points in time. The first row is represents 30 years of CO₂ injection and the second 100 years. Due to the explained convergence problems some figures are not available.

The development in liquid saturation after 50 and 100 years of CO₂ injection, show that the observed trend between the saturation tails are still valid for the observations that were noted at 30 years of CO₂ injection. Due to the fracture’s highly dominating role of redirecting carbon dioxide flow, large portions of the aquifer are consequently left unexploited at the end of the simulations.

14.5.2. Calcite dissolutions and gas saturation

Computer animations with a more frequent rate of time-steps, show quick bursts of changes in liquid saturation outside the main gas-saturated profile. Figure 14.5.6 below represents the saturation profile of case A after 3 months of simulation time. The yellow circles within the figure indicate several significant bursts of gas. Similar bursts are observable in all the eight cases, whether the case is simulated with high or low amounts of initial mineral calcite.

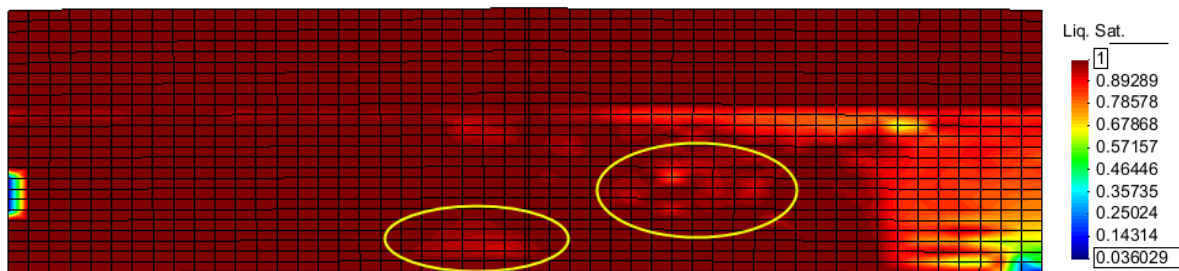


Figure 14.5.6 - Liquid saturation after 3 months

Because calcite is the salt of a weak acid, the solid will dissolve in contact with any stronger acid such carbonic acid or silicic acid. It is with good reason to believe that the cause of these illustrated burst of gas are related to the dissolution of calcite according to equation Equation 14.5.1.



The dissolved calcite, in the form of CO₂ gas, can further dissolve and buffer the solution according to Equation 7.1.5 in chapter 7.

Further observations show that the magnitude and rate of these gas bursts are much higher in the cases with high calcite content. This is only natural as there more calcite present.

14.5.3. Reservoir deformation / displacements

In addition to graphically representing the liquid saturation, the overview in Figure 14.5.5 and Appendix I are appended with the deformation of the reservoir. All of the eight simulations are illustrated with the same factor of 1.37715e6 as shown in Figure 14.5.7.

The visualized deformation of the figures are not equivalent to the real displacements, but a visual representation created in order to observe the differences between the simulations. The lower the deformation factor the more extreme the visualization will become.

step 3.13902e+9
Contour Fill of Liq. Sat..
Deformation (x1.37715e+6): Displacements of TIME ANALYSIS, step 3.13902e+9.

Figure 14.5.7 – The deformation factor for the eight simulations at any given time-step.

In transferred terminology this means that each mm of displacement in the figure is equivalent to 1.37715e6 mm in the model. Note that none of the figures contained in this thesis can be used to measure the deformation as the scale is altered when inserting the figures from the source files. As mentioned, the original files are included on the digital medium found on the final page of the thesis. The method of comparing the different cases consists of simple visual observations aided by graphical programs that include functions such as:

- Superposing and comparing images by altering the opacity of the layers
- Simple but exact measurements of angles by means of traced boundary lines

The simple method of comparing the simulations showed that the deformation in both the high and low calcite content of Case A, C and D were equal after 30 and 100 years of co2 injection. Case B and B2 have an equivalent deformation, but the pair differs from the other cases as illustrated in Figure 14.5.8.

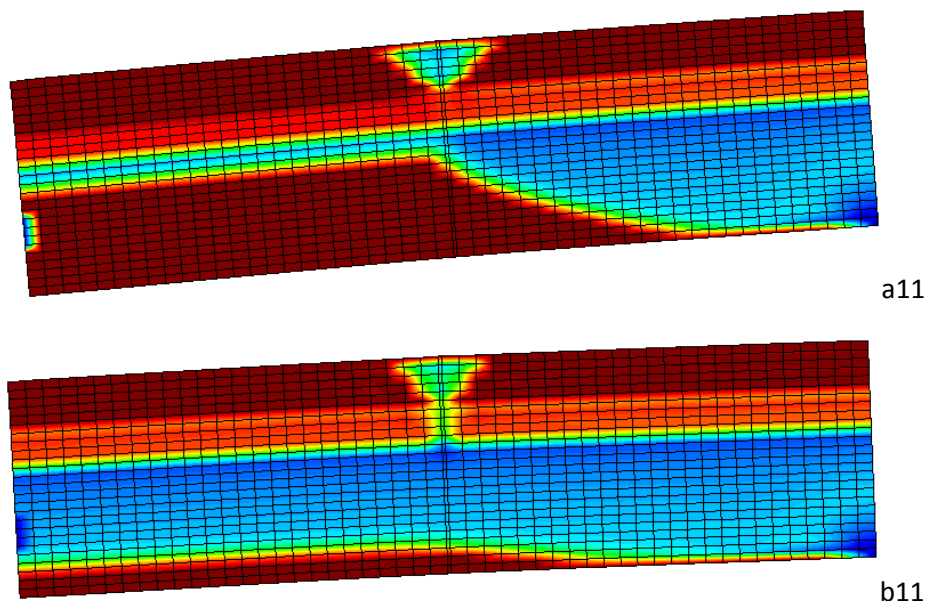


Figure 14.5.8 – Graphical representation of the geological deformation in the reservoir in Case A and B after 100 years of CO2 injection

In terms of deviation between the simulations, case A, C and D had an incline of 5°, while case B had an incline of 3°. All of cases also present a finite bend over the element that constitutes the fracture. The deviation between the two illustrated figures of deformation is probably due to the significant difference in the total gas flux which results in an increased storage efficiency. Furthermore, the slight bend over the fracture zone might be due to the increased pressure of the escaping gas plume.

14.5.4. pH profile

Chapter 7.2 explained that an aquifer system containing carbonate minerals will be geochemically buffered through the release of carbonate ions from the dissolved minerals. The graphical representation of the pH profiles in Figure 14.5.9 show that the buffering of the formation water is substantial and that the pH value does not drop below 7.0 in any of the formation regions. The magnitude and shape of the pH profile is strongly correlated to the profile of the gas saturation. Observations from the eight cases, whether high or low calcite content, show that the pH and saturation profile in simulation series A, B, C and D are similarly shaped, but with one exception.

The tail which is present in the gas saturation profile does not appear at the same extent as in the profile of the pH values. This observation is most evident case B, where the presence of the large gas saturation tail is merely indicated by a veil of a finite increase in pH value. Plausible causes for the absence could be explained by a lacking advection of solid calcite particles in the respective area, or lack in transport of dissolved charged species due to the leakage through the fracture.

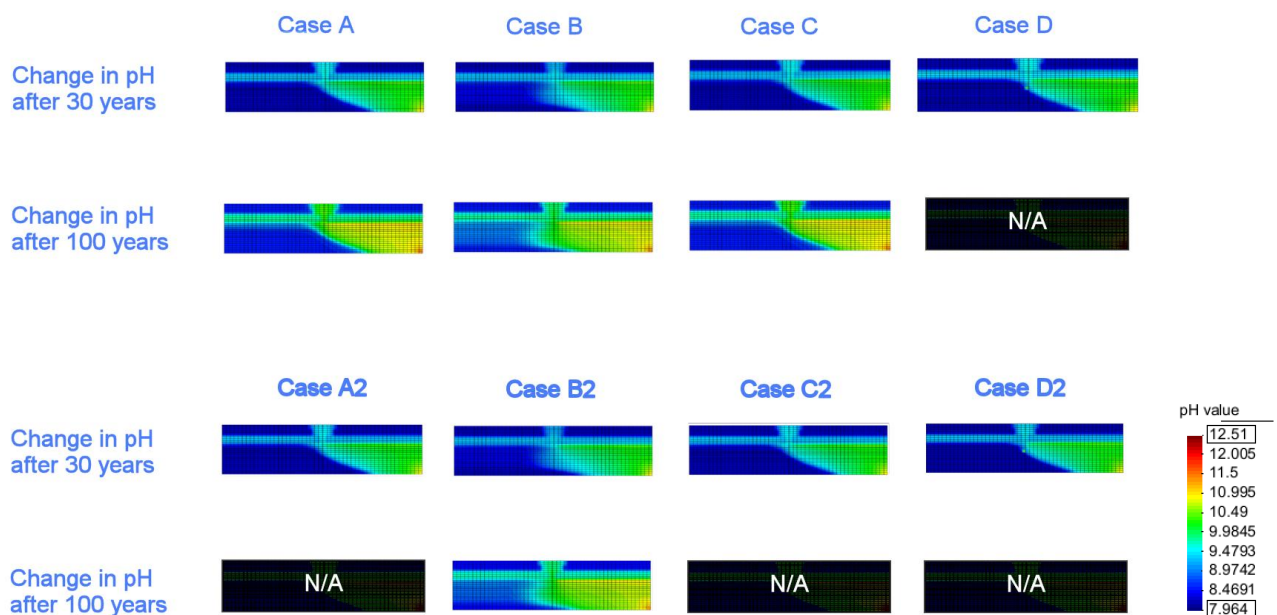


Figure 14.5.9 - A Graphical representation of the development in the pH profile for the eight represented cases. There are two represented points in time. The first row is represents 30 years of CO₂ injection and the second 100 years. Due to the explained convergence problems some figures are not available

As expected there are small observable differences in the pH values between the cases of low and high calcite content. Although hard to visually observe in the resized figures, the low fraction calcite models have a slightly more advanced pH front than the cases with high calcite content. There is also a noticeable difference in the magnitude of pH influence through the fracture. A larger increase in the fracture porosity could increase the permeability and flux enough to alter the speed of the pH front and extent of pH changes in the fracture.

As shown in Figure 14.5.10 and Figure 14.5.11, the fracture and centre of the gas plume in the upper aquifer has a slightly larger green pH-zone in the simulations with low amounts of calcite. The flux through the fracture is equivalent in both cases, which gives reason to believe that the deviation has arisen due to the lower calcite content allowing more unsaturated reservoir fluids to reach the fracture.

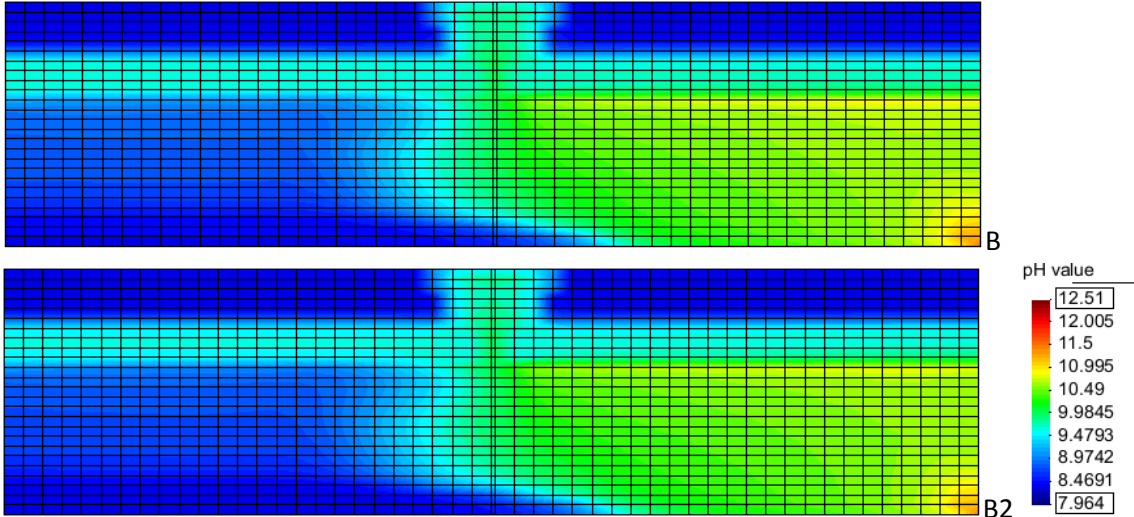


Figure 14.5.10 – Graphical representation of the pH profile in case B and B2 after 50 years of CO2 injection.

14.5.5. pH and saturation

The formation water at the bottom boundary of the injection aquifer will be saturated with dissolved CO₂ and calcite within the first months of CO₂ injection. The solubility CO₂ gas and calcite is dependent on the local pressure and temperature. A higher local pressure reduces the vapor pressure of CO₂, and thus increases the solubility of the gas. Hence the solubility will increase with a closing distance to the injection point.

On the other hand, calcite has a retrograde solubility with respect to the temperature. At the bottom of the aquifer the temperature is at its highest. In addition, the pressure would contribute to local temperature changes, but in this thesis the solver is not applied. As such the gradient temperature will remain constant during the simulation. The effects of the dynamic carbonate solubility in the injection zone are illustrated in Figure 14.5.14 with respect to porosity changes.

Compared to the conditions close to the cap rock, the solution at the bottom boundary is exposed to higher temperatures and pressures. As the fluids buoyantly rise towards the cap rock, the pressure will decrease simultaneously with the temperature. When the pressure drops, the CO₂ will be less soluble in the aqueous phase and evaporates accordingly. This combination of reduced CO₂ solubility and the reduced temperature will allow more dissolved calcite in the solution.

As shown in Figure 14.5.11 and Appendix II, the pH stabilizes at a distance from the injection point by evaporating excess CO₂ and/or precipitating solid calcite particles. After 50 years the pH in the area close to the cap rock starts to increase (See Figure 14.5.10). This is most likely due to transport (advection) of released carbonate particles in combination with the introduced gradient temperature and pressure.

In the same time interval as the buffering of the solution below the cap rock in case A and A2, there is another phenomenon taking place vertically below the fracture. Although only evident in case A2 of Figure 14.5.11, further investigations show that several other cases hold similar characteristics.

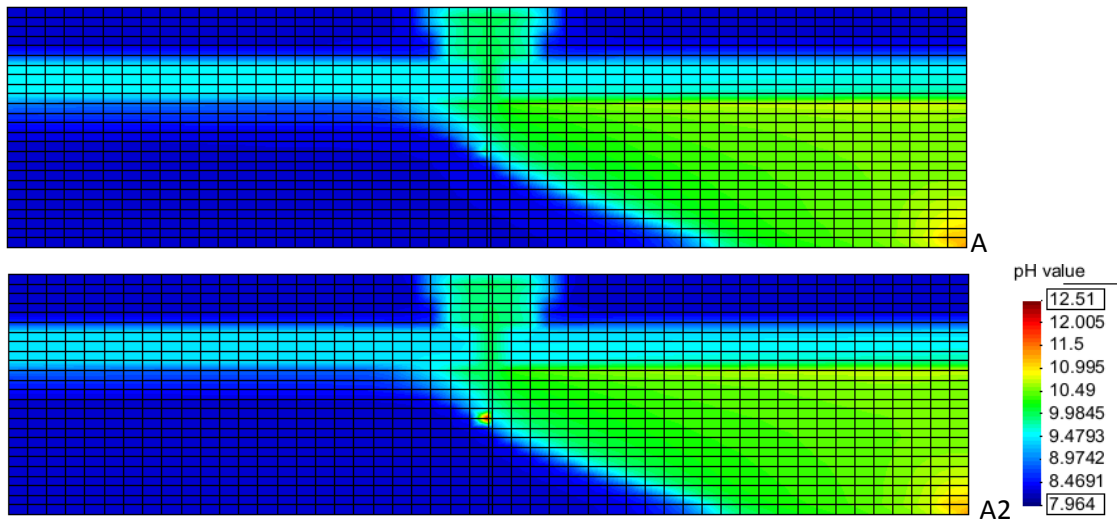


Figure 14.5.11 – Graphical illustration of the pH profile in case A and A2 after 50 years of CO2 injection

As mentioned case A did not experience the same anomaly, but it did show tendencies at the exact same spot. The only difference between the two cases is the composition of the mineral matrix. As such, the cause of the deviation must be a result increased amount of calcite, more specifically the potential larger dissolution of calcite in the fracture. Table 14.4.6 showed a slight difference in the flux through the fracture for the two cases. The difference might be significant enough to alter the flux in the reservoir, and thus inhibit the mechanics behind the formation of the anomaly.

The trend between Case A and A2 proves to be applicable on the remaining cases. The simulations with high calcite content have a higher fraction the same anomaly. Similar to Case A, the pH evolution in Case B and C does not form the pH spot below the fracture, but rather show a tendency in the same area. Case D has a significantly higher flux than the other low calcite simulations, and according to the speculations related to flux differences between A and A2, it developed a similar pH anomaly. The spot was however of a lower magnitude as shown in Figure 14.5.12.

Table 14.5.1 contains a general overview of the development in pH singularities for all eight cases with respect to the time of formation. To keep it simple, the time of formation is defined at the first observation of the yellow pH representation according to the scale in Figure 14.5.12.

Case	Images	Exact	Max value	Case	Images	Exact	Max value
A	-	-	-	A2	48.2 years	47.16	
B	-	-	-	B2	-	-	-
C	-	-	-	C2	50 years	48.68	
D	30 years	25.65		D2	30 Years	24.21	

Table 14.5.1 – A general overview of the development in pH singularities for all eight cases.

In Table 14.5.1 there were four cases that developed the abnormal pH point below the fracture. These points are presented in Figure 14.5.12 below. Case D and D2 represent the pH after 30 years, while A2 and C2 present the pH after 48.2 and 50 years.

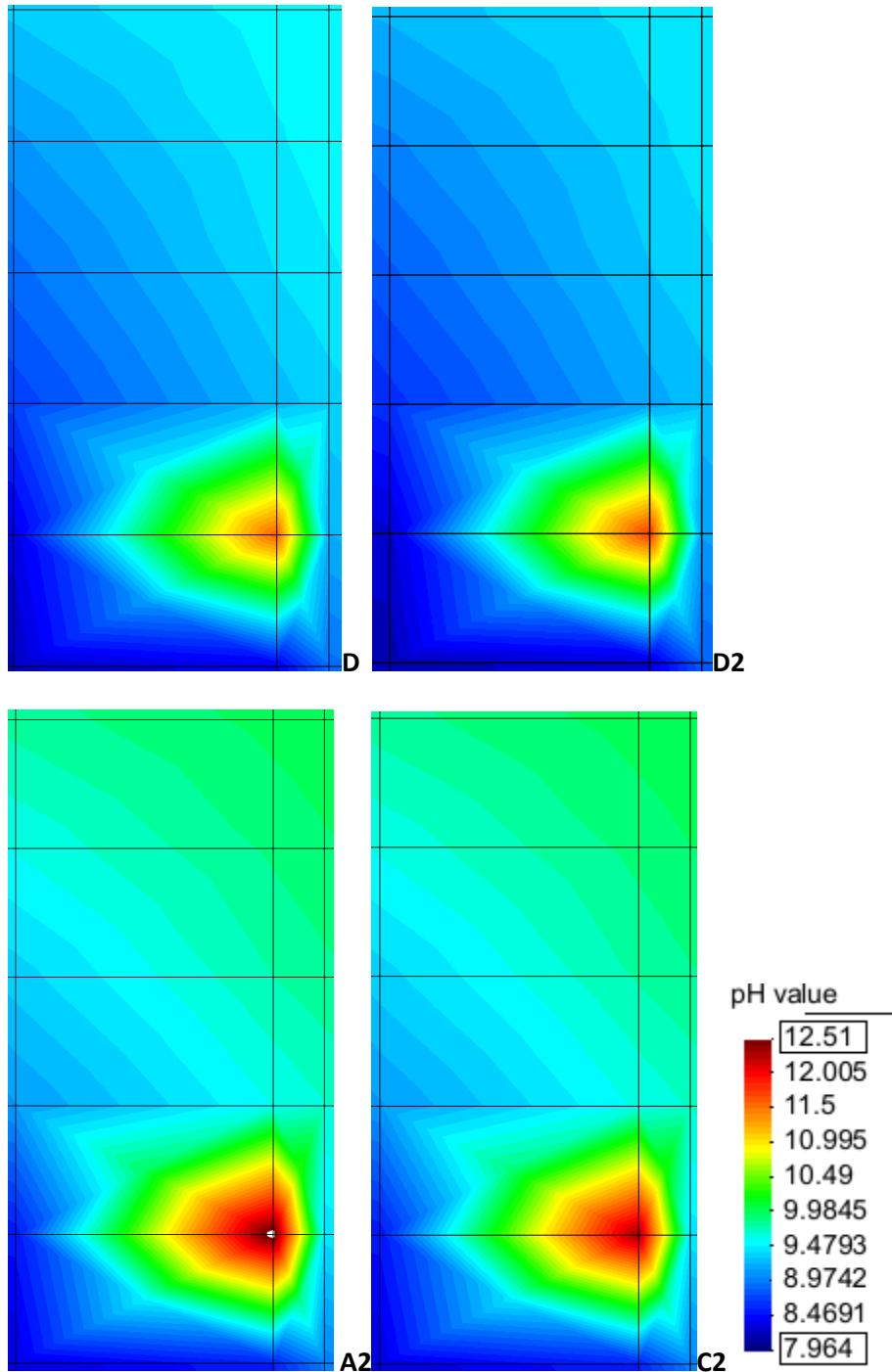


Figure 14.5.12 – Graphical representation of the pH anomalies according to the time of first observation. Case D and D2 represent the pH after 30 years, while A2 and C2 present the pH after 50 years.

As mentioned there is small observable deviation in the pH values between the cases of low and high calcite content. It is difficult to notice the difference in the normal figures, however image d and d2 in Figure 14.5.12 shows a distinctive difference between the two cases.

Similar to the tail of the liquid saturation, the advancement of the pH front is correlated to the fractural gas phase flux. The higher the flux, the less the horizontal advance of the pH front. With respect to Case A2 and C2, the magnitude of the gas flux also appears to influence the maximum pH value within the anomalies. The extent of this difference could be larger as there is almost a two year time difference between the two images.

After 50 years of CO₂ injection, the gas saturation is much higher than after 30 years of gas injection. The saturation at the interface between the liquid and gas zone would thus be higher. A higher saturation of CO₂ results in a lower pH value and thus a higher rate of calcite dissolution. The increased rate would allow a quicker buffering of the system, explaining the significant differences between image D/D2 and A2/C2 in figure Figure 14.5.12.

14.5.6. Total gas phase flux profile

The magnitude of the total gas phase flux is described in detail in Table 14.4.1 to Table 14.4.6. The case specific gas fluxes are further described by graphs in Appendix IIX and more detailed figure series in Appendix V.

Figure 14.5.13 below is a graphical representation of the total gas phase flux for case A. The scale is adjusted to a lower magnitude in order to better illustrate the flux between the injection point and fracture. As illustrated, there is an overall increase in the gas phase flux over time. The increments are correlated to the increasing gas saturation of the respective area, which alters the viscosity and thereby increases the permeability of the saturated zone.

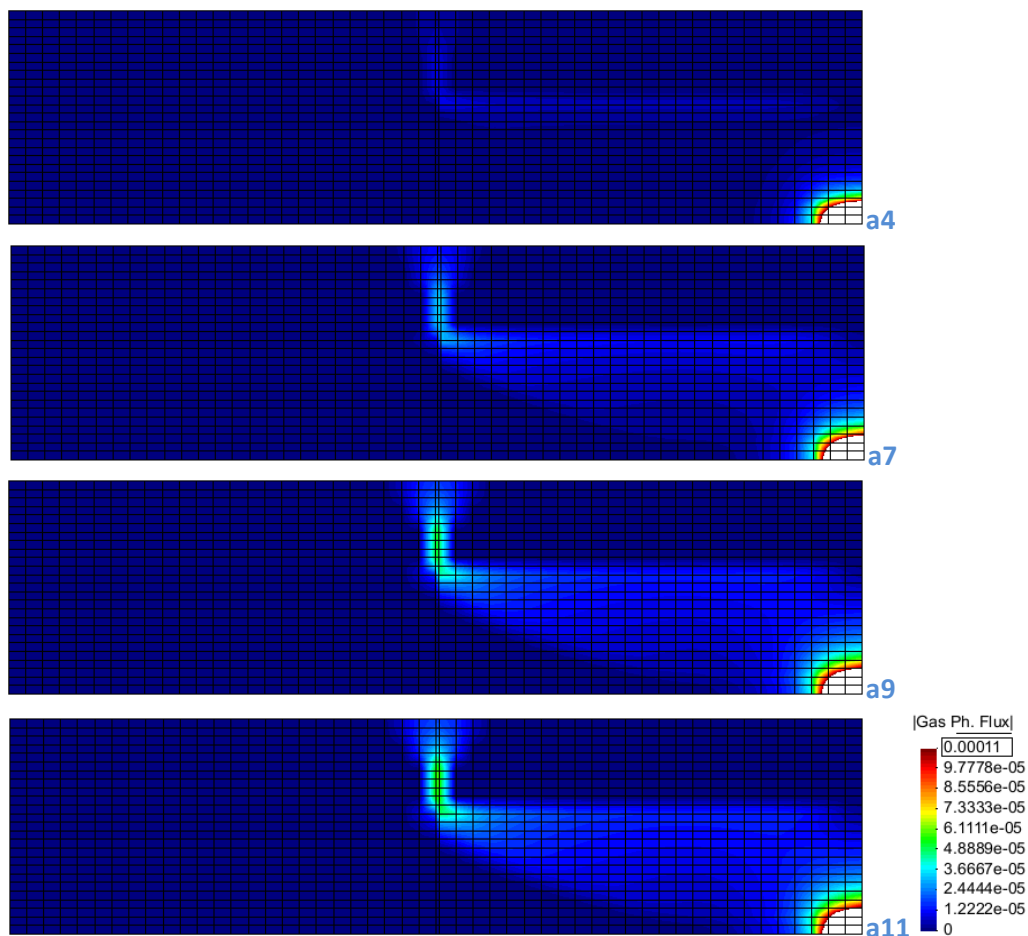


Figure 14.5.13 – Graphical representation of the total gas phase flux in case A, after 2 years (a4), 15 years (a7) 50 years (a9) and 100 years (a11) of CO₂ injection.

With respect to the figure, the largest flux in the eight represented cases is located in the injection zone, followed by the increasing flux through the fracture. The flux between these two points is greatly dominated by the buoyancy of the gas, which produces a higher flux near the cap rock and a lower flux near the bottom of the formation. The increasing flux through the fracture is due to a combination of the gas saturation, gas density, the change in porosity and the driving pressure gradient over the length of the fracture. In order to retain the same rate of flow as in the reservoir, the entering gas is compressed, increasing the gas density and thus the flux through the fracture.

The total CO₂ injection at Utsira is estimated to 1 million tons of gas per year. By means of the flux, density and two-dimensional cross section, the estimated flux at breakthrough can be calculated for case A:

$$\frac{m}{s} \cdot \frac{Kg}{m^3} = \frac{Kg}{m^2 s} \cdot m = \frac{Kg}{s} \text{ per meter}$$

$$0.010307 \frac{m}{s} \cdot 844.20 \frac{Kg}{m^3} = 8.7 \frac{Kg}{m^2 s} \cdot m = 8.7 \frac{Kg}{s} \text{ per meter}$$

Where “per meter” is the linear flux in the two-dimensional formation. 8.7 Kg/s m is equivalent to 0.27 million ton CO₂ per year per meter. In other words the injection in the simulations is but a fraction of the yearly Utsira injection.

14.5.7. Change in Porosity

With respect of the ramp loading of the injection pressure, there are no pressure situations that can cause hydraulic fracturing. Any change in porosity is thus related to the change in mineral volume fraction of calcite. As explained in chapter 7.2, calcite has a retrograde temperature dependency, and the reaction rate is dependent on the pH value of the solution. As such, calcite has a higher solubility at lower temperatures and a higher reaction rate in acidic solutions.

As expected the eight cases show finite alterations of porosity both in the cap rock and aquifer. Close to after 50 years of CO₂ injection, the cases show a uniform low increase of porosity in the cap rock. The magnitude is within the order of 1e-5%, which is not of major significance. More significant are the cases that form anomalies below the fracture as described in Table 14.5.2 and illustrated in Figure 14.5.14. Further investigation show that the location and time of appearance is equivalent to that of the anomalies found in the pH description (Table 14.5.1 and Table 14.5.3).

Case	Increased porosity by location		Reduced porosity by location	
	Below fracture	Injection zone	Below fracture	Injection zone
A	-	-	-	-
B	-	-	-	-
C	-	-	-	-
D	Yes	-	-	-
A2	Yes	-	Yes	Yes
B2	-	-	-	Yes
C2	Yes	-	-	Yes
D2	Yes	-	Yes	Yes

Table 14.5.2 – Overview of the porosity changes in the eight cases.

In addition to the increased porosity below the fracture, two cases also exhibited a reduction of porosity on the right hand side of the anomaly. The porosity change itself is relatively small with a magnitude around 1e-4 percent, but disregarding the magnitude, the observations are significant with respect to precipitation calcite. It indicates that the introduced gradient pressure and temperature works in combination with the reactive module of RCB.

Case	Increased porosity below fracture		Reduced porosity below fracture	
	First observation	Magnitude	First observation	Magnitude
D	26.9 years	9e-3	-	-
A2	47.5 years	5e-3	48,6 years	e-4
C2	49.3 years	4e-3	-*	-
D2	24.6 years	5,7e-2	29 years	e-4

Table 14.5.3 – Overview of the magnitude and initial formation of porosity changes in the eight cases.

As shown in Table 14.5.3, Case D and D2 experience the largest increase in local porosity, while case A2 and C2 develop a smaller increment.

Dissolution and precipitation in the solid matrix

After thirty to fifty years of carbon dioxide injection there are noticeable changes in the porosity right below the fracture and in the surrounding area of the injection point as shown in Figure 14.5.14. The areas marked in dark blue are the sections of the reservoir which have an initial porosity equal to 0.1, whereas the remaining white areas represent porosities outside the set scale of the graphical representation. The white belt stretching across the figure is thus due to the lower porosity of the cap rock and fracture.

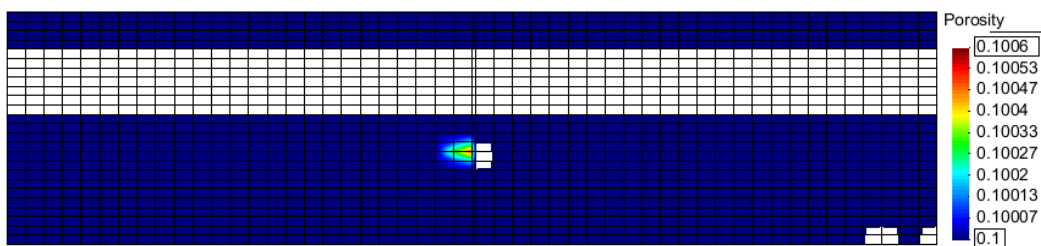


Figure 14.5.14 - Change in porosity after 50 years

The white spots within the dark blue aquifer are much more interesting, as the porosity is initially uniform at 10%. Any significant changes to this zone would be a result of dissolution or precipitation of carbonates. Contribution from dissolved quartz is negligible as the reaction rate is low and would require a reaction times equivalent to several thousands of years compared to the much more rapid dissolution rate of calcite.

A small area around the injection point is experiencing a reduction in porosity. Figure 18 below is a graphical representation of the precipitation in the lower left hand side corner of figure 15. The precipitation peaks within 2 to 5 years and steadily decreases as the simulation approaches 30 years. The change of porosity in this section is present at an early stage, whereas the increments in the porosity of figure 15 and 16 first appear after 30 years.

A closer view of Figure 14.5.14 shows the small section with an increased porosity. Although the change is noticeable, the increment is rather small ranging from 0.1 to 0.1006 which is less than 6e-2 percent.

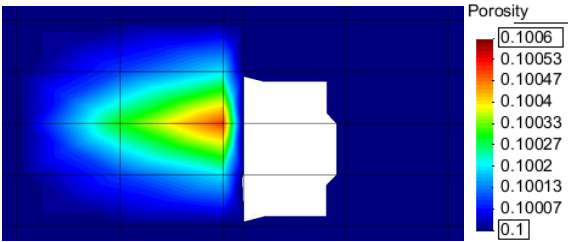


Figure 14.5.15 - Close up of Figure 14.5.14 with respect to increased porosity.

The white field to the left hand side of the same figure represents values outside the set scale of porosity, in this case that is the reduced porosity due to precipitation of calcite. Figure 14.5.16 below contains a better graphical representation the same precipitation area.

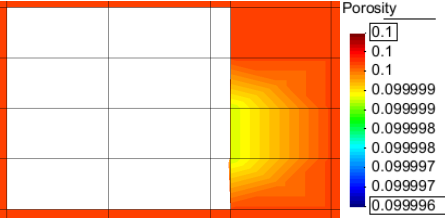


Figure 14.5.16 – Close up of Figure 14.5.14 with respect to decreased porosity

With a change in initial porosity within a range of 0.0 to 0.000004, the largest increment due to precipitation is only a tenth of the equivalent change due to dissolution. As mentioned there is also a zone around the injection point that is experiencing a decreased porosity. Figure 14.5.17 below is a graphical representation of the precipitation in the lower left hand side corner of Figure 14.5.14. Over 50 years the precipitation peaks within 2 to 5 years and steadily decreases as the simulation approaches 50 years. The change of porosity in this section is present at an early stage, whereas the increased porosity in Figure 14.5.15 only appears after 30 years.

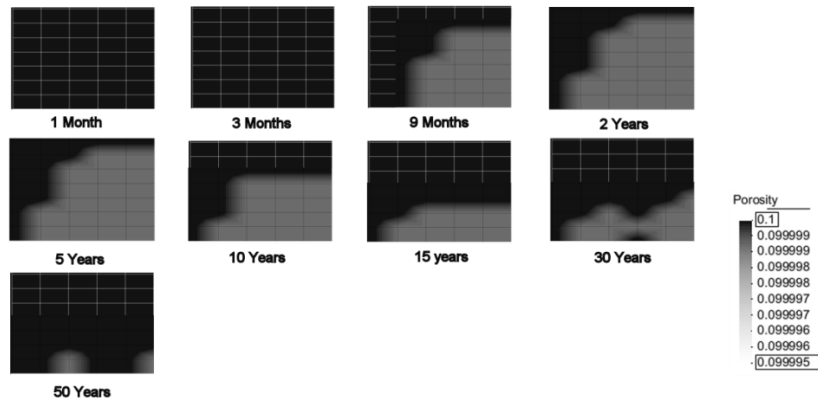


Figure 14.5.17 - Change in porosity around the injection zone over 50 years. BYTTES UT

As mentioned, the pH of the CO₂ saturated injection zone stabilizes at a distance from the injection point. In the injection point there is a very high pressure causing large gradients extending into the aquifer. As the gas and liquid is transported away from the point of injection, the pressure will fall significantly. This pressure drop causes a reduction in the fugacity of the CO₂ gas, which evidently shifts the equation of reaction in favor of aqueous CO₂ and calcite. Hence the oversaturated solution is left with two options of removing excess carbonates; either by evaporating excess CO₂ and/or precipitating solid calcite particles.

When it comes to the anomaly in porosity below the fracture, the mechanism is probably connected to the phase fluxes in the region. By examination of the gas and liquid phase flux after 50 years, Figure 14.5.18 and Figure 14.5.19 indicates that the considered point is located directly between the flux interface of liquid and gas.

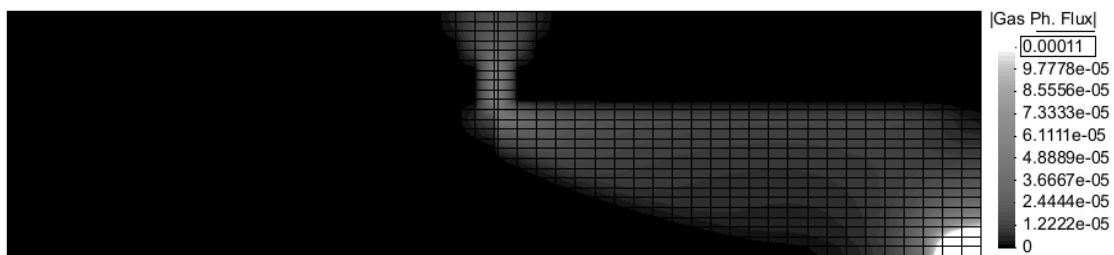


Figure 14.5.18 – Graphical representation of the gas phase flux after 50 years

The gas phase flux is dominated by the fracture, which in turn influences the magnitude and profile of the liquid phase flux as shown in Figure 14.5.19.

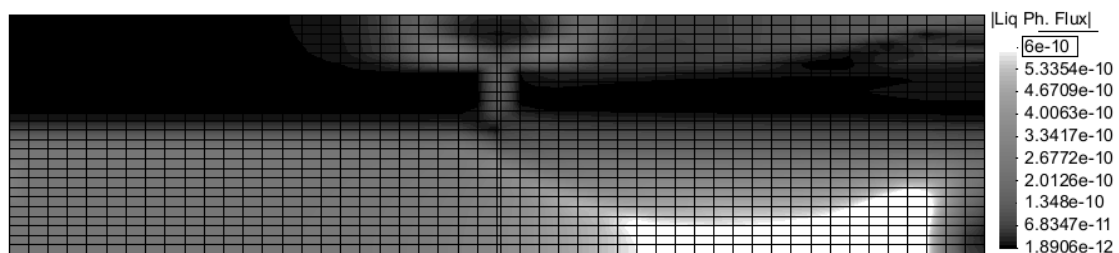


Figure 14.5.19 –Graphical representation of the total liquid phase flux 50 years

By creating a hybrid image of the two graphical representations, Figure 14.5.20 shows that the interface between total liquid and gas phase flux fits almost perfectly with each other.

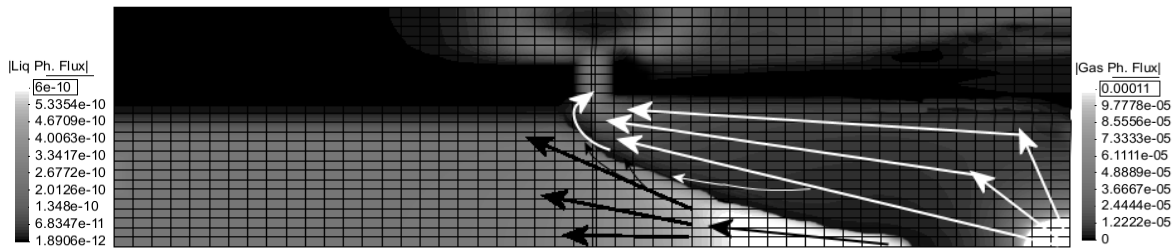


Figure 14.5.20 - A hybrid image consisting of both liquid and gas phase flux. Liquid flux is represented with black arrows, while gas flux is represented with white arrows. The flow above the cap rock is liquid phase flux. BYTTES UT

The water surrounded within the gas phase flux is saturated by dissolved gas and calcite. The buffering from calcite increases the pH value to above 8 and thereby reduces the mineral dissolution rate. At the interface shown in Figure 14.5.20, the conditions are quite different.

CO₂ gas is continuously transported into low saturated liquid and dissolved. The dissolution of CO₂ lowers the pH and shifts the chemical reaction in favor of dissolved calcite. A constant dissolution of carbon dioxide at the interface, combined with the buoyancy of gas, creates a flux vector of acidic water that flows through the very area of the porosity changes in Figure 14.5.14. At the same time some of the saturated acidic water will move into the high pH zone within the gas flux and cause precipitation of carbonates. The magnitude of the precipitation is reduced due to dissipating pressure and a lower temperature.

14.5.8. Vertical and horizontal stress profiles

The increase in liquid pore pressure due to the injected CO₂ has caused a change in the mean effective stresses of the reservoir.

The change in the mean effective stress of the aquifer and cap rock, results in a poro-elastic expansion of the rock mass and a corresponding uplift or displacement of the ground surface as shown in Figure 14.5.8.

14.5.9. Sxx, Lateral stress

The most noticeable changes in the lateral stress of case A, as illustrated in Figure 14.5.21, are limited to the lower parts of the injection aquifer and right above the cap rock.

The area at the center of the bottom aquifer boundary is experiencing a steady increase in compaction, reaching a lower limited of -3 MPa. As shown in Figure 14.5.21, the area of compaction arches between the two corners of the aquifer, and extends two gradient diagonally towards the cap rock at each side. The abnormalities located on the left hand side of the images, derive from consequent error located in either GiD or RCB and should be disregarded.

The lateral stress is highest in the area above the fracture where the escaping gas meets the upper pressure boundary. The expansion, or positive stress, is limited to a maximum of 6MPa.

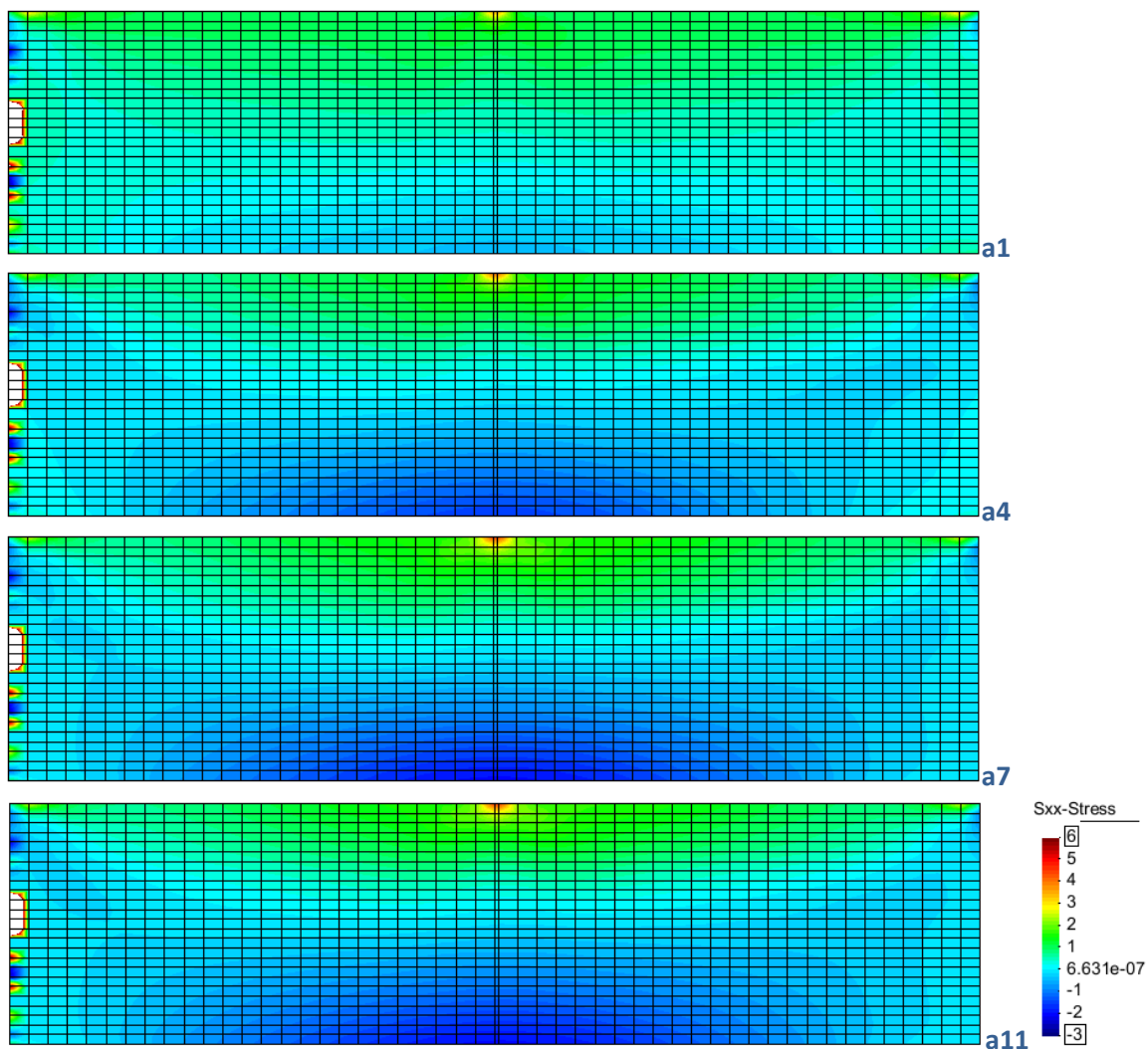


Figure 14.5.21 – Graphical representation of the lateral stress after 1 month (a1), 2 years (a4), 30 years (a7) and 100 years (a11) of CO₂ injection

As illustrated in appendix xxx, the observations are similar in all of the eight cases, only differentiated by the shape of the symmetrical time evolution.

14.5.10. S_{yy} , Vertical stress

The change in overbearing stress is limited to some compaction at the bottom of the reservoir; however the stress is mostly expansive peaking in the area directly above the fracture. The reduced effective stress in this area will influence the local permeability of the escaping gas due to the pore expansion.

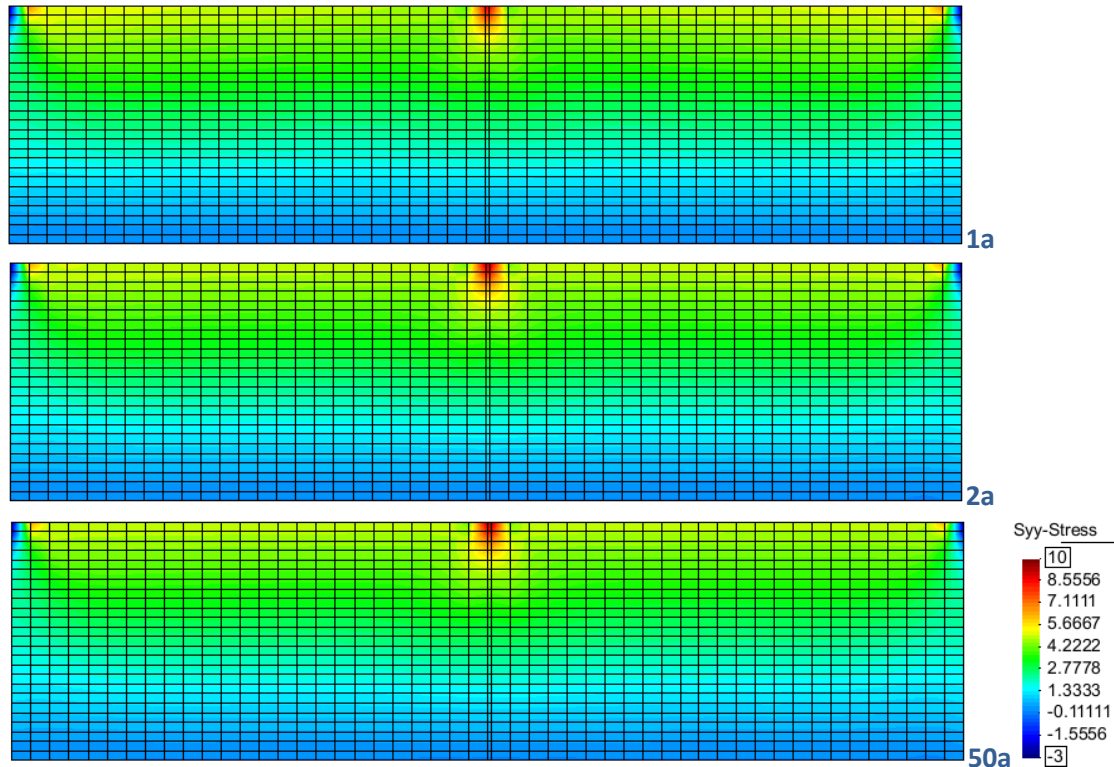


Figure 14.5.22 – Graphical representation of the vertical stress after 1 month (1a), 2 years (2a) and 50 years (50a) of CO₂ gas injection.

As presented in appendix VIII, there are little or no deviations in vertical stress for the presented cases. The main development in vertical stress is limited to the gas plume zone above the fracture. After 100 years of CO₂ injection, the only noticeable change in overbearing stress is the extent of the yellow coloured expansion around the plume. It is this pore expansion that induces the observed bending deformation at the vertical line above the fracture.

15. Discussion

Chapter 15 is divided into three primary sections. In the first section I will generally discuss the simulation software. The second section contains discussions related to the results, while the third section presents further work and possible extensions of this thesis.

15.1. The software

In this thesis the newly developed and modified coupled code RCB was applied to simulations of multiphase flow of CO₂ and saline water. The reactive and geomechanical modules consider both the rock deformation and chemical kinetics of mineral dissolution.

The code has proved to be applicable to two dimensional simulations of medium sized reservoirs over longer time intervals. As presented in the results, the reactive module Reatraso crashed due to unexpected pH and porosity developments below the virtual fracture. A revision of the uncertain approach of defining the reactive surface of the volume fraction could prove to reduce the reactive chemical convergence problems. As such, a further study and development of the existing equations in the module should also be done in order to evaluate the rigidity of the equations in the numerical Newton-Raphson approach.

In lack of relevant data from reactive reservoirs, the simulation cases were somewhat simplified approximations to articles and test sites such as the Utsira formation. With this in mind the results from the simulations in this thesis should only be regarded qualitatively because the presented quantitative results are very sensitive to the defined rock properties - especially the description of the correlated variables of stress, porosity and permeability in the fracture.

The flux of CO₂ through the fracture depends on the parameters utilized in the calculation of the stress, porosity and permeability. To achieve more realistic results, the variables should be calibrated with respect to known data from considered formations.

15.2. The results

Future work related to the consideration of fractures should attempt to use a hydrodynamical approach, as well as enabling the temperature solver, to simulate the flow through the fracture and obtain a more realistic description of the local flow and geomechanical changes. This is because the increasing gas saturation could change the elasticity of the fluids passing through the fracture, and thus induce a fractural collapse. Another scenario is that dissolved calcite might experience a significant enough temperature change in the fracture and precipitate in a magnitude that might reduce, or in the best case block the highly permeable path through the confining cap rock.

While the initial stress and pressure is defined in gradients and iterated, the reservoir temperature is constant as defined in the setup of the simulations. This is not an ideal solution as calcite and reaction kinetics in general is dependent on the temperature. A temperature gradient is especially important for calcite due to its retrograde precipitation at increasing temperatures. If the conditions are right the calcite can dissolve in one section of the reservoir and precipitate at a different location. In some cases such scenarios can reduce the permeability of affected area.

There are two components contributing to the alkalinity of the aquifer solution. Dissolved calcite and CO_2 is in equilibrium with carbonic acid and its charged species. A change in either temperature or pH would force the equilibrium to shift in one of two directions, causing further dissolution of the two components or precipitation of solid calcite.

At large depths the temperature is higher than that of the overbearing formations. The solubility of calcite, along with CO_2 , would therefore increase if the saline water were to be displaced vertically towards a weakness in the confining cap rock. In a similar context the solubility of carbonates would also decrease if the pH value should increase.

The largest reduction of mean stress was observed above the virtual fracture where the escaping CO_2 gas met the pressure boundary zone. The reduction of mean stress is not only important for the mentioned permeability changes. If the code allows it, the increased pore pressure could cause hydraulic fracturing or even introduce shear slip scenarios induced by the shear component of the stress.

When the pressure increases slowly, fluid has time to diffuse into the neighboring rock formation, which then expands and locally increases the total stress. Because of the geometry of the extensive horizontal aquifer, the total stresses increase more in the horizontal than in the vertical direction. This has two consequences. Firstly, it will prevent reduction of effective stress in the horizontal direction and thereby prevent the formation of vertical hydraulic fractures

15.3. Further work

Hydrodynamic fracture description

The eight simulated cases presented in this thesis have treated the fracture in a simplified hydromechanical approach. However, there is an additional and more realistic way of defining a fracture in the current version of the RCB code.

The hydromechanical approach defined the fracture as a highly permeable zone dimensioned by an element smaller than the other elements of the modeled grid. A hydrodynamic approach would treat a respective fracture with hydrodynamic boundary conditions calculated by the original set of chosen flow equations. Further applications of this approach would allow the inclusion of fracturing dynamics considering the stress and pore pressure. That is, whenever the stress plus the pore pressure in a respective section of the formation exceed the tensile strength of the section, a fracture analysis will be initiated.

More complex mineral description in the saline aquifer

The initial water concentration and mineral specifications are greatly simplified in this thesis. Future studies should strive to incorporate more minerals and aqueous species in order to approach real reservoir conditions. Most of the minerals presented in the papers of Helge Hellevang are already included in the master database; as such it should be easy fully define the system by adding the kinetic values in the kinetics database.

As an extension of the mineral description, it would be feasible to create more complex reservoir with several layers of different properties. The current simulations presented in this thesis are homogeneously described in the 5 defined zones. The work of including several mineral species is already in progress; however the progress substantially delayed due to unexpected numerical convergence problems.

Add temperature gradients and solve on the changes by adding definitions of heat conduction

Naturally, some of my preliminary work in approaching the case presented in the TOUGH FLAC3D article showed that a more complex definition of the zones resulted in a positive influence on the iteration process. All attempts at creating a equivalent model failed due to convergence problems. It is unknown whether it is the geomechanical specifications or the sheer size of the reservoir that caused the numerical problems. However, the combined iterations on pressure, temperature, stress and displacements reduced the increments in the time subdivisions of the two modules after allowing the code to solve the temperature changes.

As such it is believed that a better definition of the thermal variables, such as heat conductivity, and maybe some alterations to the equations might ease the conversion and allow simulations of larger reservoirs.

Apply logarithmically scaled elements around the injection point.

Another approach to help ease the conversion would be to apply logarithmically scaling of the grid in troubled areas such as the injection point or the presented porosity and pH anomalies. A more dense nodal distribution would reduce the gradient interval between each nod and thus reduce the need of incrementing the time subdivisions. In order to obtain a logarithmic grid, the input file generator Visual Retraso must undergo a series of tweaks to improve and repair the current versions.

There are two available compilations in beta versions that each has their strength and weaknesses. The current applied version R64 is fully functional except for its faulty logarithmic definition. While the newer version R71 is improved in that aspect, the generation of grid files is only successful in one of 50 cases.

Gas mixtures

The addition of gas mixtures is one of the simplest extensions since the code already has an integrated general equation of state. As mentioned in chapter xxx, the EOS is already applied on density corrections so the main alteration would be to use the estimated mixture compressibility factor. The database in Retraso Codebright is also equipped to handle reactions which involve dissolved H₂S. In order to allow calculations on gas mixtures, the existing equations for pure CO₂ solubility have to be rewritten to account for mixed gas solubility. Even though the interactions between CH₄ and CO₂ are interesting, the preliminary simulations should be limited to H₂S due to the low solubility of CH₄ in water. Other constituents of exhaust fumes like nitrogen and oxygen have an even lower solubility's. BK

Relative permeability

In RCB it is possible to add a code to change the permeability's and relative permeability's for every time step. The code that has been used here updates the permeability's as a function of changes in porosities due to mineral dissolution or mineral precipitation. It should be possible to add relative permeability in the nearest future and this will enable more realistic descriptions of surface reactions. BK

Hydrate sealing effects

There are many reservoirs that can be used for CO₂ storage. Some of them are located in regions with low temperatures and depths that can form hydrates. Hydrates do not close pore spaces, however they will reduce the permeability and allow CO₂ get more time as to dissolve into the surrounding groundwater. In RCB it is possible to include this by adding an extra mineral reaction in which hydrates form at the CO₂ interface. A study of the possibilities is already initiated by a PhD student, however further investigation is needed. BK The Utsira formation is too warm for hydrate formation whereas the Snøhvit injection site has the required cold temperatures in the upper section. If the CO₂ plume reaches the upper layers hydrates might form.

16. Conclusions

The main goal of the thesis was to contribute in the development of a totally integrated CO₂ storage evaluation tool which considers reactive transport as well as geomechanics. As an extension of this goal, the secondary aim was to investigate the effects of introducing a fracture in the confining cap rock with respect to the mechanical and chemical aspects of gas injections.

The work presented in this thesis shows that the coupled code can easily be applied on simple medium sized reservoirs. Although not as rigorous as one would want it to be, the chemical module managed to complete 4 of the eight simulations. For most simulators, the source of convergence problems was often connected to chemical reactions in the reactive module. In the presented simulations this was exactly the case.

The rapid dissolution of calcite after respectively 30 and 50 years of CO₂ injection caused spikes in both porosity changes and pH evolution. It is believed that these rapid changes, related to the chemical module, caused the time subdivision in Retraso to reduce the time intervals close to zero and eventually cause a breakpoint in the coupled code when the Newton-Raphson iteration failed.

With respect to the second goal of the thesis, the introduction of a fracture in the confining cap rock resulted in a leak that dominated both the liquid saturation and pH profiles through the flux of the escaping fluids. The leakage of CO₂ gas through the fracture redirected most of the injected gas so that large areas in several cases were left as unused potential storage space. The calcite buffering of the system was substantial. As illustrated by the pH plot in figure Figure 14.5.9, observations conclude that the pH did not drop below 7 for any of the zones in the reservoir. After 100 years of CO₂ injection and calcite buffering, the dissolution of quartz based minerals was close to non-existent.

Observations from the simulations showed that once the saturation of the gas phase increased in the fracture, so did the flux and the relative permeability. After a respective amount of time the saturation reached a point where the entire reservoir experienced a gas breakthrough. The pressure was then reduced to the shear resistance in the reservoir. The buoyant CO₂ migration through the fracture was further accelerated due to the combined effects of relative permeability, viscosity changes and pressure-induced changes in density. The general reduction in the effective mean stress, caused by the escaping CO₂ gas, also contributed to the increased permeability of the fracture through increased pore pressure and expansion.

The introduction of a fracture in a confining rock formation will cause major gas leaks to an extent that dominates the flow in the reservoir, as such it's not recommended to use reservoirs in unstable geological areas that are in danger of earthquakes and propagation of small fractures.

17. References

1. Nordbotten, J., *Sequestration of carbon in saline aquifers mathematical and numerical analysis elektronisk ressurs*. 2004, [Bergen]: University of Bergen. 1 b. (flere pag.).
2. Uppstad, D.S., *Solid-fluid interfacial structure and properties related to aquifer storage of carbon dioxide*. 2005, Bergen: [D.S. Uppstad]. 183 bl.
3. Hellevang, H., *Interactions between CO₂, saline water and minerals during geological storage of CO₂*. 2006, [Bergen]: University of Bergen. 1 b. (flere pag.).
4. Jan R. Lien, M.J.o.A.S., *PTEK100 Introduksjon til petroleums- og prosesseteknologi*. Universitetet i Bergen, 2006: p. 49-50 , .
5. Australia, D.o.P.I.a.W.-. *Dual porosity aquifers*. 2009.
6. GlobalSecurity, *Chapter 2 - Groundwater*. 2005-2009.
7. Crain, E.R.R., *CRAIN'S PETROPHYSICAL HANDBOOK*.
8. Groundwatersoftware.com, *Ground water software*.
http://www.groundwatersoftware.com/v9_n10_tortuosity.htm 29.04.2009.
9. McCabe, W.L., P. Harriott, and J.C. Smith, *Unit operations of chemical engineering*. 6th ed. McGraw-Hill chemical engineering series. 2001, Boston: McGraw-Hill. XVII, 1114 s.
10. Gill, R., *Chemical fundamentals of geology*. 1989, London: Unwin Hyman. xii, 291 s.
11. Lien, J.R., *PTEK213 Reservoarteknikk II*. Universitetet i Bergen, 2009: p. 1-25.
12. Lien, J.R., *PTEK212 Reservoarteknikk I*. Universitetet i Bergen, 2009: p. 1-16, 20-23, 51-56.
13. Cramer, C.J., *Essentials of computational chemistry theories and models*. 2nd ed. 2004, Chichester: Wiley. XX, 596 s.
14. Pashley, R.M. and M.E. Karaman, *Applied colloid and surface chemistry*. 2004, Chichester: Wiley. IX, 188 s.
15. Walther, J.V., *Essentials of geochemistry*. 2005, Sudbury, Mass.: Jones and Bartlett Publishers. XV, 704 s.
16. Dr.Hobart_King, *Geology.com - Calcite*.
17. Prausnitz, J.M., R.N. Lichtenthaler, and E.G.d. Azevedo, *Molecular thermodynamics of fluid-phase equilibria*. 3rd ed. Prentice-Hall international series in the physical and chemical engineering sciences. 1999, Upper Saddle River, N.J.: Prentice-Hall PTR. XXIII, 860 s.
18. Daintith, J., *A dictionary of chemistry*. 5th ed. 2004, Oxford: University Press. 3 bl, 602 s.
19. Encarta.com, *Encarta database - Calcite*. p.
http://encarta.msn.com/encyclopedia_761573488/calcite.html.
20. Wang, H.F., *Theory of linear poroelasticity with applications to geomechanics and hydrogeology*. Princeton series in geophysics. 2000, Princeton, N.J.: Princeton University Press. XII, 287 s.
21. efunda.com, *Engineering fundamentals*.
http://www.efunda.com/formulae/solid_mechanics/mat_mechanics/stress.cfm 2008: p.
http://www.efunda.com/formulae/solid_mechanics/mat_mechanics/stress.cfm
22. Menke, W. and D. Abbott, *Geophysical theory*. 1990, New York: Columbia University Press. xi, 458 s.
23. Bjørn Kvamme, S.L., *A NEW REACTIVE TRANSPORT RESERVOIR SIMULATOR FOR AQUIFER STORAGE OF CO₂ - WITH IMPLICIT GEOMECHANICAL ANALYSIS*. Carbon Dioxide Capture for Storage in Deep Geologic Formations, 2009. **Volume 3**.
24. Engineering, I.C.f.N.M.i., *GiD user manual*. http://gid.cimne.upc.es/support_team/, 2008: p. 11.
25. Jonny Rutqvist, C.-F.T., *A study of cap rock hydromechanical changes associated with CO₂ injection into a brine formation*. Environmental Geology, 2002.

26. Dandekar, A.Y., *Petroleum reservoir rock and fluid properties*. 2006, Boca Raton, Fla.: Taylor & Francis. 460 s.
27. www.tel-tek.no: p.
<http://holga.no/upload/Dokmntr/CCS%20Teknologiutfordringer%20%E2%80%93%20CO2%20transport.ppt>.

Appendix A – Input files for the simulation

Included on the disk

Appendix B – Guide to creating input files in Visual Retraso

General guidelines for the creation of input- files, initiation of a simulations and the process of viewing results in the postprocessor. In order to save pages the file has been included on the disc.

Appendix I

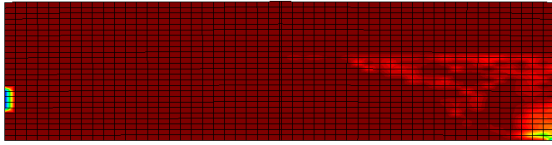
Liquid saturation

Appendix I contains a range of graphical representations of the liquid saturation through a 100 year simulated carbon dioxide injection. There are a total of 8 cases or runs with a maximum of 11 images representing the respective times of injection. However, some cases are incomplete with respect to total simulation time and images. This is due to convergence problems.

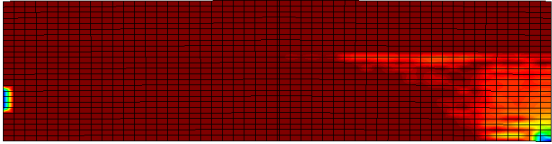
Each set of images have their respective gradient colour indicator which illustrates the saturation condition at any given time and position. The higher limit is always 1.0 and the lower limit is alternating according to the lower boundary of saturation for the entire simulation.

All figures are also deformed with a factor of $1.37715e6$ to illustrate displacements. In translated meaning this gives a relationship between the dimensions of the figure, the respective factor and the true deformed reservoir matrix. One millimetre of grid movement is equivalent to **xxx real units**

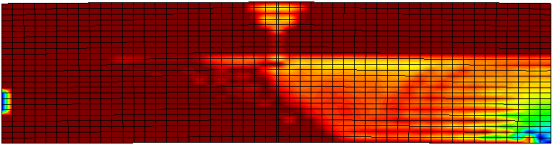
17.1. Case A



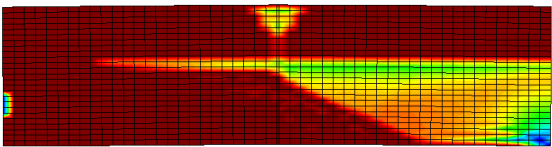
(a1) – Liquid saturation after 1 month



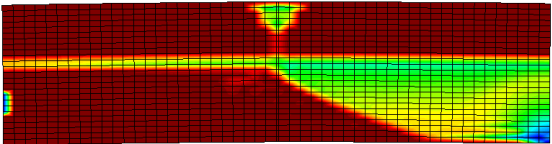
(a2) – Liquid saturation after 3 months



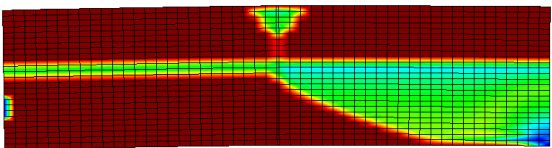
(a3) – Liquid saturation after 9 months



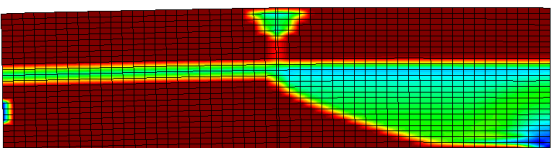
(a4) – Liquid saturation after 2 years



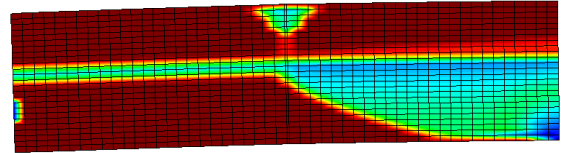
(a5) – Liquid saturation after 5 years



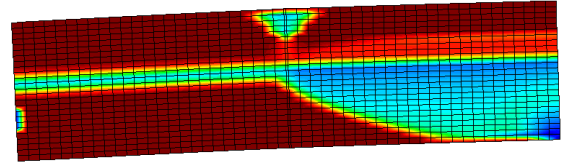
(a6) – Liquid saturation after 10 years



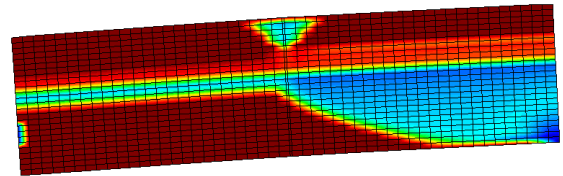
(a7) – Liquid saturation after 15 years



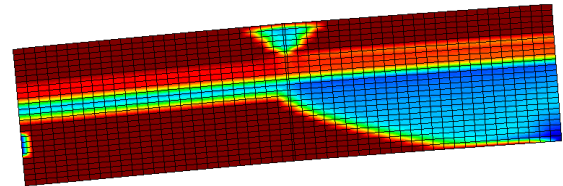
(a8) – Liquid saturation after 30 years



(a9) – Liquid saturation after 50 years



(a10) – Liquid saturation after 75 years



(a11) – Liquid saturation after 100 years

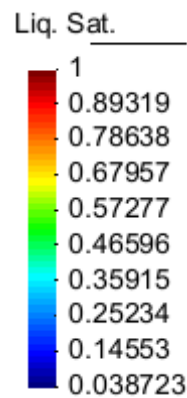
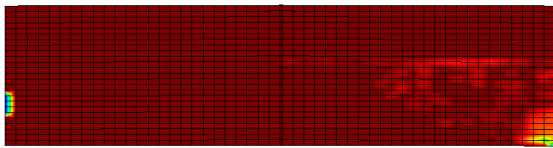


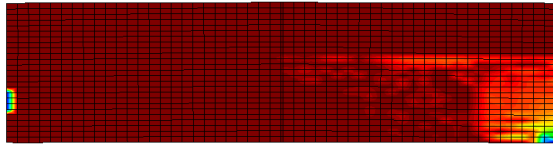
Figure 14.5.1 – Graphical representation of the liquid saturation over 100 years.

Deformation with a factor of 1.37715×10^6 is also applied to the grid.

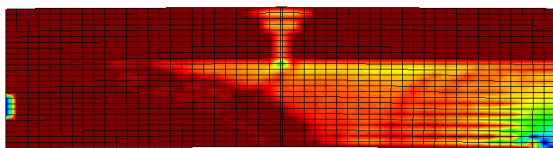
17.2. Case B



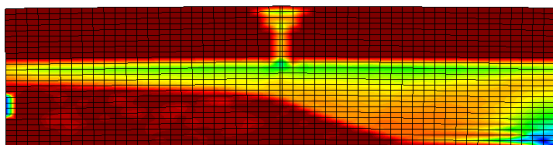
(b1) – Liquid saturation after 1 month



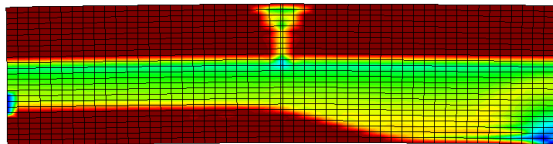
(b2) – Liquid saturation after 3 months



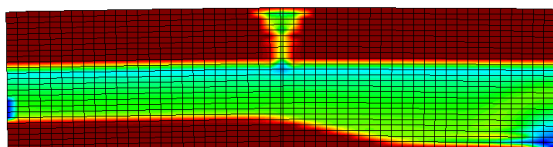
(b3) – Liquid saturation after 9 months



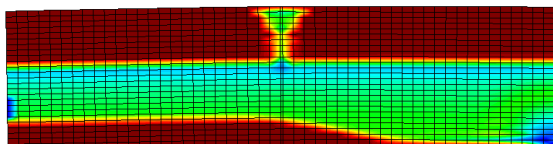
(b4) – Liquid saturation after 2 years



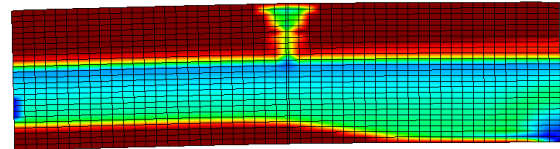
(b5) – Liquid saturation after 5 years



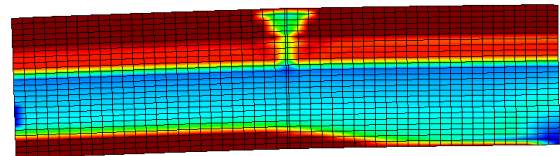
(b6) – Liquid saturation after 10 years



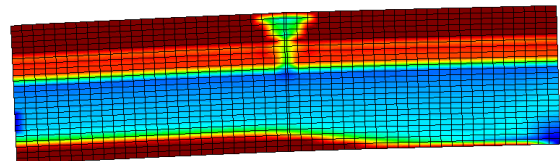
(b7) – Liquid saturation after 15 years



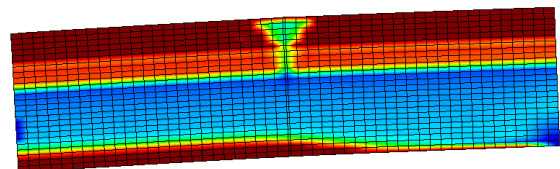
(b8) – Liquid saturation after 30 years



(b9) – Liquid saturation after 50 years



(b10) – Liquid saturation after 75 years



(b11) – Liquid saturation after 100 years

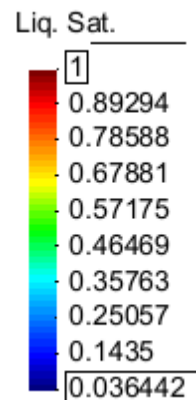
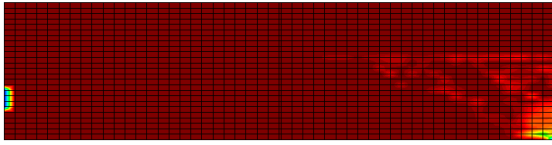


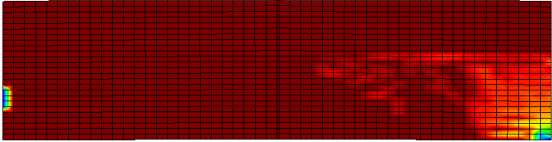
Figure 17.2.1 – Graphical representation of the liquid saturation over 100 years.

Deformation with a factor of 1.37715×10^6 is also applied to the grid.

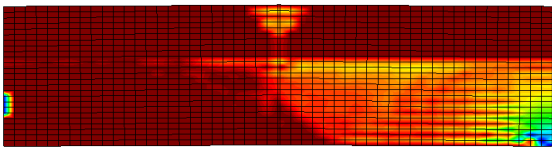
17.3. Case C



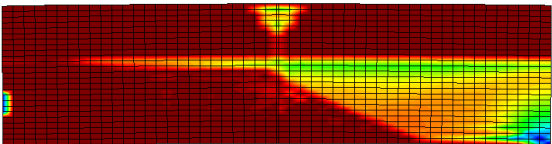
(c1) – Liquid saturation after 1 month



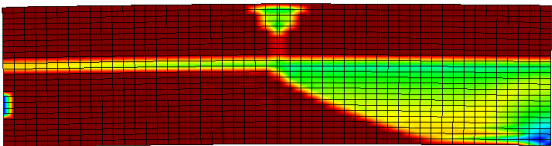
(c2) – Liquid saturation after 3 months



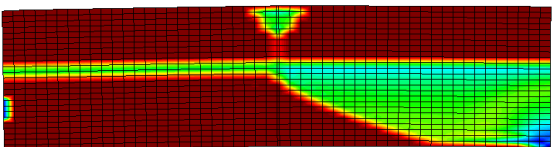
(c3) – Liquid saturation after 9 months



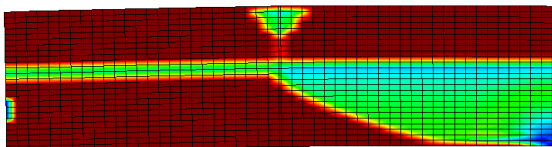
(c4) – Liquid saturation after 2 years



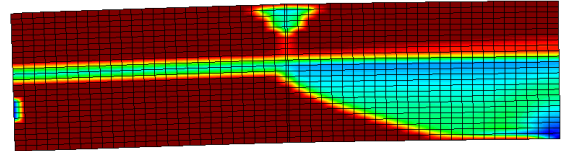
(c5) – Liquid saturation after 5 years



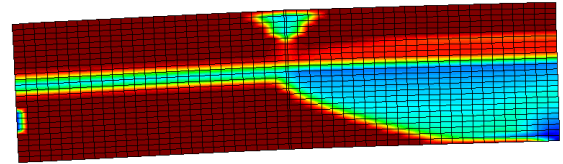
(c6) – Liquid saturation after 10 years



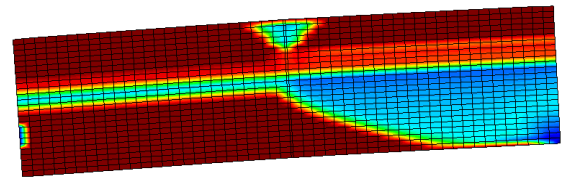
(c7) – Liquid saturation after 15 years



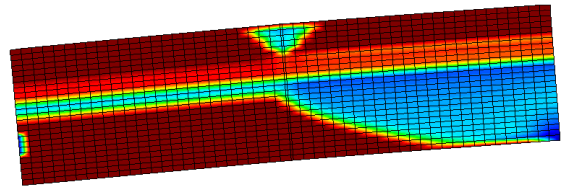
(c8) – Liquid saturation after 30 years



(c9) – Liquid saturation after 50 years



(c10) – Liquid saturation after 75 years



(c11) – Liquid saturation after 100 years

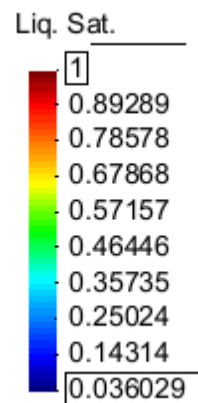
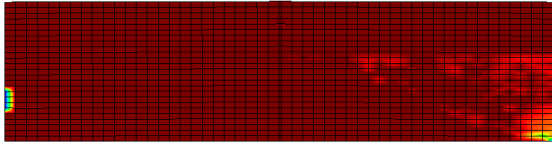


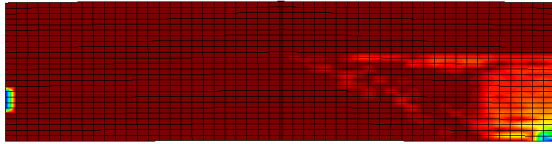
Figure 17.3.1 – Graphical representation of the liquid saturation over 100 years.

Deformation with a factor of $1.37715e+6$ is also applied to the grid.

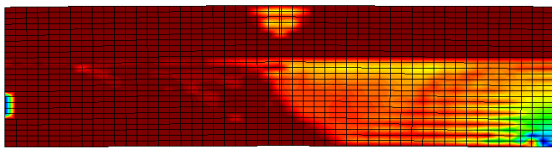
17.4. Case D



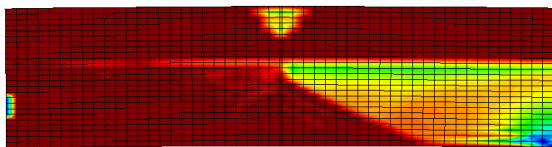
(d1) – Liquid saturation after 1 month



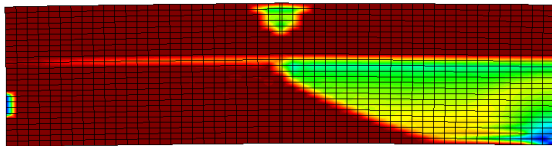
(d2) – Liquid saturation after 3 months



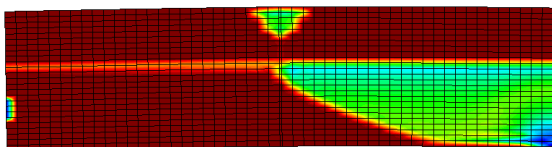
(d3) – Liquid saturation after 9 months



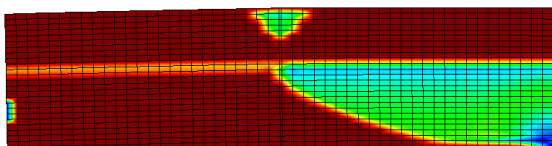
(d4) – Liquid saturation after 2 years



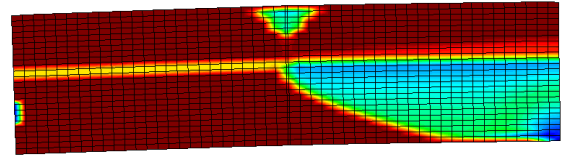
(d5) – Liquid saturation after 5 years



(d6) – Liquid saturation after 10 years



(d7) – Liquid saturation after 15 years



(d8) – Liquid saturation after 30 years

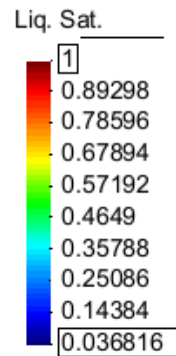
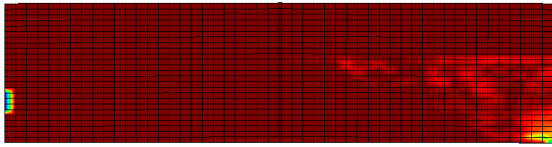


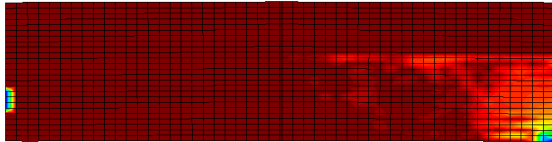
Figure 17.4.1 - Figure xx – Graphical representation of the liquid saturation over 30 years.

Deformation with a factor of 1.37715×10^6 is also applied to the grid.

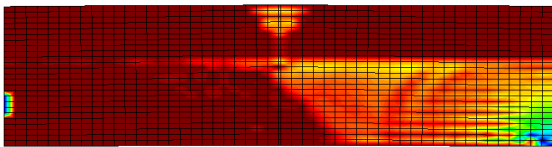
17.5. Case A2



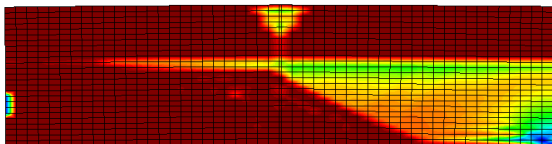
(A1) – Liquid saturation after 1 month



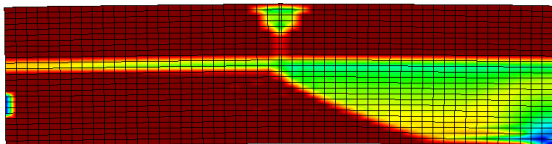
(A2) – Liquid saturation after 3 months



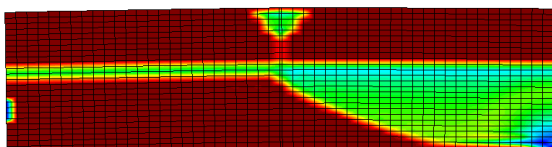
(A3) – Liquid saturation after 9 months



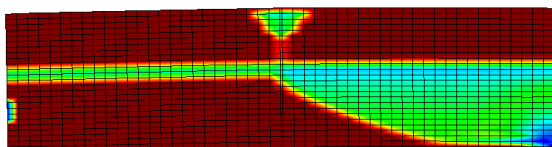
(A4) – Liquid saturation after 2 years



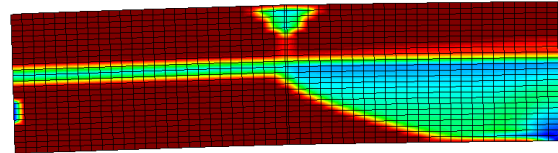
(A5) – Liquid saturation after 5 years



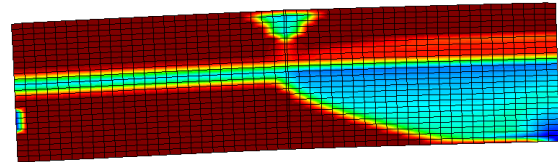
(A6) – Liquid saturation after 10 years



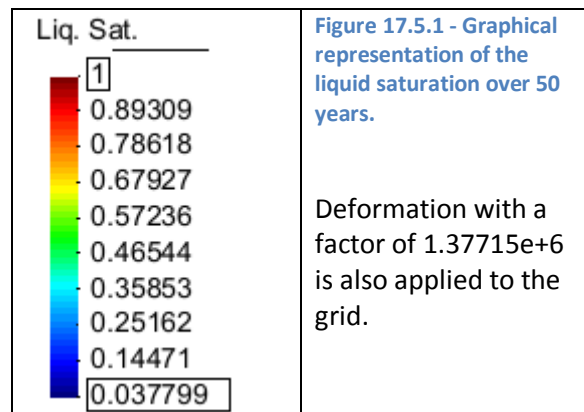
(A7) – Liquid saturation after 15 years



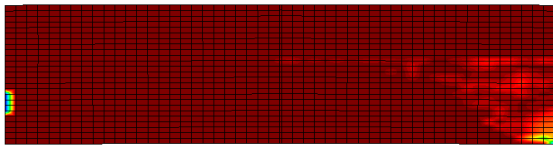
(A8) – Liquid saturation after 30 years



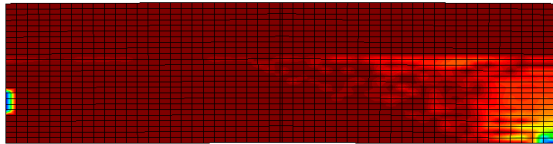
(A9) – Liquid saturation after 48.7 years



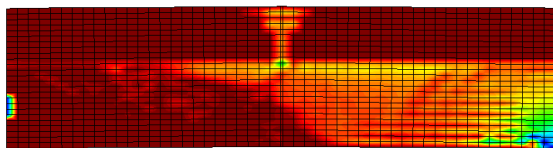
17.6. Case B2



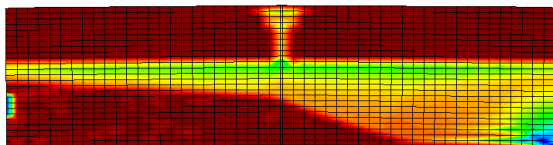
(B1) – Liquid saturation after 1 month



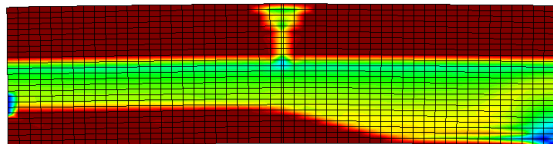
(B2) – Liquid saturation after 3 months



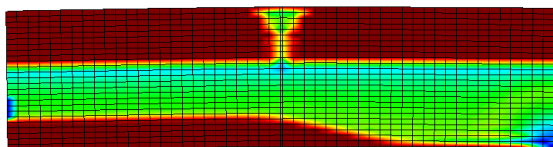
(B3) – Liquid saturation after 9 months



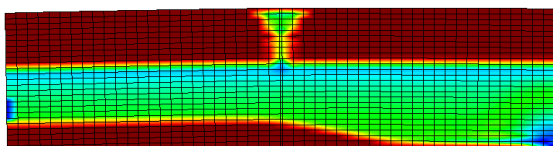
(B4) – Liquid saturation after 2 years



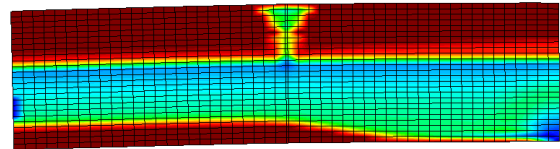
(B5) – Liquid saturation after 5 years



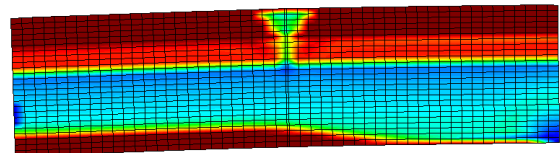
(B6) – Liquid saturation after 10 years



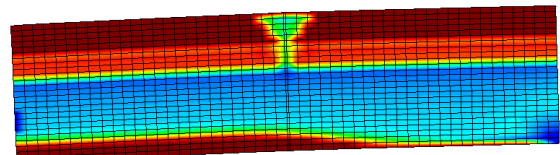
(C7) – Liquid saturation after 15 years



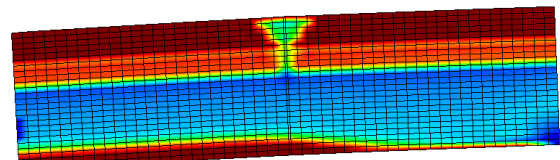
(B8) – Liquid saturation after 30 years



(B9) – Liquid saturation after 50 years



(B10) – Liquid saturation after 75 years



(B11) – Liquid saturation after 100 years

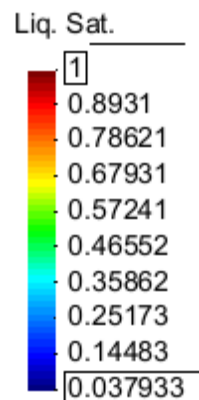
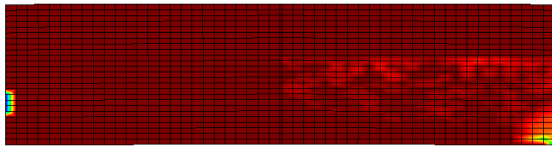


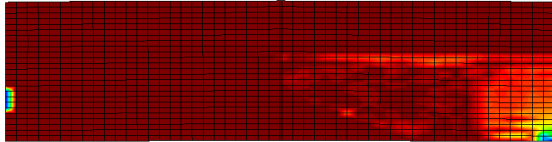
Figure 17.6.1 – Graphical representation of the liquid saturation over 100 years.

Deformation with a factor of $1.37715e+6$ is also applied to the grid.

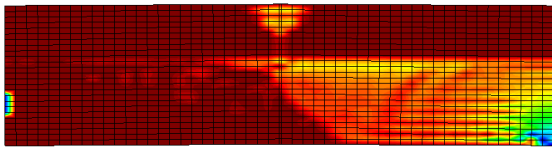
17.7. Case C2



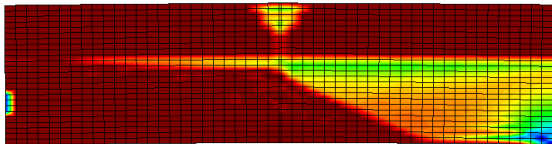
(C1) – Liquid saturation after 1 month



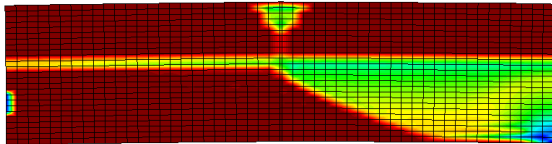
(C2) – Liquid saturation after 3 months



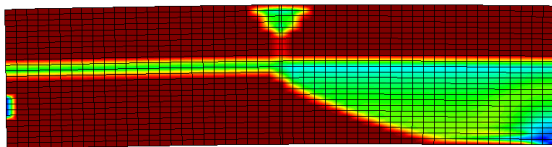
(C3) – Liquid saturation after 9 months



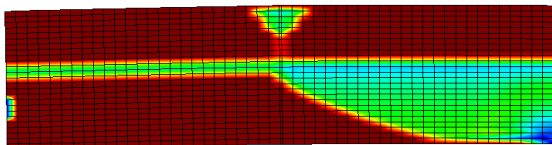
(C4) – Liquid saturation after 2 years



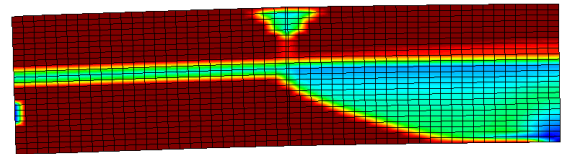
(C5) – Liquid saturation after 5 years



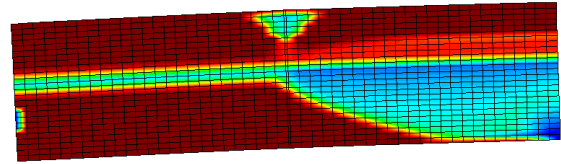
(C6) – Liquid saturation after 10 years



(C7) – Liquid saturation after 15 years



(C8) – Liquid saturation after 30 years



(C9) – Liquid saturation after 50 years

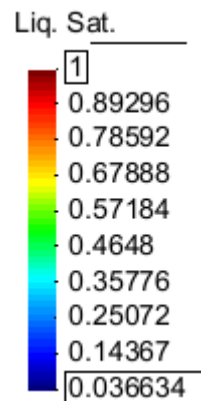
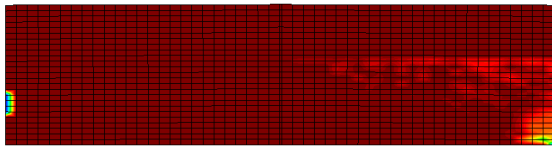


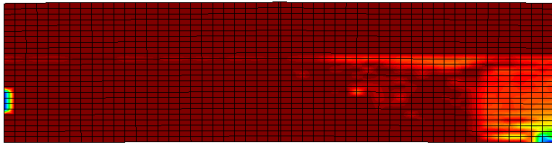
Figure 17.7.1 – Graphical representation of the liquid saturation over 100 years.

Deformation with a factor of 1.37715×10^6 is also applied to the grid.

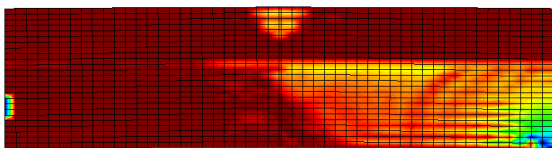
17.8. Case D2



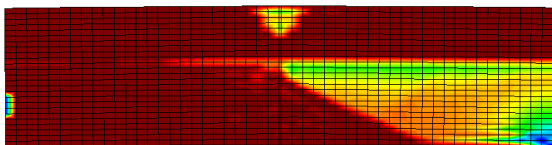
(D1) – Liquid saturation after 1 month



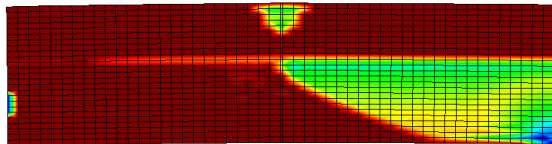
(D2) – Liquid saturation after 3 months



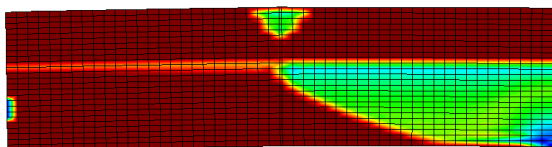
(D3) – Liquid saturation after 9 months



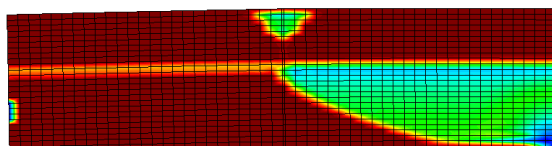
(D4) – Liquid saturation after 2 years



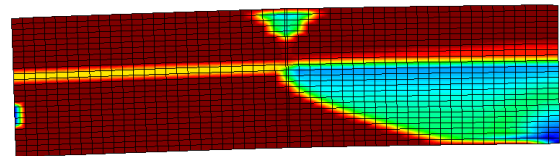
(D5) – Liquid saturation after 5 years



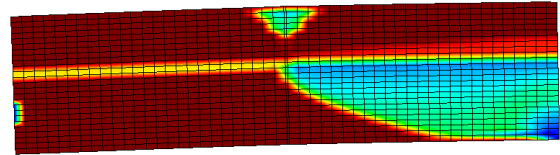
(D6) – Liquid saturation after 10 years



(D7) – Liquid saturation after 15 years



(D8) – Liquid saturation after 30 years



step 1.04221e+9
Contour Fill of Liq. Sat..
Deformation (x1.37715e+6): Displacements of TIME ANALYSIS, step 1.04221e+9.

(D9) – Liquid saturation after 33 years

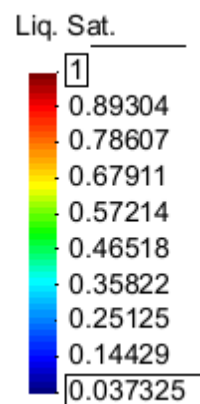


Figure 17.8.1 - Graphical representation of the liquid saturation over 30 years.

Deformation with a factor of 1.37715×10^6 is also applied to the grid.

Appendix II

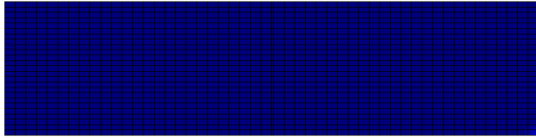
Aquifer pH values

Appendix II contains a range of graphical representations for the pH values thorough a 100 year simulated carbon dioxide injection. There are a total of 8 cases or runs with a maximum of 11 images representing the respective times of injection. However, some cases are incomplete with respect to total simulation time and images. This is due to convergence problems.

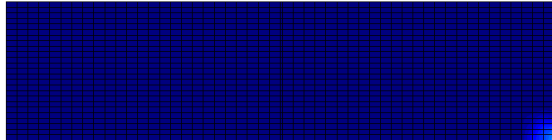
Each set of images have their respective gradient color indicator which illustrates the saturation condition at any given time and position. The higher limit is always 12.51 and the lower limit 7.964. These values are manually set so that a comparison of the cases is feasible.

Some of the cases are further specified by means of enlarged images of specific areas of interest. These include anomalies in case A, A2 and B2.

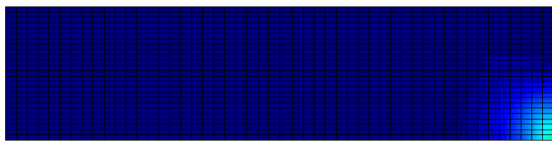
17.9. Case A



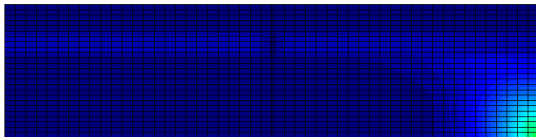
(a1) – pH value after 1 month



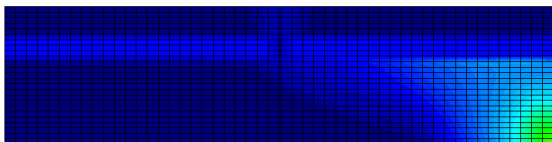
(a2) – pH value after 3 months



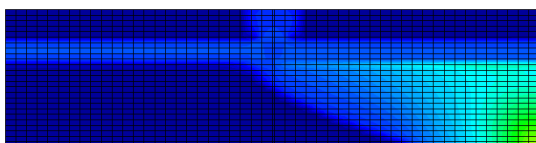
(a3) – pH value after 9 months



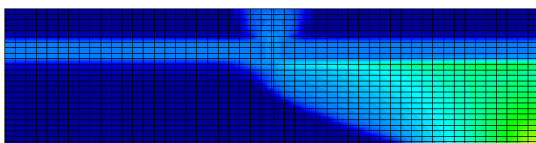
(a4) – pH value after 2 years



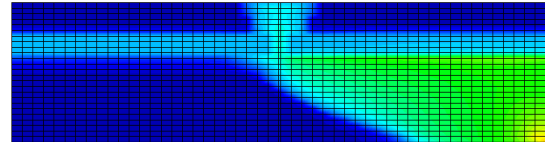
(a5) – pH value after 5 years



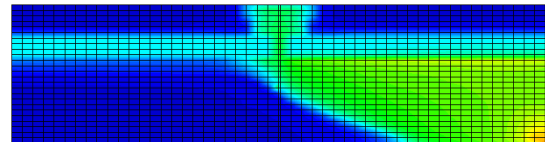
(a6) – pH value after 10 years



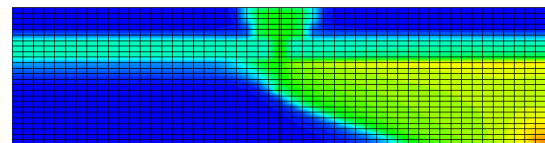
(a7) – pH value after 15 years



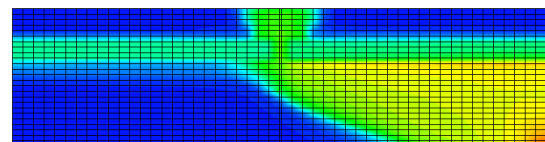
(a8) – pH value after 30 years



(a9) – pH value after 50 years



(a10) – pH value after 75 years



(a11) – pH value after 100 years

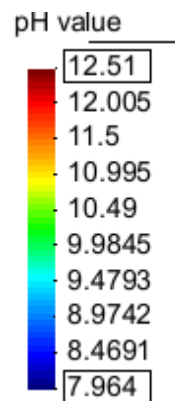
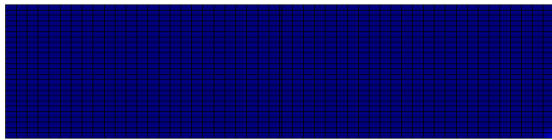
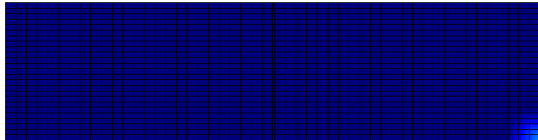


Figure 17.8.1 - Graphical representation of the change in pH value over 100 years.

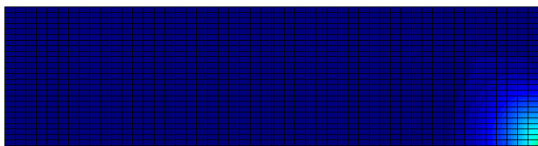
17.10. Case B



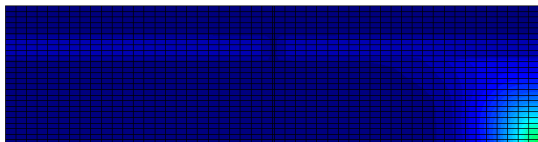
(b1) – pH value after 1 month



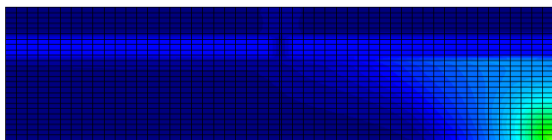
(b2) – pH value after 3 months



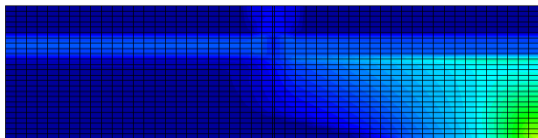
(b3) – pH value after 9 months



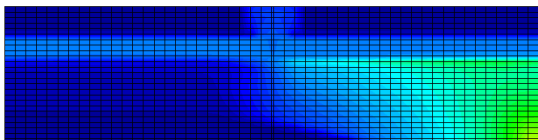
(b4) – pH value after 2 years



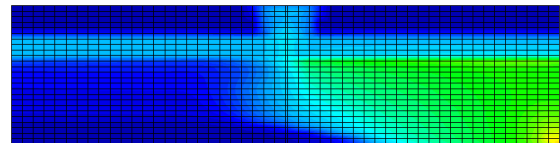
(b5) – pH value after 5 years



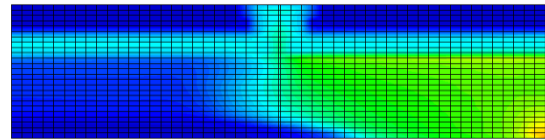
(b6) – pH value after 10 years



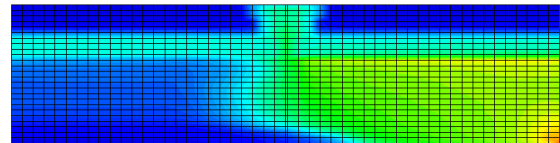
(b7) – pH value after 15 years



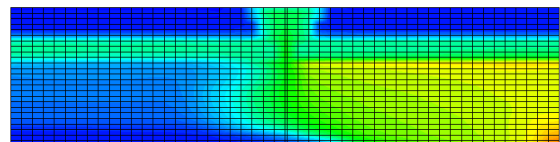
(b8) – pH value after 30 years



(b9) – pH value after 50 years



(b10) – pH value after 75 years



(b11) – pH value after 100 years

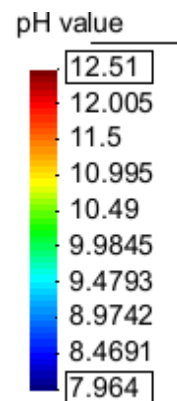
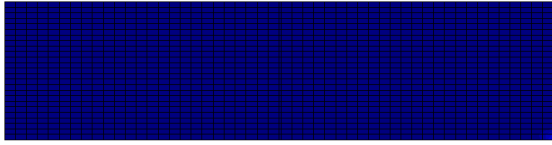


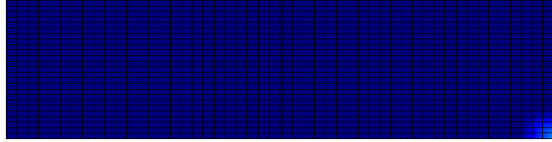
Figure 17.10.1

Figure xx – Graphical representation of the change in pH value over 100 years.

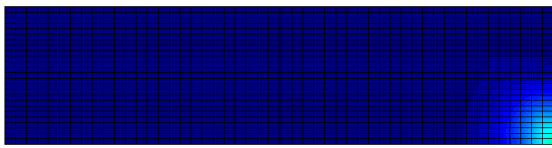
17.11. Case C



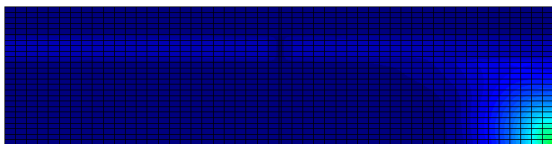
(c1) – pH value after 1 month



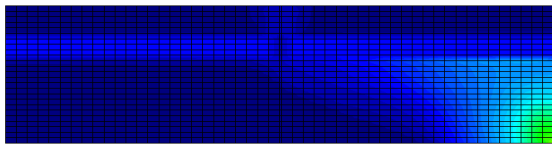
(c2) – pH value after 3 months



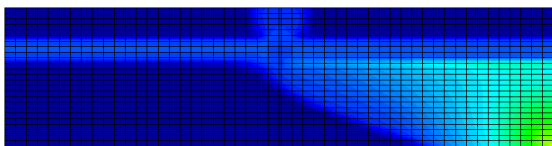
(c3) – pH value after 9 months



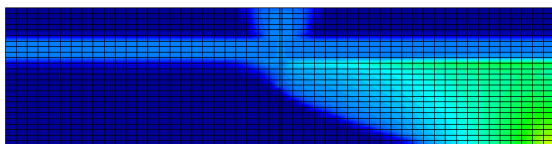
(c4) – pH value after 2 years



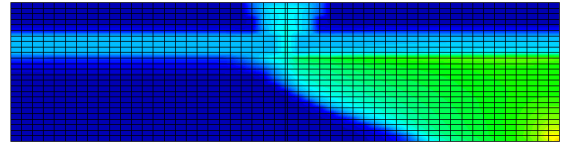
(c5) – pH value after 5 years



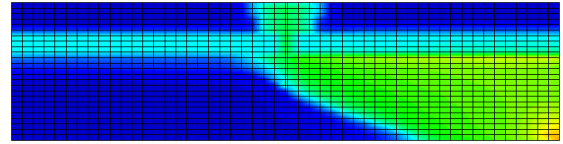
(c6) – pH value after 10 years



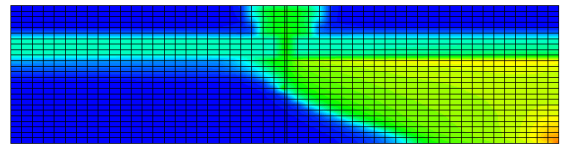
(c7) – pH value after 15 years



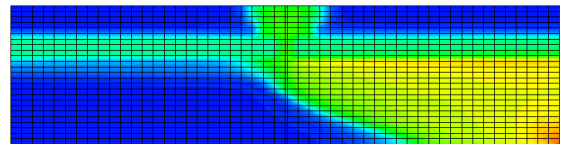
(c8) – pH value after 30 years



(c9) – pH value after 50 years



(c10) – pH value after 75 years



(c11) – pH value after 100 years

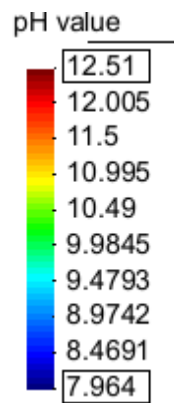
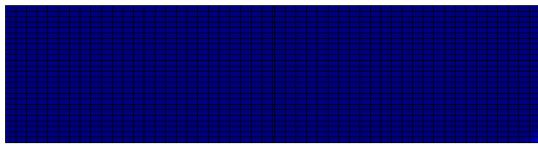
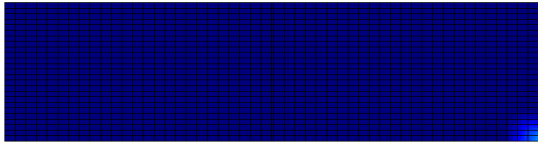


Figure 17.11.1 – Graphical representation of the change in pH value over 100 years.

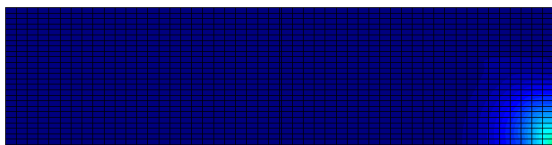
17.12. Case D



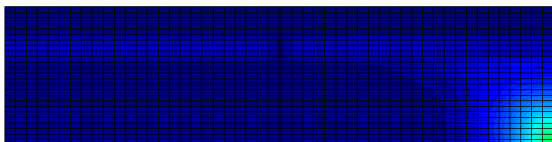
(d1) – pH value after 1 month



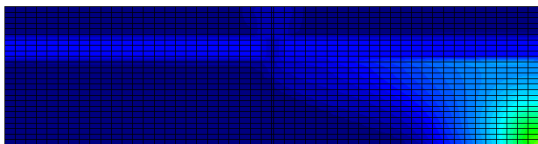
(d2) – pH value after 3 months



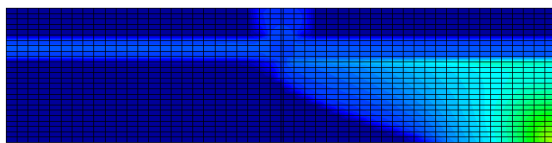
(d3) – pH value after 9 months



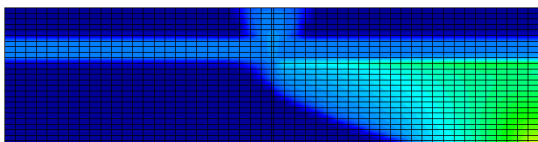
(d4) – pH value after 2 years



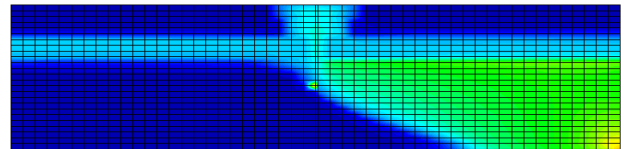
(d5) – pH value after 5 years



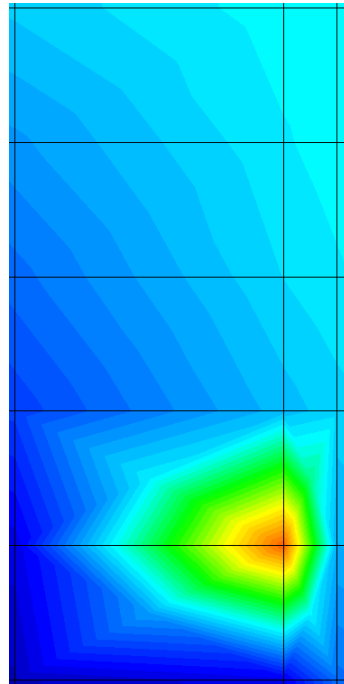
(d6) – pH value after 10 years



(d7) – pH value after 15 years



(d8) – pH value after 30 years



(dd) – Closer view of the pH anomaly below the fracture in figure d8

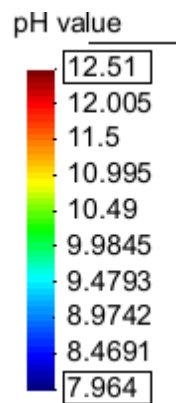
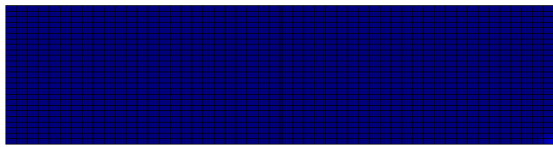
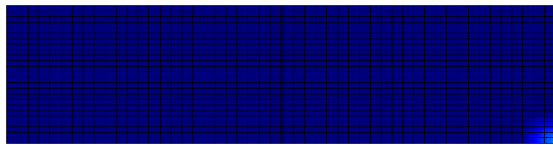


Figure 17.12.1 – Graphical representation of the change in pH value over 100 years.

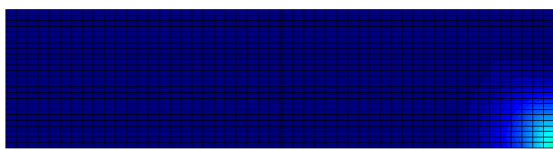
17.13. Case A2



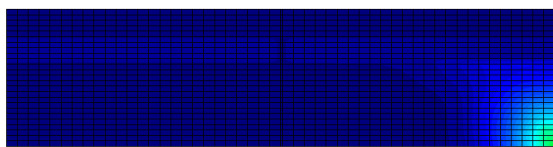
(A1) – pH value after 1 month



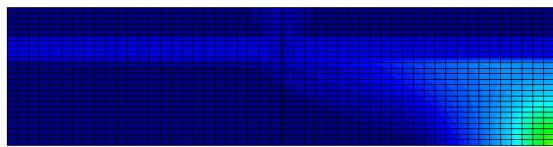
(A2) – pH value after 3 months



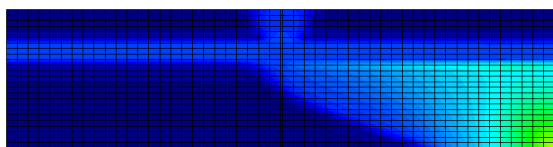
(A3) – pH value after 9 months



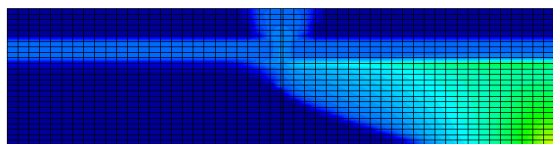
(A4) – pH value after 2 years



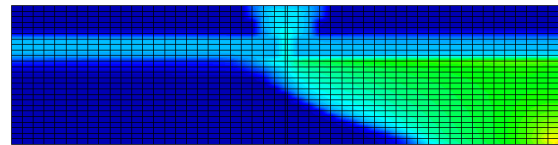
(A5) – pH value after 5 years



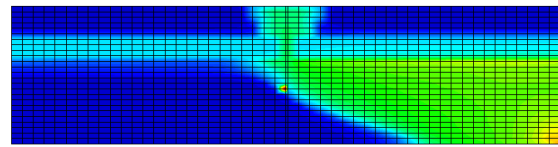
(A6) – pH value after 10 years



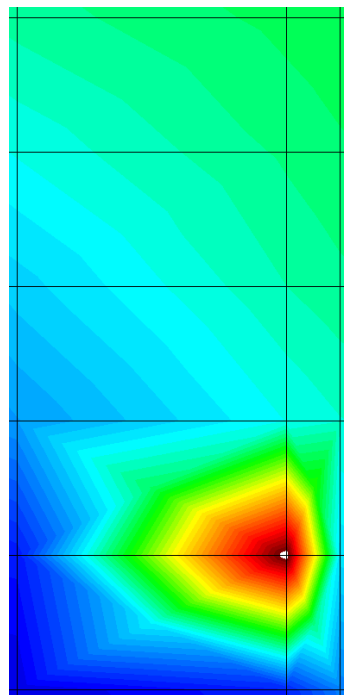
(A7) – pH value after 15 years



(A8) – pH value after 30 years



(A9) – pH value after 47.8 years



(AA) – Closer view of pH point below the fracture in figure A9

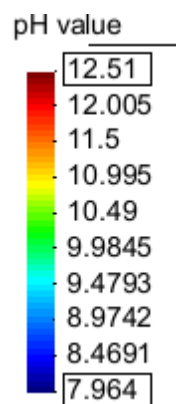
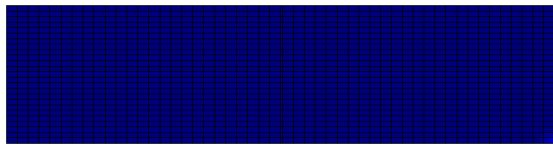
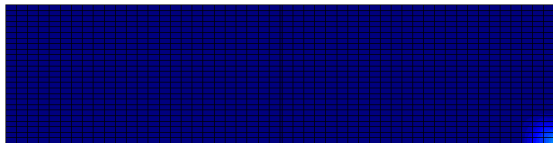


Figure 17.13.1 - Graphical representation of the change in pH value over 100 years.

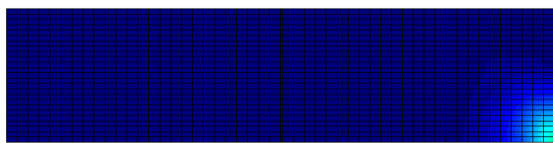
17.14. Case B2



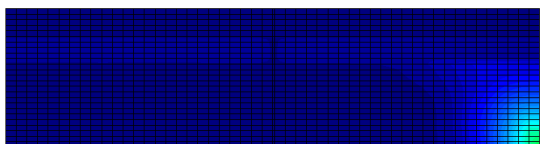
(B1) – pH value after 1 month



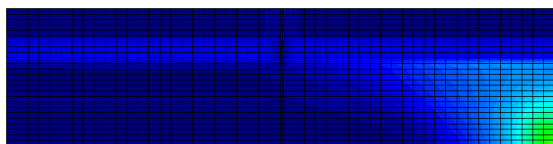
(B2) – pH value after 3 months



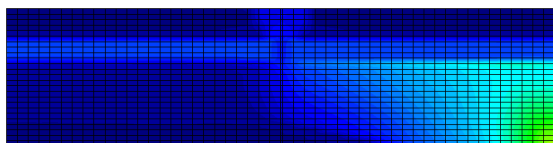
(B3) – pH value after 9 months



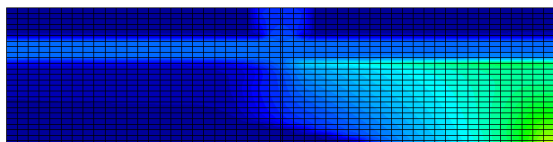
(B4) – pH value after 2 years



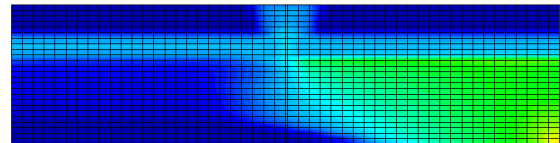
(B5) – pH value after 5 years



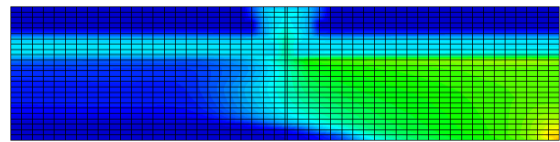
(B6) – pH value after 10 years



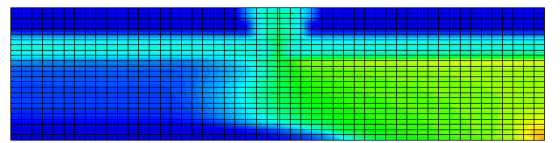
(B7) – pH value after 15 years



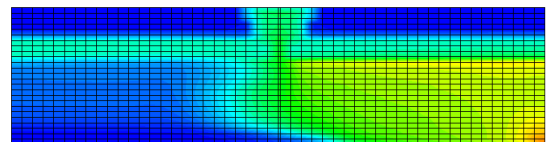
(B8) – pH value after 30 years



(B9) – pH value after 50 years



(B10) – pH value after 75 years



(B11) – pH value after 100 years

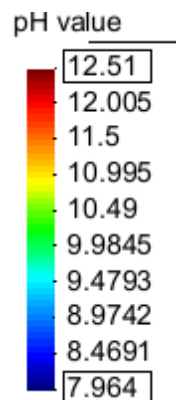
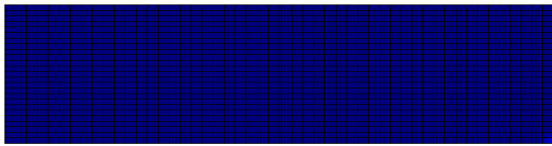
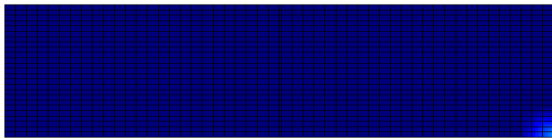


Figure 17.14.1 - Graphical representation of the change in pH value over 100 years.

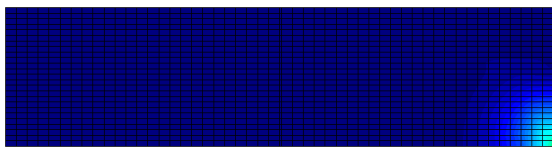
17.15. Case C2



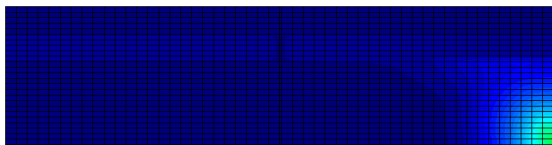
(C1) – pH value after 1 month



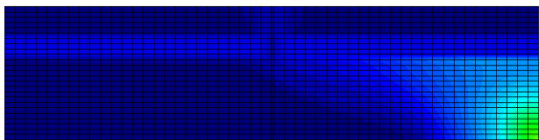
(C2) – pH value after 3 months



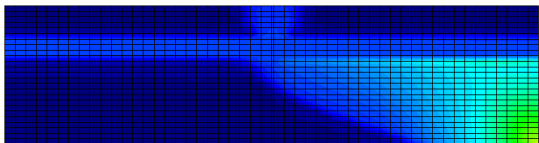
(C3) – pH value after 9 months



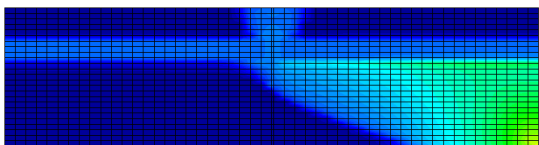
(C4) – pH value after 2 years



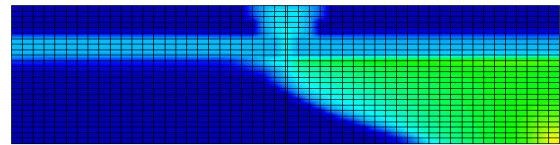
(C5) – pH value after 5 years



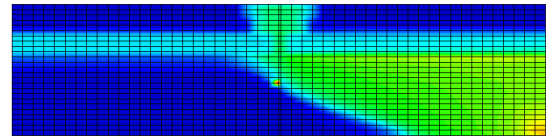
(C6) – pH value after 10 years



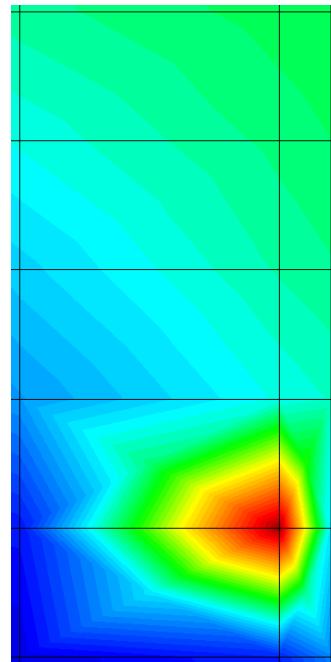
(C7) – pH value after 15 years



(C8) – pH value after 30 years



(C9) – pH value after 50 years



(CC) – Closer view of pH point below the fracture in figure C9

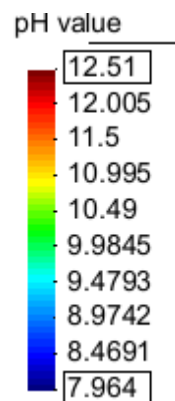
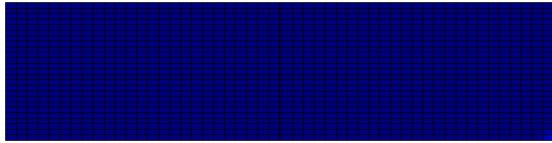
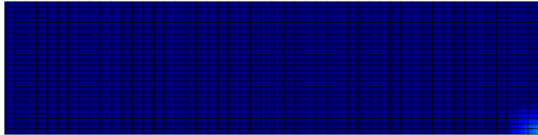


Figure 17.15.1 - Graphical representation of the change in pH value over 100 years.

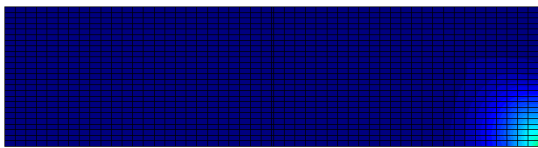
17.16. Case D2



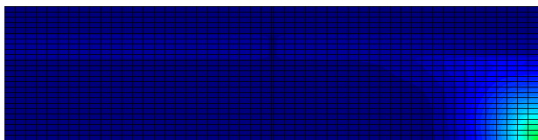
(D1) – pH value after 1 month



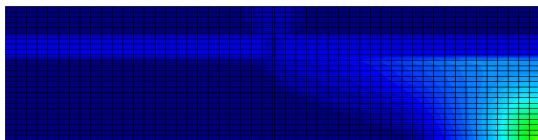
(D2) – pH value after 3 months



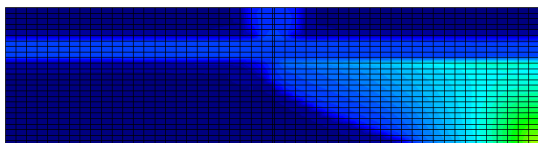
(D3) – pH value after 9 months



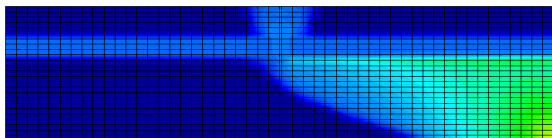
(D4) – pH value after 2 years



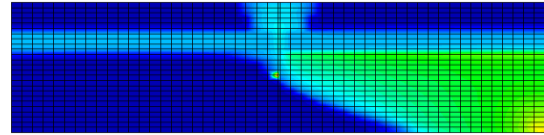
(D5) – pH value after 5 years



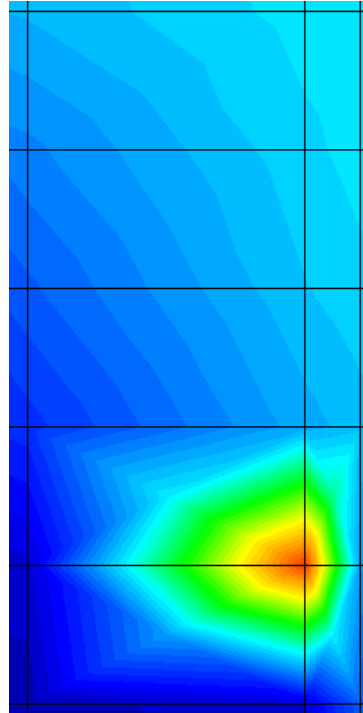
(D6) – pH value after 10 years



(D7) – pH value after 15 years



(D8) – pH value after 30 years



(DD) – Closer view of pH point below the fracture in figure A8

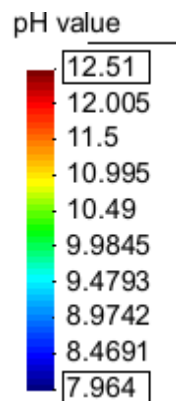
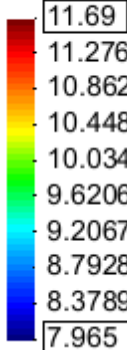
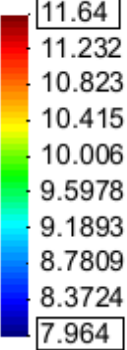
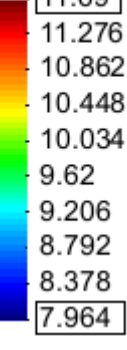
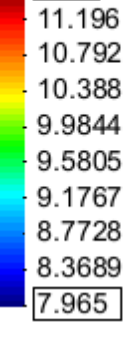
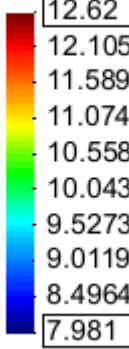
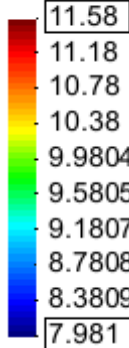
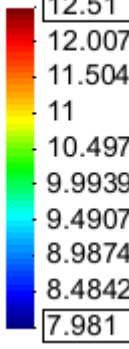
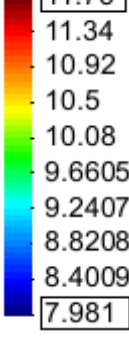


Figure 17.16.1 - Graphical representation of the change in pH value over 100 years.

17.17. pH values

Simulation	pH limits	
Case A	<p>pH value</p>  <p>11.69 11.276 10.862 10.448 10.034 9.6206 9.2067 8.7928 8.3789 7.965</p>	
Case B	<p>pH value</p>  <p>11.64 11.232 10.823 10.415 10.006 9.5978 9.1893 8.7809 8.3724 7.964</p>	
Case C	<p>pH value</p>  <p>11.69 11.276 10.862 10.448 10.034 9.62 9.206 8.792 8.378 7.964</p>	
Case D	<p>pH value</p>  <p>11.6 11.196 10.792 10.388 9.9844 9.5805 9.1767 8.7728 8.3689 7.965</p>	

Simulation	pH limits	
Case A2	<p>pH value</p>  <p>12.62 12.105 11.589 11.074 10.558 10.043 9.5273 9.0119 8.4964 7.981</p>	
Case B2	<p>pH value</p>  <p>11.58 11.18 10.78 10.38 9.9804 9.5805 9.1807 8.7808 8.3809 7.981</p>	
Case C2	<p>pH value</p>  <p>12.51 12.007 11.504 11 10.497 9.9939 9.4907 8.9874 8.4842 7.981</p>	
Case D2	<p>pH value</p>  <p>11.76 11.34 10.92 10.5 10.08 9.6605 9.2407 8.8208 8.4009 7.981</p>	

Appendix III

Change in Porosity

Appendix III contains a range of graphical representations for the porosity changes over 100 years of simulated carbon dioxide injection.

The figures contained in this appendix represent the change in porosity due to precipitation and dissolution

17.18. Case A

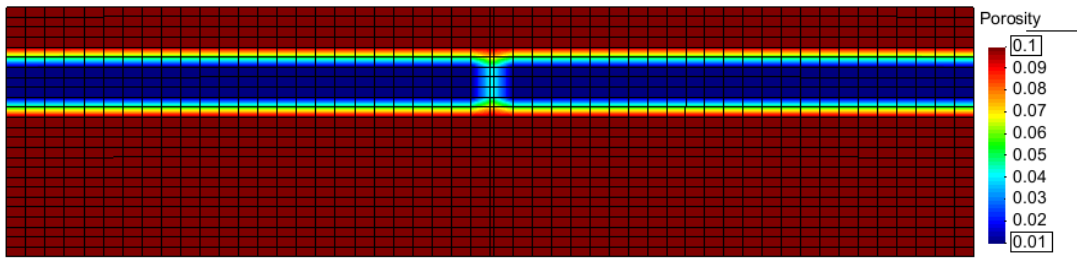


Figure 17.17.1 - Graphical representation of the initial Porosity

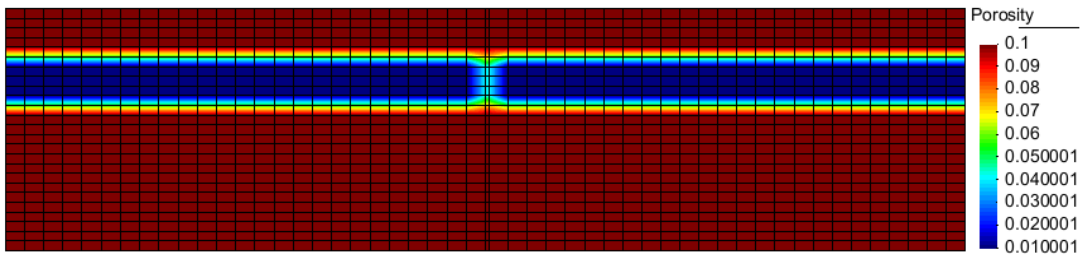
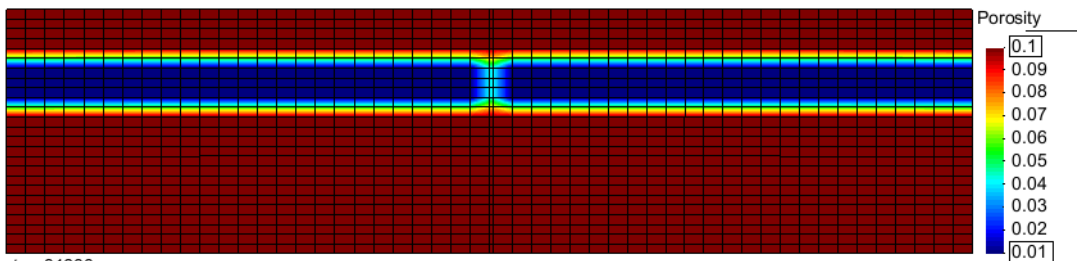


Figure 17.17.2 - Graphical representation of the porosity after 100 years!!!!!!XXX!!!!!!

17.19. Case B



step 31600
 Contour Fill of Porosity.
 Deformation ($\times 1.37715e+6$): Displacements of TIME ANALYSIS, step 31600.

Figure 17.19.1 - Graphical representation of the Initial porosity

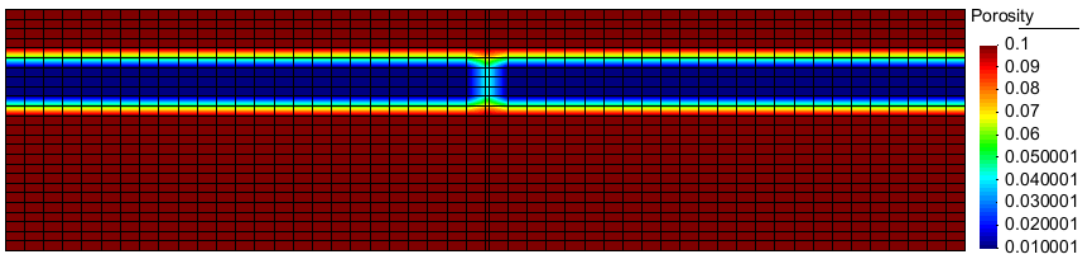


Figure 17.19.2 - Graphical representation of the porosity after 100 years

17.20. Case C

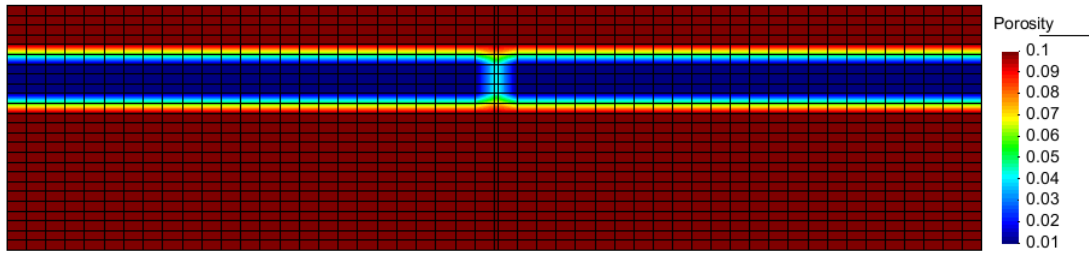


Figure 17.20.1 - Graphical representation of the Initial porosity

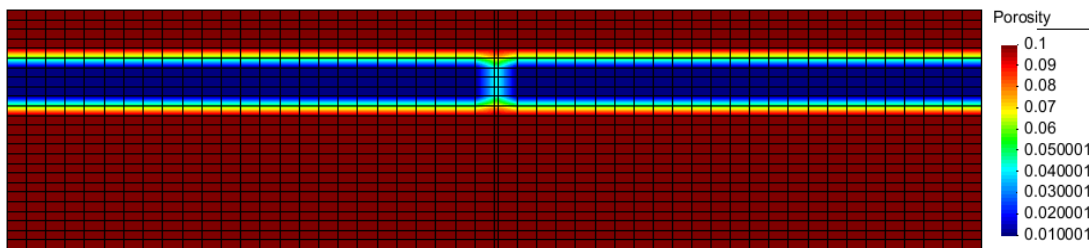


Figure 17.20.2 - Graphical representation of the porosity after 100 years

17.21. Case D

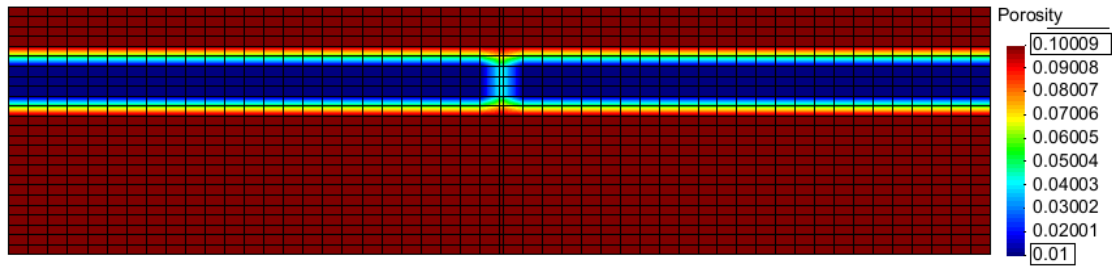


Figure 17.21.1 - Porosity after 30 years

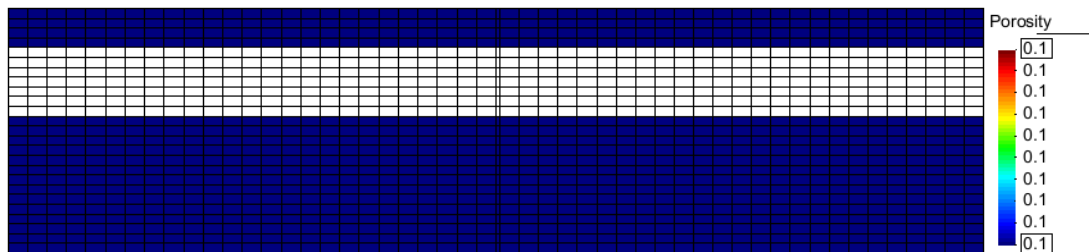


Figure 17.21.2 – Initial porosity

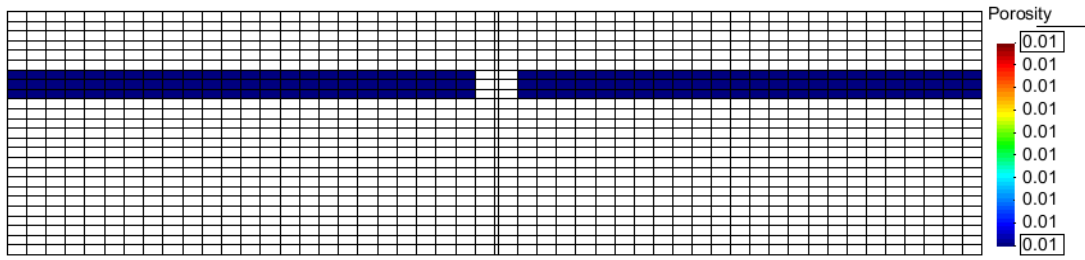
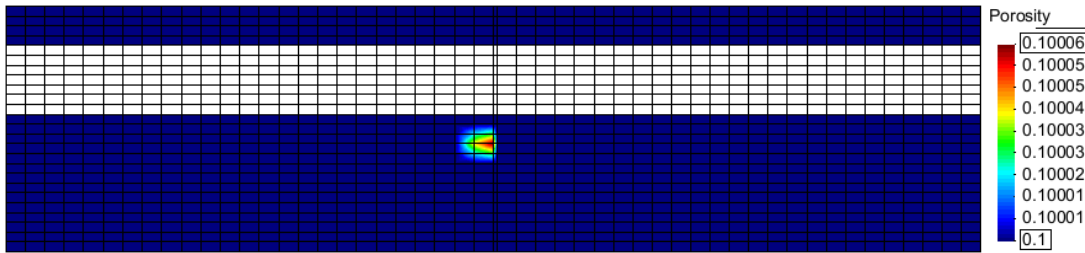
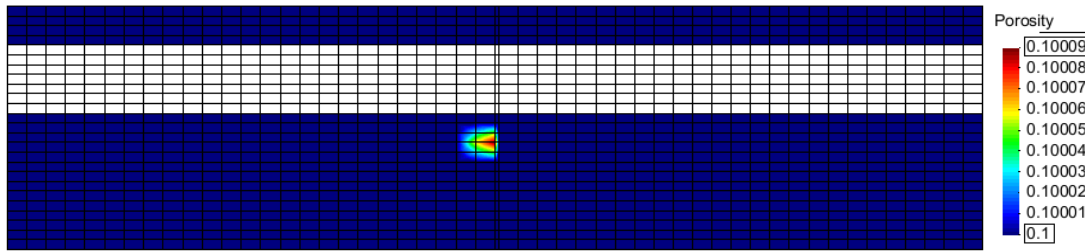


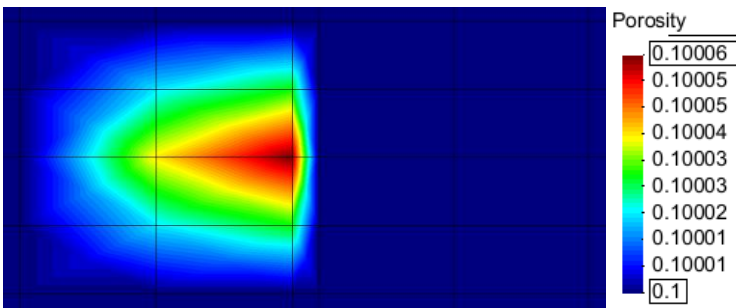
Figure 17.21.3 - porosity after 30 years in the cap rock



porosity after 30 years



porosity after 32,1 years



Close up of the porosity after 30 years

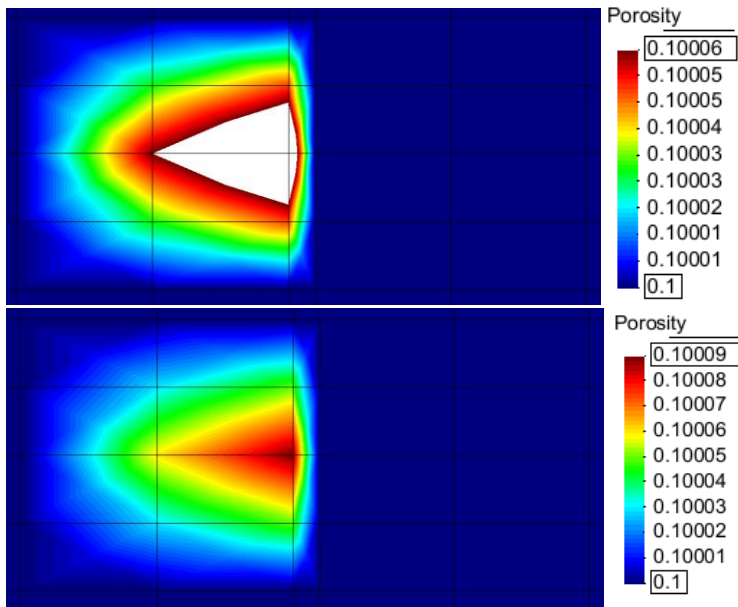


Figure 17.21.4 - Close up of anomaly in figure at 32.1 years

17.22. Case A2

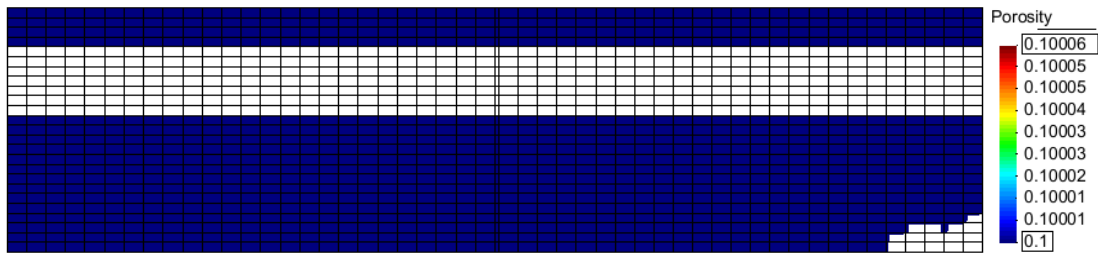


Figure 17.22.1 -Change in porosity after 30 years

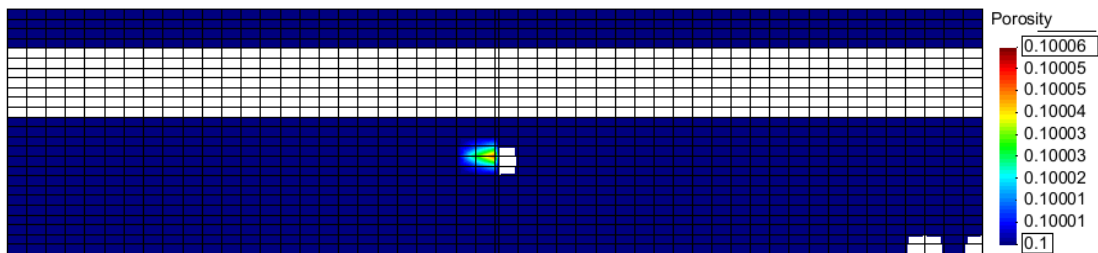


Figure 17.22.2 -Change in porosity after 48,7 years

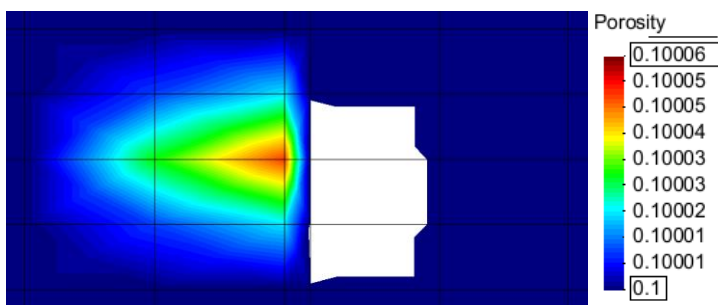


Figure 17.22.3 -Close view of porosity change in figure xxx

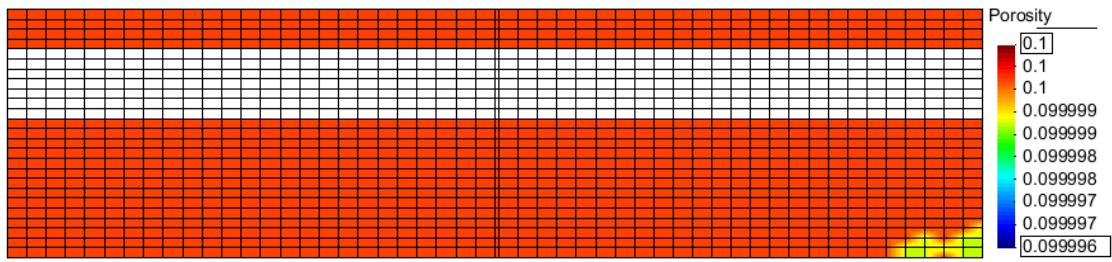


Figure 17.22.4 -Precipitation after 30 years

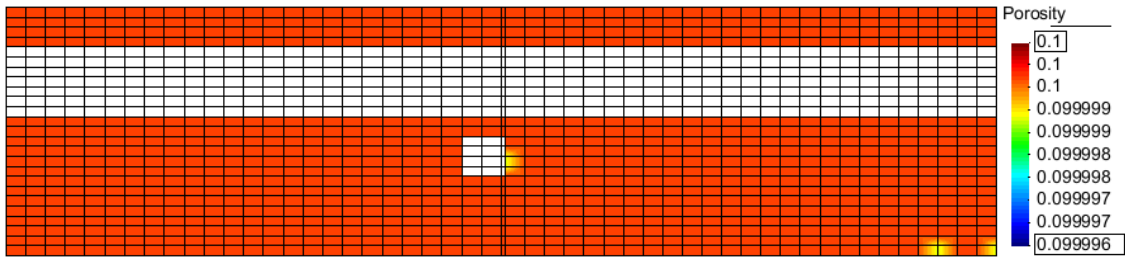


Figure 17.22.5 -Precipitation after 48.7 years

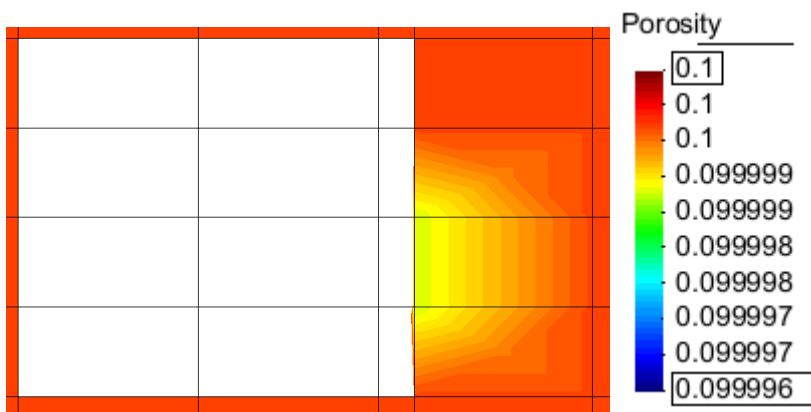


Figure 17.22.6 -Close view of the precipitation after 48.7 years

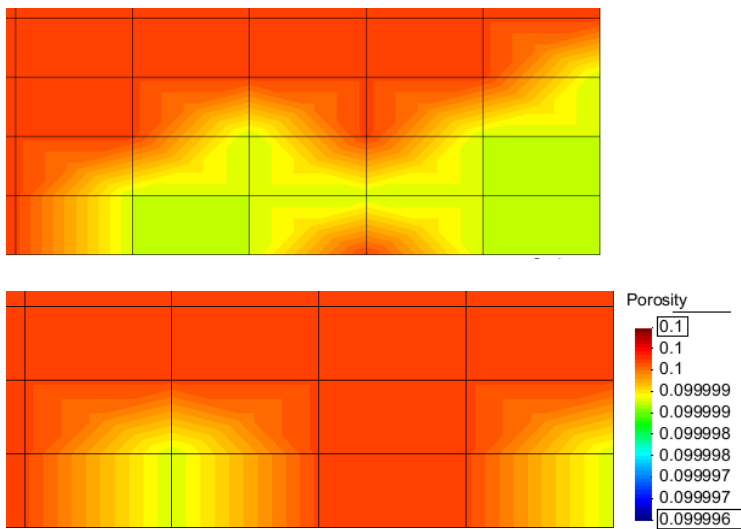
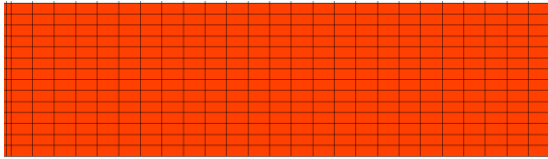
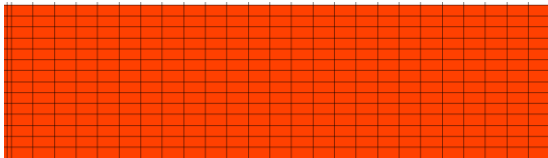


Figure 17.22.7 - view of the precipitation after 48.7 years Close view of

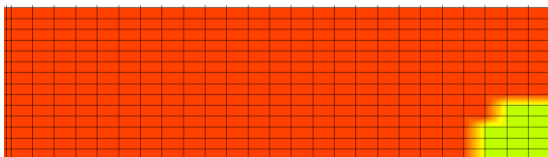
Precipitation timeline



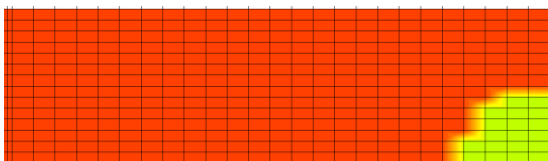
(D1) – Precipitation after 1 month



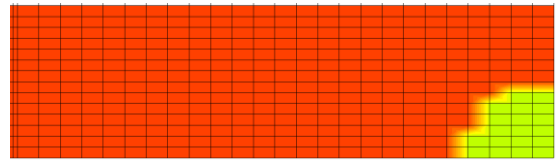
(D2) – Precipitation after 3 months



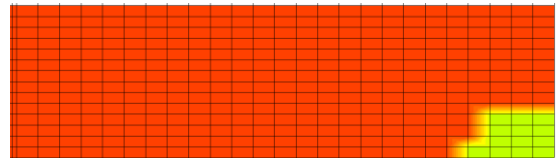
(D3) – Precipitation after 9 months



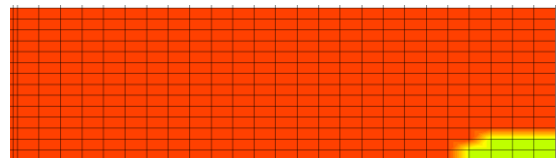
(D4) – Precipitation after 2 years



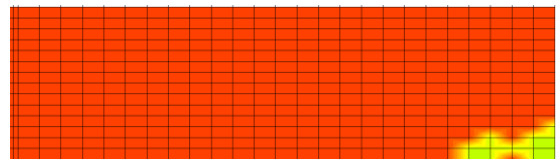
(D5) – Precipitation after 5 years



(D6) – Precipitation after 10 years



(D7) – Precipitation after 15 years



(D8) – Precipitation after 30 years

17.23. Case B2

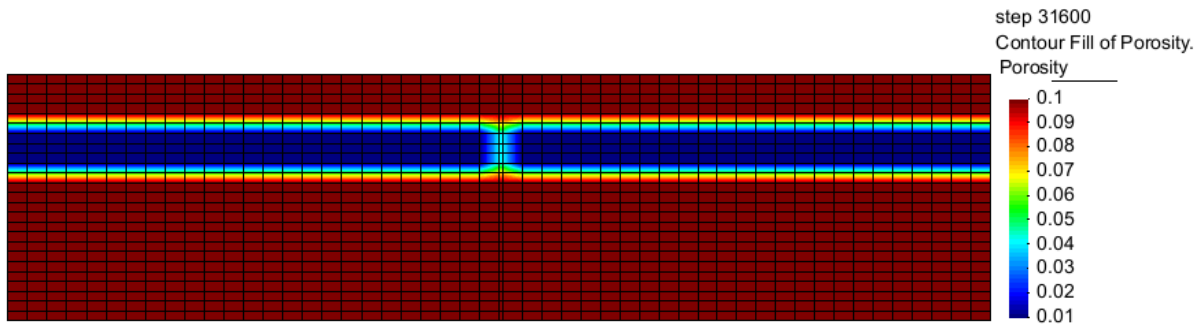


Figure 17.23.1 -Graphical representation of the porosity initial porosity

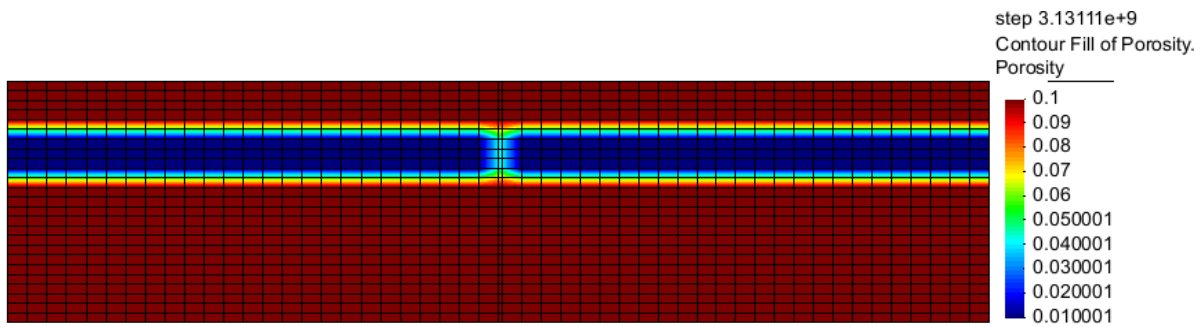


Figure 17.23.2 -Graphical representation of the porosity after 100 years

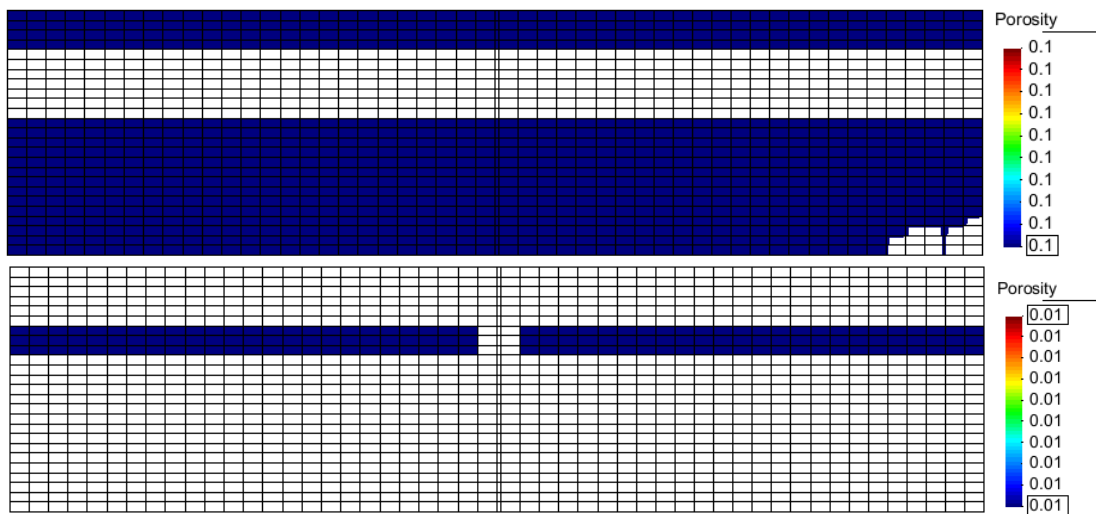
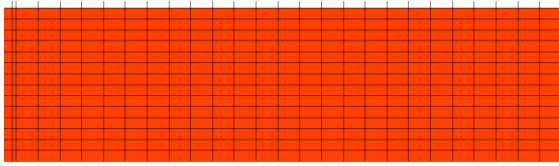
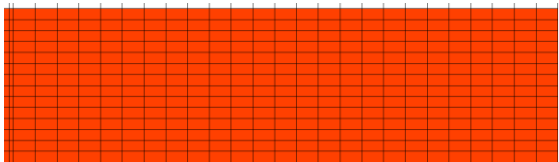


Figure 17.23.3 – Porosity in cap rock after 30 years

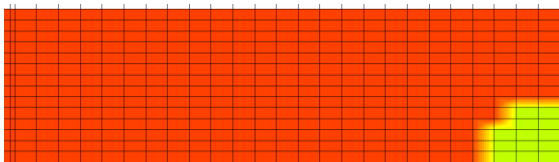
Precipitation timeline



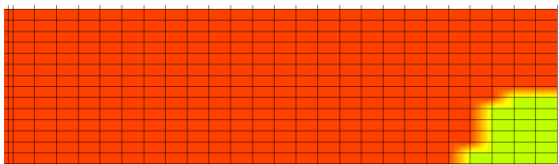
(C1) – Precipitation after 1 month



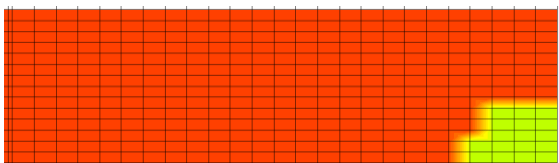
(C2) – Precipitation after 3 months



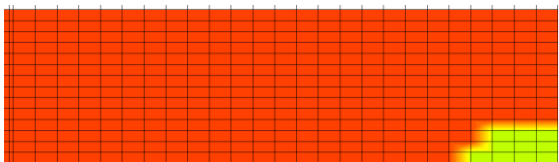
(C3) – Precipitation after 9 months



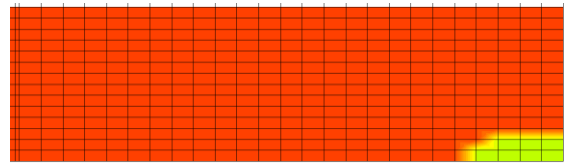
(C4) – Precipitation after 2 years



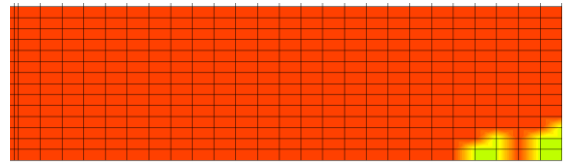
(C5) – Precipitation after 5 years



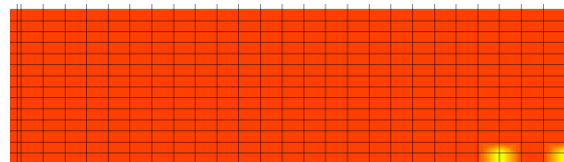
(C6) – Precipitation after 10 years



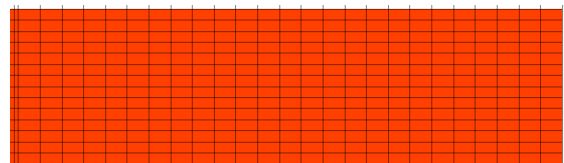
(C7) – Precipitation after 15 years



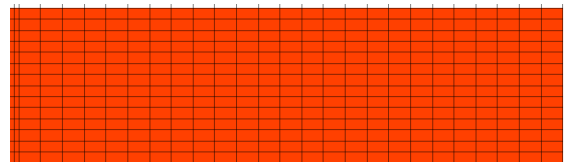
(C8) – Precipitation after 30 years



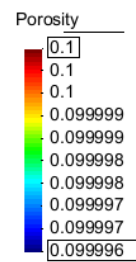
(C9) – Precipitation after 50 years



(C10) – Precipitation after 75 years



(C11) – Precipitation after 100 years



17.24. Case C2

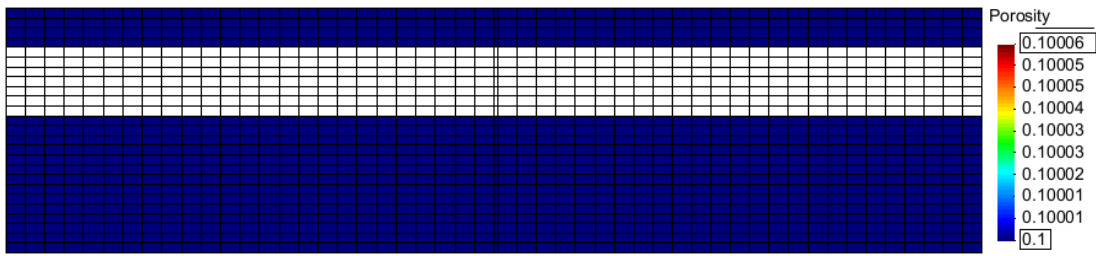


Figure 17.24.1 – Initial Porosity

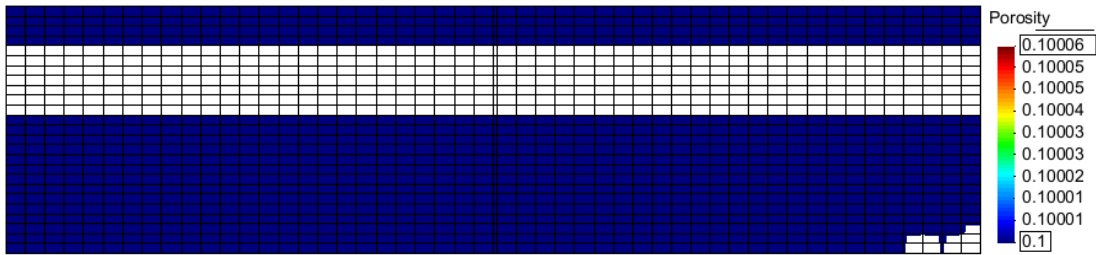


Figure 17.24.2 – Porosity after 30 years

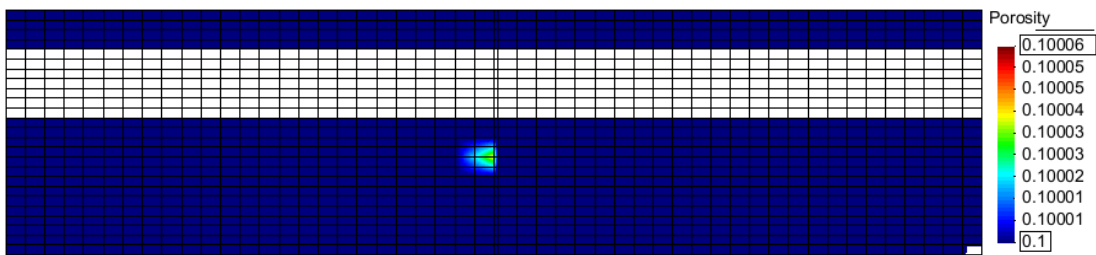


Figure 17.24.3 – Porosity after 50 years

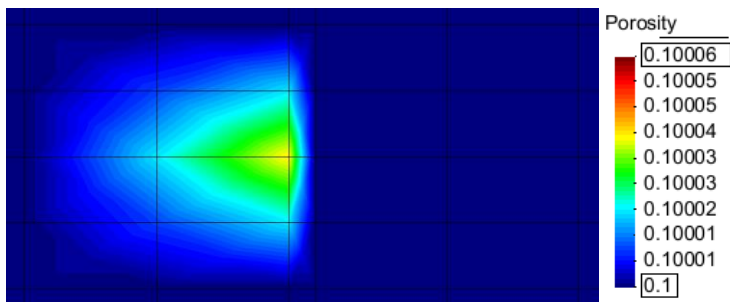


Figure 17.24.4 -Close up of the porosity at 50 years

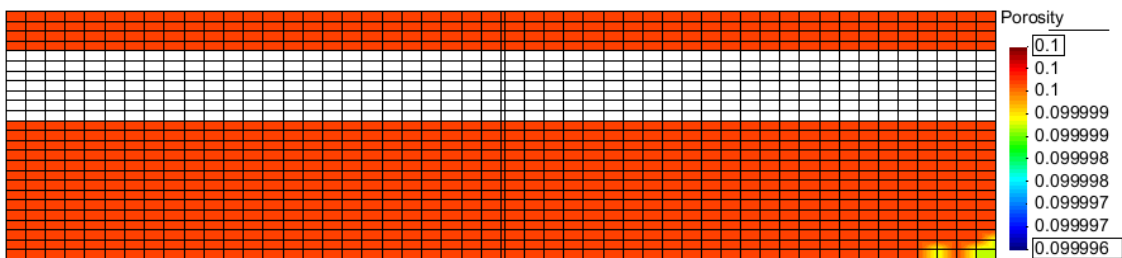


Figure 17.24.5 – Precipitations after 30 years

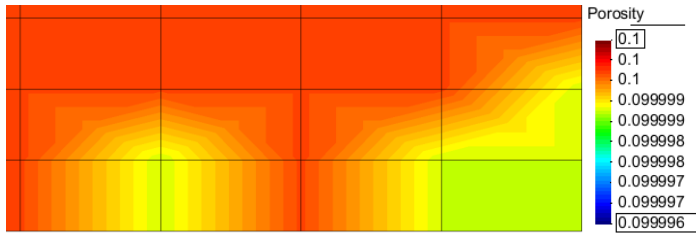


Figure 17.24.6 - (C1) – Close up of the precipitation after 30

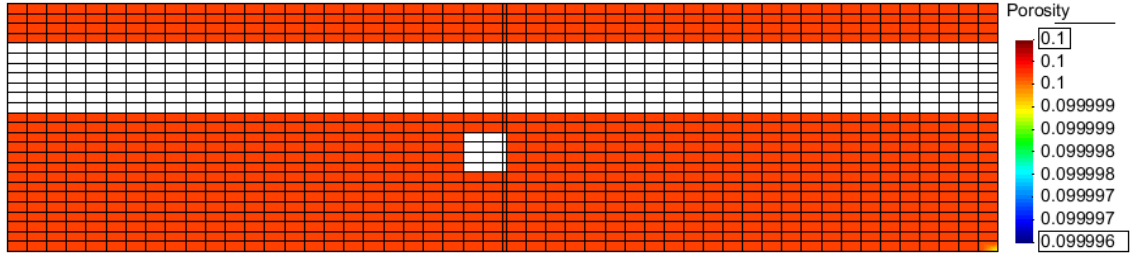


Figure 17.24.7 - (C1) – Precipitation after 50 years

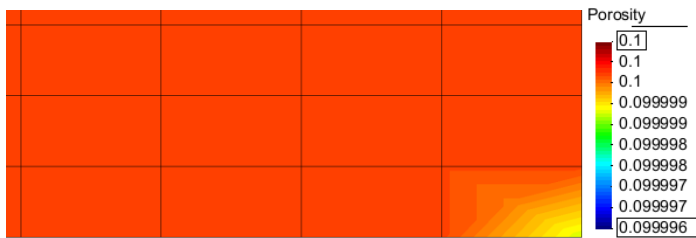
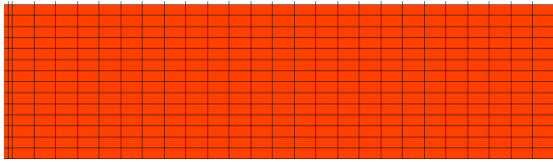
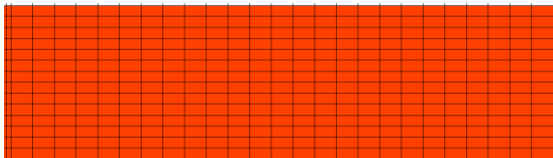


Figure 17.24.8 - (C1) – Close up of precipitations after 50 years

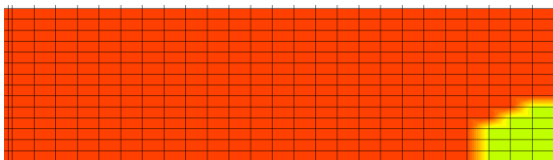
Precipitation timeline



(C1) – Precipitation after 1



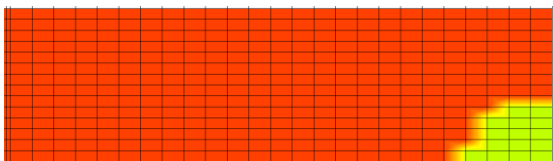
(C1) – Precipitation after 3



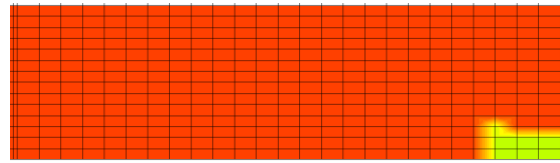
(C1) – Precipitation after 9



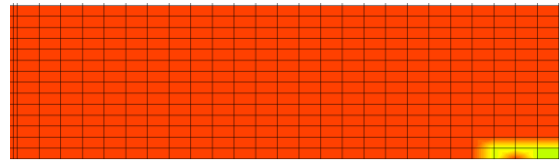
(C1) – Precipitation after 2



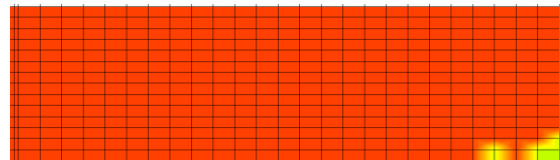
(C1) – Precipitation after 5



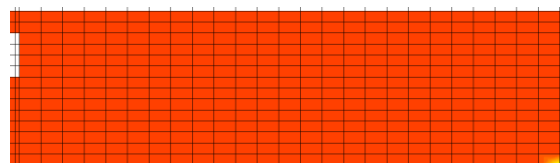
(C1) – Precipitation after 10



(C1) – Precipitation after 15



(C1) – Precipitation after 30



(C1) – Precipitation after 50

17.25. Case D2

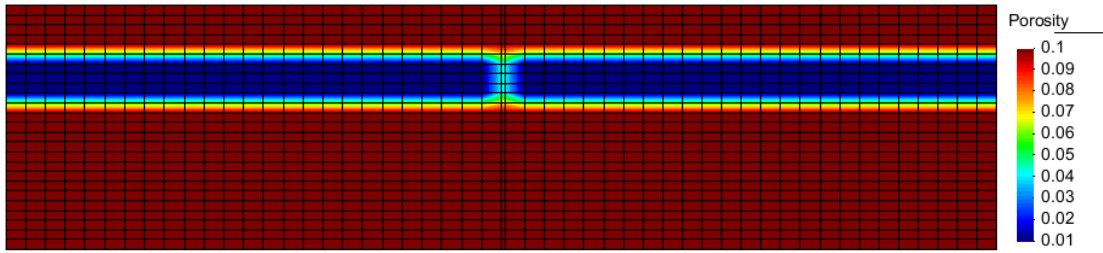


Figure 17.25.1 - Graphical representation of the initial porosity with automatic limits

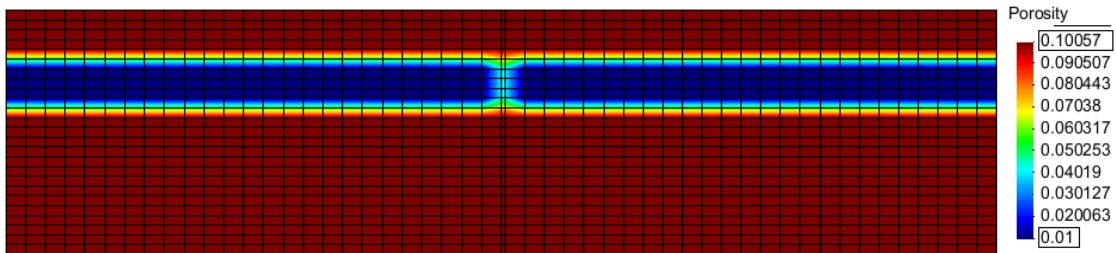


Figure 17.25.2 - Graphical representation of the porosity after 30 years

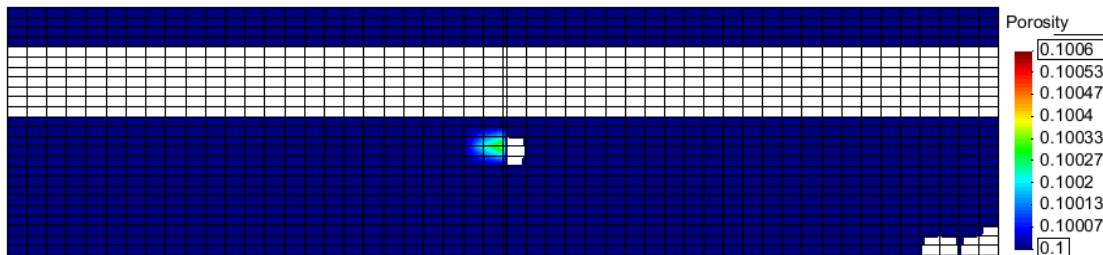


Figure 17.25.3 - Graphical representation of the porosity after 30 years

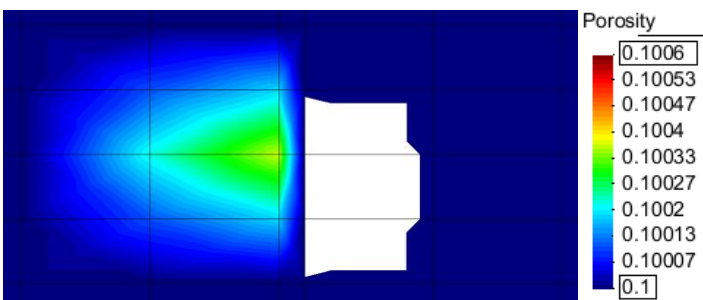


Figure 17.25.4 - Graphical representation of the porosity after 30 years

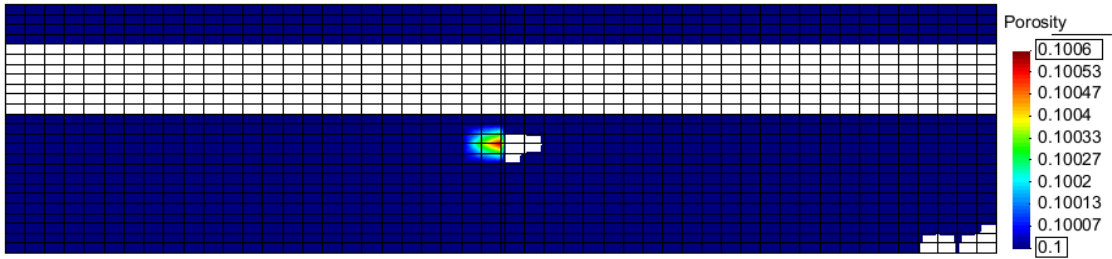


Figure 17.25.5 - Graphical representation of the porosity after 33 years

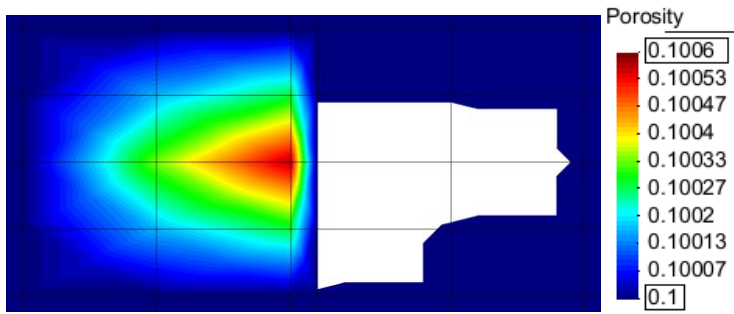
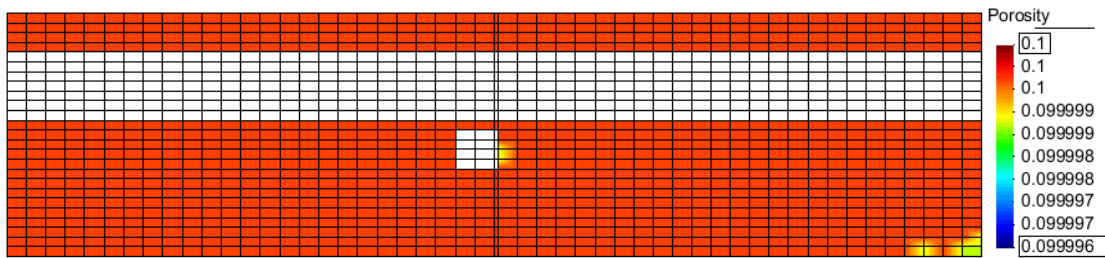
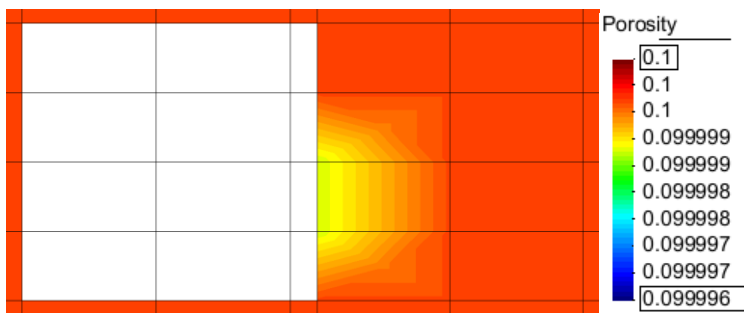


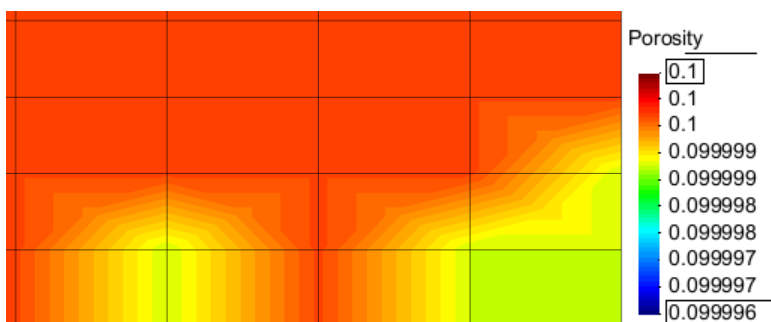
Figure 17.25.6 – Close view of the graphical representation of the porosity after 33 years



30



Close 30



Close 30 -2

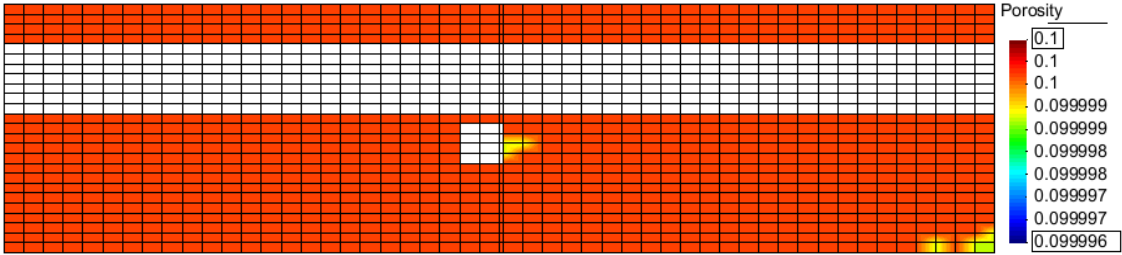


Figure 17.25.7 -(C1) – Precipitation after 33

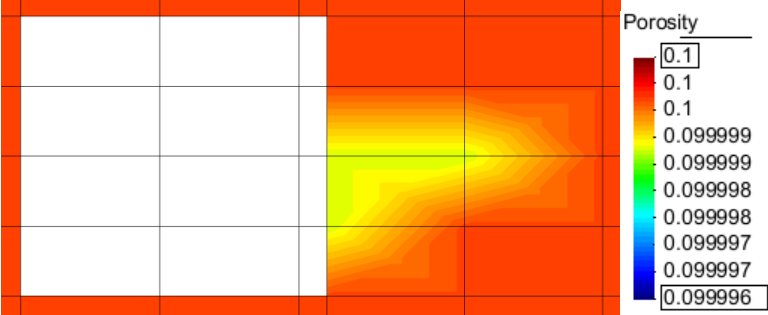
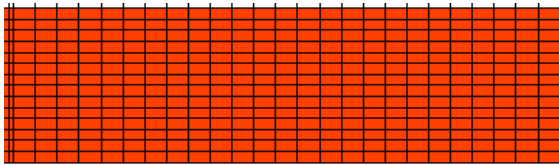
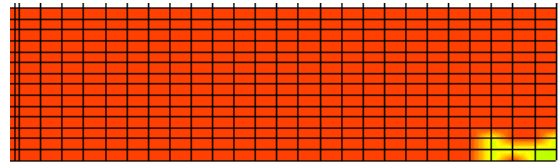


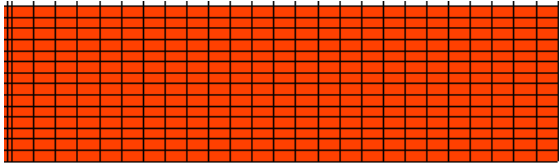
Figure 17.25.8 - Precipitation after Close 33



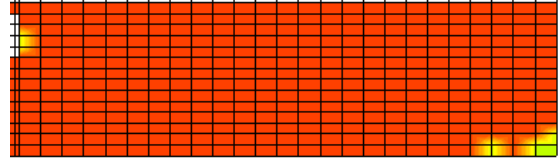
Precipitation after 1 month



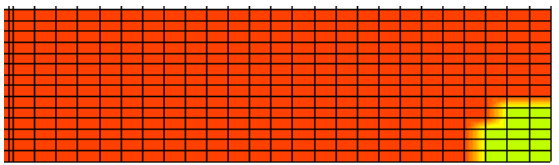
(D) – Precipitation after 15 years



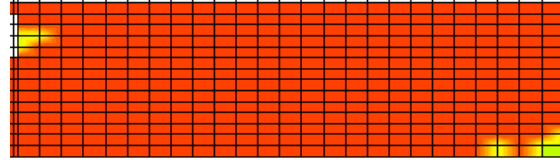
(C1) – Precipitation after 3 months



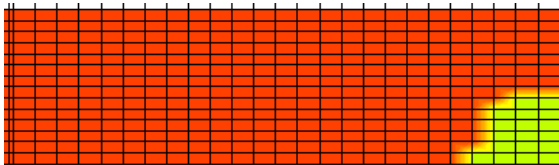
(C1) – Precipitation after 30 years



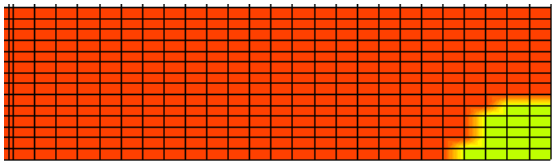
(C1) – Precipitation after 9 months



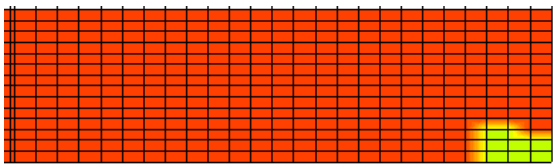
(C1) – Precipitation after 33 years



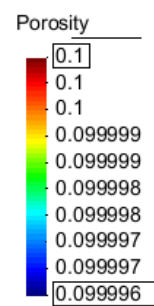
(C1) – Precipitation after 2 years



(C1) – Precipitation after 5 years



(C1) – Precipitation after 10 years



Appendix IV

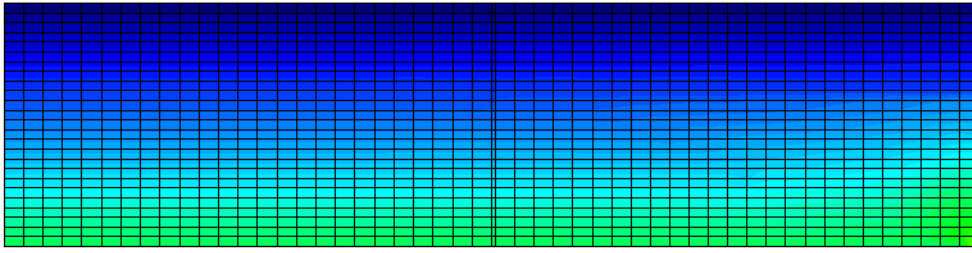
Gas Pressure

Appendix IV contains a range of graphical representations for the gas pressures in the two first years of the simulated carbon dioxide injection. There are a total of 8 cases or runs with a maximum of 11 images representing the respective times of injection. However, some cases are incomplete with respect to total simulation time and images. This is due to convergence problems.

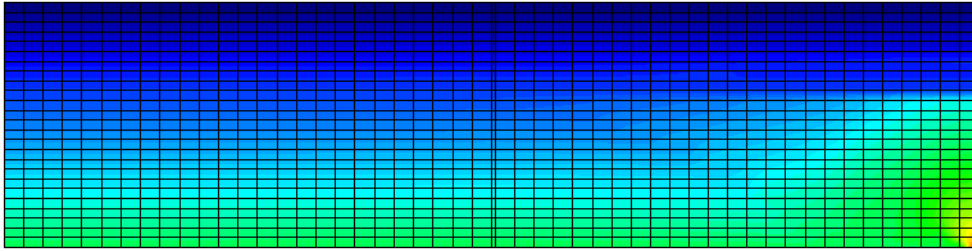
Each set of images have their respective gradient color indicator which illustrates the saturation condition at any given time and position. The higher limit is always 15.0 MPa and the lower limit is 9.5 MPa. These values are chosen based on the settling values after the gas breakthrough and to obtain a decent graphical representation at high pressures.

Some figures contain a white spot in the injection corner. White spots represent areas which contain pressures outside the defined color interval. These pressures are better described in Appendix VI – Carbon dioxide breakthrough.

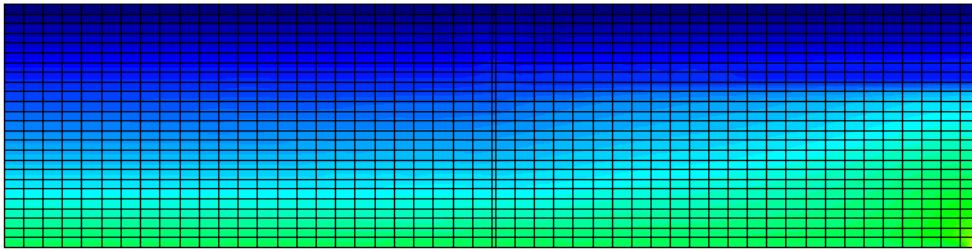
17.26. Case A



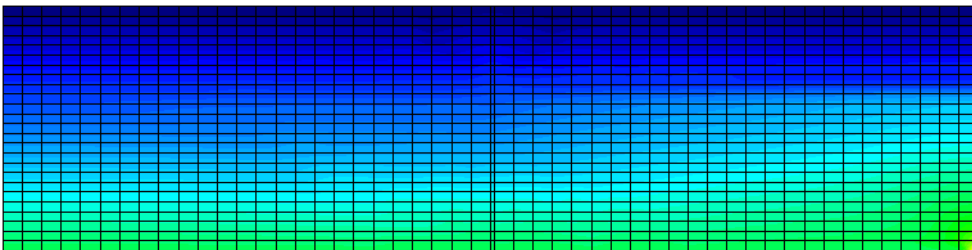
(a1) – Gas pressure after 1 month



(a2) – Gas pressure after 3 months



(a3) – Gas pressure after 9 months



(a4) – Gas pressure after 2 years

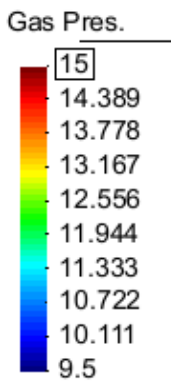
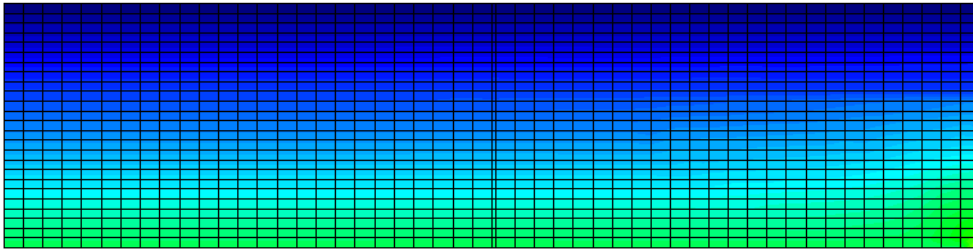
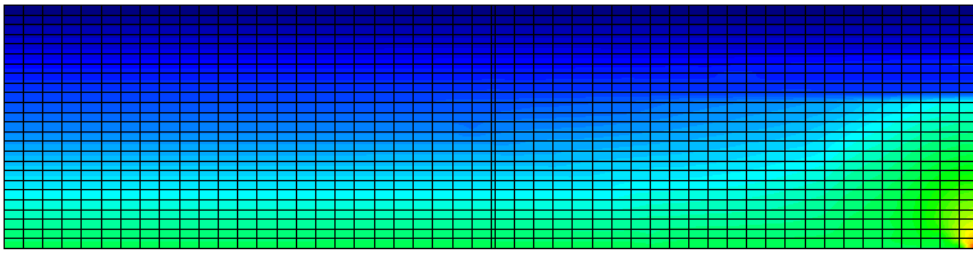


Figure 17.25.1 - Graphical representation of the change in gas pressure over 2 years.

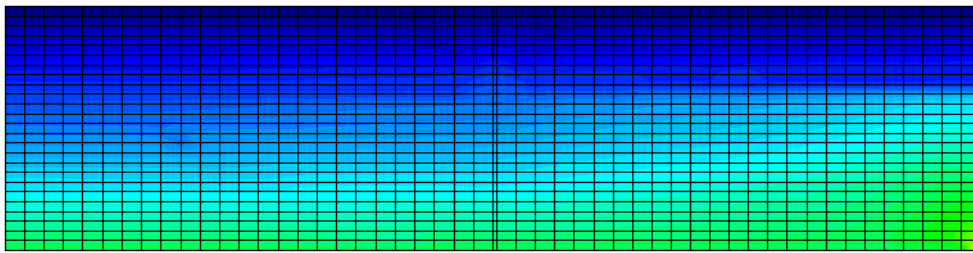
17.27. Case B



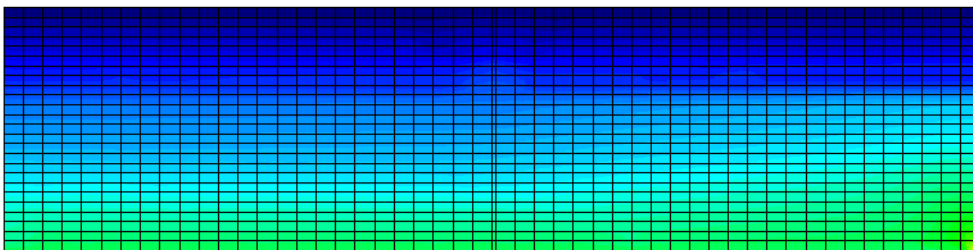
(b1) – Gas pressure after 1 month



(b2) – Gas pressure after 3 months



(b3) – Gas pressure after 9 months



(b4) – Gas pressure after 2 years

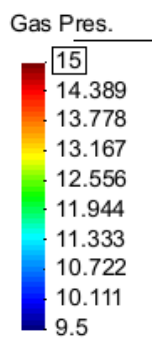
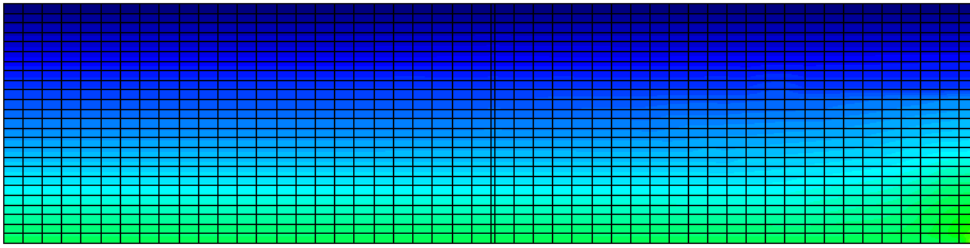
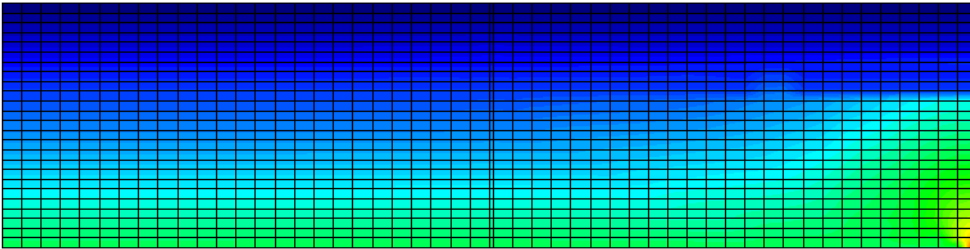


Figure 17.27.1 - Graphical representation of the change in gas pressure over 2 years.

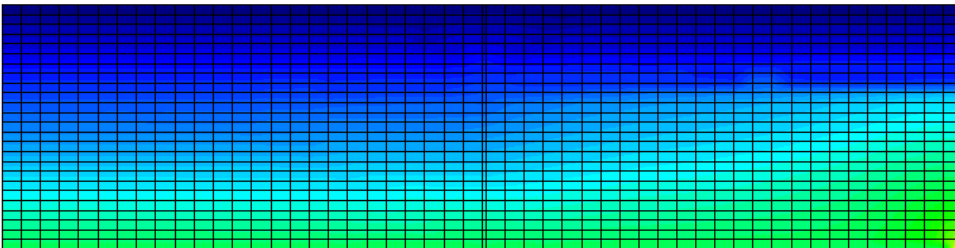
17.28. Case C



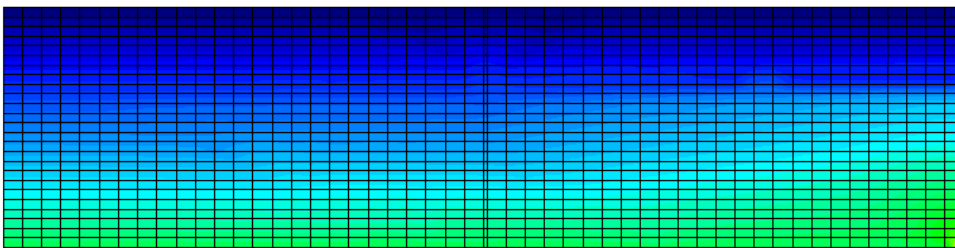
(c1) – Gas pressure after 1 month



(c2) – Gas pressure after 3 months



(c3) – Gas pressure after 9 months



(c4) – Gas pressure after 2 years

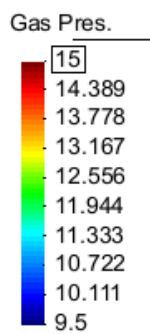
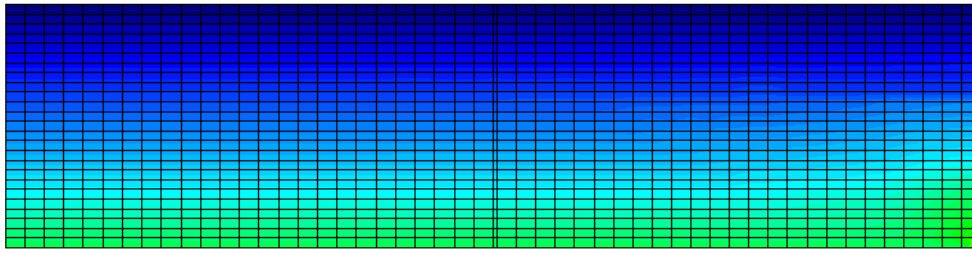
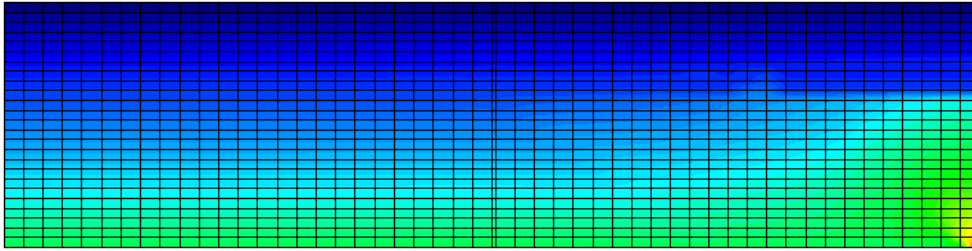


Figure 17.28.1 - Graphical representation of the change in gas pressure over 2 years.

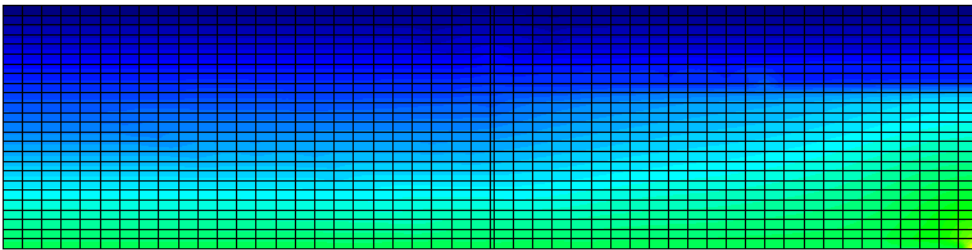
17.29. Case D



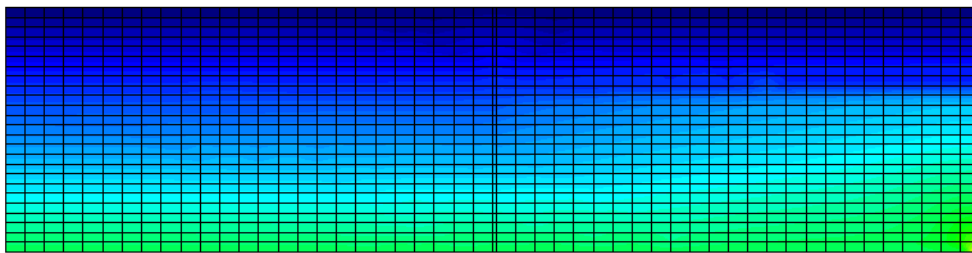
(d1) – Gas pressure after 1 month



(d2) – Gas pressure after 3 months



(d3) – Gas pressure after 9 months



(d4) – Gas pressure after 2 years

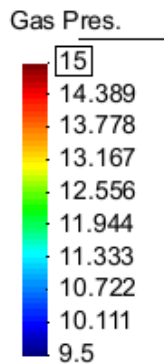
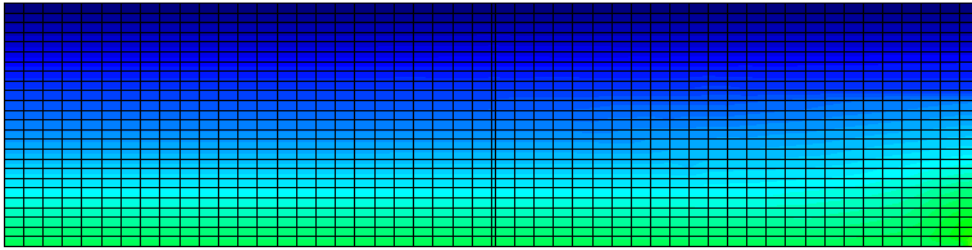
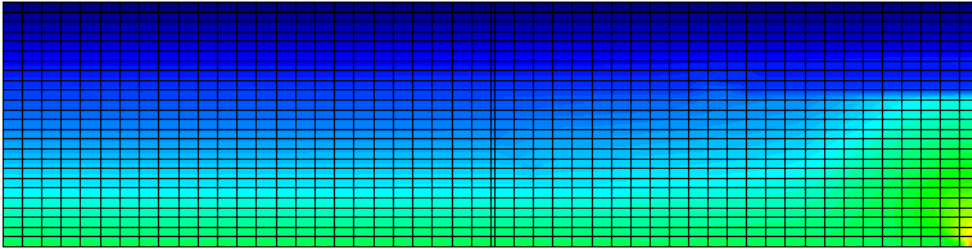


Figure 17.29.1 - Graphical representation of the change in gas pressure over 2 years.

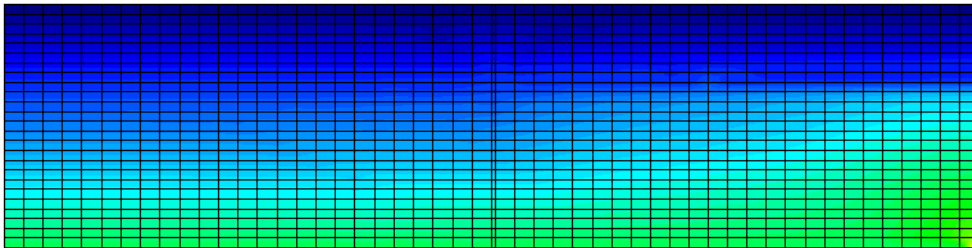
17.30. Case A2



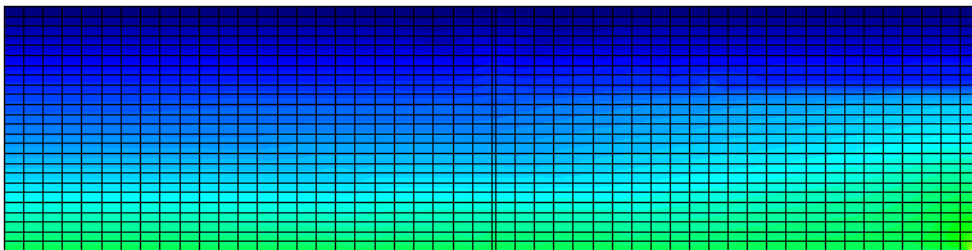
(A1) – Gas pressure after 1 month



(A2) – Gas pressure after 3 months



(A3) – Gas pressure after 9 months



(A4) – Gas pressure after 2 years

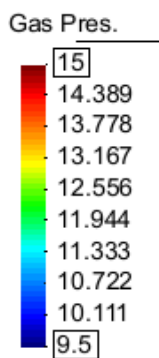
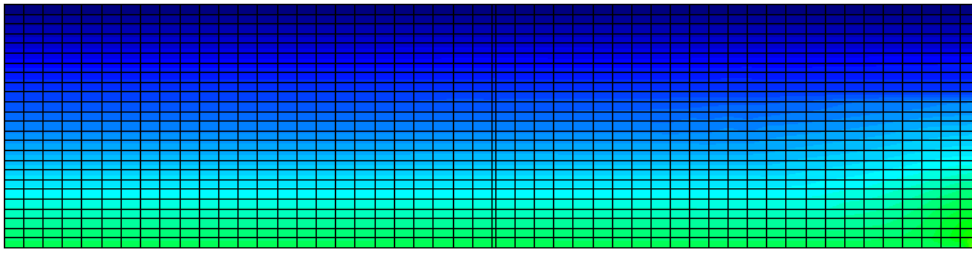
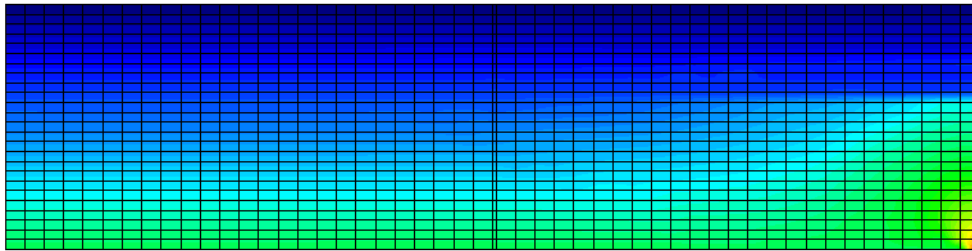


Figure 17.30.1 - Graphical representation of the change in gas pressure over 2 years.

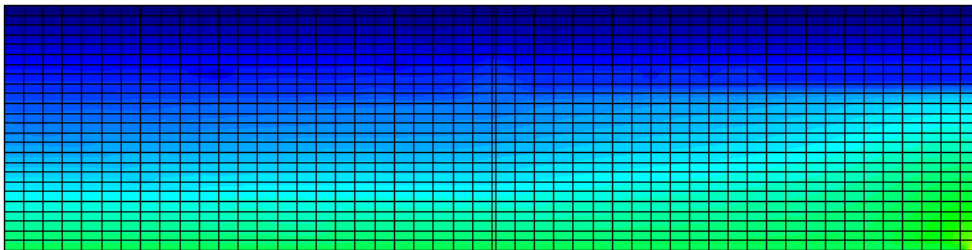
17.31. Case B2



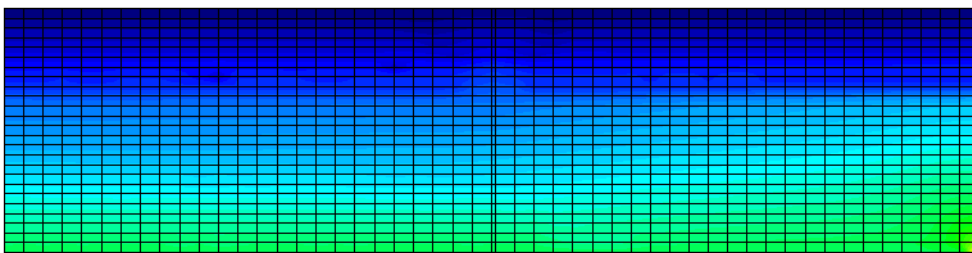
(B1) – Gas pressure after 1 month



(B2) – Gas pressure after 3 months



(B3) – Gas pressure after 9 months



(B4) – Gas pressure after 2 years

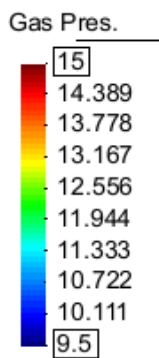
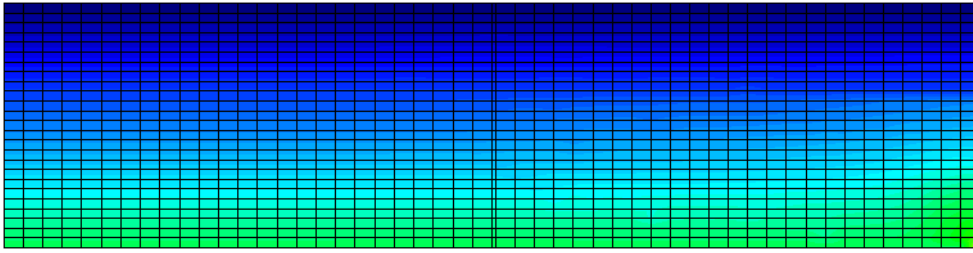
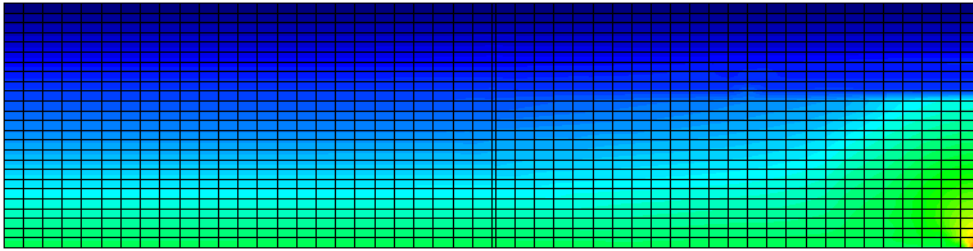


Figure 17.31.1 - Graphical representation of the change in gas pressure over 2 years.

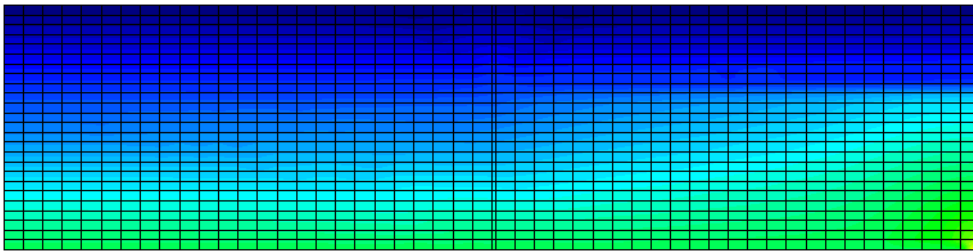
17.32. Case C2



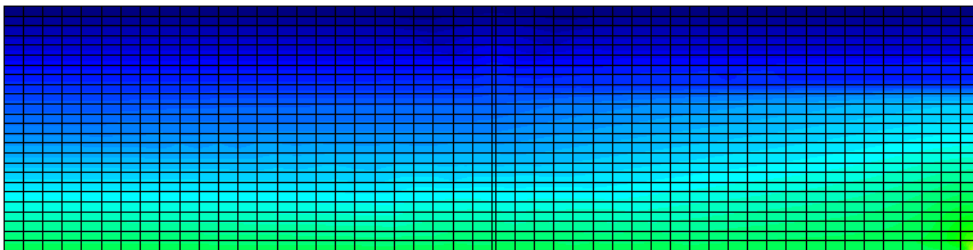
(C1) – Gas pressure after 1 month



(C2) – Gas pressure after 3 months



(C3) – Gas pressure after 9 months



(C4) – Gas pressure after 2 years

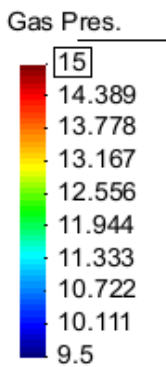
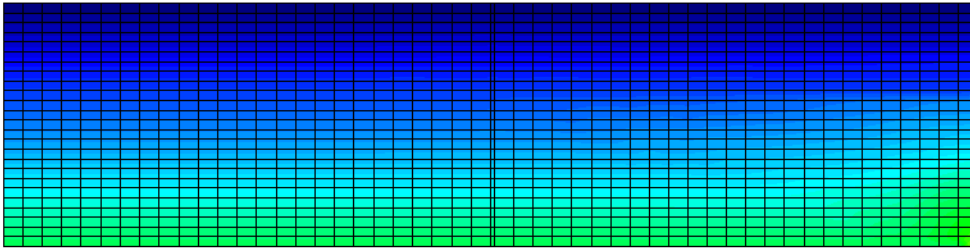
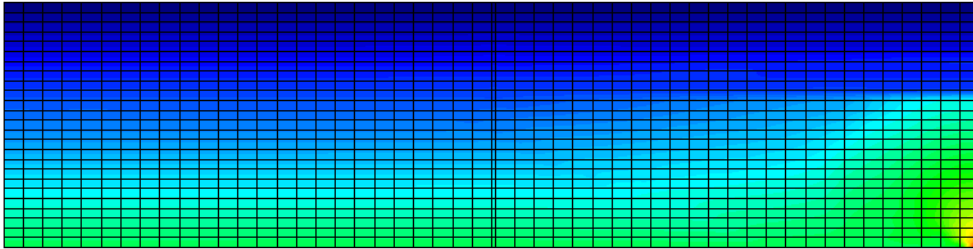


Figure 17.32.1 - Graphical representation of the change in gas pressure over 2 years.

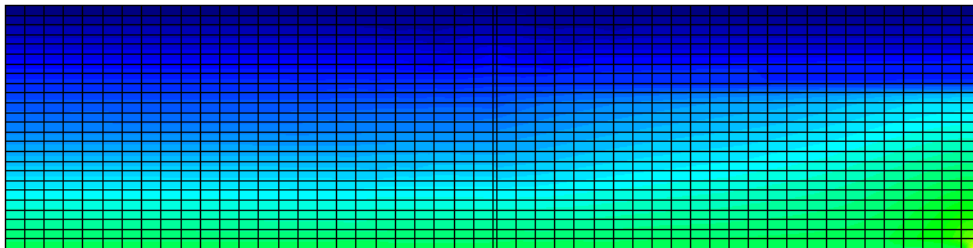
17.33. Case D2



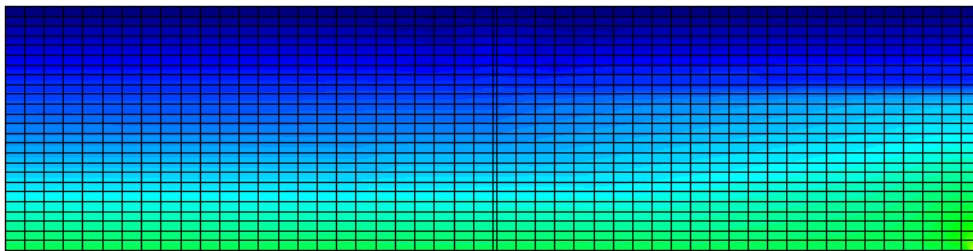
(D1) – Gas pressure after 1 month



(D2) – Gas pressure after 3 months



(D3) – Gas pressure after 9 months



(D4) – Gas pressure after 2 years

Gas Pres.

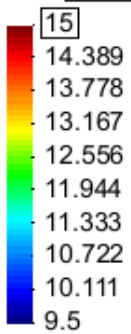


Figure 17.33.1 - Graphical representation of the change in gas pressure over 2 years.

Appendix V

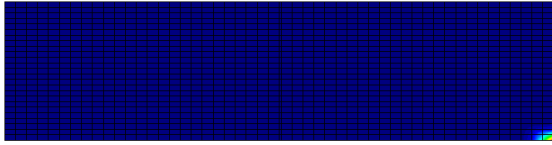
|Gas Phase Flux|

Appendix V contains a range of graphical representations for the net gas phase flux thorough a 100 years of simulated carbon dioxide injection. There are a total of 8 cases or runs with a maximum of 11 images representing the respective times of injection. However, some cases are incomplete with respect to total simulation time and images. This is due to convergence problems.

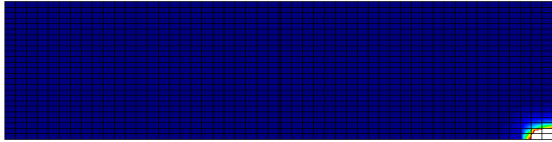
Each set of images have their respective gradient color indicator which illustrates the saturation condition at any given time and position. The higher limit is always 0.0102 and the lower limit 0.0.

Where possible, the last time-step in each case, is appended with an enlarged image of the respective flux in the fracture region.

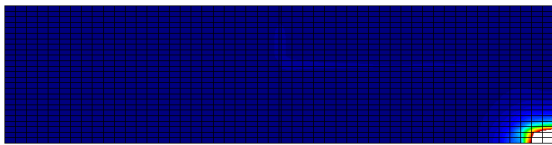
17.34. Case A



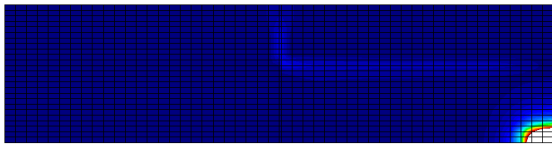
(a1) – Gas Phase flux after 1 month



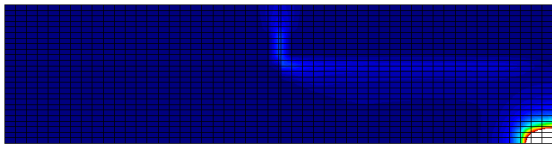
(a2) Gas Phase flux after 3 months



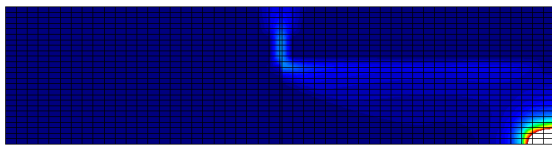
(a3) – Gas Phase flux after 9 months



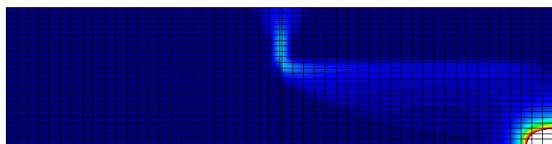
(a4) – Gas Phase flux after 2 years



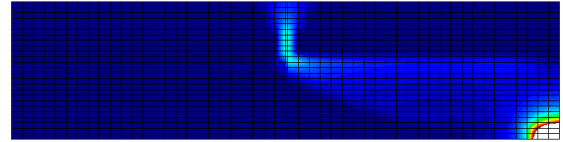
(a5) – Gas Phase flux after 5 years



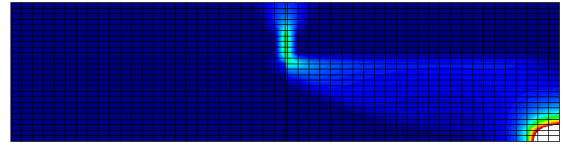
(a6) – Gas Phase flux after 10 years



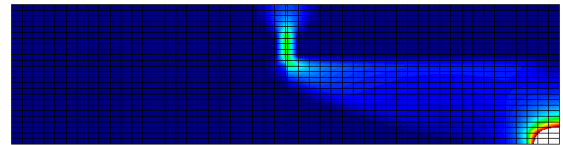
(a7) – Gas Phase flux after 15 years



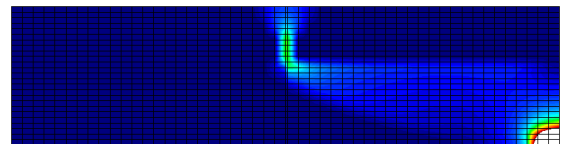
(a8) – Gas Phase flux after 30 years



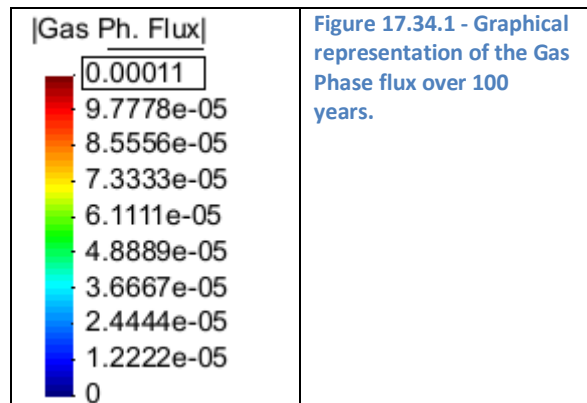
(a9) – Gas Phase flux after 50 years



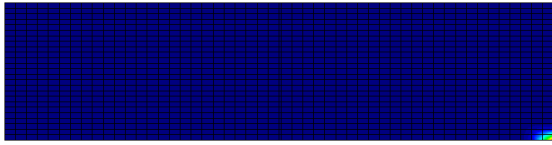
(a10) – Gas Phase flux after 75 years



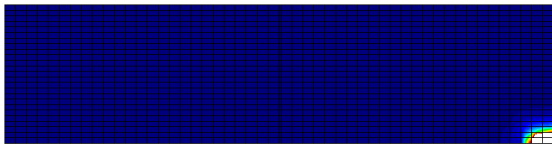
(a11) – Gas Phase flux after 100 years



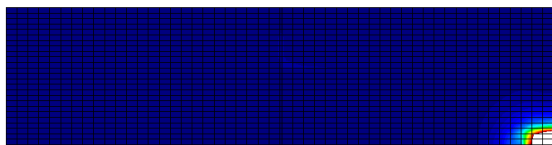
17.35. Run B



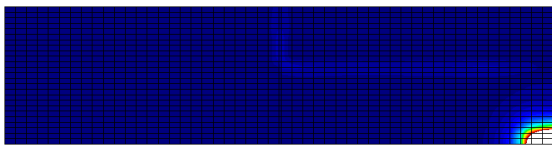
(b1) – Gas Phase flux after 1 month



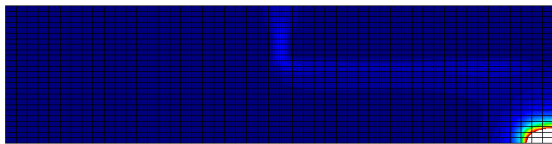
(b2) Gas Phase flux after 3 months



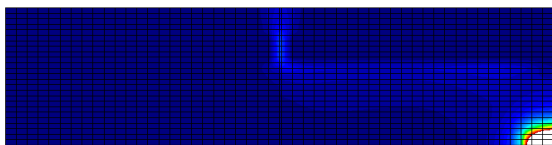
(b3) – Gas Phase flux after 9 months



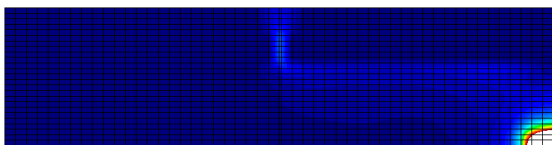
(b4) – Gas Phase flux after 2 years



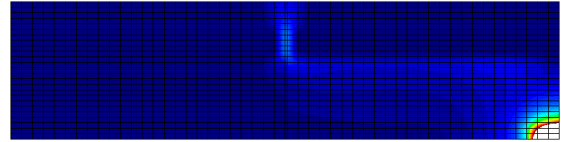
(b5) – Gas Phase flux after 5 years



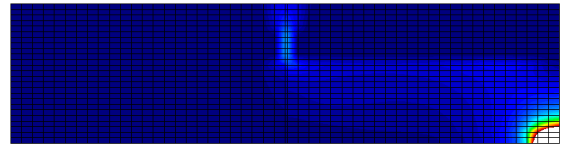
(b6) – Gas Phase flux after 10 years



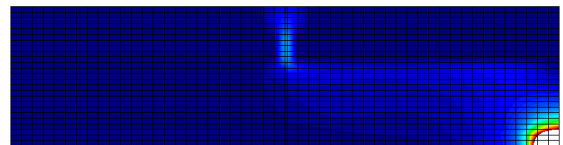
(b7) – Gas Phase flux after 15 years



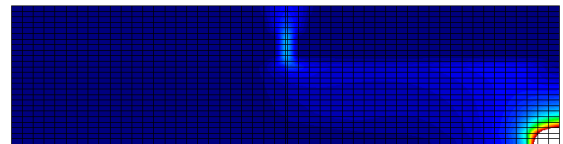
(b8) – Gas Phase flux after 30 years



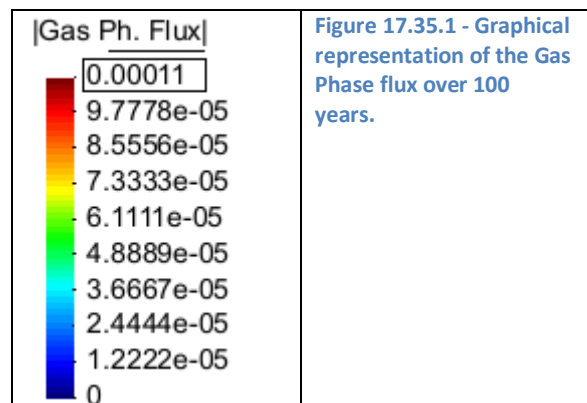
(b9) – Gas Phase flux after 50 years



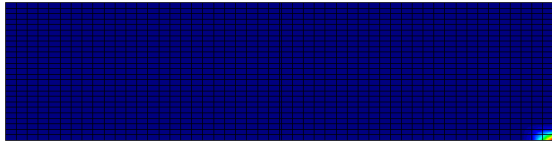
(b10) – Gas Phase flux after 75 years



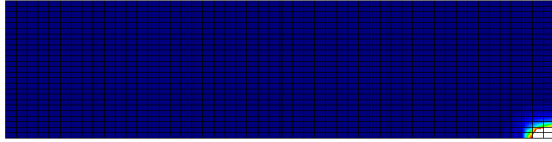
(b11) – Gas Phase flux after 100 years



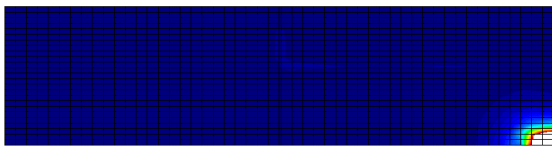
17.36. Case C



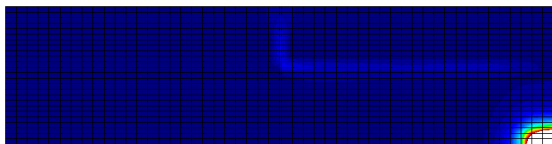
(c1) – Gas Phase flux after 1 month



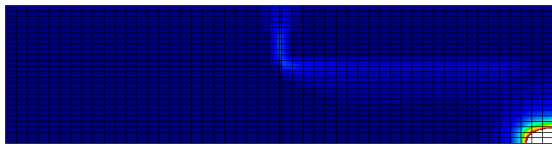
(c2) Gas Phase flux after 3 months



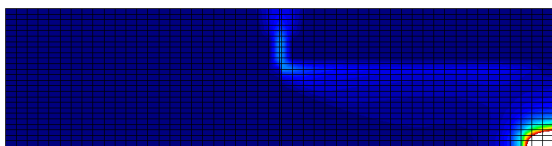
(c3) – Gas Phase flux after 9 months



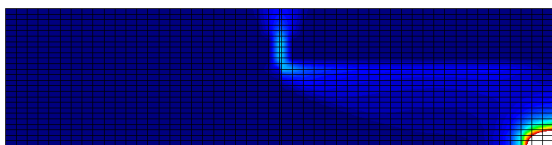
(c4) – Gas Phase flux after 2 years



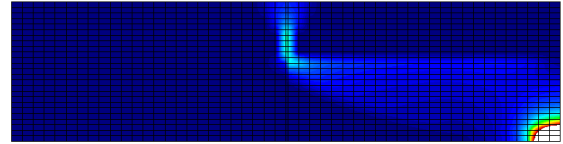
(c5) – Gas Phase flux after 5 years



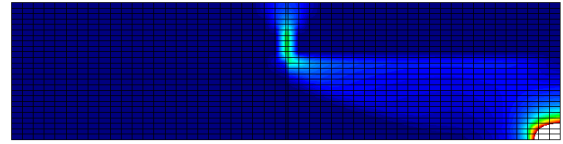
(c6) – Gas Phase flux after 10 years



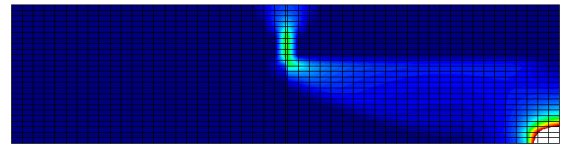
(c7) – Gas Phase flux after 15 years



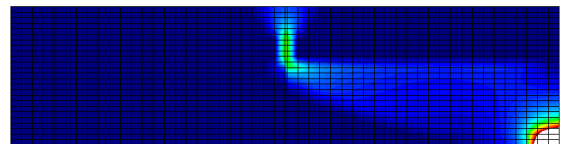
(c8) – Gas Phase flux after 30 years



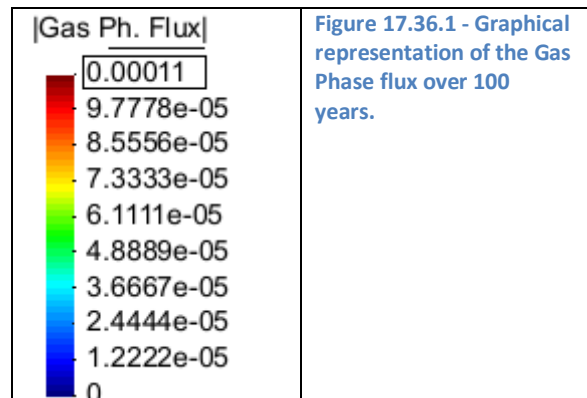
(c9) – Gas Phase flux after 50 years



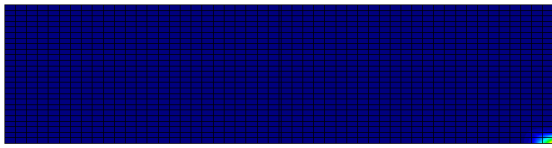
(c10) – Gas Phase flux after 75 years



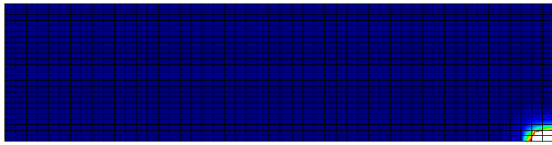
(c11) – Gas Phase flux after 100 years



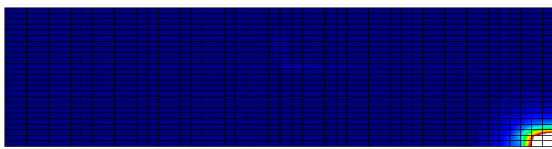
17.37. Case D



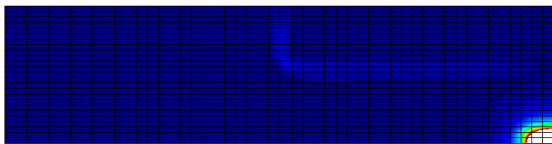
(d1) – Gas Phase flux after 1 month



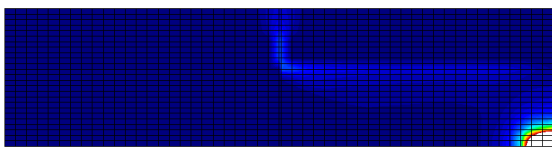
(d2) Gas Phase flux after 3 months



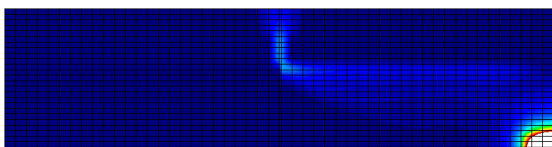
(d3) – Gas Phase flux after 9 months



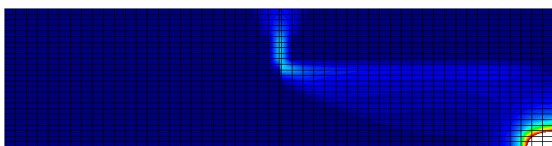
(d4) – Gas Phase flux after 2 years



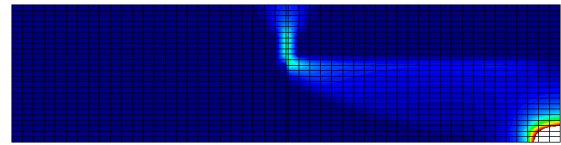
(d5) – Gas Phase flux after 5 years



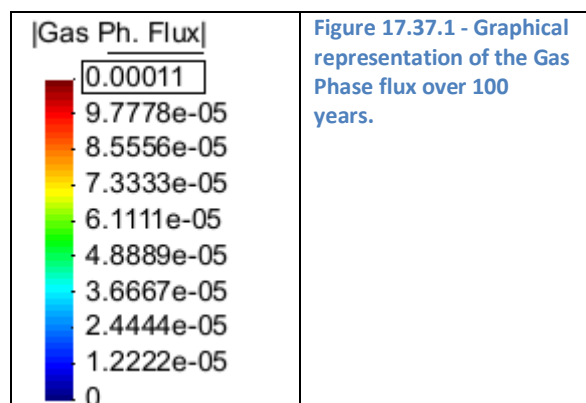
(d6) – Gas Phase flux after 10 years



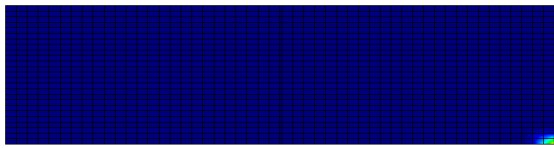
(d7) – Gas Phase flux after 15 years



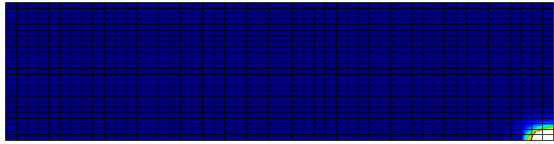
(d8) – Gas Phase flux after 30 years



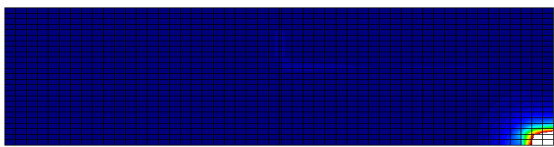
17.38. Case A2



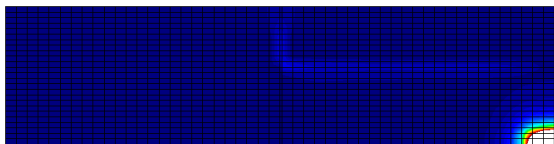
(A1) – Gas Phase flux after 1 month



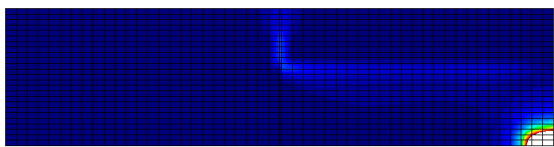
(A2) Gas Phase flux after 3 months



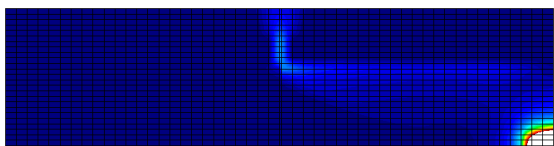
(A3) – Gas Phase flux after 9 months



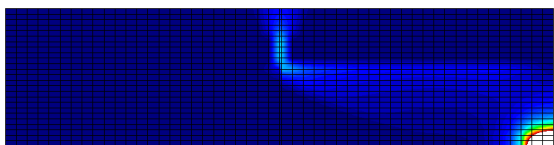
(A4) – Gas Phase flux after 2 years



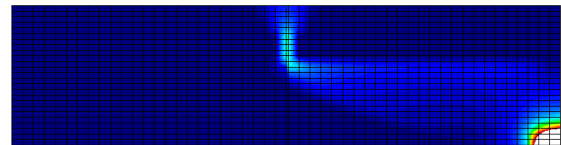
(A5) – Gas Phase flux after 5 years



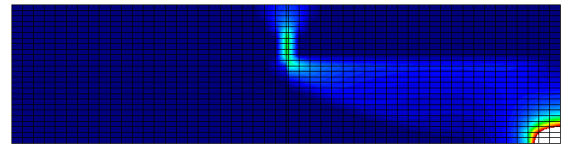
(A6) – Gas Phase flux after 10 years



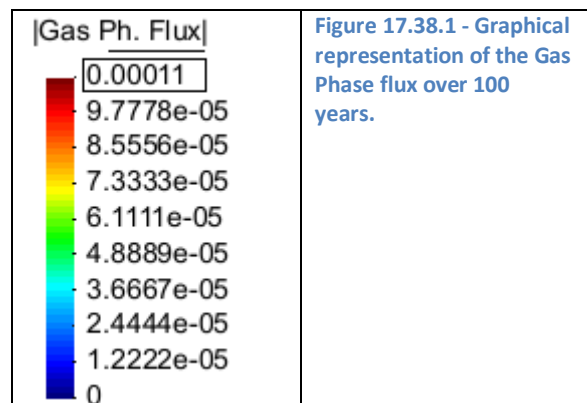
(A7) – Gas Phase flux after 15 years



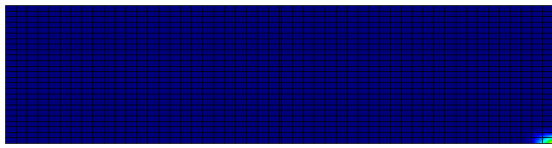
(A8) – Gas Phase flux after 30 years



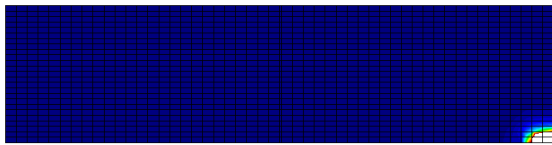
(A9) – Gas Phase flux after 48.7 years



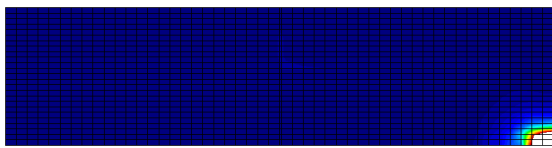
17.39. Case B2



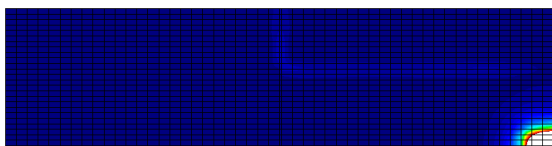
(B1) – Gas Phase flux after 1 month



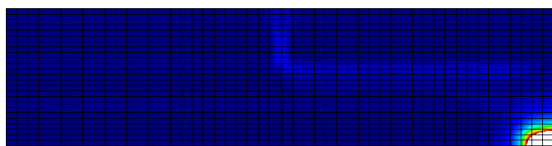
(B2) Gas Phase flux after 3 months



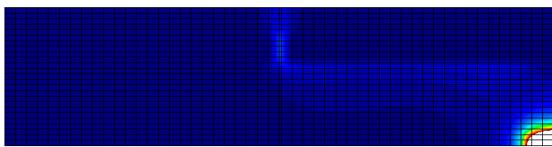
(B3) – Gas Phase flux after 9 months



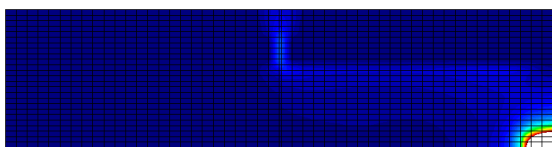
(B4) – Gas Phase flux after 2 years



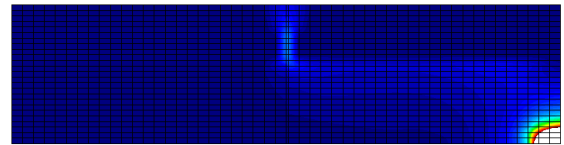
(B5) – Gas Phase flux after 5 years



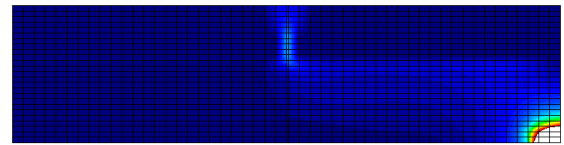
(B6) – Gas Phase flux after 10 years



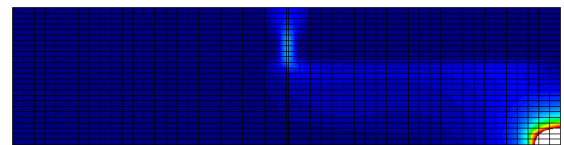
(B7) – Gas Phase flux after 15 years



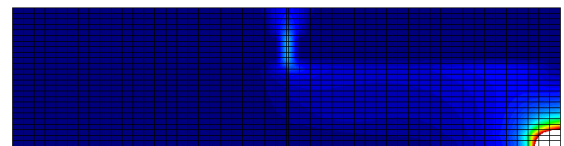
(B8) – Gas Phase flux after 30 years



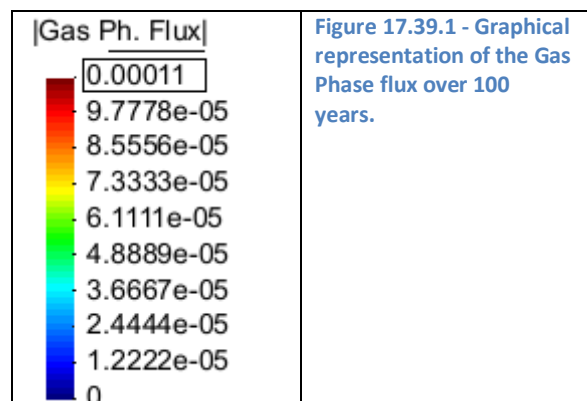
(B9) – Gas Phase flux after 50 years



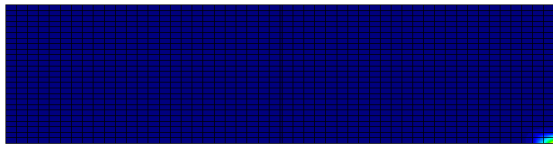
(B10) – Gas Phase flux after 75 years



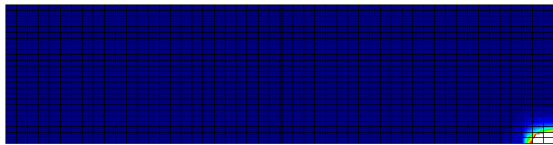
(B11) – Gas Phase flux after 100 years



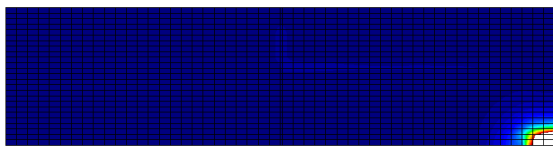
17.40. Case C2



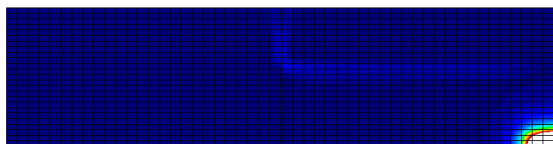
(C1) – Gas Phase flux after 1 month



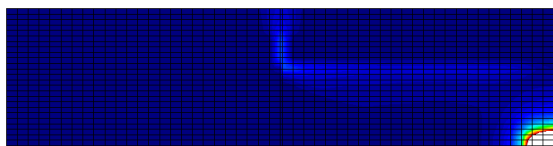
(C2) Gas Phase flux after 3 months



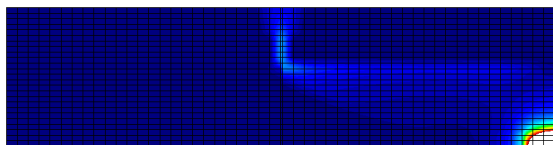
(C3) – Gas Phase flux after 9 months



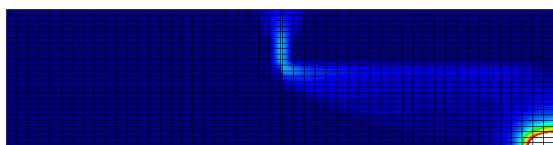
(C4) – Gas Phase flux after 2 years



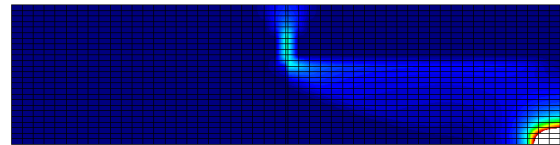
(C5) – Gas Phase flux after 5 years



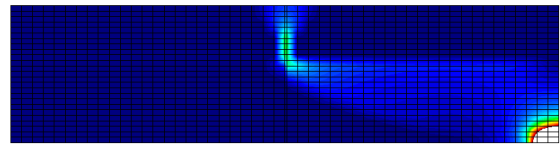
(C6) – Gas Phase flux after 10 years



(C7) – Gas Phase flux after 15 years



(C8) – Gas Phase flux after 30 years



(C9) – Gas Phase flux after 50 years

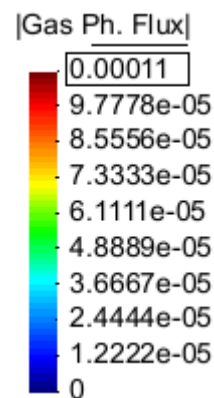
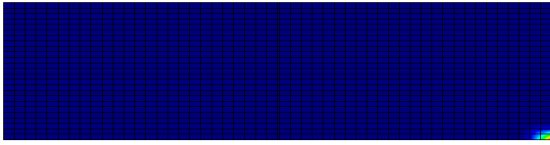
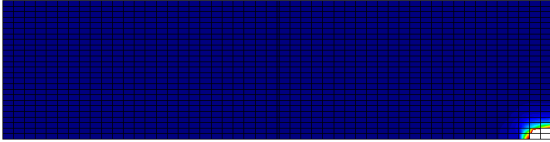


Figure 17.40.1 - Graphical representation of the Gas Phase flux over 100 years.

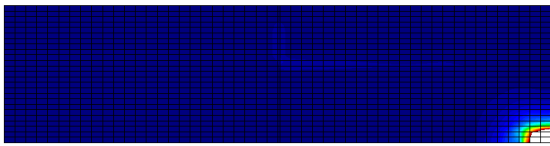
17.41. Case D2



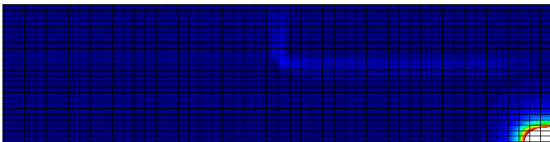
(D1) – Gas Phase flux after 1 month



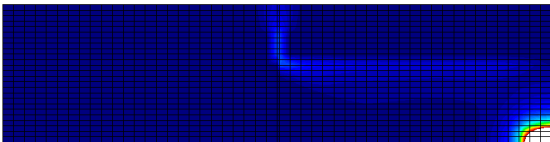
(D2) Gas Phase flux after 3 months



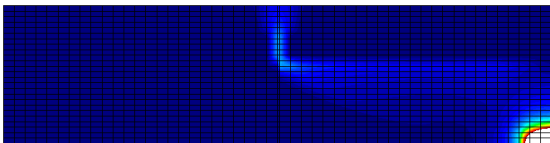
(D3) – Gas Phase flux after 9 months



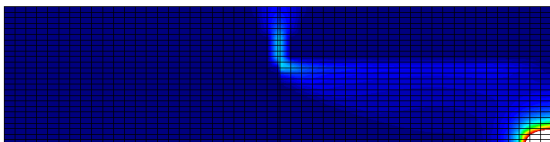
(D4) – Gas Phase flux after 2 years



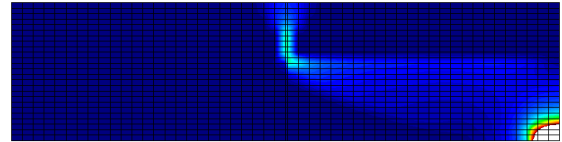
(D5) – Gas Phase flux after 5 years



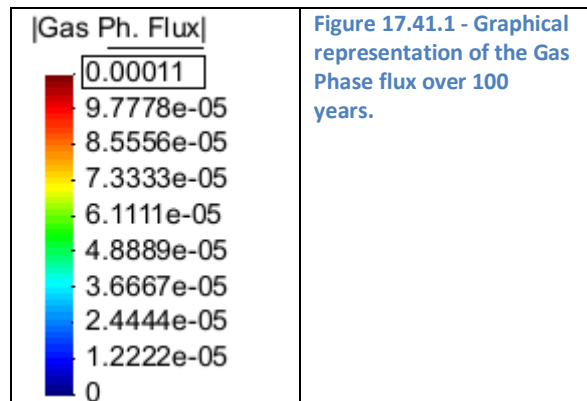
(D6) – Gas Phase flux after 10 years



(D7) – Gas Phase flux after 15 years



(D8) – Gas Phase flux after 30 years



Appendix VI

Breakthrough of Carbon dioxide

Appendix VI contains graphical representations for the gas pressure, gas density and gas phase flux at the time-step in closest vicinity of the actual CO₂ breakthrough. For each case the breakthrough is manually located by comparing the graphical representation respective to each time-step. At a certain interval the pressure, and the coherent properties like density and phase flux, will drop significantly and thereby allow the selection of a representative image.

Each set of images have their respective gradient colour indicator which illustrates the aquifer condition at any given time and position. The gradient limits are equal for the respective properties throughout appendix VI.

Appendix IIX contains a more elaborate pressure, density and phase flux trends in the form of point evaluation graphs.

17.42. Case A

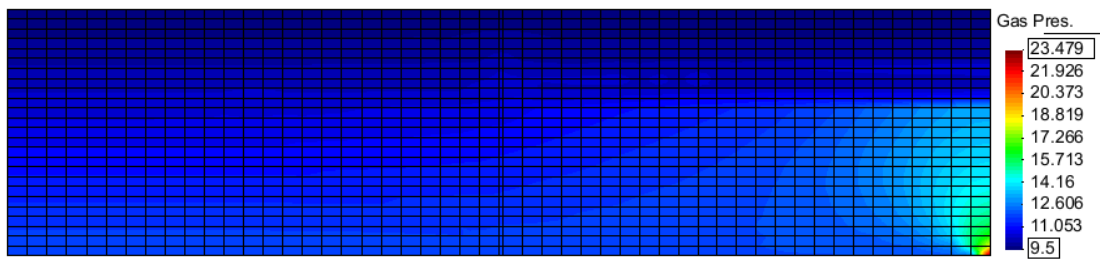


Figure 17.42.1 - Gas Pressure

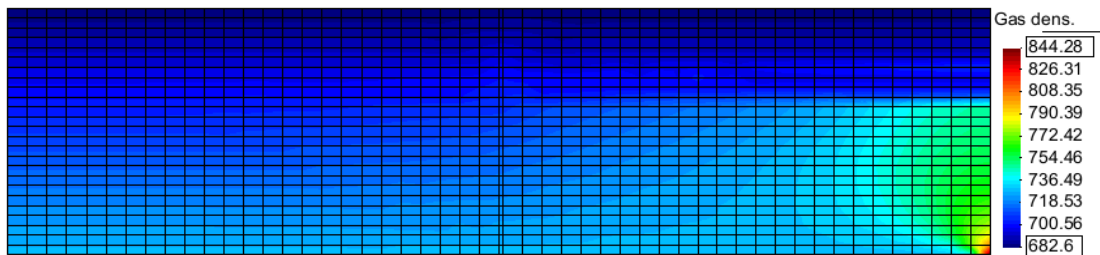


Figure 17.42.2 - Gas density

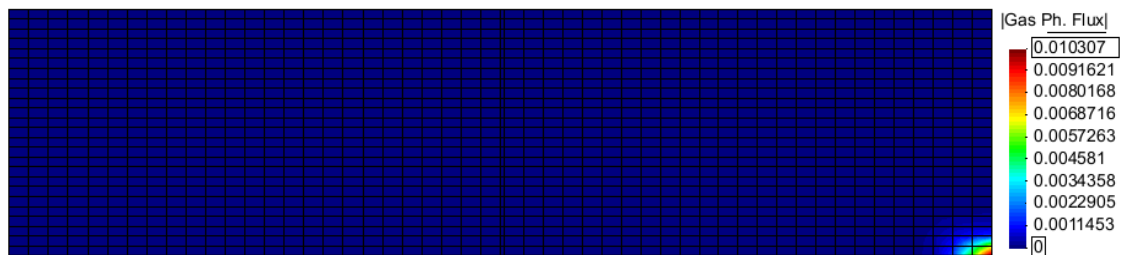


Figure 17.42.3 - |Gas Phase Flux|

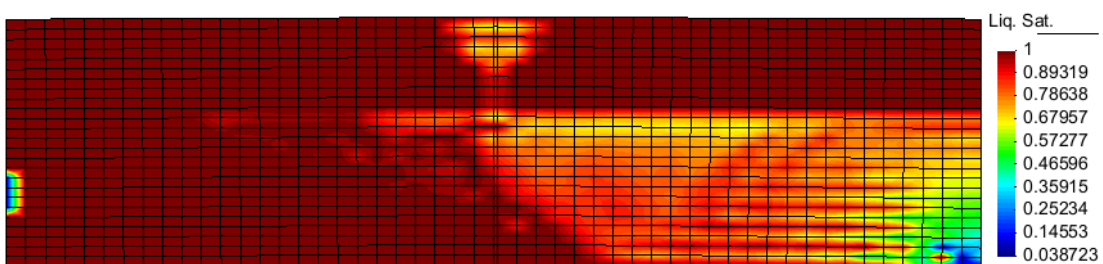


Figure 17.42.4 - Liquid saturation

17.43. Case B

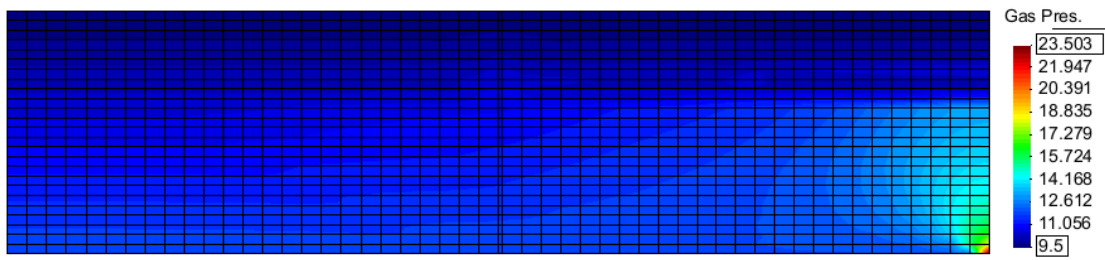


Figure 17.43.1 - Gas Pressure

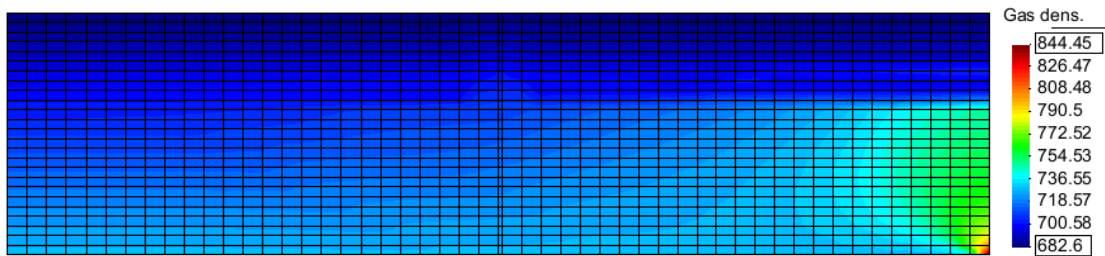


Figure 17.43.2 - Gas density

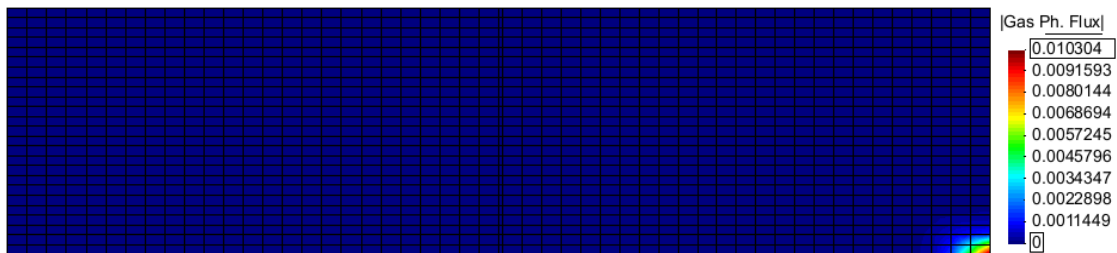


Figure 17.43.3 - |Gas Phase Flux|

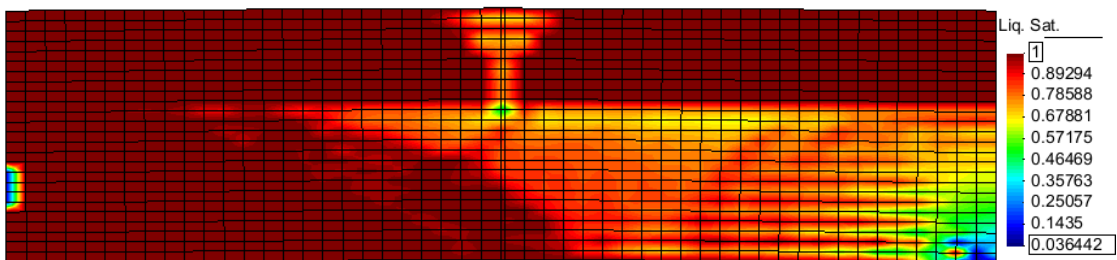


Figure 17.43.4 - Liquid saturation

17.44. Case C

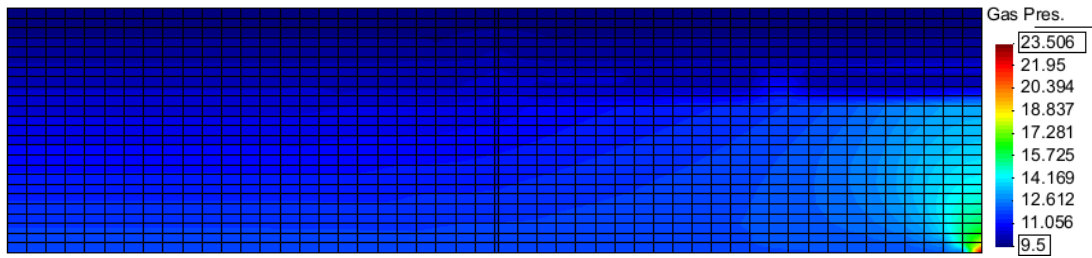


Figure 17.44.1 - Gas Pressure

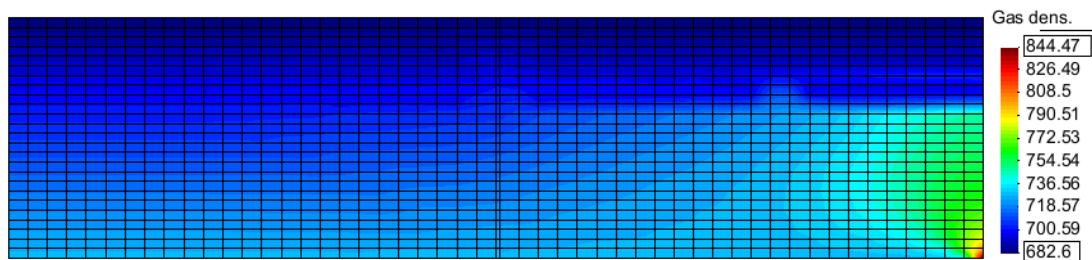


Figure 17.44.2 - Gas density

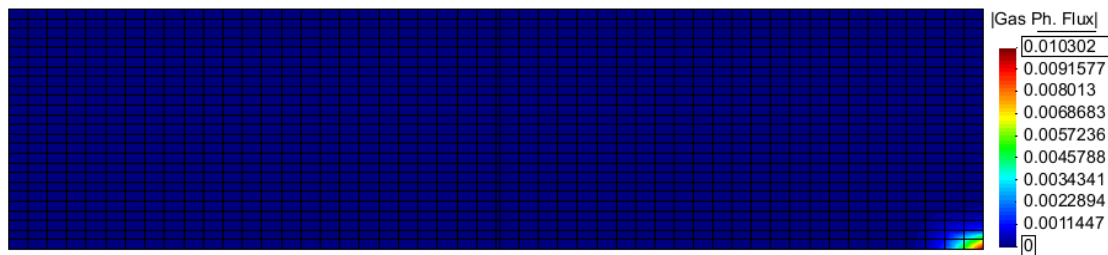


Figure 17.44.3 - |Gas Phase Flux|

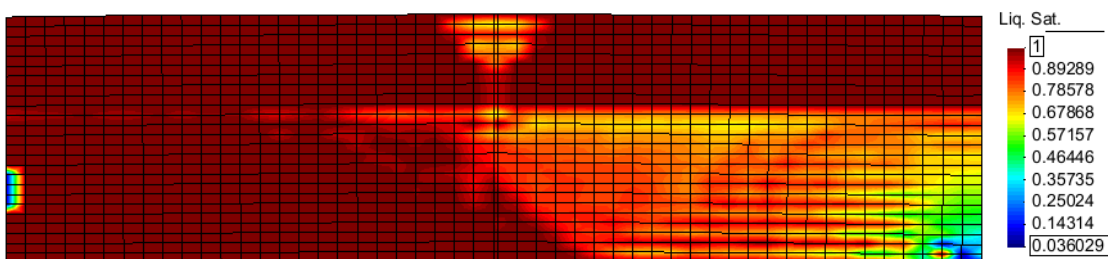


Figure 17.44.4 - Liquid saturation

17.45. Case D

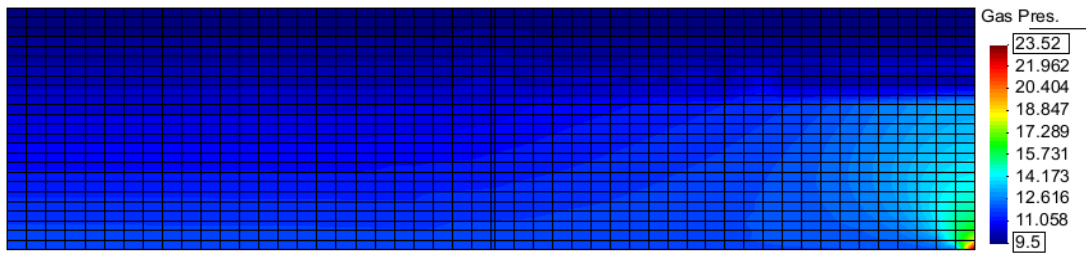


Figure 17.45.1 - Gas Pressure

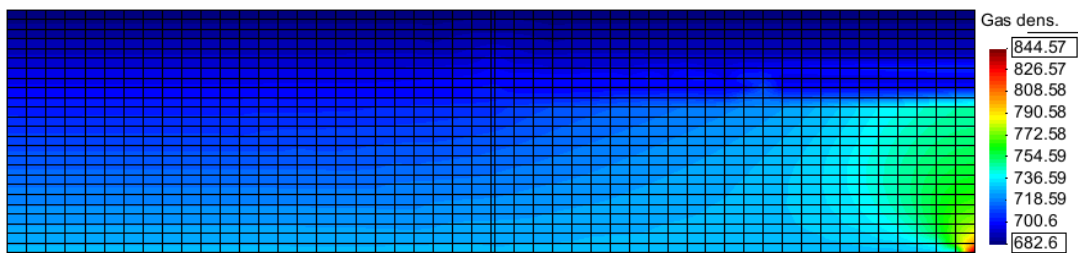


Figure 17.45.2 - Gas density

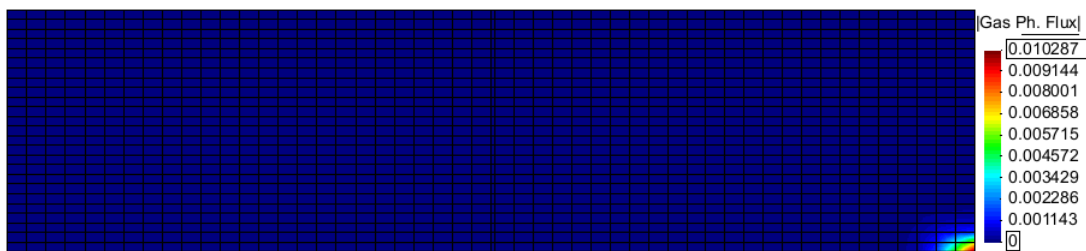


Figure 17.45.3 - |Gas Phase Flux|

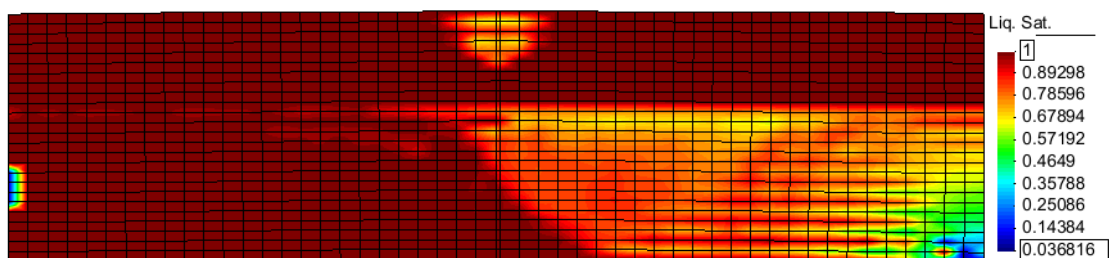


Figure 17.45.4 - Liquid saturation

17.46. Case A2

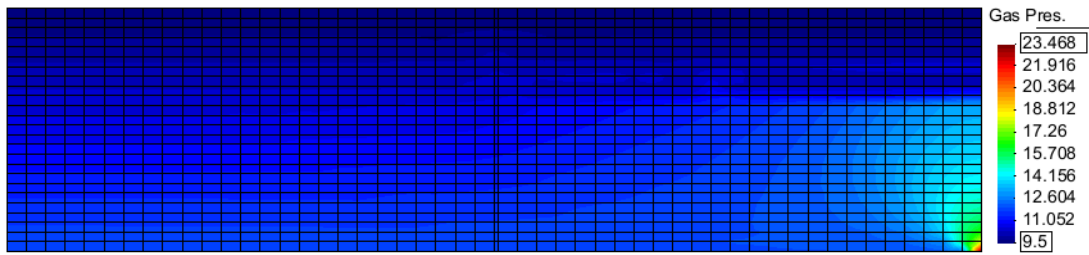


Figure 17.46.1 - Gas Pressure

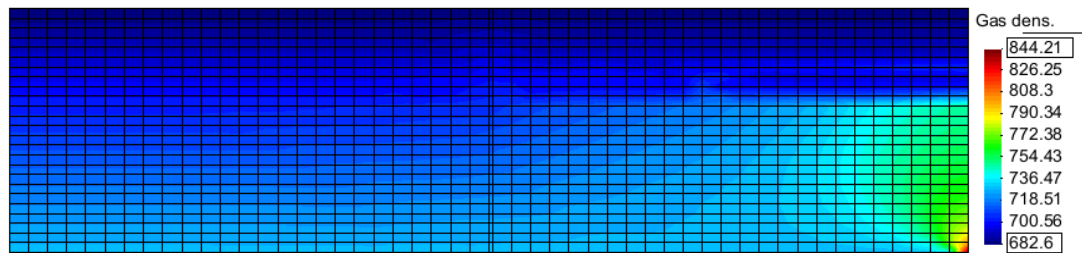


Figure 17.46.2 - Gas density

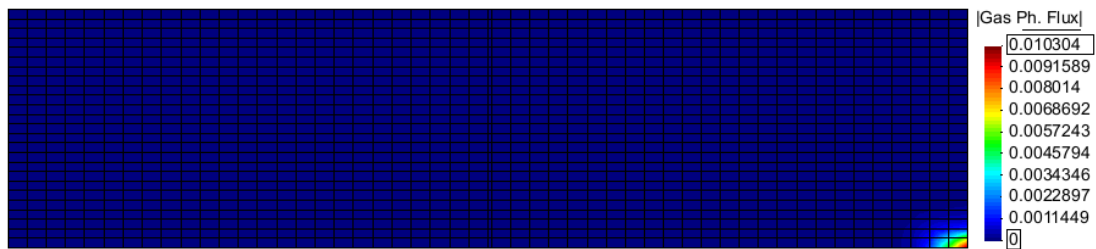


Figure 17.46.3 - |Gas Phase Flux|

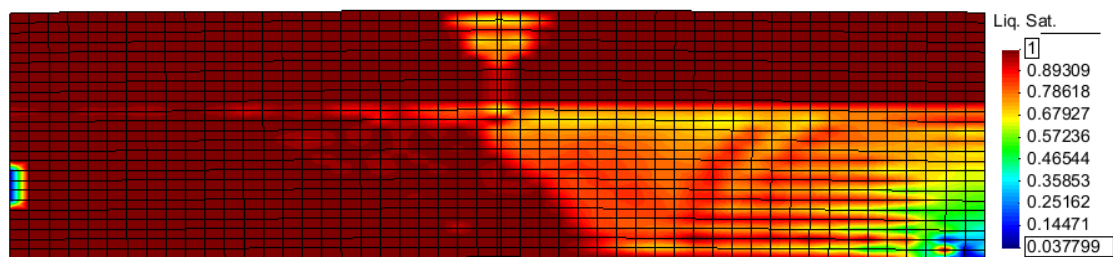


Figure 17.46.4 - Liquid saturation

17.47. Case B2

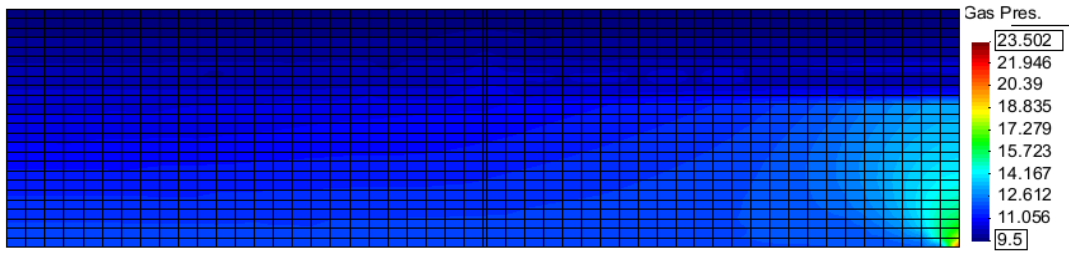


Figure 17.47.1 - Gas Pressure

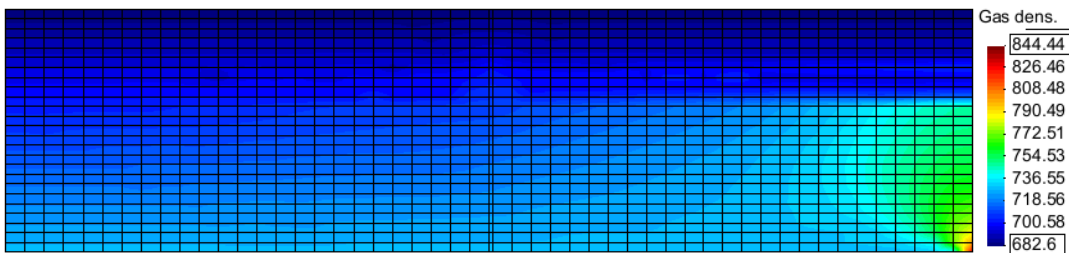


Figure 17.47.2 - Gas density

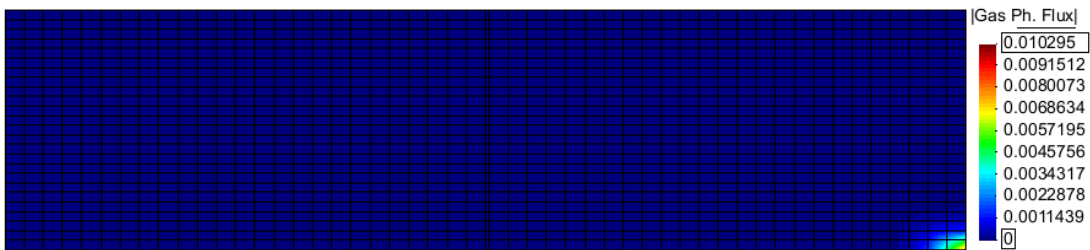


Figure 17.47.3 - |Gas Phase Flux|

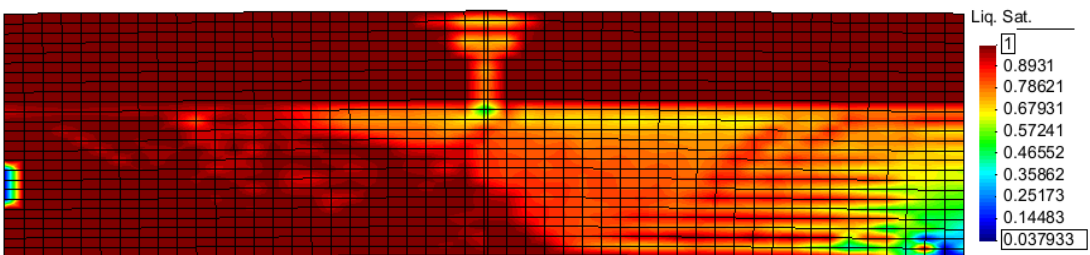


Figure 17.47.4 - Liquid saturation

17.48. Case C2

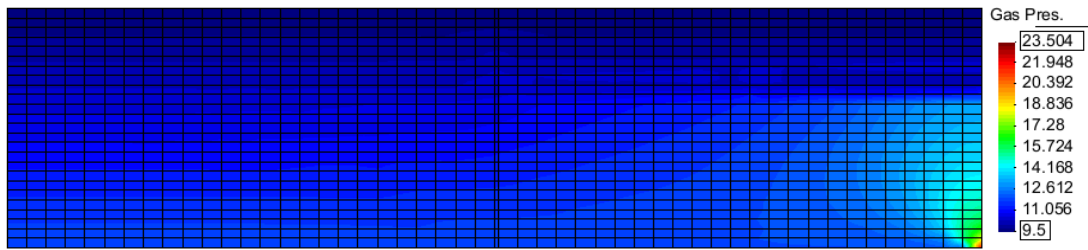


Figure 17.48.1 - Gas Pressure

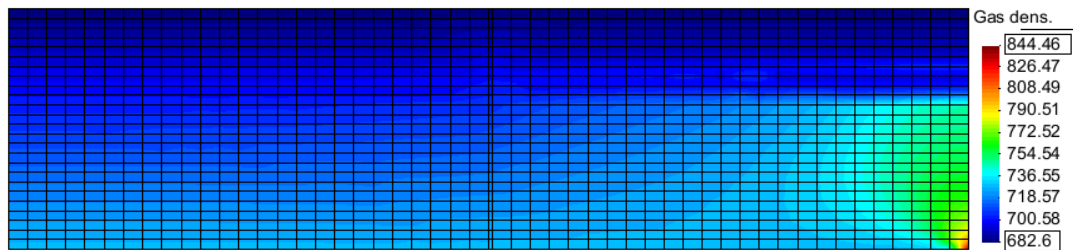


Figure 17.48.2 - Gas density

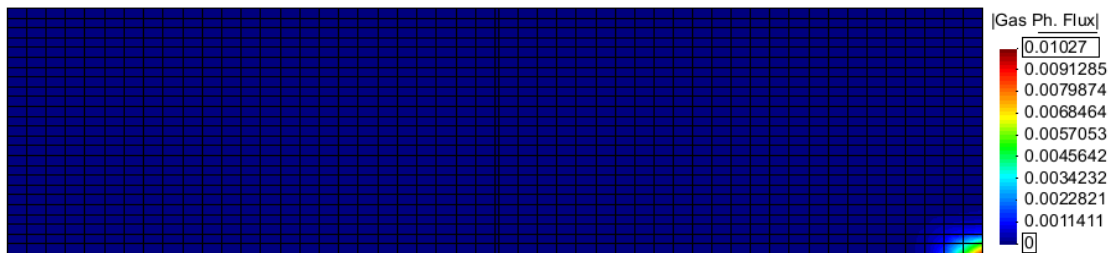


Figure 17.48.3 - |Gas Phase Flux|

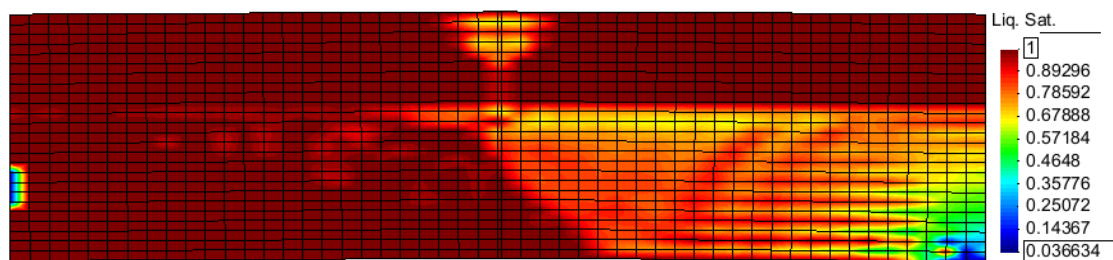


Figure 17.48.4 - Liquid saturation

17.49. Case D2

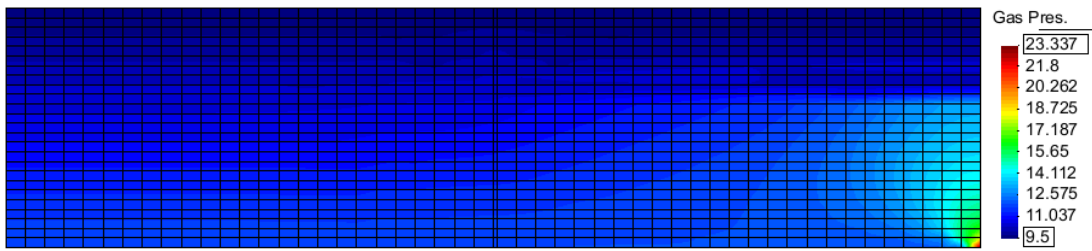


Figure 17.49.1 - Gas Pressure

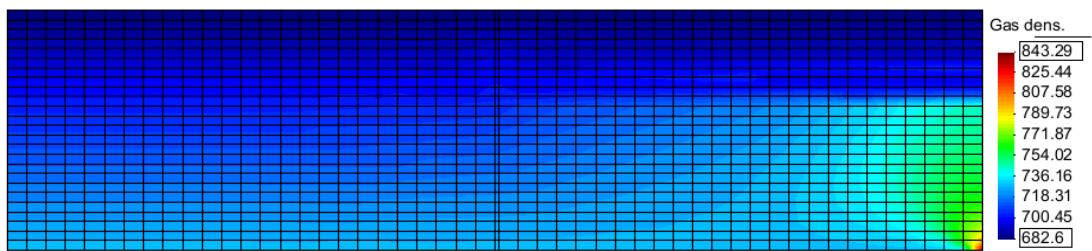


Figure 17.49.2 - Gas density

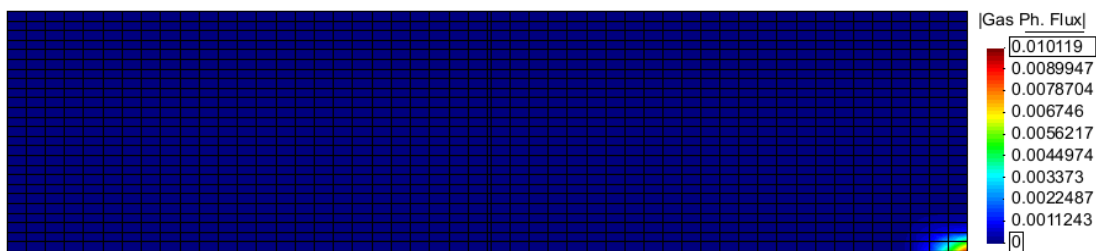


Figure 17.49.3 - |Gas Phase Flux|

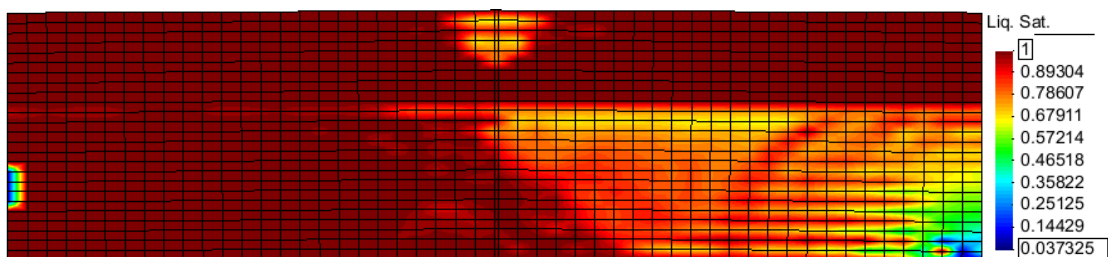


Figure 17.49.4 - Liquid saturation

Appendix VII

- Graphs- Properties plotted against time

Appendix IIX contains several graphs respective to each case, with gaseous properties plotted against time thorough 100 years of simulated carbon dioxide injection. There are a total of 8 cases or runs with 4 graphs each.

The two first graphs in each case are that of pressure and density plotted against time. The two remaining graphs represent the net gas phase flux, where the last graph is more accurate with respect to the lower overlapping fluxes. It is imperative to be aware that some of the simulations are incomplete due to conversion problems; hence the x- axes are not equal in all cases.

The four lines constituting the graphs represent four points in the reservoir. Node 1 and 2 are located in the injection zone, while node 3 and 4 are placed linearly between the injection point and the fracture. Node 4 is more precise located in the middle of the fracture.

17.50. Case A

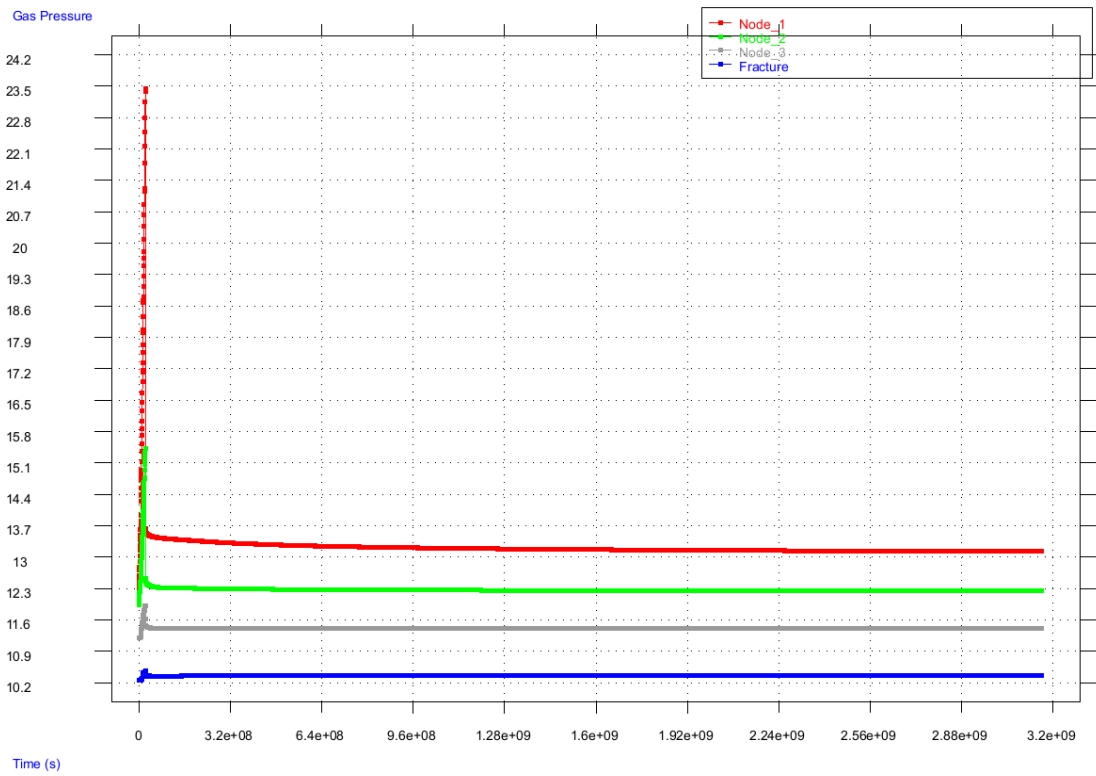


Figure 17.50.1 - Gas pressure plotted against time in run A

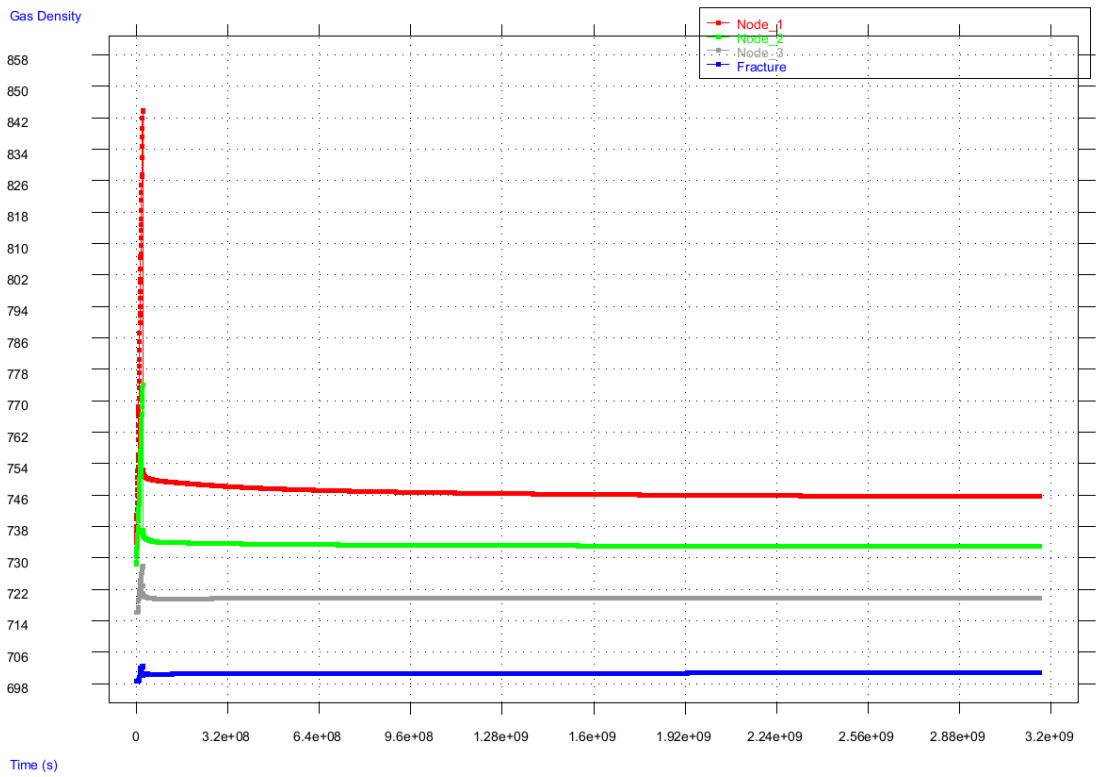


Figure 17.50.2 - Gas density plotted against time in run A

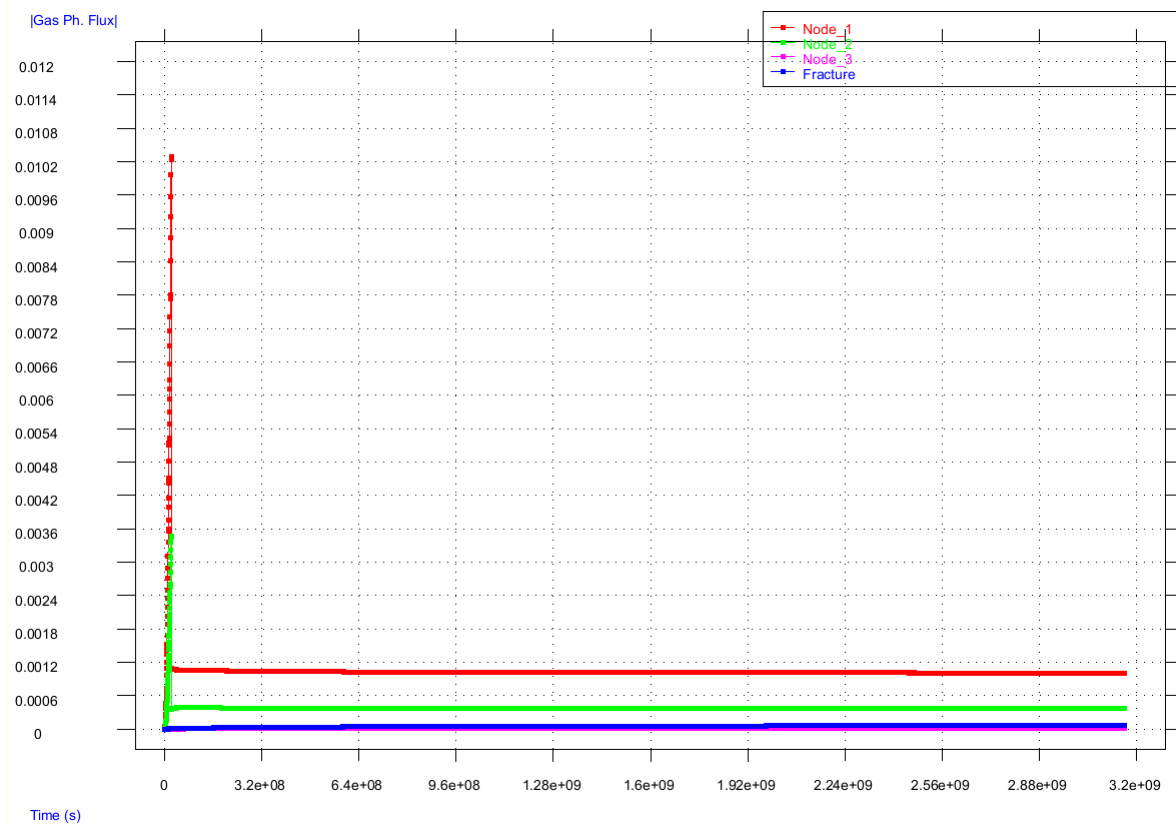


Figure 17.50.3 - Gas phase flux plotted against time in run A

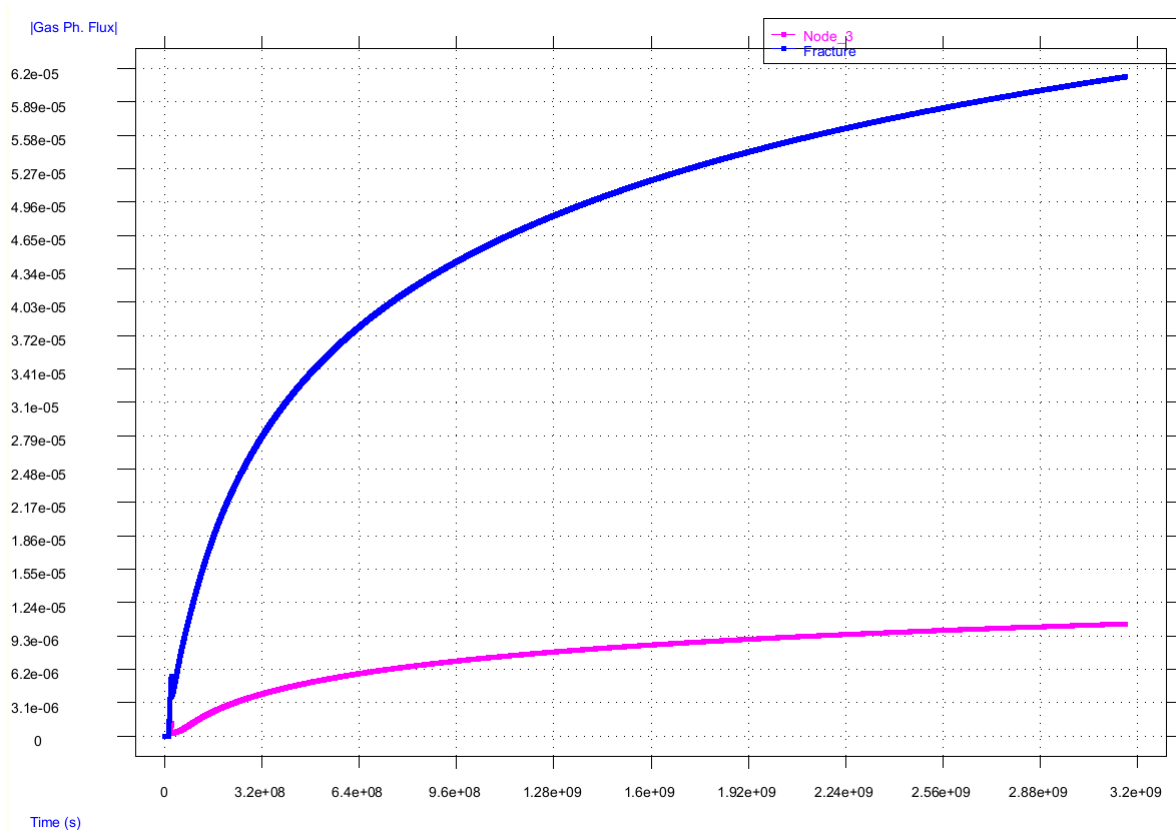


Figure 17.50.4 - Gas phase flux plotted against time in run A

17.51. Case B

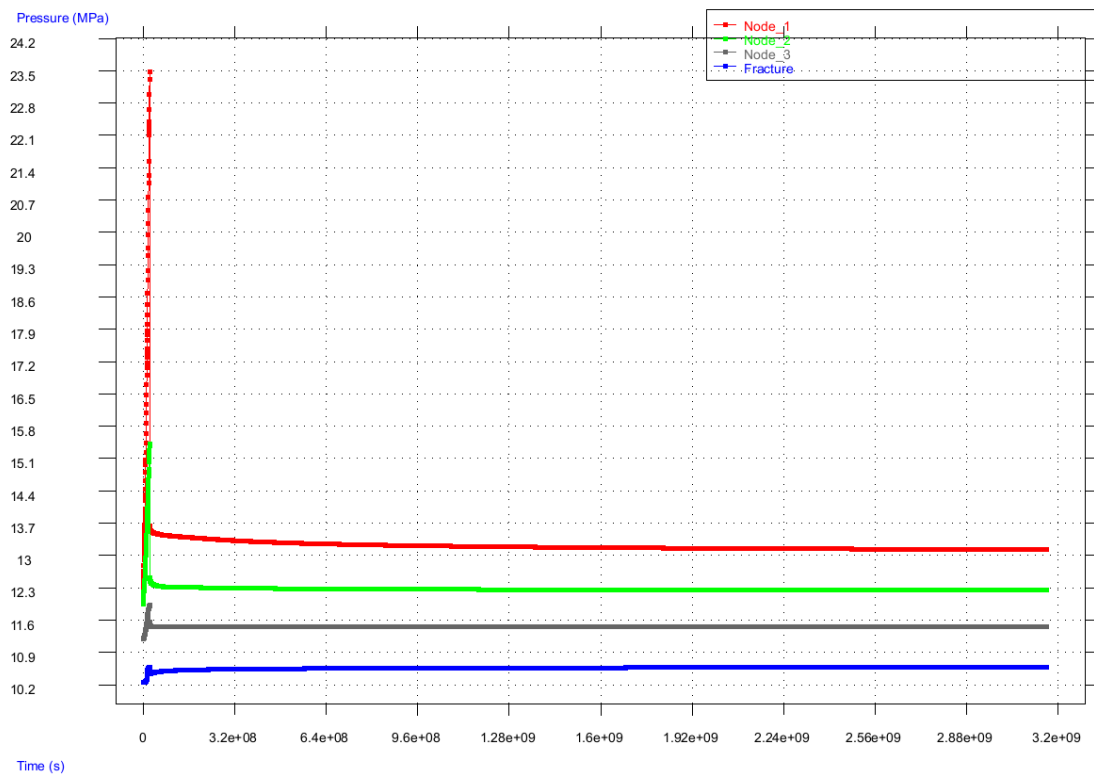


Figure 17.51.1 - Gas pressure plotted against time in run B

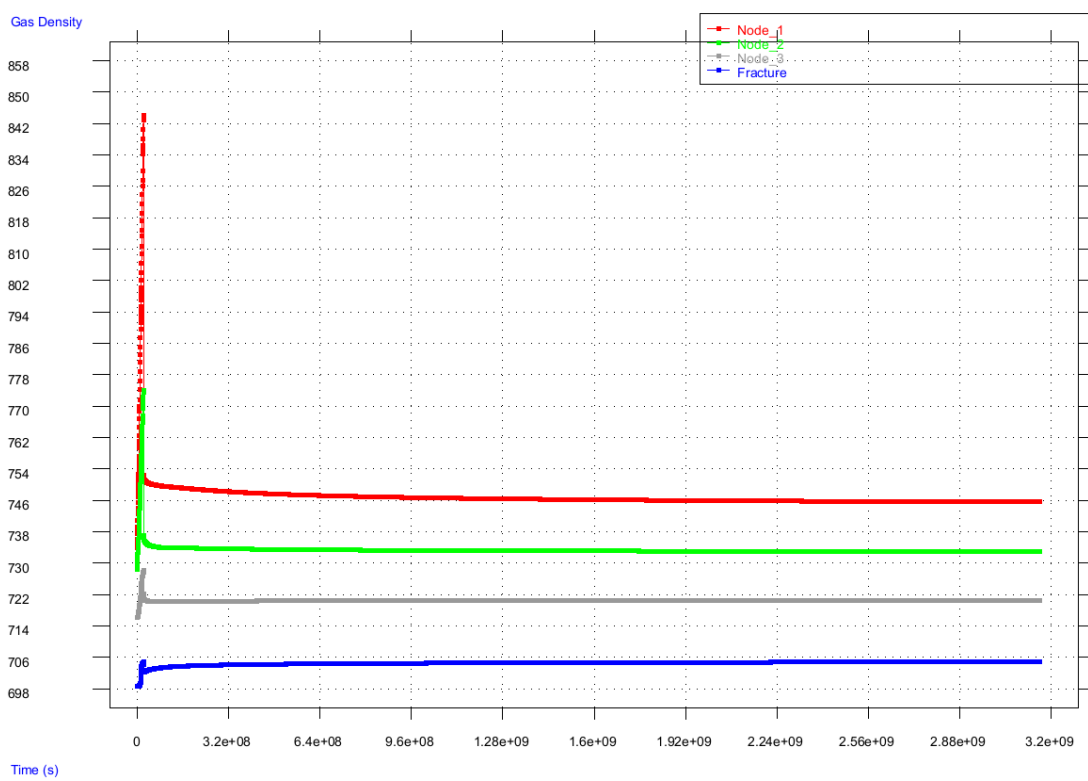


Figure 17.51.2 - Gas density plotted against time in run B

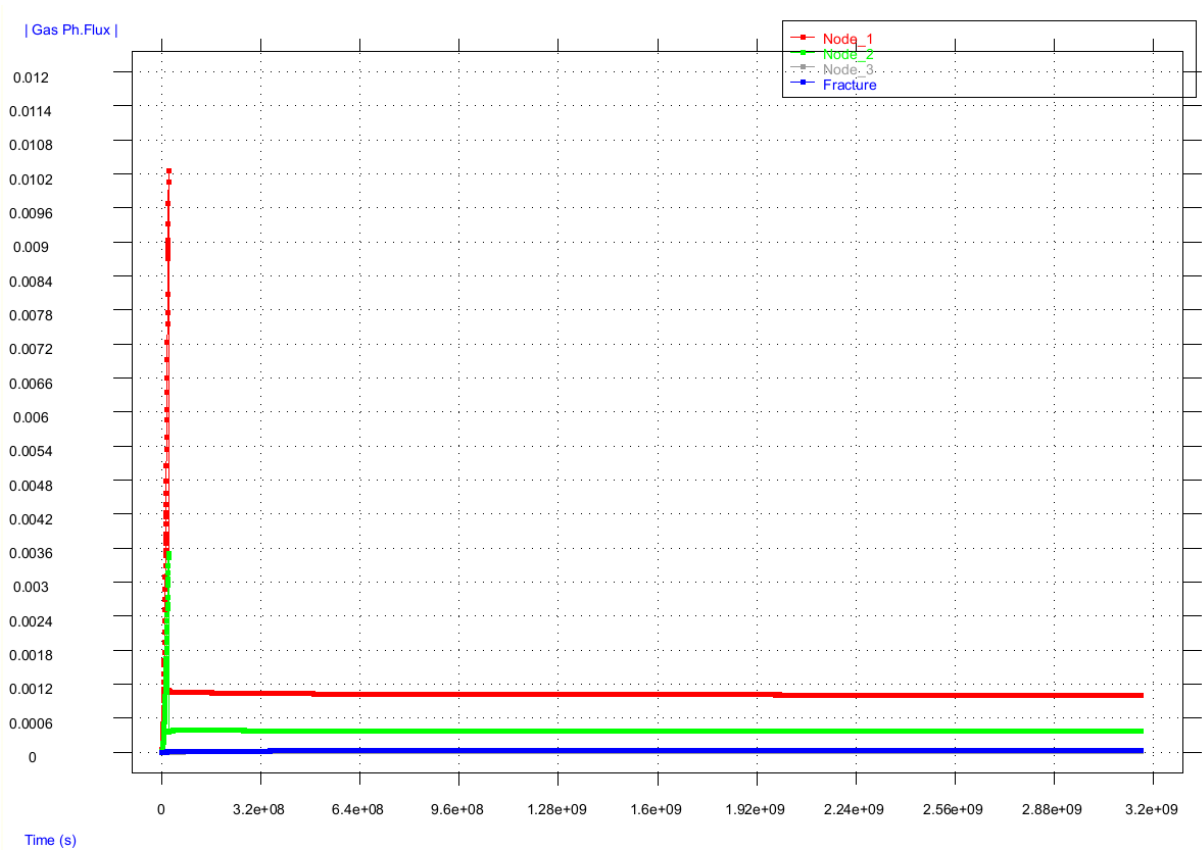


Figure 17.51.3 -Gas phase flux plotted against time in run B

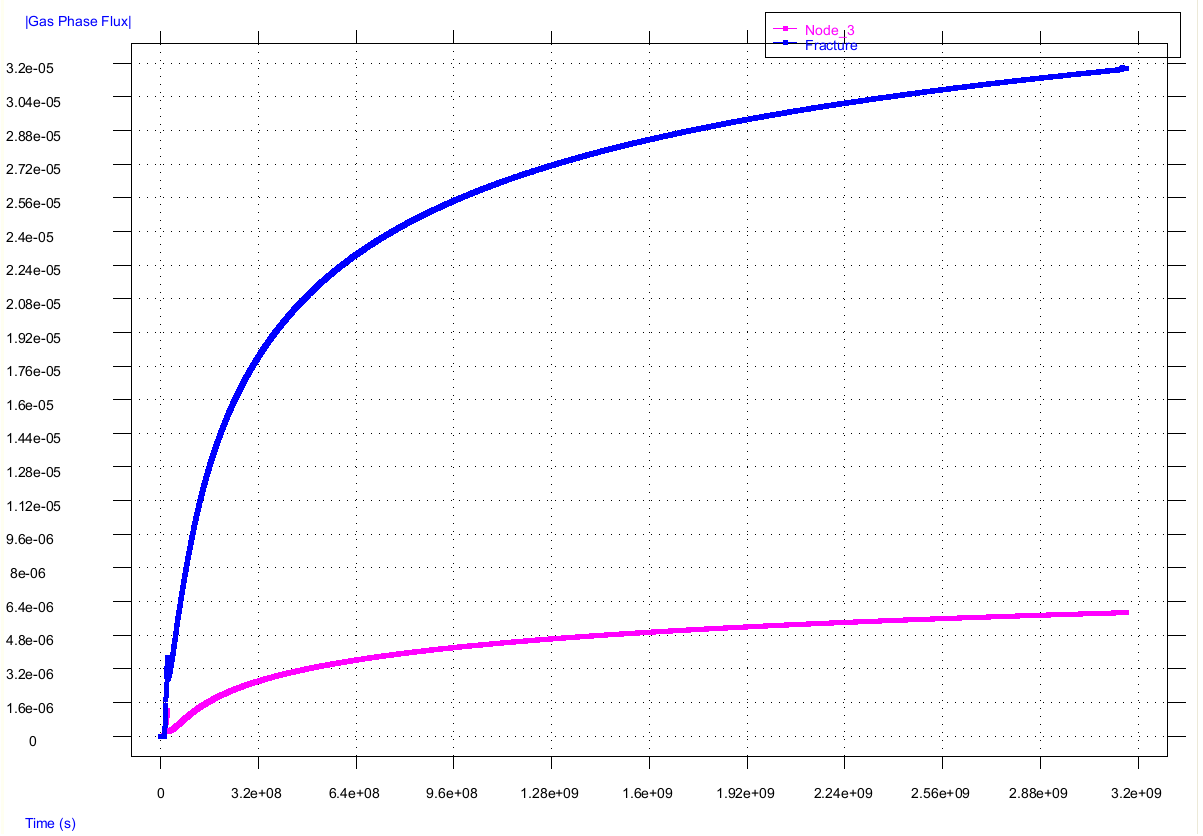


Figure 17.51.4 - Gas phase flux plotted against time in run B

17.52. Case C

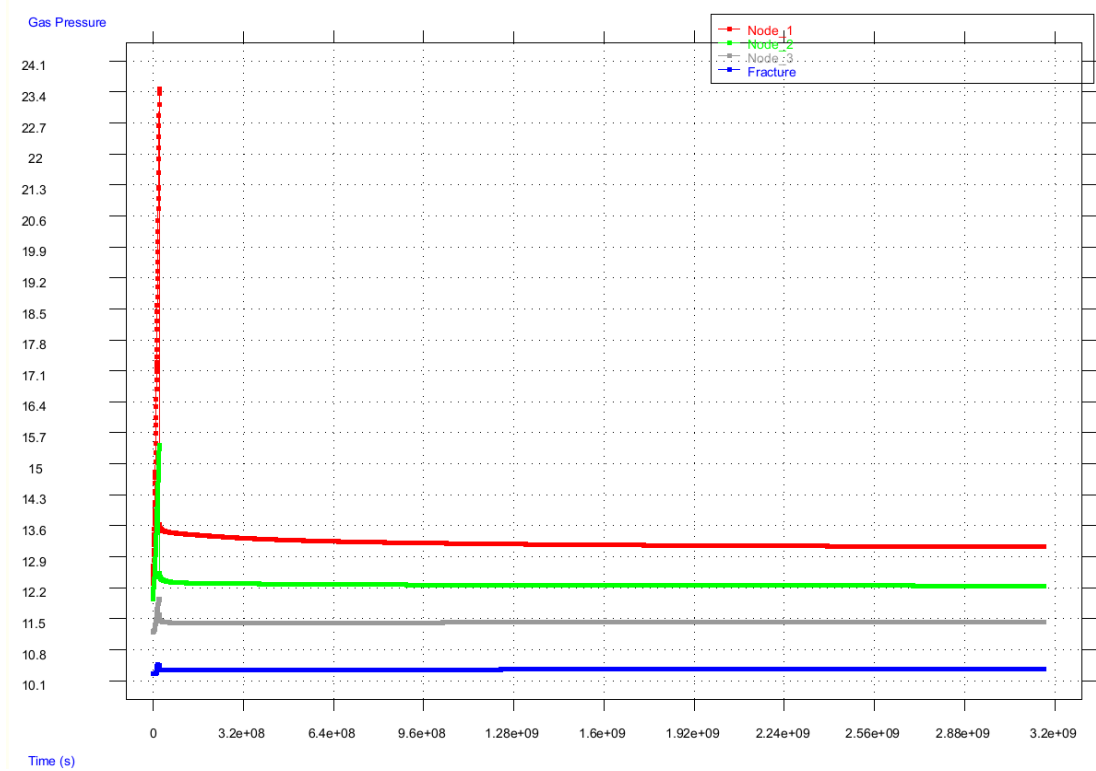


Figure 17.52.1 - Gas pressure in MPa plotted against time in run C

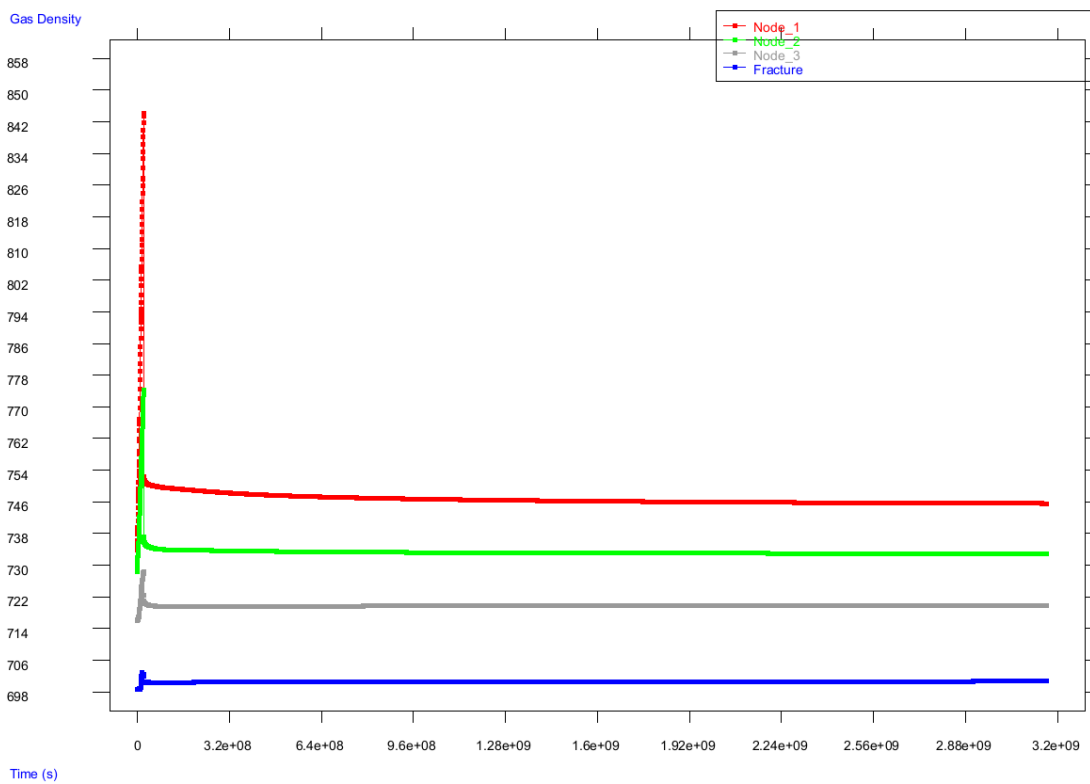


Figure 17.52.2 - Gas density plotted against time in run C

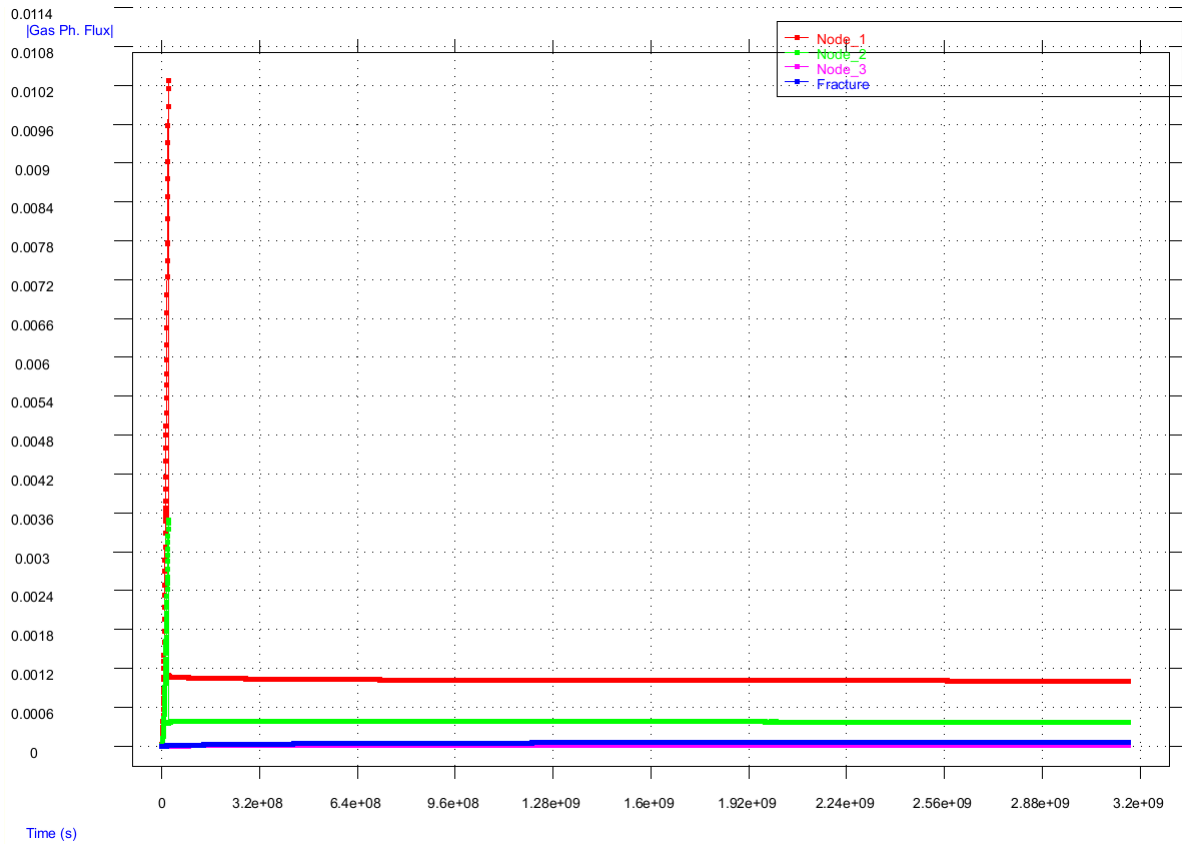


Figure 17.52.3 - Gas phase flux plotted against time in run C

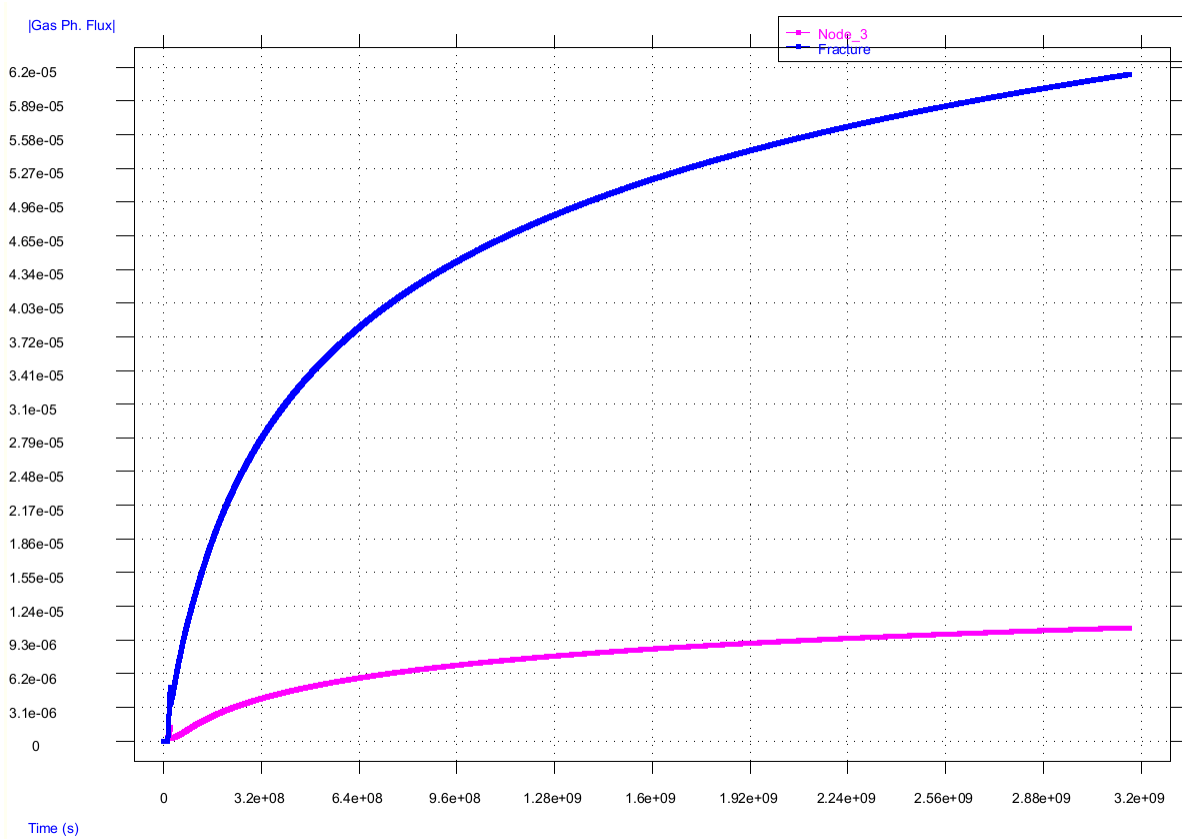


Figure 17.52.4 - Gas phase flux plotted against time in run C

17.53. Case D

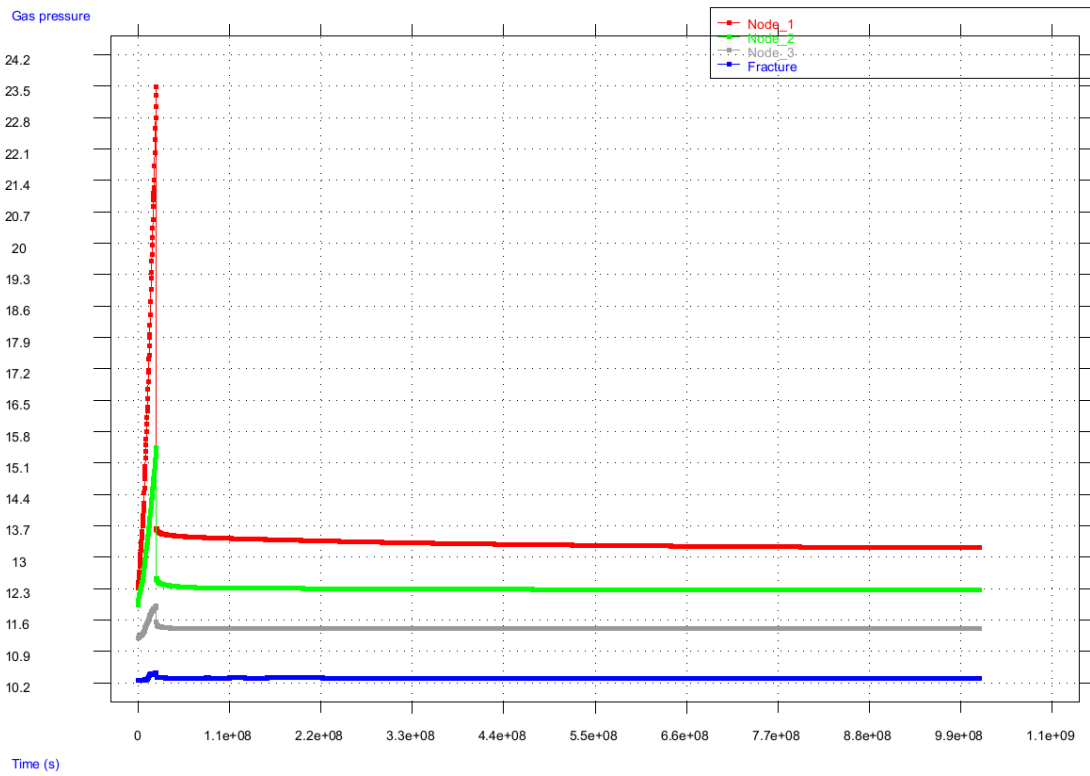


Figure 17.53.1 - Gas pressure plotted against time in run D

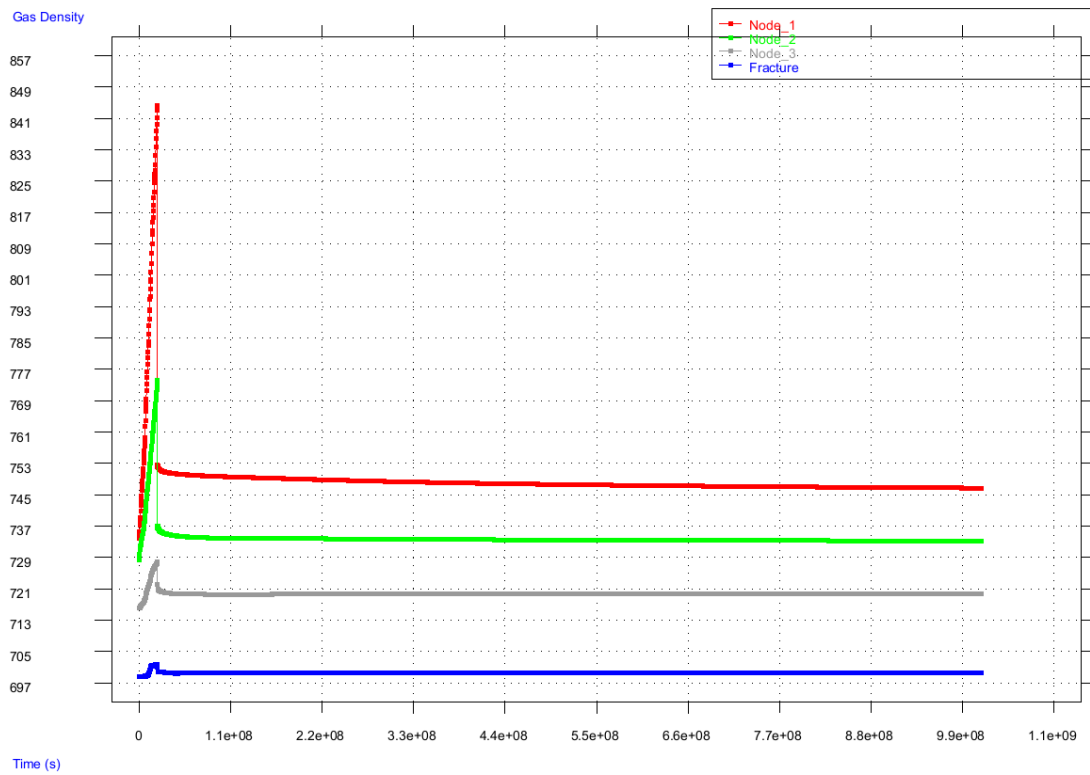


Figure 17.53.2 - Gas density plotted against time in run D

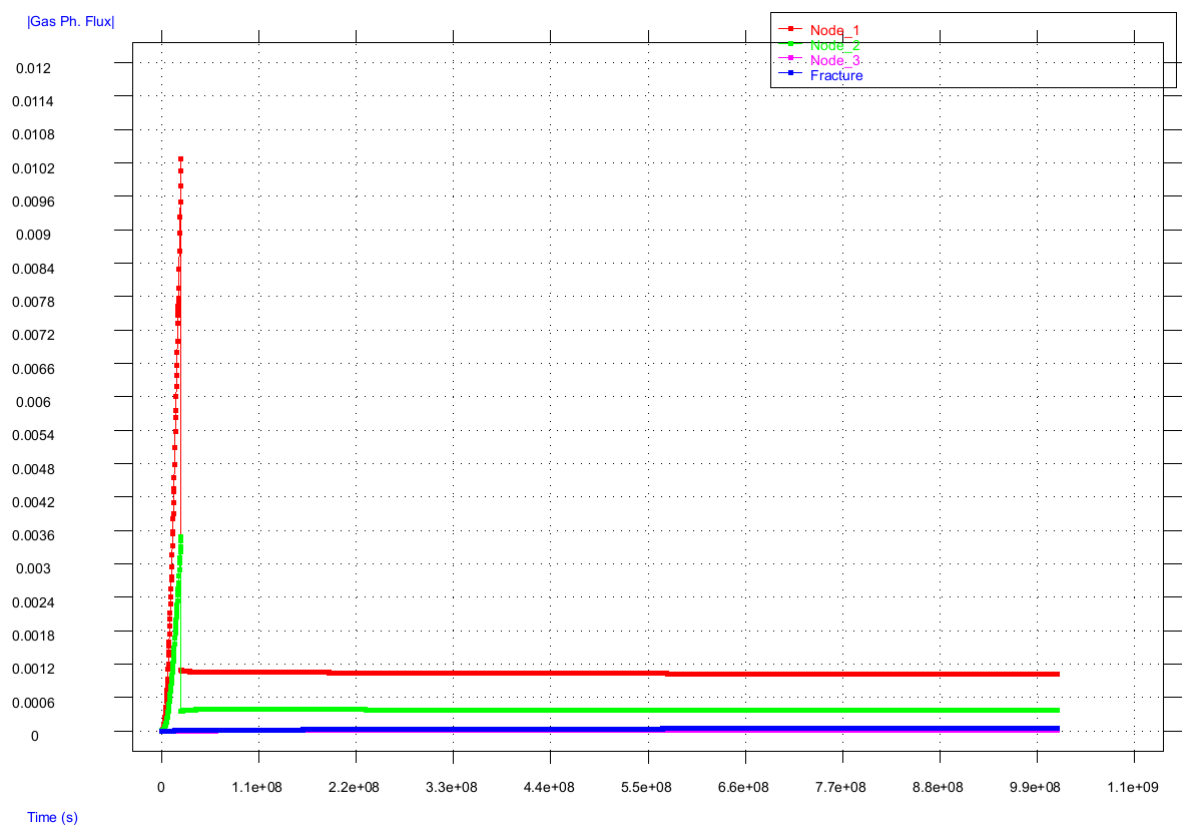


Figure 17.53.3 - Gas phase flux plotted against time in run D

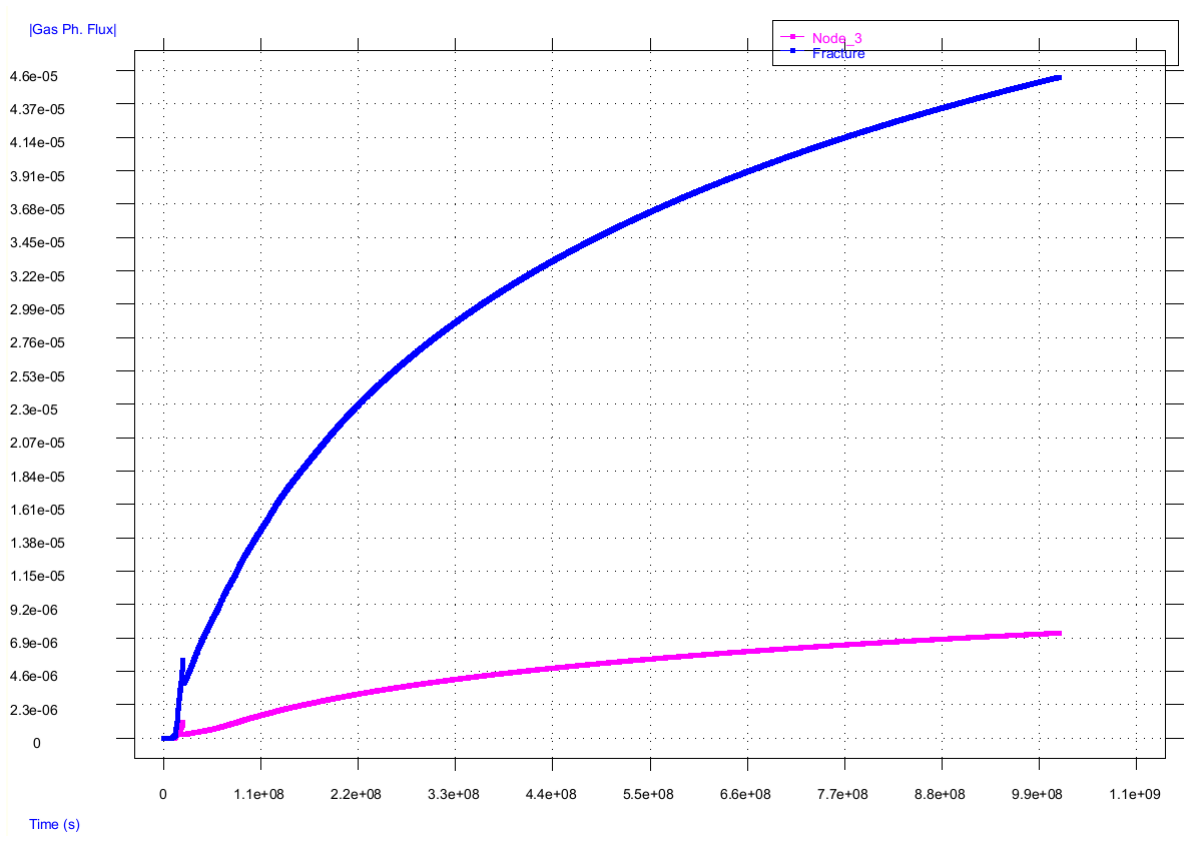


Figure 17.53.4 - Gas phase flux plotted against time in run D

17.54. Case A2

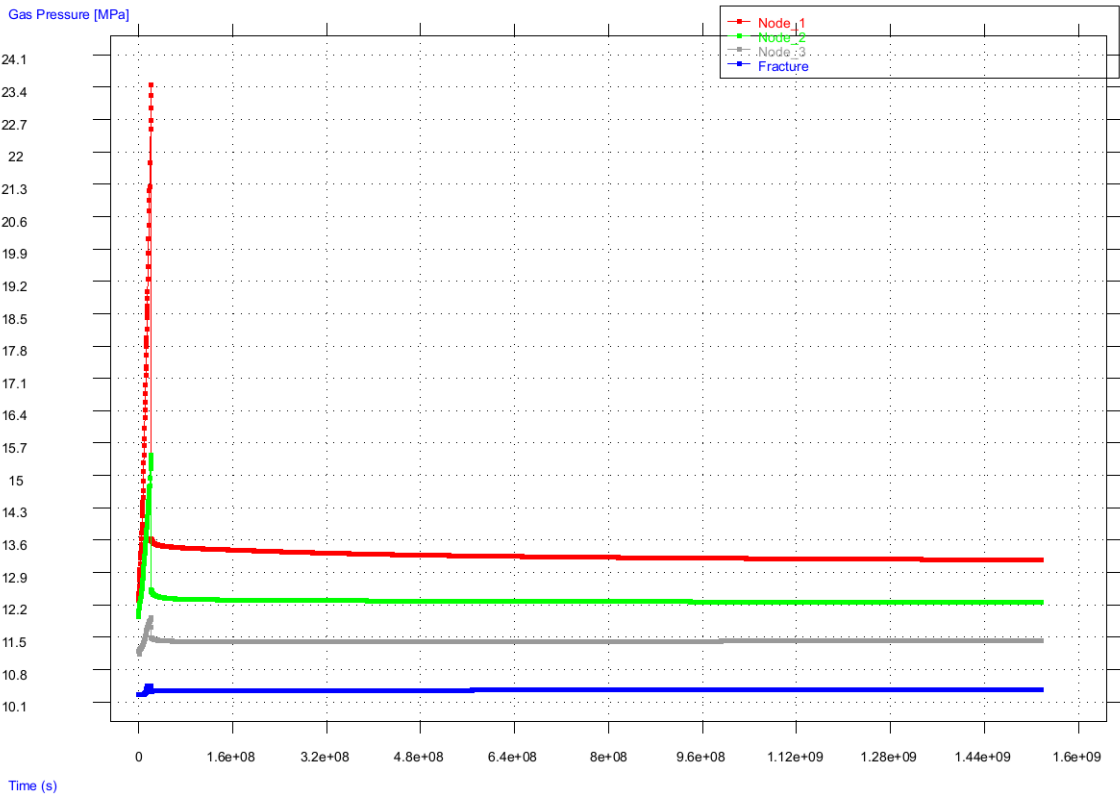


Figure 17.54.1 - Gas pressure plotted against time in run A2

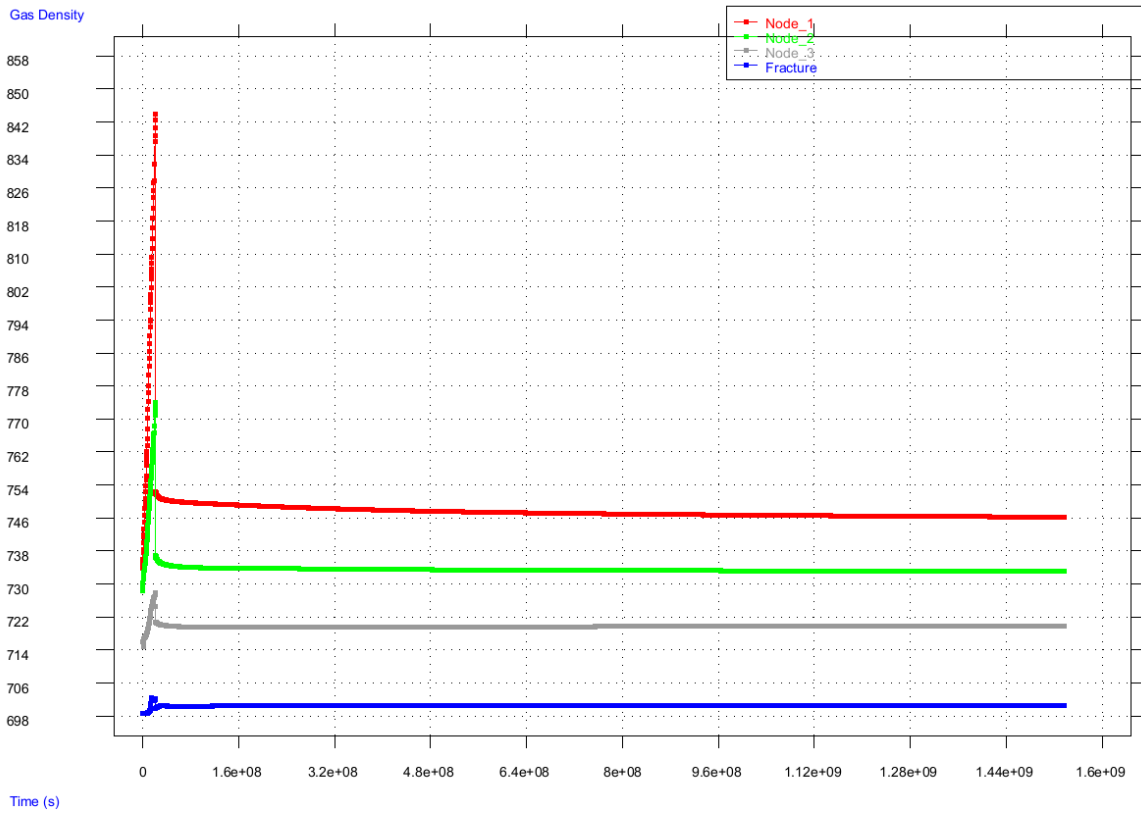


Figure 17.54.2 - Gas density plotted against time in run A2

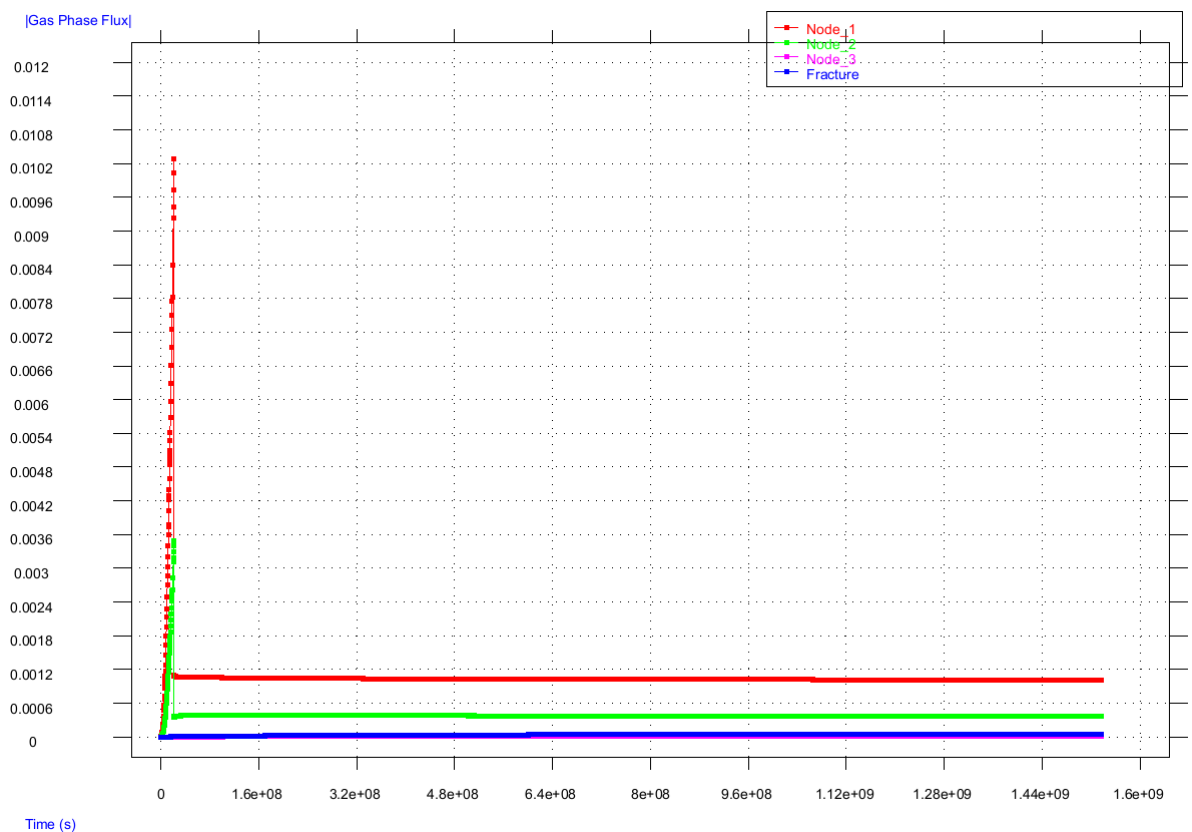


Figure 17.54.3 - Gas phase flux plotted against time in run A2

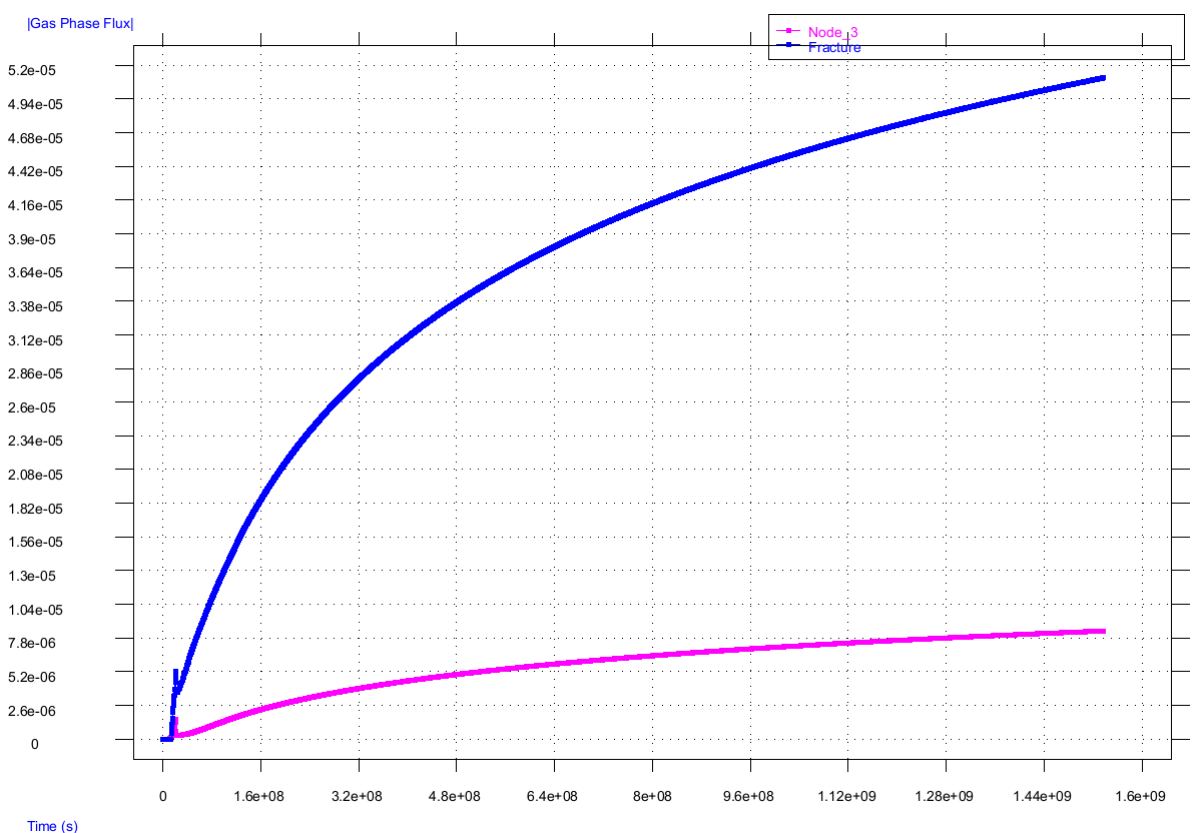


Figure 17.54.4 - Gas phase flux plotted against time in run A2

17.55. Case B2

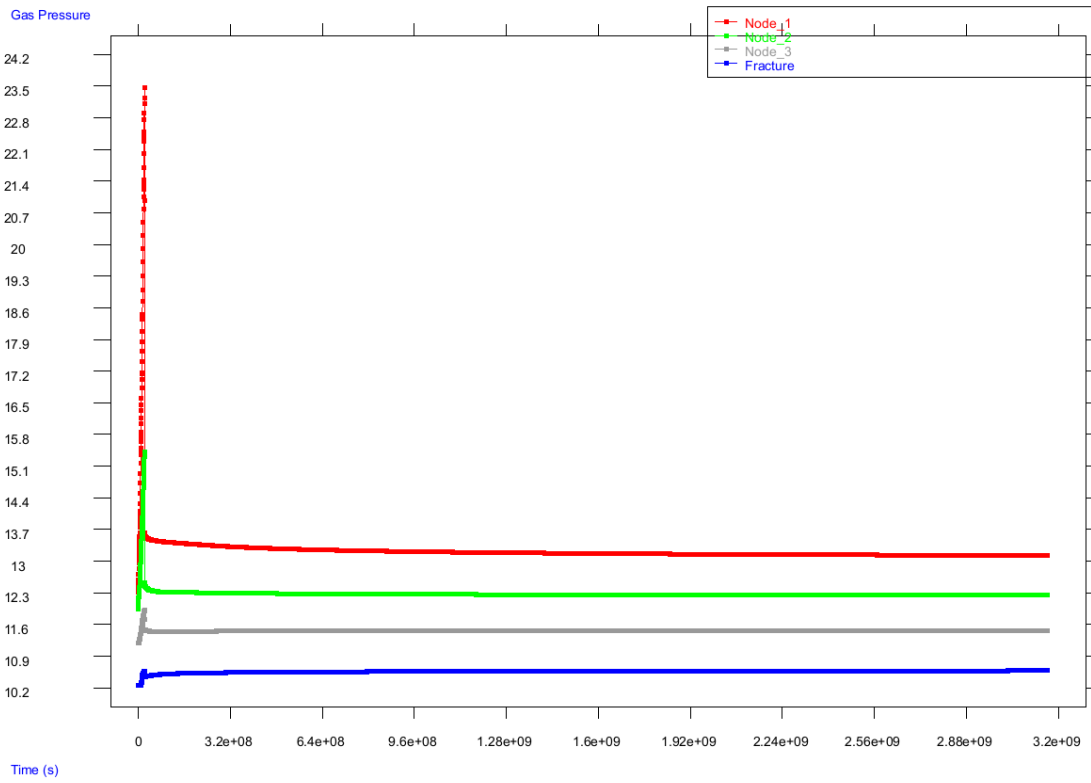


Figure 17.55.1 - Gas pressure plotted against time in run B2

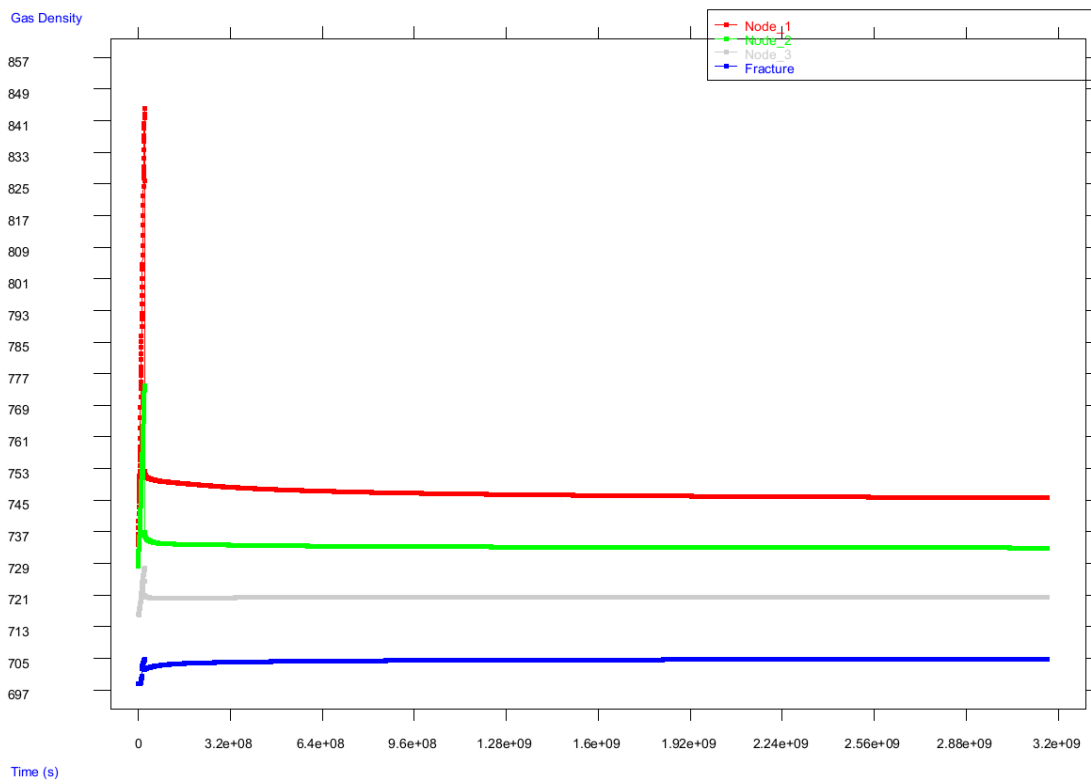


Figure 17.55.2 - Gas density plotted against time in run B2

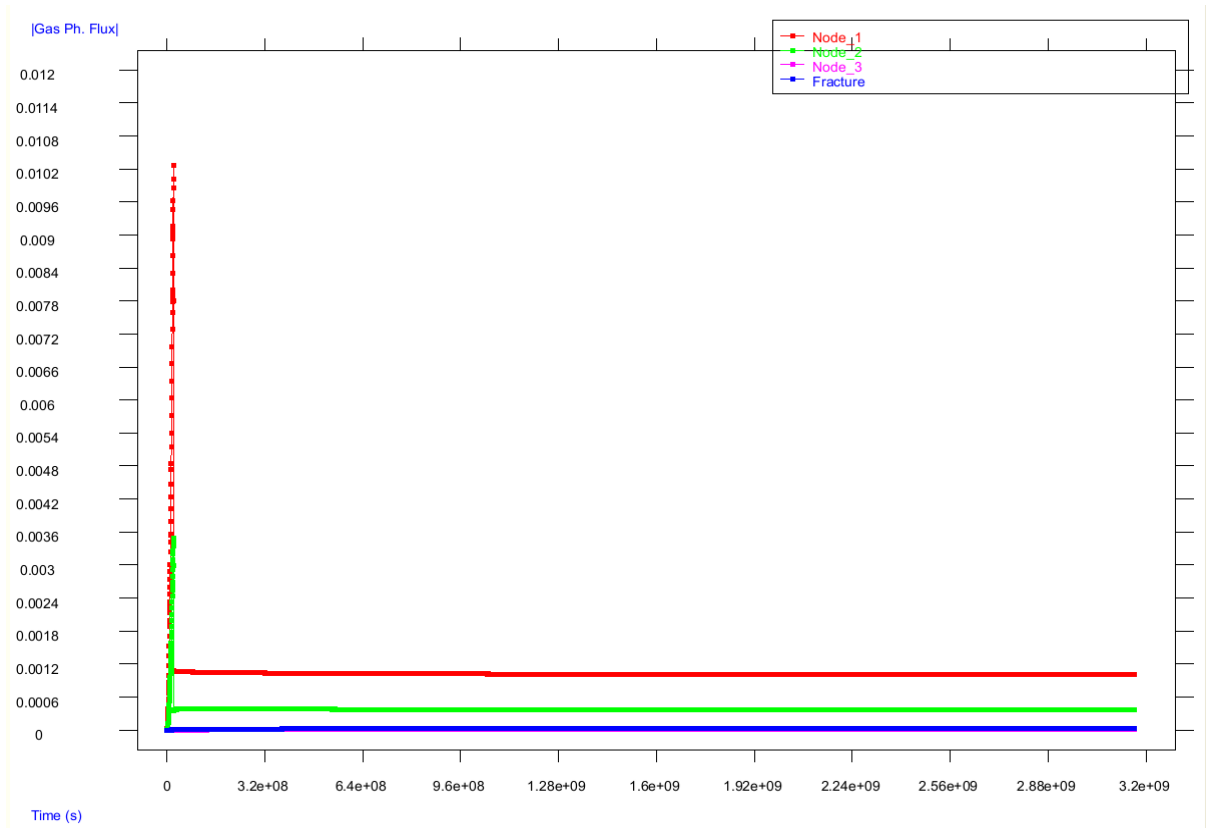


Figure 17.55.3 - Gas phase flux plotted against time in run B2

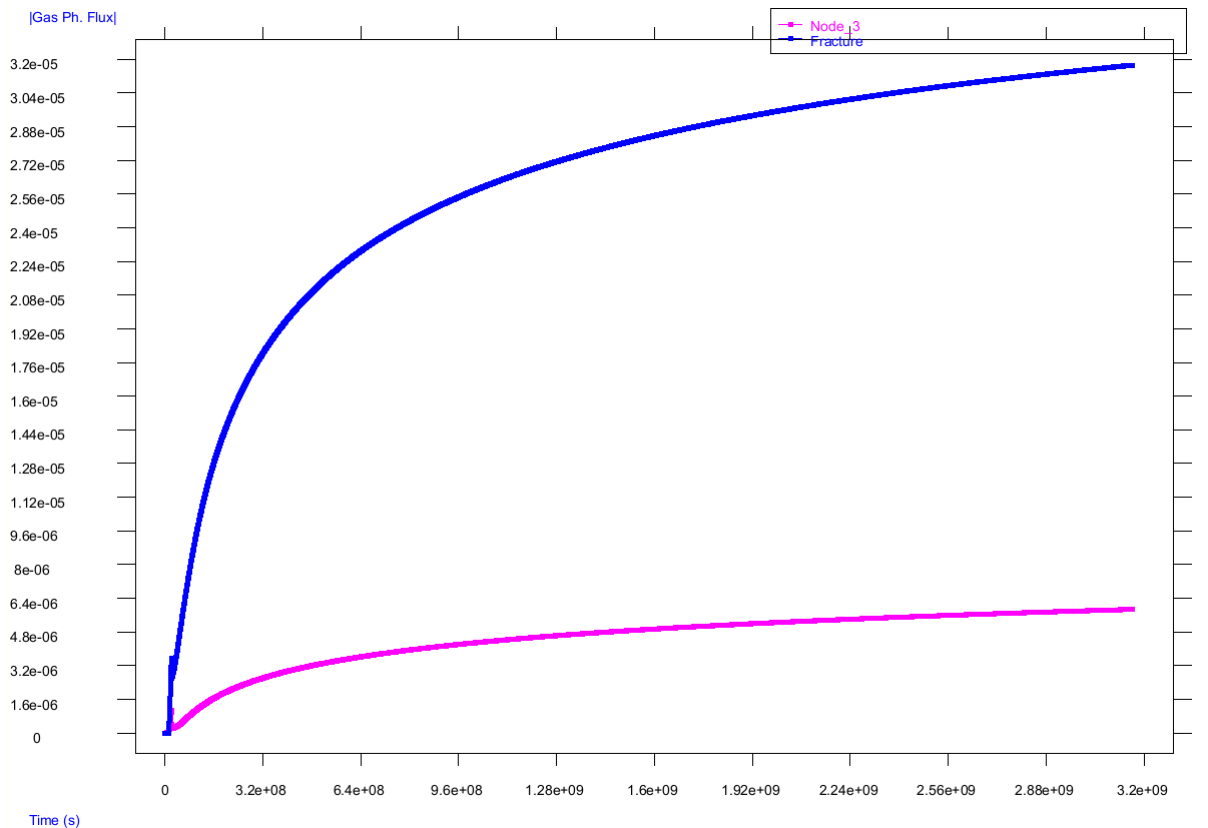


Figure 17.55.4 - Gas phase flux plotted against time in run B2

17.56. Case C2

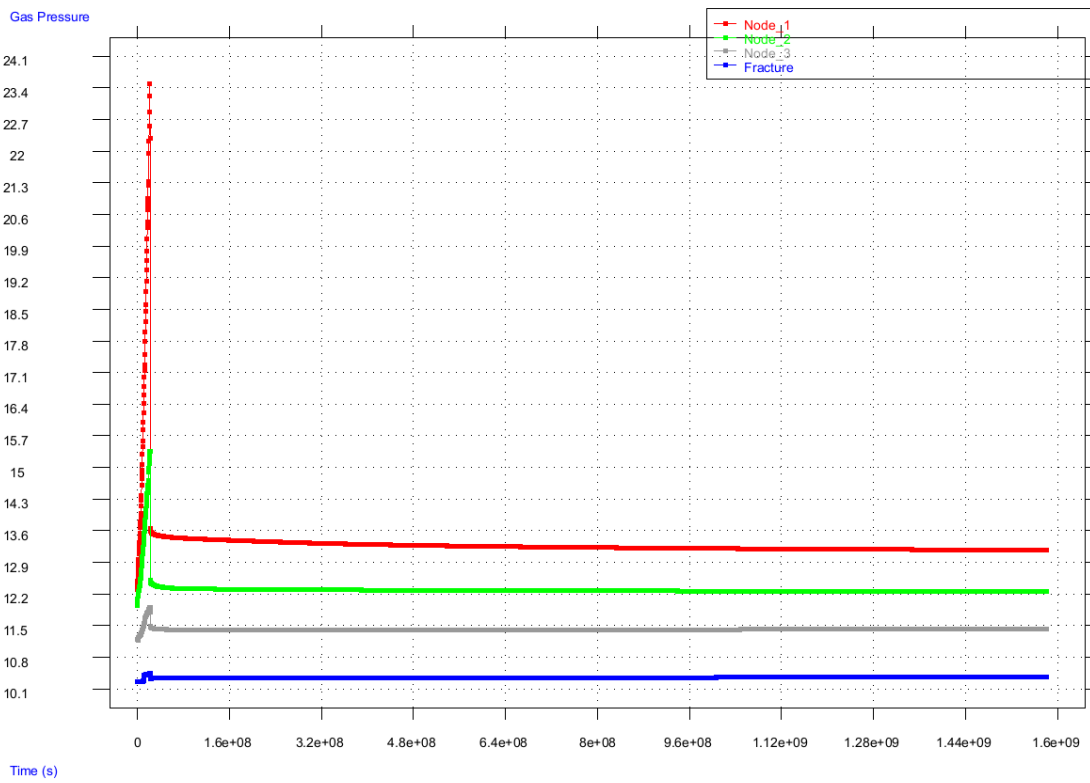


Figure 17.56.1 - Gas pressure plotted against time in run C2

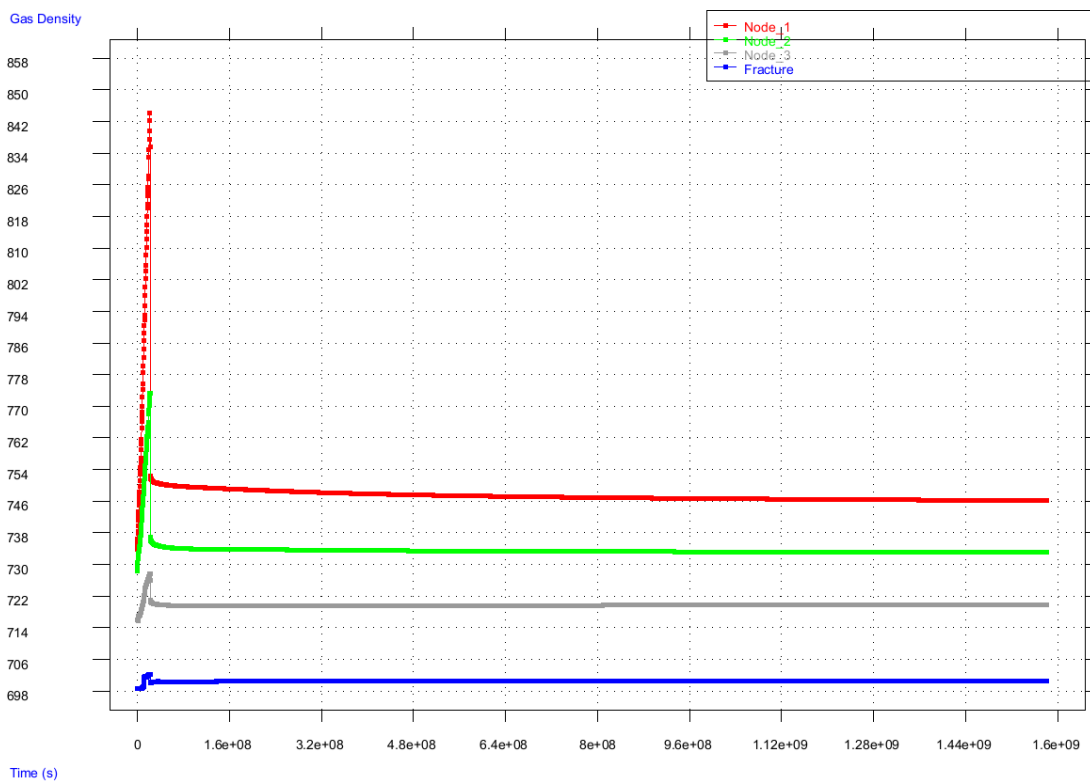


Figure 17.56.2 - Gas density plotted against time in run C2

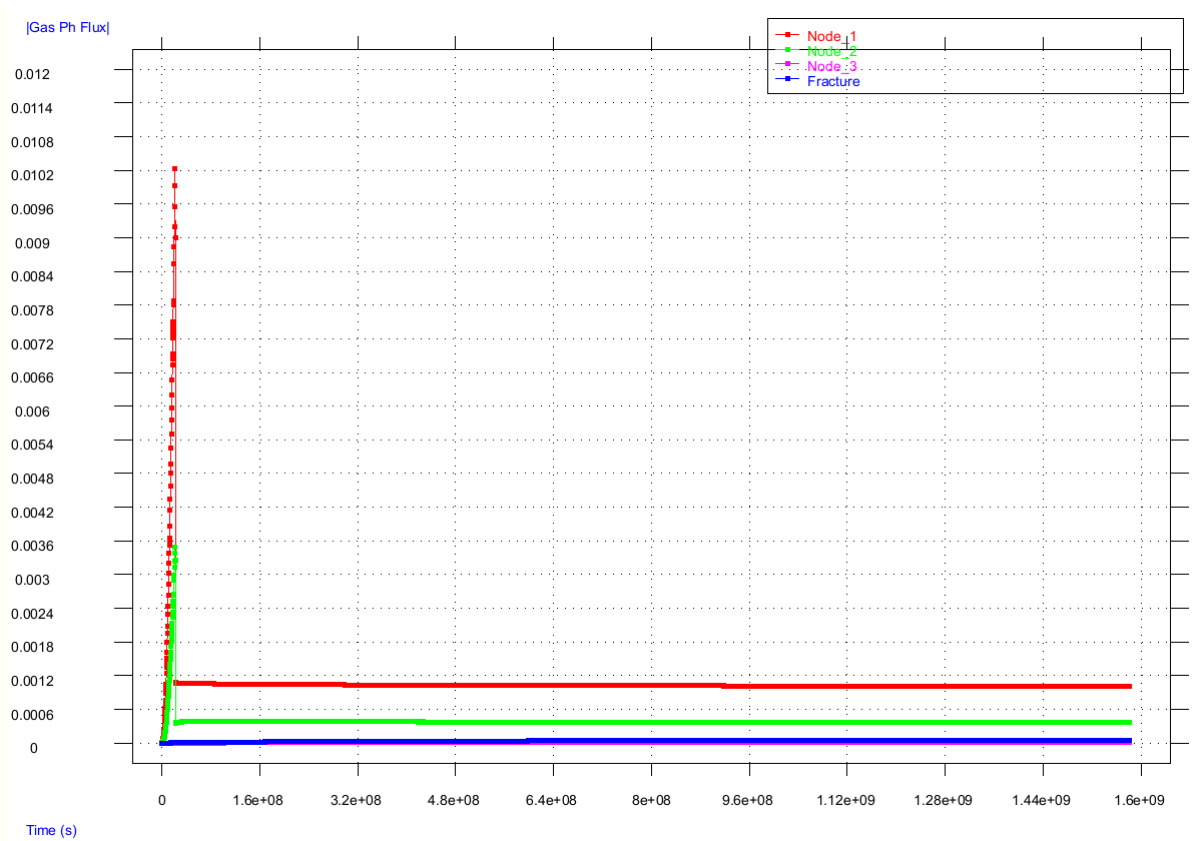


Figure 17.56.3 - Gas phase flux plotted against time in run C2

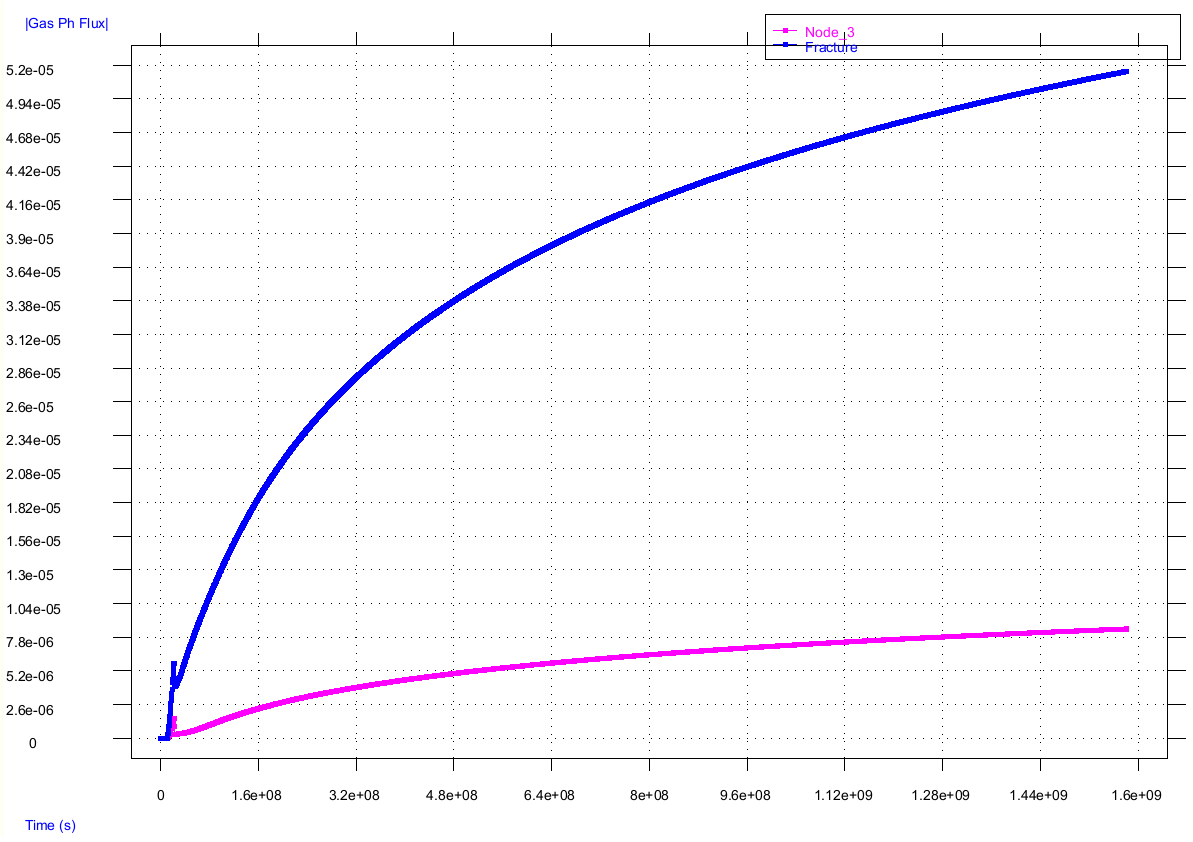


Figure 17.56.4 - Gas density plotted against time in run C2

17.57. Case D2

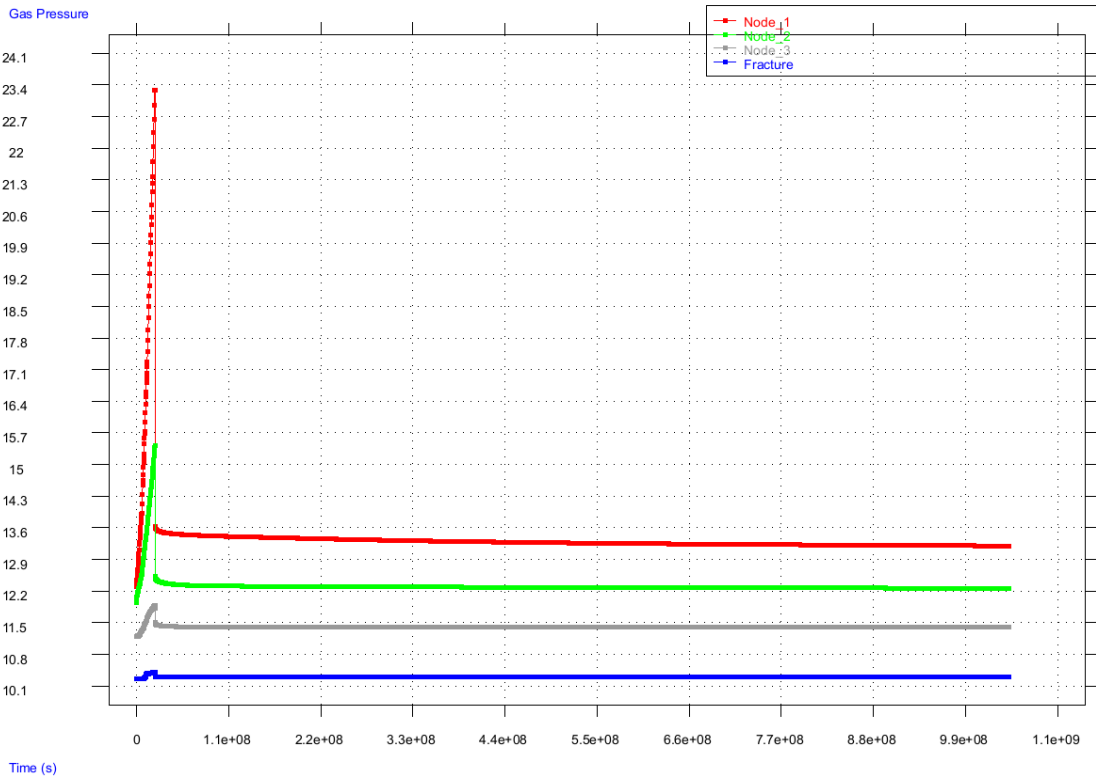


Figure 17.57.1 - Gas pressure plotted against time in run D2

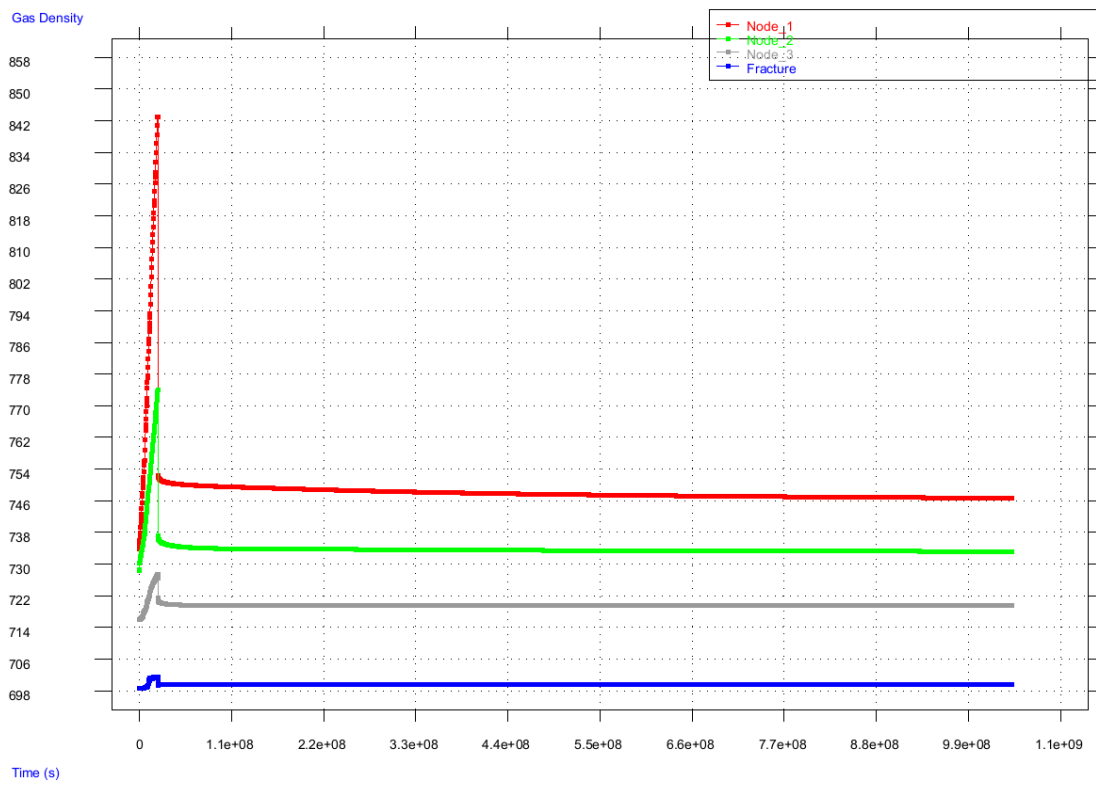


Figure 17.57.2 - Gas density plotted against time in run D2

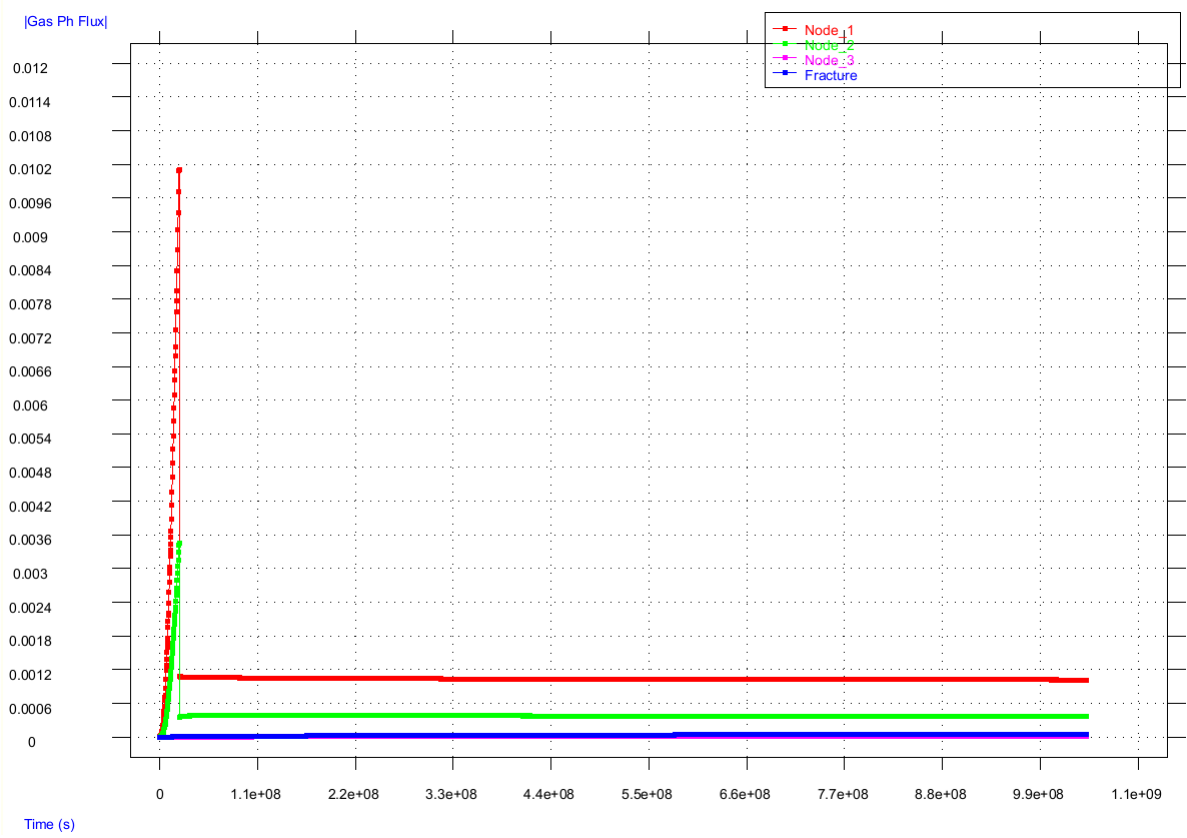


Figure 17.57.3 - Gas phase flux plotted against time in run D2

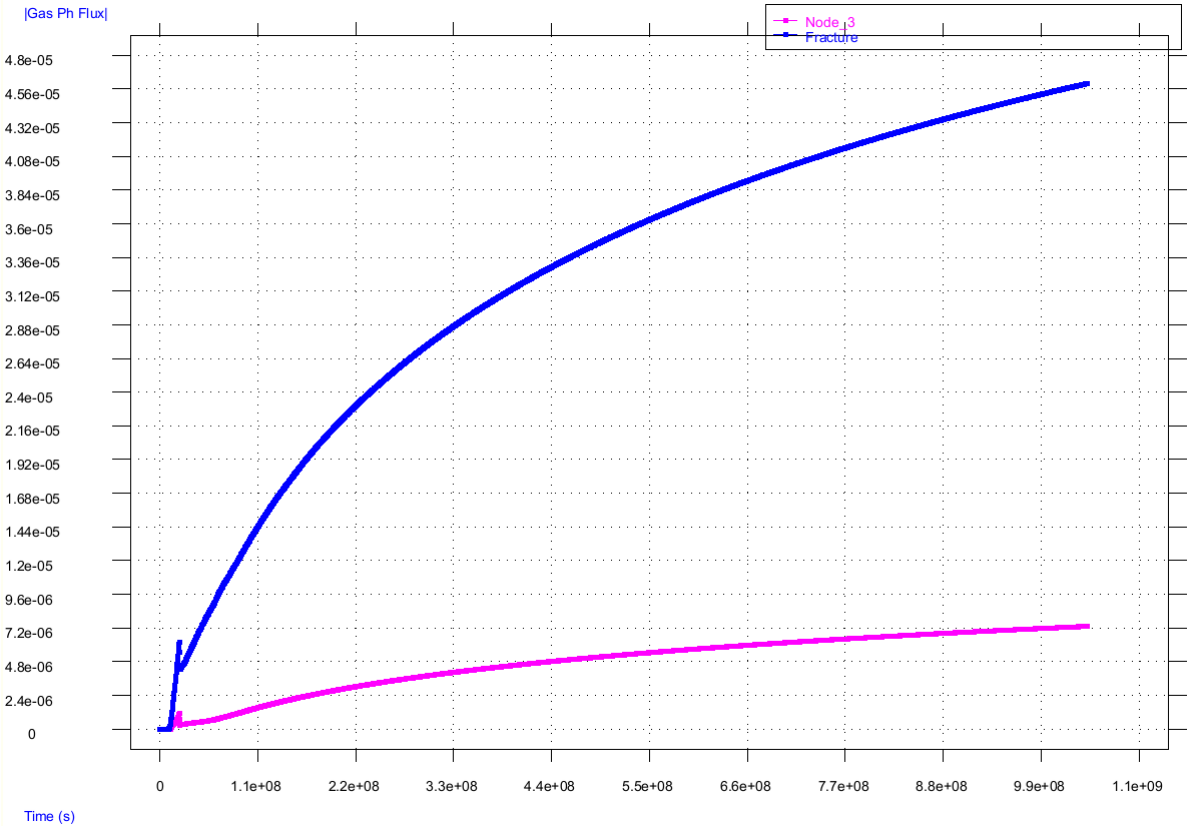


Figure 17.57.4 - Gas phase flux plotted against time in run D2

17.1. Tables

GiD is equipped with an auto-limit function for the colour interval representing the changes in aquifer properties versus time. The auto-limit function is adjusted to the higher and lower bounds of the values present throughout the 100 simulated years. Hence the values from the auto-limited scales can be used to estimate the extremal values of a respective property.

Simulation	Estimated Breakthrough time by means of nearest time-step			Maximum values at CO ₂ breakthrough		
	GiD Step #	Time (s)	Time (d)	Gas pressure [MPa]	Gas density [Kg/m ³]	Gas phase flux [m/s]
Case A	80	2.20939e7	255.71	23.479	844.28	0.010307
Case B	98	2.21236e7	256.06	23.503	844.45	0.010304
Case C	83	2.21282e7	256.11	23.506	844.47	0.010302
Case D	100	2.21453e7	256.31	23.520	844.57	0.010287
Case A2	81	2.20798e7	255,55	23.468	844.21	0.010304
Case B2	107	2.21263e7	256,09	23.502	844.44	0.010295
Case C2	95	2.21712e7	256,61	23.504	844.46	0.010270
Case D2	83	2.05620e7	237.99	23.337	843.29	0.010119

Table 17.1.1 – The estimated breakthrough time and maximum values for gas pressure, gas density and |Gas phase flux|.

Appendix VIII

Stress in lateral direction - S_{xx}

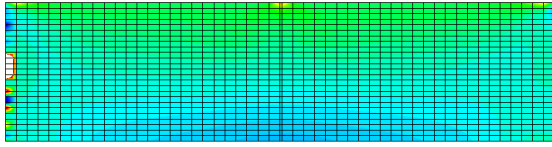
Appendix VII contains a range of graphical representations for the lateral stress, S_{xx} , through 100 years of simulated carbon dioxide injection. There are a total of 8 cases or runs with a maximum of 11 images representing the respective times of injection. However, some cases are incomplete with respect to total simulation time and images. This is due to convergence problems.

Each set of images have their respective gradient color indicator which illustrates the saturation condition at any given time and position. The higher limit is always 6.0 and the lower limit (-3.0).

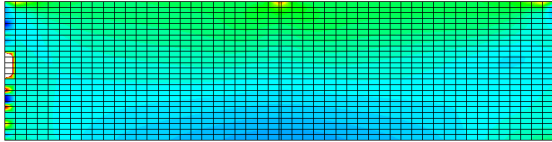
At the left hand side of all the figures in appendix VII there are several errors or anomalies that are not related to the results of the simulation. These spots are assumed to be descendants from the grid input files created in visual retraso or an error in the RCB code itself.

The gradient values represent the total stress in the respective direction. The x and y axis are extending positively from the lower left hand side corner. All negative values represent compression, while positive values represent tension. [Sebastia Olivella]

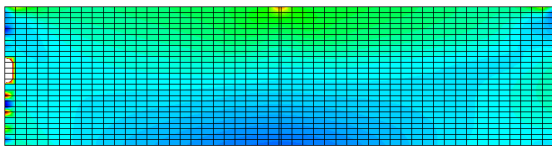
17.2. Case A



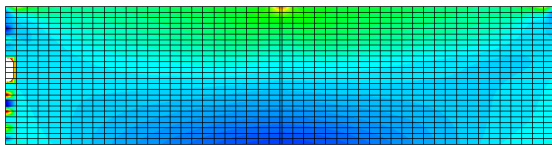
(a1) – Lateral stress after 1 month



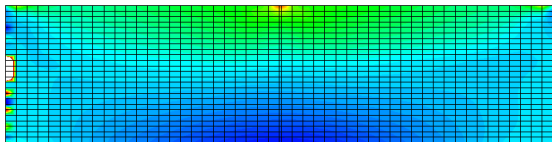
(a2) – Lateral stress after 3 months



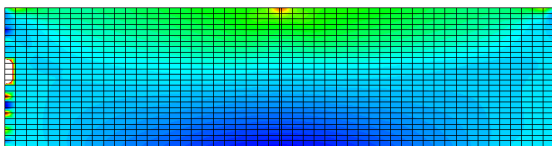
(a3) – Lateral stress after 9 months



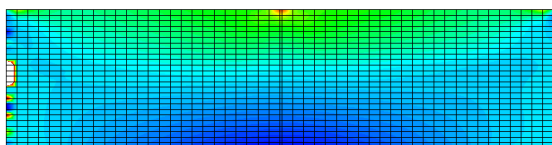
(a4) – Lateral stress after 2 years



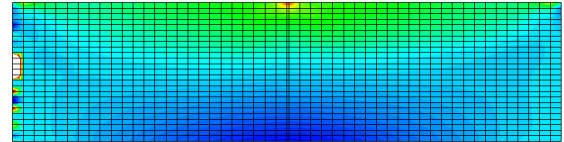
(a5) – Lateral stress after 5 years



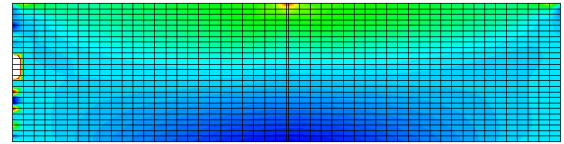
(a6) – Lateral stress after 10 years



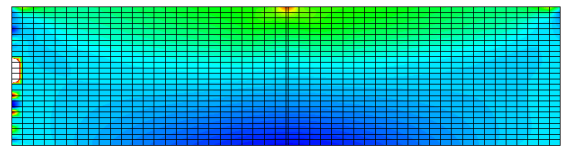
(a7) – Lateral stress after 15 years



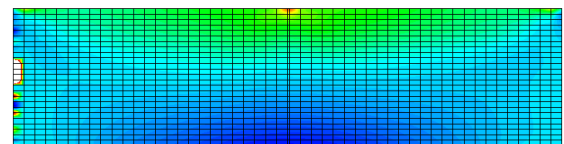
(a8) – Lateral stress after 30 years



(a9) – Lateral stress after 50 years



(a10) – Lateral stress after 75 years



(a11) – Lateral stress after 100 years

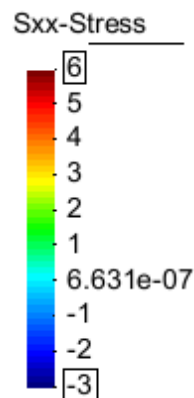
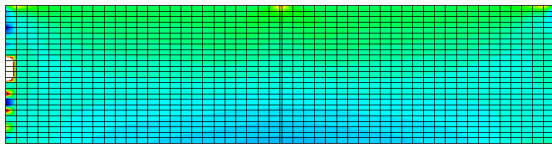
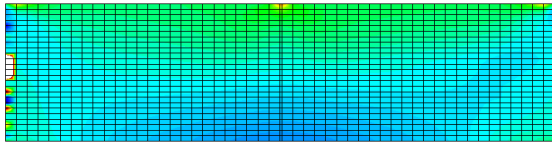


Figure 17.1.1 - Graphical representation of the change in lateral stress over 100 years.

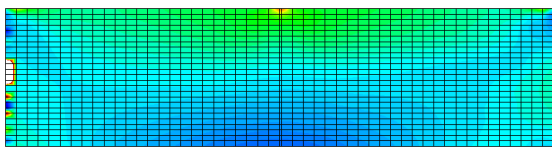
17.3. Case B



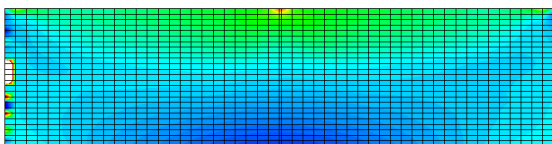
(b1) – Lateral stress after 1 month



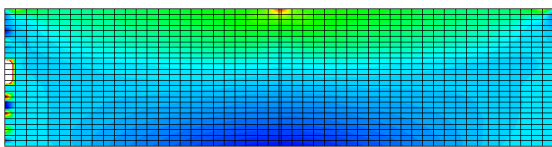
(b2) – Lateral stress after 3 months



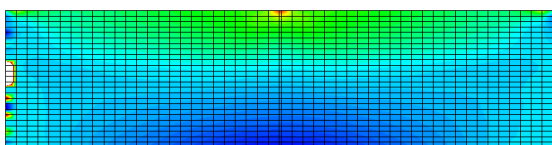
(b3) – Lateral stress after 9 months



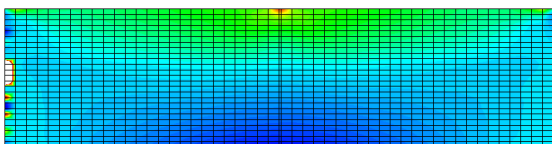
(b4) – Lateral stress after 2 years



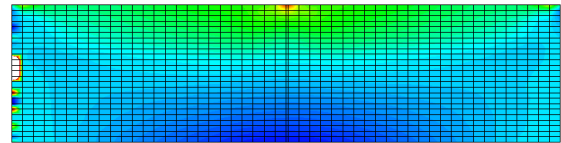
(b5) – Lateral stress after 5 years



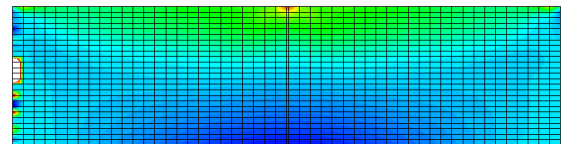
(b6) – Lateral stress after 10 years



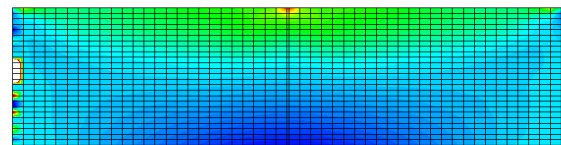
(b7) – Lateral stress after 15 years



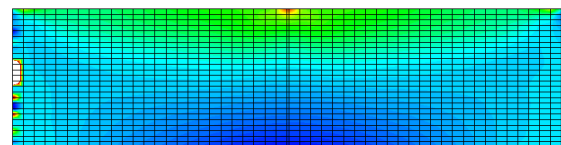
(b8) – Lateral stress after 30 years



(b9) – Lateral stress after 50 years



(b10) – Lateral stress after 75 years



(b11) – Lateral stress after 100 years

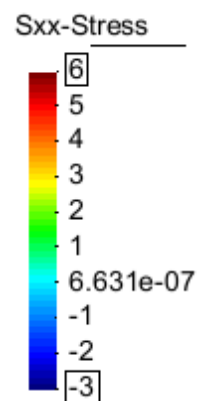
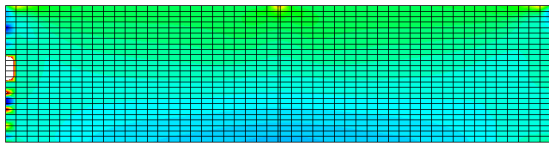
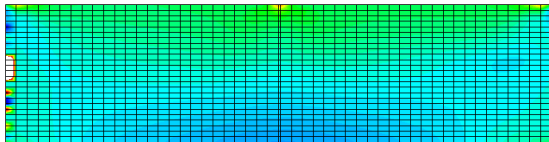


Figure 17.3.1 - Graphical representation of the change in lateral stress over 100 years.

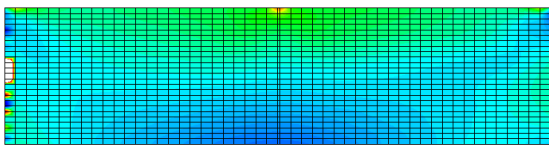
17.4. Case C



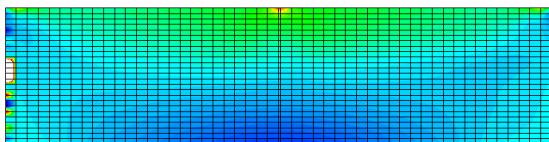
(d1) – Lateral stress after 1 month



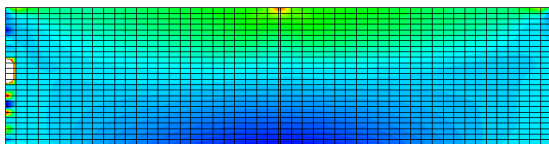
(d2) – Lateral stress after 3 months



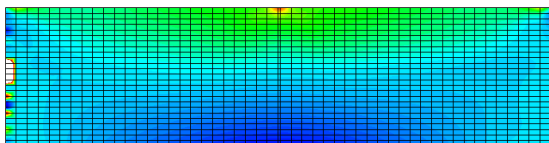
(d3) – Lateral stress after 9 months



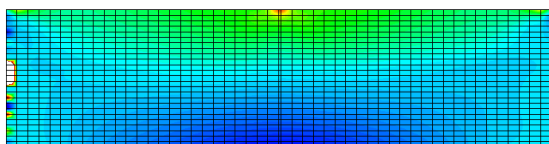
(d4) – Lateral stress after 2 years



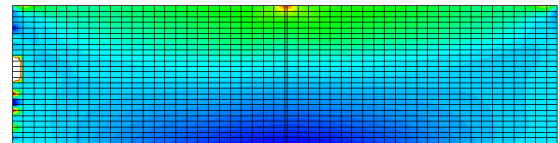
(d5) – Lateral stress after 5 years



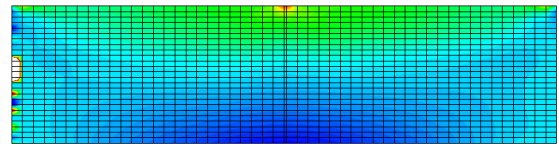
(d6) – Lateral stress after 10 years



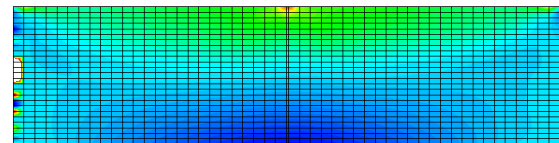
(d7) – Lateral stress after 15 years



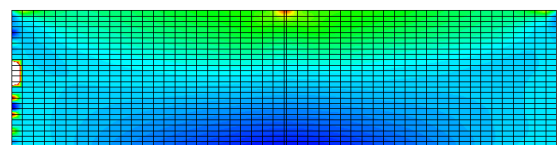
(db) – Lateral stress after 30 years



(d9) – Lateral stress after 50 years



(d10) – Lateral stress after 75 years



(d11) – Lateral stress after 100 years

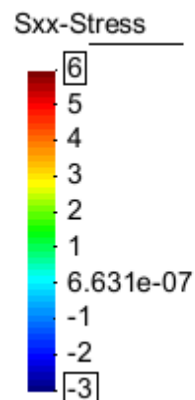
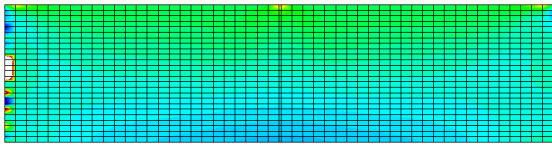
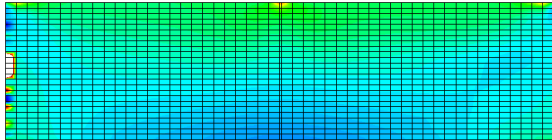


Figure 17.4.1 - Graphical representation of the change in lateral stress over 100 years.

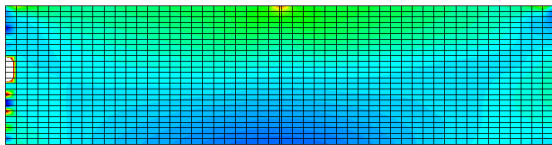
17.5. Case D



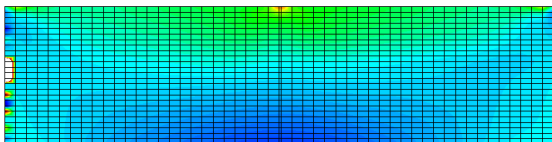
(d1) – Lateral stress after 1 month



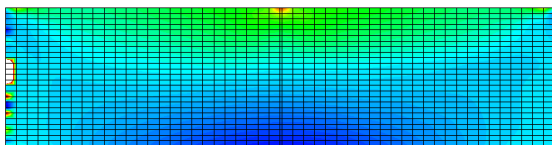
(d2) – Lateral stress after 3 months



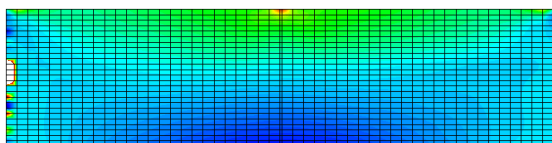
(d3) – Lateral stress after 9 months



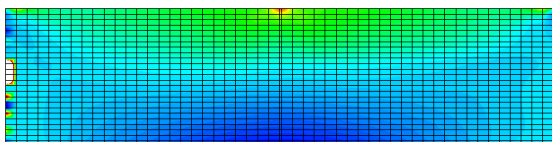
(d4) – Lateral stress after 2 years



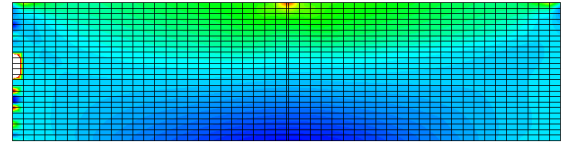
(d5) – Lateral stress after 5 years



(d6) – Lateral stress after 10 years



(d7) – Lateral stress after 15 years



(d8) – Lateral stress after 30 years

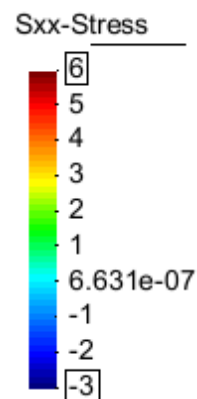
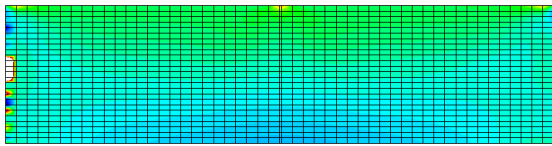
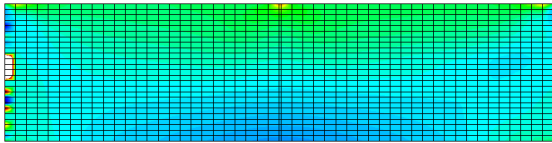


Figure 17.5.1 - Graphical representation of the change in lateral stress over 30 years.

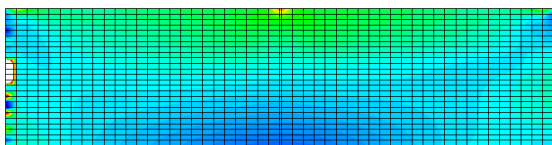
17.6. Case A2



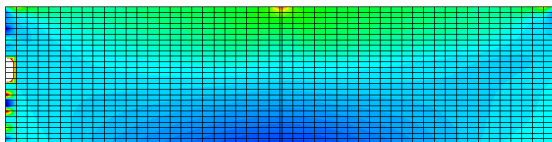
(A1) – Lateral stress after 1 month



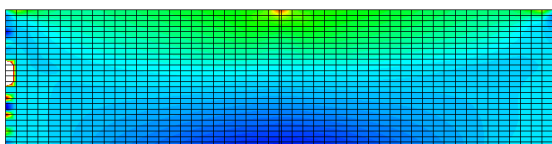
(A2) – Lateral stress after 3 months



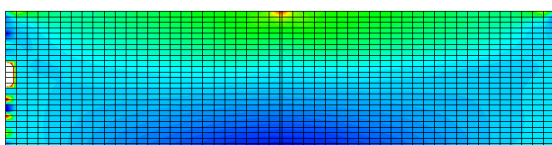
(A3) – Lateral stress after 9 months



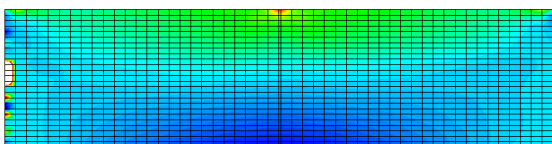
(A4) – Lateral stress after 2 years



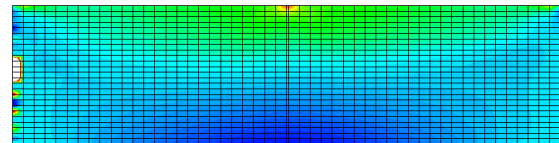
(A5) – Lateral stress after 5 years



(A6) – Lateral stress after 10 years



(A7) – Lateral stress after 15 years



(A8) – Lateral stress after 30 years

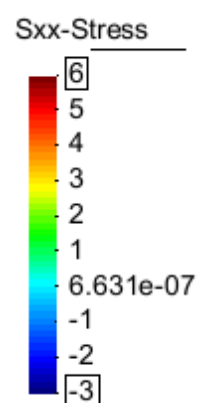
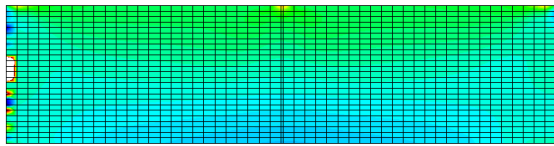
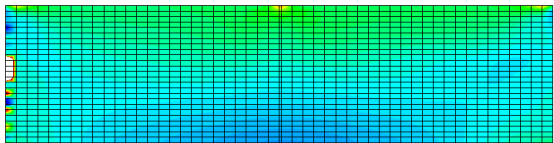


Figure 17.6.1 - Graphical representation of the change in lateral stress over 100 years.

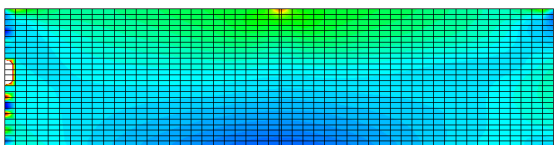
17.7. Case B2



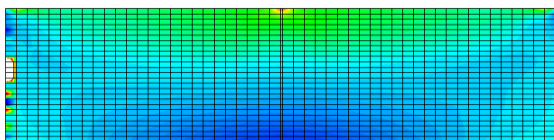
(B1) – Lateral stress after 1 month



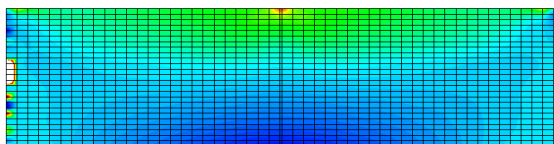
(B2) – Lateral stress after 3 months



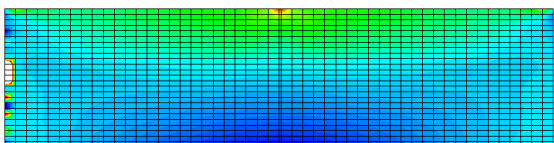
(B3) – Lateral stress after 9 months



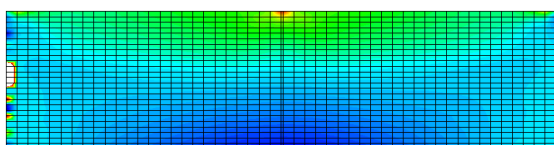
(B4) – Lateral stress after 2 years



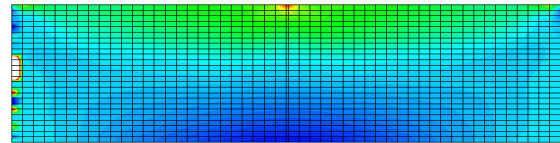
(B5) – Lateral stress after 5 years



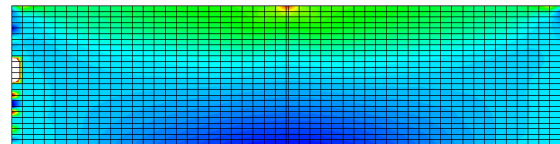
(B6) – Lateral stress after 10 years



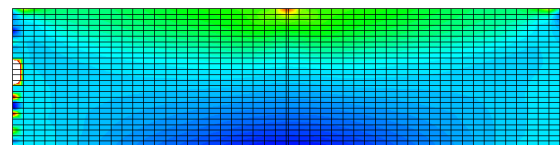
(B7) – Lateral stress after 15 years



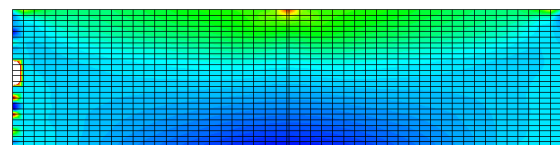
(B8) – Lateral stress after 30 years



(B9) – Lateral stress after 50 years



(B10) – Lateral stress after 75 years



(B11) – Lateral stress after 100 years

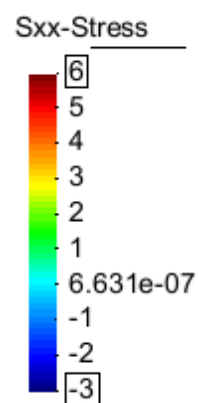
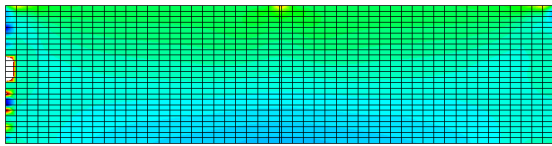
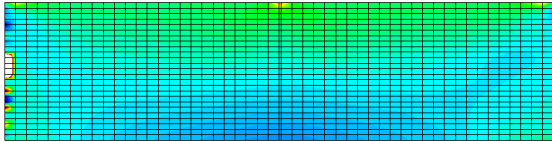


Figure 17.7.1 - Graphical representation of the change in lateral stress over 100 years.

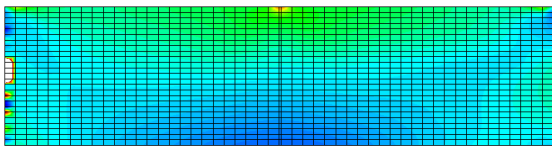
17.8. Case C2



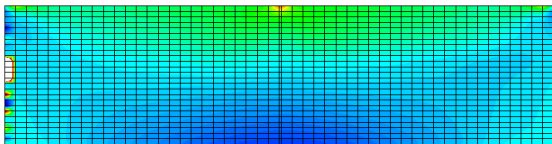
(C1) – Lateral stress after 1 month



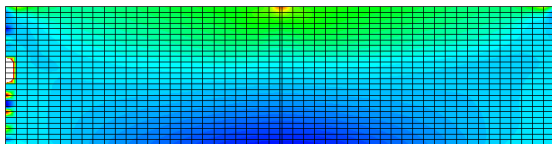
(C2) – Lateral stress after 3 months



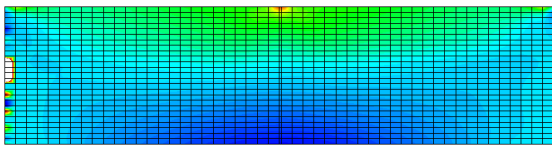
(C3) – Lateral stress after 9 months



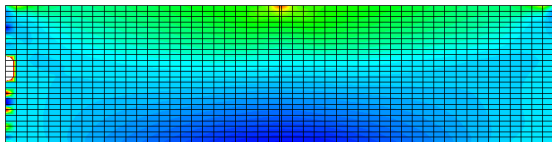
(C4) – Lateral stress after 2 years



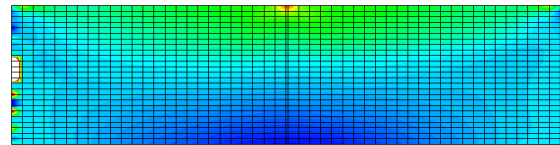
(C5) – Lateral stress after 5 years



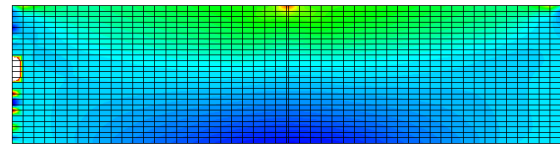
(C6) – Lateral stress after 10 years



(C7) – Lateral stress after 15 years



(C8) – Lateral stress after 30 years



(C9) – Lateral stress after 50 years

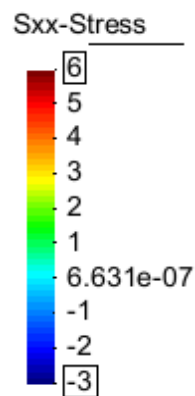
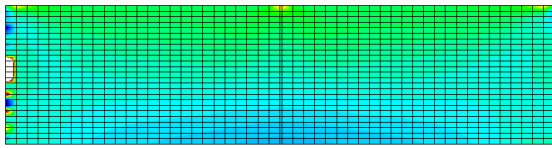
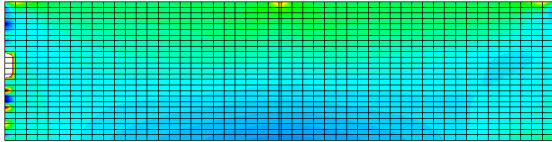


Figure 17.8.1 - Graphical representation of the change in lateral stress over 50 years.

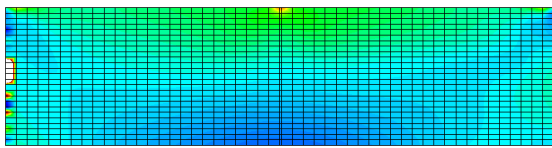
17.9. Case D2



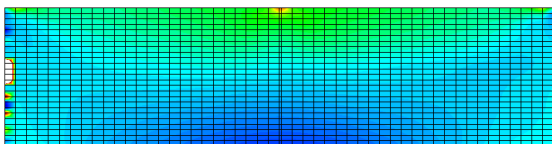
(D1) – Lateral stress after 1 month



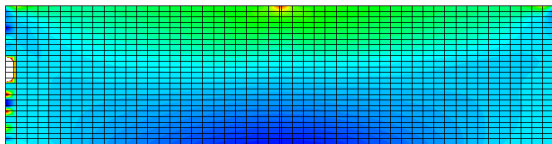
(D2) – Lateral stress after 3 months



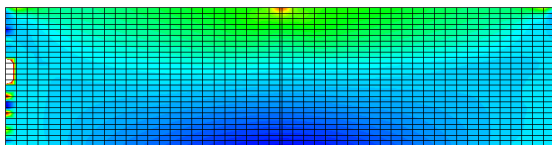
(D3) – Lateral stress after 9 months



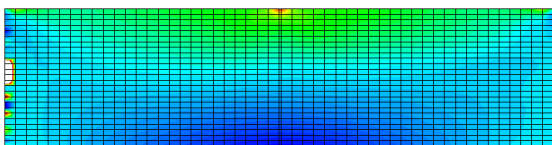
(D4) – Lateral stress after 2 years



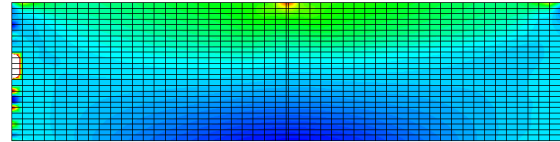
(D5) – Lateral stress after 5 years



(D6) – Lateral stress after 10 years



(D7) – Lateral stress after 15 years



(D8) – Lateral stress after 30 years

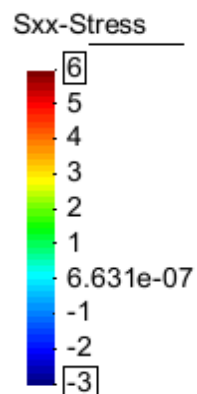


Figure 17.9.1 - Graphical representation of the change in lateral stress over 30 years.

Appendix IIX

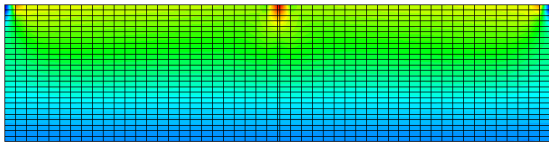
Stress in vertical direction – S_{yy}

Appendix VIII contains a range of graphical representations for the vertical lateral stress, S_{yy} , through 100 years of simulated carbon dioxide injection. There are a total of 8 cases or runs with a maximum of 5 images representing the respective times of injection. However, some cases are incomplete with respect to total simulation time and images. This is due to convergence problems.

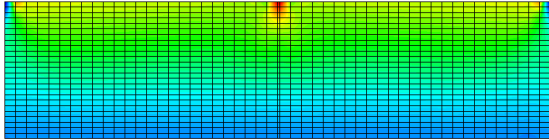
Each set of images have their respective gradient color indicator which illustrates the saturation condition at any given time and position. The higher limit is always 10.0 and the lower limit (-3.0).

The gradient values represent the total stress in the respective direction. The x and y axis are extending positively from the lower left hand side corner. All negative values represent compression, while positive values represent tension. [Sebastia Olivella]

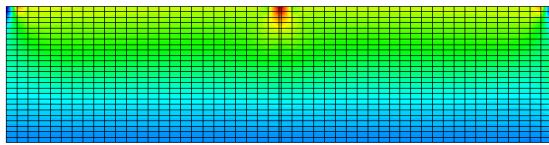
17.10. Case A



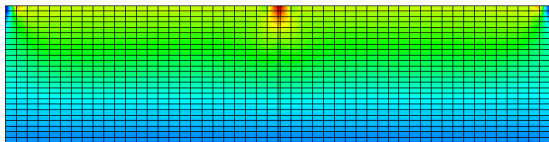
(A1) – Vertical stress after 1 month



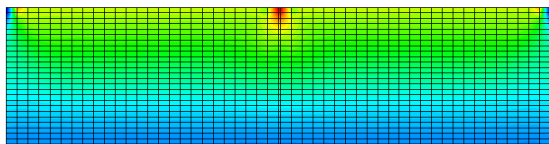
(A2) – Vertical stress after 3 months



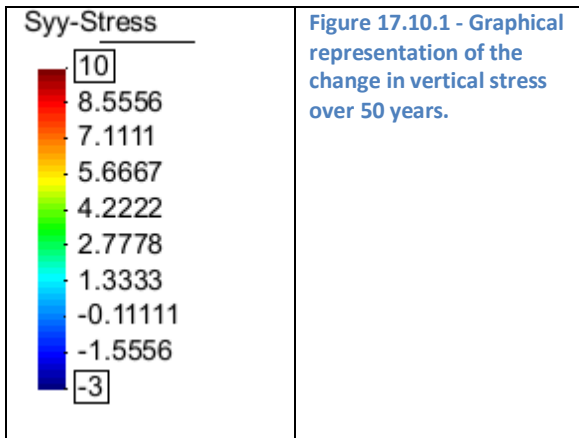
(A3) – Vertical stress after 9 months



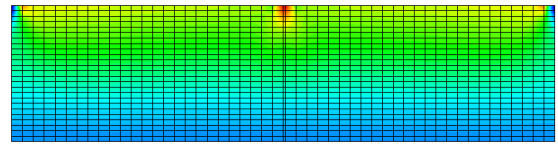
(A4) – Vertical stress after 2 years



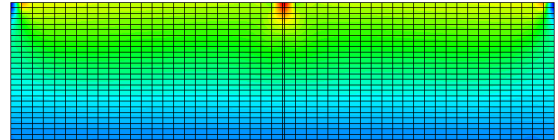
(A5) – Vertical stress after 50 years



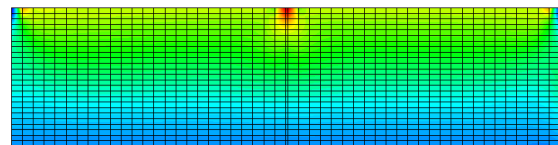
17.11. Case B



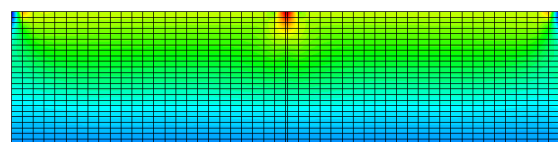
(B1) – Vertical stress after 1 month



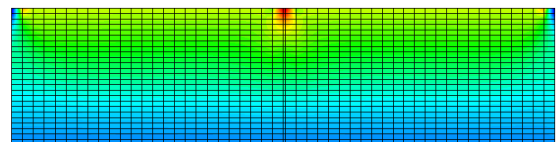
(B2) – Vertical stress after 3 months



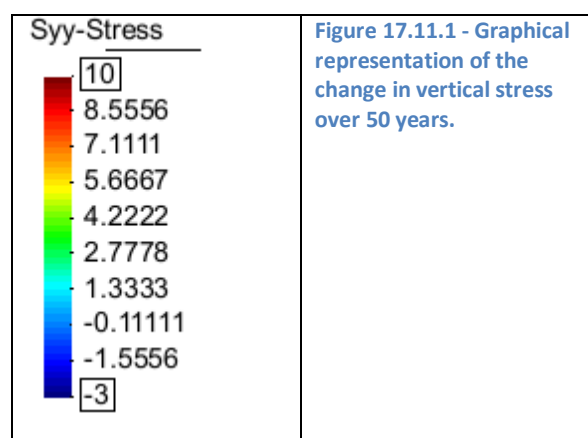
(B3) – Vertical stress after 9 months



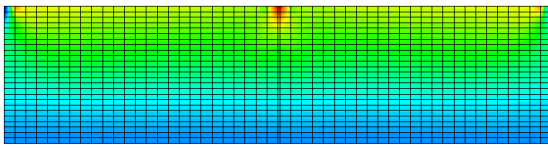
(B4) – Vertical stress after 2 years



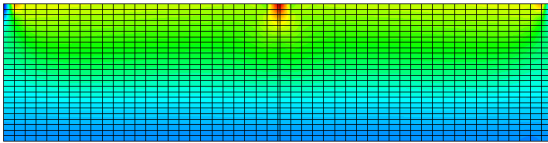
(B5) – Vertical stress after 50 years



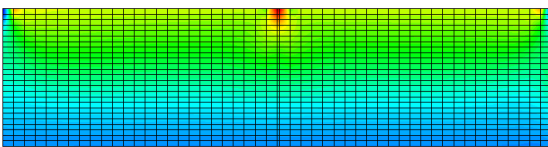
17.12. Case C



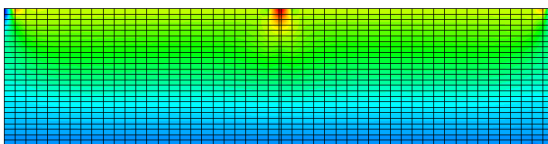
(C1) – Vertical stress after 1 month



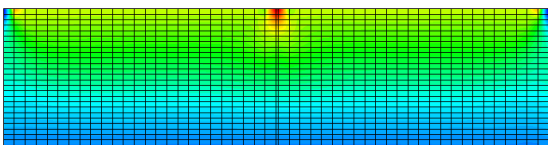
(C2) – Vertical stress after 3 months



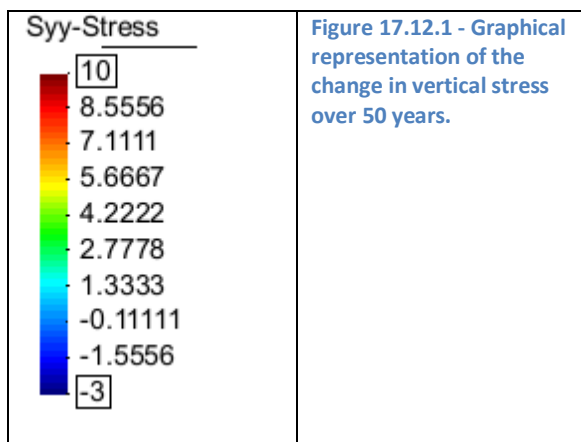
(C3) – Vertical stress after 9 months



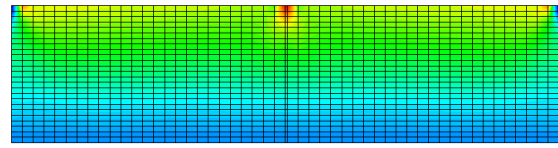
(C4) – Vertical stress after 2 years



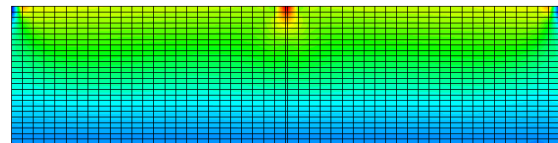
(C5) – Vertical stress after 50 years



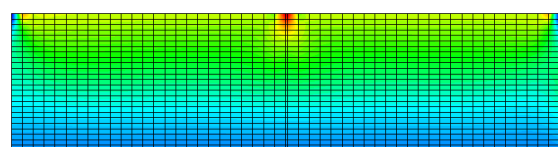
17.13. Case D



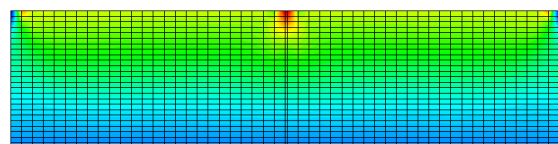
(D1) – Vertical stress after 1 month



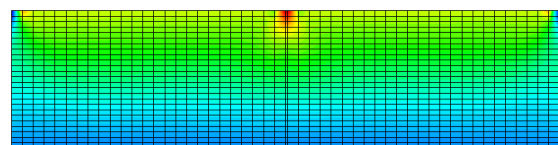
(D2) – Vertical stress after 3 months



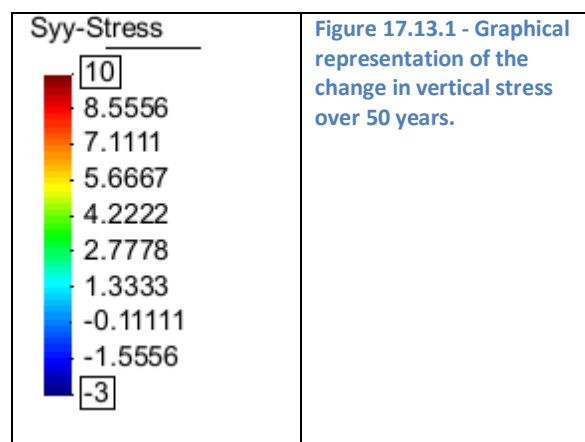
(D3) – Vertical stress after 9 months



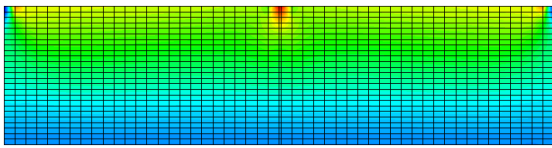
(D4) – Vertical stress after 2 years



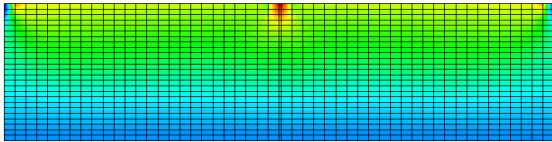
(D5) – Vertical stress after 50 years



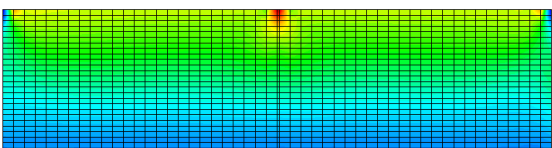
17.14. Run A2



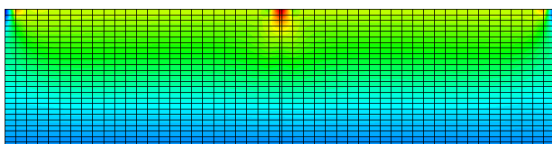
(A1) – Vertical stress after 1 month



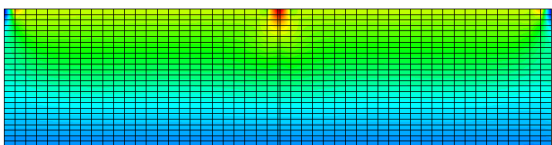
(A2) – Vertical stress after 3 months



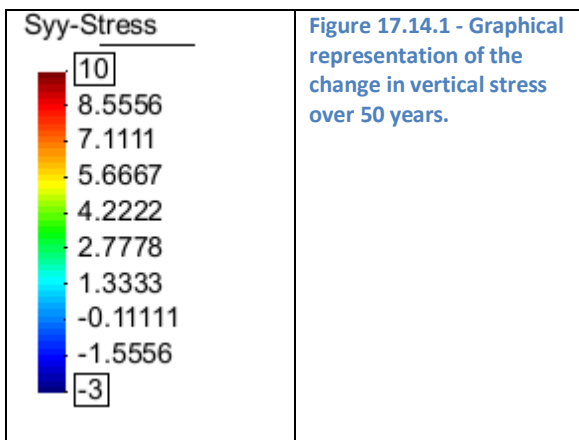
(A3) – Vertical stress after 9 months



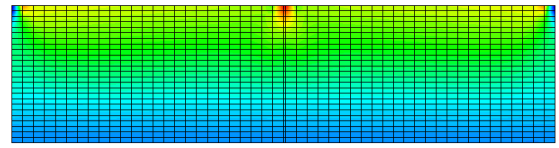
(A4) – Vertical stress after 2 years



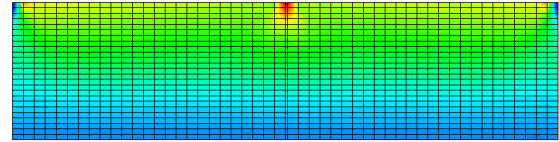
(A9) – Vertical stress after 50 years



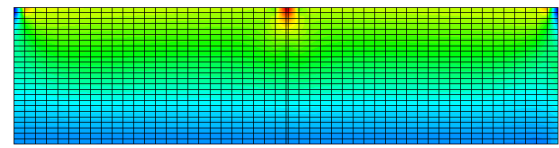
17.15. Run B2



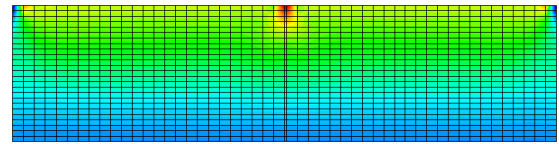
(B1) – Vertical stress after 1 month



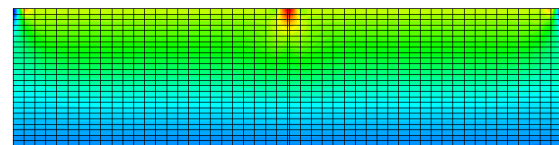
(B2) – Vertical stress after 3 months



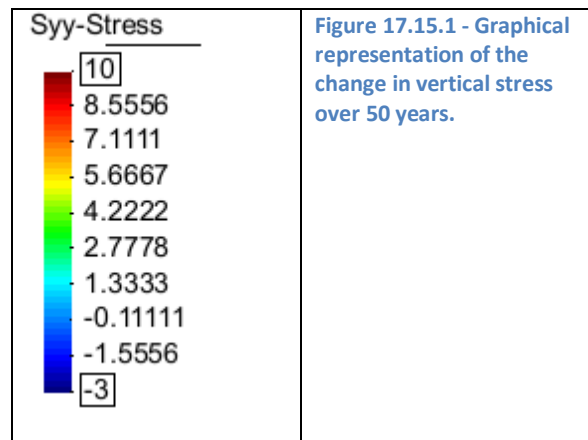
(B3) – Vertical stress after 9 months



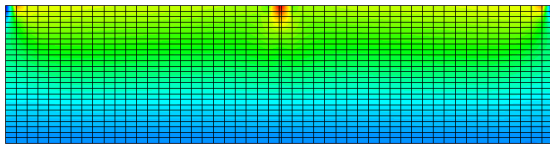
(B4) – Vertical stress after 2 years



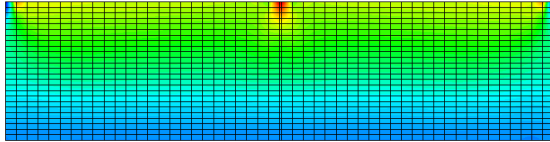
(B5) – Vertical stress after 50 years



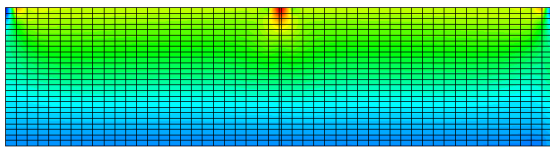
17.16. Run C2



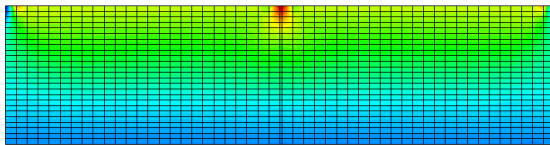
(C1) – Vertical stress after 1 month



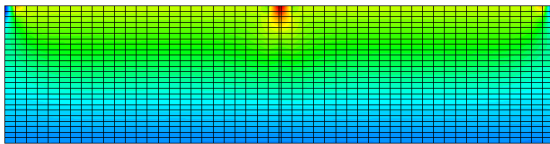
(C2) – Vertical stress after 3 months



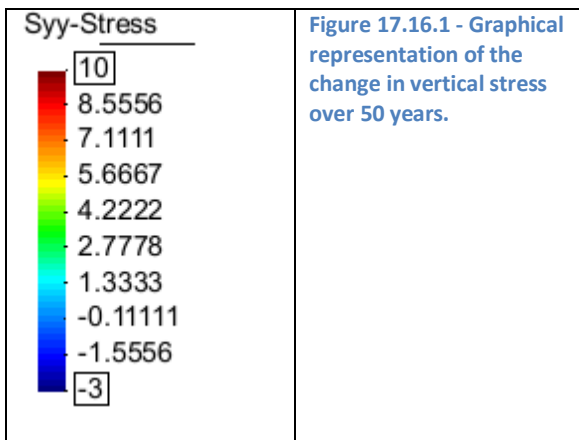
(C3) – Vertical stress after 9 months



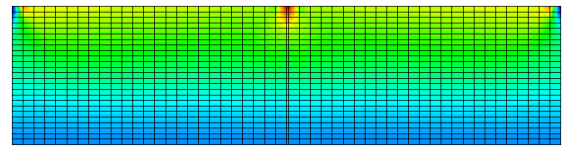
(C4) – Vertical stress after 2 years



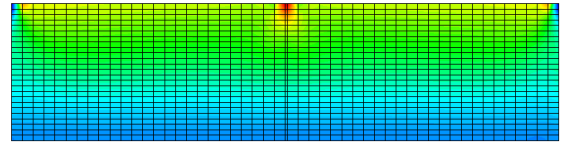
(C5) – Vertical stress after 50 years



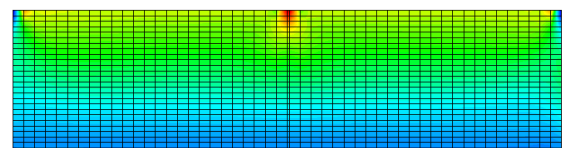
17.17. Run D2



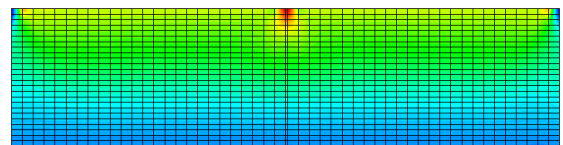
(C1) – Vertical stress after 1 month



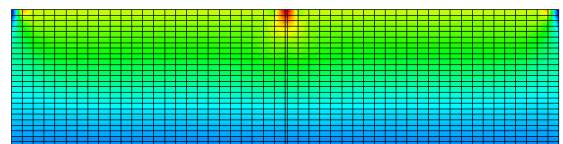
(C2) – Vertical stress after 3 months



(C3) – Vertical stress after 9 months



(C4) – Vertical stress after 2 years



(C5) – Vertical stress after 50 years

